Verstuiving van alternatieve brandstoffen
in middelsnellopende dieselmotoren

Spray Atomization of Alternative Fuels
in Medium Speed Diesel Engines

Jonas Galle

Promotor: prof. dr. ir. S. Verhelst
Proefschrift ingediend tot het behalen van de graad van
Doctor in de Ingenieurswetenschappen: Werktuigkunde-Elektrotechniek

Vakgroep Mechanica van Stroming, Warmte en Verbranding
Voorzitter: prof. dr. ir. J. Vierendeels
Faculteit Ingenieurswetenschappen en Architectuur
Academiejaar 2013 - 2014

UNIVERSITEIT
GENT

ISBN 978-90-8578-653-5
NUR 977, 978
Wettelijk depot: D/2013/10.500/86

Universiteit Gent
Faculteit Ingenieurswetenschappen en Architectuur
Vakgroep Mechanica van Stroming, Warmte en Verbranding

Verstuiving van alternatieve brandstoffen in middelsnellopende dieselmotoren

Spray Atomization of Alternative Fuels in Medium Speed Diesel Engines

Jonas Galle

Department of Flow, Heat and Combustion Mechanics

Proefschrift tot het bekomen van de graad van
Doctor in de Ingenieurswetenschappen:
Werktuigkunde-elektrotechniek
Academiejaar 2013-2014

Universiteit Gent
Faculteit Ingenieurswetenschappen en Architectuur
Vakgroep Mechanica van Stroming, Warmte en Verbranding

Promotor: Prof. Dr. Ir. Sebastian Verhelst

Universiteit Gent
Faculteit Ingenieurswetenschappen en Architectuur

Vakgroep Mechanica van Stroming, Warmte en Verbranding
Sint-Pietersnieuwstraat 41, B-9000 Gent, België

Tel.: +32-9-264.34.53
Fax.: +32-9-264.35.90

Dit werk kwam tot stand in het kader van een specialisatiebeurs van het IWT-Vlaanderen (Instituut voor de aanmoediging van Innovatie door Wetenschap en Technologie in Vlaanderen).

Department of Flow, Heat and Combustion Mechanics

Proefschrift tot het behalen van de graad van
Doctor in de Ingenieurswetenschappen:
Werktuigkunde-elektrotechniek
Academiejaar 2013-2014

Dankwoord

Door dit doctoraat neer te leggen bewijs ik in staat te zijn om zelfstandig onderzoek te verrichten. Maar zonder de steun van anderen zou ik er uiteraard nooit in geslaagd zijn om het voorgelegde resultaat te bereiken. Ik wil hier dan ook de mensen bedanken die mij rechtstreeks of onrechtstreeks geholpen hebben tijdens mijn onderzoek.

Op de eerste plaats dank ik mijn promotor prof. dr. ir. Sebastian Verhelst die mij de mogelijkheid aanbood om te doctoreren, waarvan het onderwerp in de lijn van mijn masterthesis lag. Het onderwerp liet toe om mijn experimentele & praktische interesses te combineren met het theoretische.
Zonder financiële steun zou dit onderzoek echter niet mogelijk geweest zijn. Ik dank dan ook het IWT voor het toekennen van mijn specialisatiebeurs en het FWO en CWO voor het ter beschikking stellen van een krediet voor de aankoop van onderdelen en meetapparatuur van de, toch wel, kapitaalsintensieve meetopstelling die werd opgebouwd. Ook Anglo Belgian Corporation Diesel verdient een speciale vermelding omdat zonder hen het onderwerp en het realiseren van de opstelling niet mogelijk zouden geweest zijn. Hierbij in het bijzonder bedank ik dan ing. Marc Bastiaen, ir. Lieven Vervaeke en ir. Tim Berckmoes.
Een bijzonder dankwoord mag ook toegeschreven worden aan onderzoekers van andere onderzoeks- en vakgroepen die mij rechtstreeks met mijn onderzoek hebben geholpen. Ik denk hierbij aan prof. dr. Roland Verhé (vakgroep Duurzame Organische Scheikunde en Technologie, UGent), die voor contacten zorgde bij leveranciers van oliën en me de geheimen van de oliën mee hielp ontrafelen.
Prof. dr. ir. Jan Wastiels, dr. ir. Johan Van Ackeren en Rene Heremans (vakgroep Mechanica van materialen en constructies, VUB) voor het behandelen van onderdelen van mijn opstelling met hun hittebestendig composiet 'Vubonite'.
ir. Maarten Meijer, dr. ir. Bart Somers en prof. dr. ir. Philip de Goey (groep Verbrandingstechnologie, TU Eindhoven) om me de opportuniteit te geven metingen te mogen meevolgen en uitvoeren in het kader van een internationaal project.
Prof. dr. ir. Joris Degrieck, prof. dr. ir. Patricia Verleysen en prof. dr. ir. Wim Van Paepegem (vakgroep Toegepaste Materiaalwetenschappen) voor de toelating tot bruikleen van de hogesnelheidscamera en optische componenten.
Prof. dr. ir. Bruno de Meulenaer (vakgroep Voedselveiligheid en Kwaliteit,

UGent), Quenten Denon (vakgroep Toegepaste Analyse en Fysische Scheikunde) en prof. dr. ir. Frederic Lynen (vakgroep Organische Scheikunde, UGent) voor bruikleen van hun apparatuur en labo voor de brandstofanalyses.
Prof. dr. ir. Ramon Piloto Rodriguez en prof. dr. ir. Leonardo Goyos Perez (Instituto Superior Politécnico José Antonio Echeverria, Cuba) voor het verblijf in Cuba en de hulp voor brandstof- en materiaalanalyses.
Ik wil ook ereprof. dr. ir. Roger Sierens bedanken voor het delen van zijn ervaring en voor zijn blijvende interesse in mijn onderwerp, ook na zijn pensionering.
De leden van mijn doctoraatjury wil ik danken voor hun input, want dat liet mij toe om dit doctoraat net dat niveau hoger te tillen. Verder wil ik ook de vele master studenten bedanken voor het kiezen van een thesis onderwerp in het kader van mijn doctoraat, want hun werk leverde mij telkens grote hoeveelheden meetdata waarmee ik aan de slag kon.
Verder dank ik al mijn collega's voor hun bijdrage aan dit werk. Mijn mede doctoraatstudenten doorspartel(d)en natuurlijk een gelijkaardig parcours en waren het ideale klankbord om gedachten uit te wisselen in de zoektocht naar oplossingen. In het bijzonder dank ik Joachim Demuynck met zijn jaar meer ervaring voor de hulp met alle administratieve/praktische problemen, Jeroen Vancoillie en Louis Sileghem voor het delen van de bureau en als uitlaatklep als het wat moeilijk ging en tenslotte Roel Verschaeren om me te helpen met de opstelling. Verder zou ik zonder de technische assistentie van Koen Chielens, Patrick De Pue, Rene Janssens en Robert Gillis geen experimenteel onderzoek kunnen gedaan hebben. Ook Annie Harri en Griet Blondé wil ik van harte danken, want zonder hen zou ik ettelijke uren verloren zijn in het ontwarren van administratieve regels. Yves Maenhout wil ik bedanken voor het aan de praat houden van pc gerelateerde zaken, gezien ik op vlak van software en computers een totale leek ben.
Tenslotte wil ik ook mijn familie bedanken voor de oprechte interesse in mijn onderzoek. Die lieten me toe om mijzelf te blijven uitdagen om mijn onderzoek in eenvoudige taal uit te leggen. Ondanks verschillende tegenslagen en moeilijke momenten heeft dit doctoraat een belangrijke wending in mijn leven veroorzaakt. De mogelijkheid om praktisch werk te verrichten heeft mijn hobby en praktische kennis & denkvermogen knallend de hoogte ingeschoten. Verder ben ik door mijn doctoraat in contact gekomen met de salsa (bedankt Cuba) waarin ik ontspanning vond en eveneens mijn vriendin Tine heb leren kennen, die me meegesleurd heeft tot het einde.

Kortom, bedankt aan iedereen voor zijn bijdrage aan dit onderzoek, hoe klein die op het eerste zicht ook lijkt.

Tenslotte draag ik dit doctoraat op aan mijn moeder die tijdens de duur van mijn doctoraat is overleden.

Gent, December 2013
Jonas Galle

Table of Contents

Nomenclature

Symbols

C_c	Nurick contraction coefficient	-
c	speed of sound	m/s
f	fuel volume fraction	-
F	F-term from the spray model	kg/m^2
h	enthalpy	J/kg
l	characteristic length	m
L	linoleic acid	-
Ln	linolenic acid	-
L_v	latent heat	J/kg
Le	Lewis number	-
m	mass	kg
M	molar mass	g/mol
M	myristic acid	-
n	amount of mol	mol
O	oleic acid	-
P	pressure	Pa
P	palmitic acid	-
P_{sat}	saturation pressure	Pa
Pr	Prandtl number	-
q	conservation parameter	-
r	position in radial direction	m
R	gas constant	$J/molK$
$\bar{R}$	universal gas constant	$8.314\ J/molK$
S	stearic acid	-
Sc	Schmidt number	-
t	time	s
T	temperature	K
x	position along spray axis	m
Y	volume fraction	-
Z	mixture fraction	-

Greek symbols

λ	air-to-fuel ratio	-
ν	kinematic viscosity	m^2/s
μ	dynamic viscosity	$Pa.s$
Ω	oxygen ratio	-
ϕ	vapor fraction	-
ψ	equivalence ratio	-
ρ	density	kg/m^3
θ	spray angle	$^\circ$
ζ	dimensionless radial position	-

Subscripts

0	initial condition
a	ambient condition
atm	atmospheric condition
av	average
b	condition at the pre-combustion [Burned condition]
cet	cetane
cl	condition on the spray axis
cyl	in-cylinder condition
$evap$	total evaporation condition
f	fuel condition
i	space variable along spray axis
inj	injector condition
k	variable for mixture components
l	liquid condition
${}_LT$	linoleic triglyceride
ma	moving average
mix	mixture condition
PT	palmitic triglyceride
r	space variable along the radial direction
ST	stearic triglyceride
TC	triacontane
u	condition prior to pre-combustion [Unburned condition]
v	vapor condition
∞	bulk condition

Superscripts

j	time variable

Acronyms

ABC	Anglo Belgian Corporation
ABDC	After Bottom Dead Center
ATDC	After Top Dead Center
BLDC	Brushless Direct Current
BTDC	Before Top Dead Center
Ca	Calcium
CFD	Computational Fluid Dynamics
CN	Cetane Number
CO	Carbon Monoxide
CO_2	Carbon Dioxide
Cu	Copper
ECN	Engine Combustion Network
EOI	End of Injection
Fe	Iron
FFA	Free Fatty Acids
FLOL	Flame Lift-Off Length
FWHM	Full Width Half Maximum
GC-MS	Gas Chromatography - Mass Spectroscopy
HFO	Heavy Fuel Oil
IV	Iodine Value
K	Cavitation Number
LL	Liquid Length
MB	Methyl-Butanoate
MD	Methyl-Decanoate
MSDE	Medium Speed Diesel Engines
Na	Natrium
ND	Needle Drop
NL	Needle Lift
NO	Nitrogen Monoxide
NO_2	Nitrogen Dioxide
NOP	Needle Opening Pressure
NOx	Nitrogen Oxides (NO_2 + NO)
NTC	Negative Temperature Coefficient
PAH	Polycyclic-Aromatic Hydrocarbons
pAV	p-Anisidine Value
PIV	Particle Image Velocimetry
PLN	Pump-Line-Nozzle injection
PV	Peroxide Value
RME	Rapeseed Methyl Ester
rpm	rounds per minute
Si	Silicium
SMD	Sauter Mean Diameter
soi	Start Of Injection (in the engine)

Acronyms (continued)

SOI	Start Of Injection (in the GUCCI-setup or EHPC)
TDC	Top Dead Center
UHC	Unburned Hydro-Carbons

List of publications

Publications in peer reviewed international journals

Publications directly related to the Ph.D. topic

1. Galle, J., Verhelst, S. (2013) Evaluation of the surrogate choice for (bio-) diesel considering spray model hypotheses: illustration for a mixing-limited phenomenological model. In preparation.

2. Meijer, M., Galle, J., Griensven, J.G.H., et al. (2013) High speed ECN spray a characterization, by using various diagnostic techniques. SAE Int. J. Engines 6(2):2013, doi:10.4271/2013-01-1616.

3. Galle, J., Van de Maele, C., Defruyt, S., Verhelst, S., Rodriguez, R.P., *et al.* (2013) Experimental investigation concerning the influence of fuel type and properties on the injection and atomization of liquid biofuels in an optical combustion chamber. Biomass & Bioenergy, 57(2013)215-228

4. Galle, J., Verhelst, S., Sierens, R., Goyos, L., Castaneda, R., *et al.* (2012) Failure of fuel injectors in a medium speed diesel engine operating on bio-oil. Biomass & Bioenergy, 40(5)27-35.

Other journal publications

5. Vancoillie, J., Demuynck, J., Galle, J., Verhelst, S., van Oijen, J.A. (2012) A laminar burning velocity and flame thickness correlation for ethanol-air mixtures valid at spark-ignition engine conditions, Fuel, 102 460-469

6. Sileghem, L., Vancoillie, J., Demuynck, J., Galle, J., Verhelst, S. (2012) Alternative fuels for spark-ignition engines: mixing rules for the laminar burning velocity of gasoline-alcohol blends. Energy & Fuels, 26(8) 4721-4727.

7. Rodriguez, R.P., Perez, L., Alfonso, M., Duarte, M., Caro, R., Galle, J., Sierens, R., Verhelst, S. (2012) Thermal behavior of Jatropha curcas oils and their derived fatty acid ethyl esters as potential feedstocks for energy production in Cuba. Thermal Analysis and Calorimetry. 109(2)1005-1012.

8. Rodrigues, R.P., Perez, L., Alfonso, M., Duarte, M., Caro, R., Galle, J., Sierens, R., Verhelst, S. (2011) Characterization of Jatropha curcas oils and their derived fatty acid ethyl esters obtained from two different plantations in Cuba. Biomass & Bioenergy, 35(9)4092-4098

Related publications in proceedings of international conferences

9. Galle, J., Van de Maele, C., Defruyt, S., Verhelst, S., Verschaeren R. (2013) Evaluation of some important boundary conditions for spray measurements in a constant volume combustion chamber. In: SAE World Congress 2013, Detroit, MI, USA. SAE paper no. 2013-01-1610.

10. Galle, J., Demuynck, J., Vancoillie, J., Verhelst, S. (2012) Spray parameter comparison between diesel and vegetable oils for non-evaporating conditions. In: SAE World Congress 2012, Detroit, MI, USA. SAE paper no. 2012-01-0461.

11. Galle, J., Verhelst, S. (2012) Influence of diesel surrogates on the behavior of simplified spray models. In: Proceedings of the FISITA 2012 World Automotive Congress, Beijing, China. FISITA paper no. F2012-A02-012.

12. Galle, J., Van De Maele, C., Defruyt, S., Verhelst, S. (2012) Fuel injection temperature determination and effect on the injection process for different alternative fuels. THIESEL 2012 Conference on Thermo- and Fluid Dynamic Processes in Direct Injection Engines. Valencia, Spain

13. Galle, J., Verhelst, S. (2011) Sprays of alternative fuels for medium speed diesel engines: modelling and optical experiments, 8th International symposium towards clean diesel engines, proceeding p.47-49

14. Verhelst, S., Demuynck, J., Vancoillie, J., Galle, J., Sierens R. (2010) Alternative fuels for road transport. In: 11th International congress on automotive and transport engineering. Brasov, Romania, p.72-82

Nederlandse samenvatting –Summary in Dutch–

De inwendige verbrandingsmotor met compressieontsteking (type dieselmotor) is nog steeds de belangrijkste aandrijfbron voor zwaar wegtransport, spoorvervoer, scheepvaart, elektriciteitsopwekking in warmtekrachtcentrales (kleinschalige elektriciteitsproductie) en de landbouwsector. Afnemende reserves van fossiele brandstoffen, de toenemende energievraag van de transportsector en de opwarming van de aarde (CO_2-uitstoot) zijn de voornaamste drijfveren voor onderzoek naar het gebruik van alternatieve brandstoffen voor verbrandingsmotoren. De visie van de overheid is dat tegen 2030 het aandeel van brandstoffen voor wegtransport met hernieuwbare oorspong 25% moet bedragen. Deze ambitieuze doelstellingen vereisen intensief onderzoek naar biobrandstoffen en het gebruik ervan in motoren.
Ook zorgen de hoge brandstofprijzen voor een snel oplopend kostenplaatje. Dit is vooral voelbaar bij de sectoren die gebruik maken van middelsnellopende motoren en betekent dat er nood is aan een alternatieve brandstof die economisch verantwoord is.

Eén van de potentiële alternatieve brandstoffen voor dit toepassingsgebied zijn pure plantaardige oliën (PPO's) en dierlijke vetten. Verschillende constructeurs van middelsnellopende motoren en hun toepassingen tonen hierbij hun interesse.
Het gebruik van dergelijke biobrandstoffen in motoren vereist echter aanpassingen van de motor t.g.v. de verschillen in fysische en chemische eigenschappen in vergelijking met diesel. Afgezien van de sterke diversiteit van de (chemische) samenstelling van de verschillende biobrandstoffen en afhankelijkheid van herkomst, is de hoge viscositeit een belangrijk probleem voor de injectie. Problemen die op termijn optreden in niet (optimaal) aangepaste motoren, zijn voornamelijk het dichtslibben van filters en leidingen, polymerisatie, afzettingen op de cilinderwanden en injector, corrosie en oxidatie van de brandstof. Hoewel deze problemen bij gebruik van biobrandstoffen reeds gekend zijn, zijn de oorzaak en ontstaan nog onvoldoende doorgrond om de juiste aanpassingen te doen.

Diepgaander onderzoek dan zuivere motortesten werd in de literatuur maar zelden verricht waardoor het proces in de verbrandingskamer nog zo goed als niet gekend is. Doordat de motorprestaties het meest beïnvloed worden door het vernevelings- en verbrandingsproces, is een directe studie hiervan onontbeerlijk.

Dit doctoraatsonderzoek focust zich op het vernevelingsproces, zowel op experimenteel als op numeriek vlak. Om de verneveling en verbranding van een dieselbrandstof te bestuderen is er nood aan een optisch toegankelijke verbrandingskamer waarin de motorcondities kunnen gecontroleerd worden. Dergelijke opstelling werd in dit doctoraat uitgebouwd met een injectiesysteem zoals die te vinden is op dergelijke hedendaagse motoren. De samenwerking met Anglo Belgian Corporation (ABC) Diesel, een Gentse en de enige Belgische constructeur van middelsnellopende dieselmotoren, laat toe om de experimenten op deze fundamentele optische opstelling in de nabije toekomst te vertalen naar experimenten op een motor.
Verder is het eveneens niet volledig duidelijk of de dynamica van de fysische processen van de verneveling en verdamping vergelijkbaar is met deze van fossiele diesel. Hiervoor zal de modelleringstrategie, die voor diesel reeds is verantwoord, moeten geëvalueerd worden voor deze alternatieve brandstoffen. Dit zijn de 2 voornaamste doelen waarnaar dit doctoraatsonderzoek streeft.

Alvorens van start te gaan met experimenten of modellering, werd een literatuurstudie uitgevoerd die het dieselvernevelings- en verdampingsproces beschrijft en welke parameters een belangrijke bijdrage hebben op het gedrag van deze processen. Op deze manier kan doelgerichter naar de invloed van de pure oliën worden gezocht. Verschillende aanvaarde conceptuele modellen worden kort toegelicht, gevolgd door een gedetailleerdere studie van de verschillende processen die deel uitmaken van een volledige dieselinjectie.

In een volgende stap werd nagegaan hoe injecties kunnen beschreven of gespecifieerd worden. Een brede kennis omtrent optische diagnostieken is reeds beschikbaar in de literatuur. De beschrijving van de diagnostieken en parameters voor het vernevelingsproces, is in deze thesis beperkt tot deze die werden gebruikt.

Om de experimenten te kunnen uitvoeren, was nood aan een meetopstelling. Er werd gekozen voor een optisch toegankelijke constant volume verbrandingskamer voor zijn eenvoudige optische toegang, flexibiliteit en het ontbreken van bewegende onderdelen. De motorcondities kunnen nagebootst worden door een vooraf bepaald gasmengsel tot ontbranding te brengen alvorens te injecteren (de zogenaamde "voorverbranding"). De verschillende subsystemen zoals brandstofcircuit, gasvulsysteem, synchronisatie & acquisitie van de meetsignalen worden uitgebreid beschreven.

Vervolgens werd bepaald in welke mate de randcondities voor de experimenten kunnen gehaald worden. Zo werd bestudeerd welke temperatuur de brandstof heeft in de injector in combinatie met de injectorkoeling en kamerverwarming. De voorbranding veroorzaakt een belangrijke temperatuurstijging in de injector net voor injectie van de dieselbrandstof indien de verstuiver niet wordt afgeschermd. In de huidige configuratie wordt over de verstuiver een hoedje geschoven dat het moge-

lijk maakt slechts 1 spray te bestuderen van de meergatsverstuiver. Hierdoor werd de invloed van de temperatuursstijging op de injectietemperatuur verwaarloosbaar. De distributie van de temperatuur in de verbrandingskamer werd opgemeten met snelle thermokoppels, waarbij geconcludeerd werd dat een goede homogeniteit kon behaald worden als de mengventilator geactiveerd was: de verhouding van de kerntemperatuur en uitgemiddelde temperatuur bedroeg 1.04 (voor kleinere gelijkaardige opstellingen wordt een verhouding tussen 1.03 en 1.08 gerapporteerd). Het snelheidsveld werd opgemeten met een eenvoudige schaduwgrafie techniek en de maximale waarden lagen gemiddeld onder $3m/s$. Gezien de hoge initiële injectiesnelheid ($200-500m/s$ voor het geïmplementeerde systeem) kan de omgevingssnelheid als verwaarloosbaar beschouwd worden.

Naast het ontwerpen en valideren van een tool voor het experimenteel werk, werd een tool voor het numerieke luik ontworpen en gevalideerd. Het doel van dit modelleringwerk was om een tool te ontwikkelen dat voldoende nauwkeurig en snel is om het onderscheid in de verschillende oliën zichtbaar te maken in het dieselvernevelings- en verbrandingsproces zodat de vermogenoutput en emissievorming bij middelsnellopende dieselmotoren kan voorspeld worden. Na een intensieve literatuurstudie betreffende de modellering van dieselinjecties, werd er besloten om een eendimensionale aanpak te implementeren. Op basis van de eenvoud, detailweergave en rekentijd werd een bestaand transiënt dieselvernevelingsmodel gekozen. Dit transiënt model laat toe te werken met een tijdsveranderlijk injectiesnelheidsprofiel. Dit is interessant voor zowel het pomp-leiding-verstuiver injectiesysteem, dat is geïmplementeerd in de optische opstelling, als het gebruik van meervoudige injectie met common-rail systemen in moderne dieselmotoren.

Het modelleren van het fysische injectieproces alleen is niet voldoende om een correcte voorspelling te krijgen. De brandstofeigenschappen spelen evenzeer een heel belangrijke rol. De moeilijkheid bestaat erin om de complexe samenstelling van de realistische brandstoffen te reduceren tot eenvoudige mengsels van componenten waarvan een uitgebreide dataset van de eigenschappen beschikbaar is. Voor diesel en biodiesel is reeds heel wat onderzoek omtrent de keuze van surrogaten beschikbaar, maar dit ontbreekt voor pure oliën.
Aan de hand van een literatuurstudie werd nagegaan hoe de surrogaten voor diesel en biodiesel werden gekozen. Vervolgens worden de eigenschappen en samenstelling van pure oliën beschreven om zo samen met eerdere literatuursstudie tot een voorstel te komen voor een surrogaatolie. Een belangrijke conclusie dat werd getrokken is de sterke afhankelijkheid van de keuze van de surrogaatbrandstof op de gemodelleerde verdamping van de jet, als gevolg van één van de strenge hypothesen in het model. Uit deze bevindingen kan besloten worden dat het belangrijk is om een surrogaatbrandstof niet alleen te kiezen op basis van het fysisch gedrag van de experimenten, maar ook op basis van de gemaakte hypotheses in het model.
Het gemaakte voorstel voor de surrogaatolie bestaat uit de samenstelling van 4 moleculen die zo worden gekozen dat 3 eigenschappen overeenkomen met de doel-olie: de viscositeit bij injectie (deze eigenschap beïnvloedt de verneveling

en druppelgrootte), de hoeveelheid zuurstof in de olie (deze eigenschap beïnvloedt de verbranding en emissievorming), de hoeveelheid dubbele bindingen (deze parameter beïnvloedt het ontstekingsmoment en reactiviteit). De saturatiedruk die het verdampingsproces in het beschouwde vernevelingsproces beïnvloedt, wordt niet in rekening gebracht gezien *a)* de saturatiedruk voor de verschillende brandstoffen weinig verschilt en *b)* weinig temperatuursafhankelijke data beschikbaar is.

Bovenvermelde studies en werk zijn de noodzakelijke fundamenten om meer specifiek en betrouwbaar onderzoek te kunnen verrichten op dieselinjecties. Om vertrouwen en ervaring te krijgen met deze basiskennis werden experimenten uitgevoerd op de optische verbrandingskamer aan de Technische Universiteit van Eindhoven in samenwerking met de lokale motoronderzoeksgroep. Hierbij werden metingen uitgevoerd voor een gespecifieerde configuratie, nl. '*Spray A*', bepaald door een internationale groep die zich bezig houdt met het trachten standaardiseren van dergelijk experimenten en diagnostieken: '*the Engine Combustion Network*'. Naast het opdoen van ervaring, was het de bedoeling om data aan te leveren voor deze configuratie, net als andere onderzoeksinstellingen. Zo kan nagegaan worden of de gebruikte opstelling invloed heeft op de metingen. De uitgevoerde metingen omvatten het opmeten van de vloeistoflengte, penetratieverloop, ontstekingsuitstel en positie van de start van het vlamfront. Uit de vergelijking met de andere onderzoeksinstellingen was het duidelijk dat het verschil in injector (vnl. de diameter van de verstuivergaatjes) een sterke invloed heeft op de resultaten. Na een mathematische correctie voor de diameter van de verstuivergaatjes, kwamen de resultaten overeen (binnen de standaardafwijkingen).
Tenslotte werd het eerder beschreven injectiemodel succesvol toegepast op deze '*Spray A*'.

Als laatste onderdeel van dit doctoraat werden injecties verricht in een inerte en koude (tot $150°C$) atmosfeer voor diesel, biodiesel, dierlijke vetten, palm- en koolzaadolie. Hierbij werden verschillende parameters zoals de motorsnelheid, brandstof- & kamertemperatuur en kamerdruk gewijzigd. Gezien een volumetrische pomp voor de injecties gebruikt wordt, is het gedrag van de injectiedruk sterk afhankelijk van het toerental en eigenschappen van de brandstoffen. Zo stijgt de injectiedruk met toerental, viscositeit en bulkmodulus. Het moment van start van injectie vervroegt met stijgende bulkmodulus en een hogere brandstofdensiteit verhoogt de injectieduur. Voor de inerte injecties is de penetratie voor de verschillende brandstoffen zeer gelijkaardig in het begin, maar naarmate de injectie vordert, penetreren de oliën sneller, wat te wijten is aan de hogere inertie van de grotere druppels. De sproeihoek bleek weinig af te hangen van de gebruikte brandstof in tegenstelling tot de structuur van de jet, vooral bij lagere temperaturen. Bij lage temperaturen is de viscositeit hoog en sterk temperatuursafhankelijk. Als gevolg hiervan zal de verneveling sterk variëren: een slechte verneveling was zichtbaar door de concentratie van brandstof in de kern van de jet en merkelijk grotere druppels aan de rand van de jet. Voor hogere temperaturen ($>60°C$) en dus meer motorrealistische condities was dit fenomeen nagenoeg niet meer zichtbaar

in de beelden.

Dit doctoraat heeft de basis gelegd voor een vervolgonderzoek dat zich kan focussen op de verdamping en verbranding van injecties van pure oliën en vetten. Alle hiervoor nodige tools werden verschaft:

- een flexibele optische opstelling voor dieselinjecties met controle over de randcondities zoals die in de motor voorkomen
- een transiënt injectiemodel, gevalideerd voor fossiele diesel in eerste instantie
- een voorstel werd geformuleerd voor het modelleren van pure oliën
- metingen van injecties van oliën onder inerte atmosfeer waarbij het verkregen inzicht van belang zal zijn voor de verdampende en reagerende injecties

English summary

Until today, the compression ignition engine (type diesel engine) is still the most important power source for heavy duty road transport, rail transport, marine, genset and agriculture applications. The decreasing reserves of fossil fuels, the increasing energy demand of the transportation sector and the greenhouse effect (CO_2-emissions) are the main motives for research on the use of alternative fuels in internal combustion engines. The vision of the government is that by 2030 the fuel for road transportation should consist for 25% of renewable origin.
These ambitious objectives require intensive investigation of bio-fuels and its use in internal combustion engines.
Furthermore, the increasing fuel prices are responsible for a quickly increasing energy bill. This is a sensitive factor especially for the sectors that make use of medium speed diesel engines and indicates that there is a need for an alternative fuel which has economical potential.

Potential alternative fuels for this application, are straight vegetable oils (SVO's) and animal fats (AF). Several manufacturers of medium speed diesel engines and their applications show interest.
The use of such bio-fuels require however modifications to the engines as a consequence of the differences in physical and chemical properties compared to fossil diesel. Apart from the strong diversity of the (chemical) composition of the different bio-fuels and the dependence of their origin, the high viscosity is an important issue for the injection. Long term problems that occur in unmodified engines are mainly the clogging of filters & supply pipes, polymerization, deposits on the cylinder walls & nozzle, corrosion and oxidation of the fuel prior to injection. Although the problems with the use of bio-fuels are mostly known, the knowledge about the causes and origin is still lacking, so it is hard to apply the correct engine modifications.

Research apart from the engine tests is barely reported in literature with the result that the process in the combustion chamber is not yet well understood and inconsistencies exist in literature. Since the engine performance is mostly determined by the injection and combustion process, a direct fundamental study is indispensable.

This PhD research focuses on the diesel atomization process, both experimentally and numerically. In order to study the atomization and combustion, an optically

accessible combustion chamber is required in which engine-like conditions can be simulated and controlled. Such setup with an injection system as can be found on most medium speed diesel engines, was designed and constructed during this PhD. The cooperation with ABC Diesel, the only Belgian medium speed diesel engine manufacturer and located in Ghent, allows to translate the experiments with the fundamental optically accessible combustion chamber to engine tests in the future. Further, it is not yet completely clear whether the dynamics of the physical processes of the atomization and evaporation are similar to the fossil diesel. This will require the evaluation of the modeling strategy, valid for diesel, for the alternative fuels, with the focus on straight oils. These are the 2 main goals of this PhD work.

Prior to starting with experiments or modeling, a literature study was performed on the diesel atomization and evaporation process and the most important influencing parameters. In this way, the search to the influence of the straight oils can happen more efficiently. Different, generally accepted, conceptual models are briefly explained, followed by a more detailed study of the different processes of which a diesel injection consists.

In a next step, it is explored how injections can be described or specified. A wide range of knowledge and different optical diagnostics is already reported in literature. The description of the diagnostics and spray parameters is limited to the ones used in this work.

To perform the experiments, an experimental test rig is necessary. An optically accessible constant volume combustion chamber was chosen for its easy optical access, flexibility and the absence of moving parts. The engine-like conditions can be simulated by the ignition of a predetermined gas mixture prior to the diesel injection (the so-called “pre-combustion”). The different subsystems such as the fuel circuit, gas supply system, synchronization & acquisition of the signals are comprehensively explained.

Next, the boundary conditions were evaluated for their accuracy and repeatability. The fuel temperature prior to injection was measured for different combination of injector cooling and vessel temperature, as well as the influence of the pre-combustion. The pre-combustion process causes an important temperature increase in the injector before the start of injection if the nozzle is not covered. In the current configuration, a thimble is fitted over the nozzle to allow the optical study of only 1 spray of the multi-hole nozzle. This ensures that the influence of the temperature rise can be neglected.
The temperature distribution inside the combustion vessel was evaluated with fast reacting thermocouples and it was concluded that a good homogeneity could be obtained when the mixing fan was activated: the ratio of the core to bulk temperature was about 1.04 (for other smaller, but similar, rigs, a ratio of 1.03 up to 1.08 is reported).
The ambient velocity field was obtained by the image processing of simple shad-

owgraph images and the average maximum were found to be $3m/s$. Due to the initial high injection velocities ($200-500m/s$ for the implemented injection system) the velocity of the ambient gases can be neglected.

Apart from the design and validation of a tool for the experimental work, a tool for the numerical part is developed and validated. The goal of this modeling work was to create a tool that is accurate and fast enough to make distinction between the different oils in the injection and combustion process the such that the engine power output and emission formation can be predicted. After an intensive literature study concerning diesel spray modeling it was decided to implement a 1-dimensional approach. After a careful trade-off between the simplicity, accuracy and resolving time, an existing transient spray model was proposed. This transient model allows time varying injection velocity profiles. This is interesting for both pump-line-nozzle injection systems, as is implemented on the optical combustion chamber, as for the use of multiple injection common-rail systems in modern diesel engines.

The modeling of only the physical injection processes is not enough to correctly predict the engine outputs. The fuel properties have an important contribution as well. The difficulty involves the reduction of the complexity of the realistic fuels to simple mixtures of components of which extensive datasets of properties are available. A lot of research concerning surrogates of fossil diesel and biodiesel has already been conducted, but this is not the case for straight oils.

Based on a literature study, the methods for selecting a surrogate fuel were summarized, followed by the description of the properties and general composition of straight oils. From this knowledge, a proposal is made to construct a surrogate oil. An important conclusion that was drawn is the strong dependency of the surrogate on the modeled evaporation of the jet (in essence the liquid length) as a consequence of the model hypotheses.
The proposed surrogate model consists of 4 molecules that are chosen in such way that 3 properties equal the target oil: the fuel viscosity at injection (this property influences the atomization and evaporation), the amount of oxygen contained in the fuel (this parameter influences the combustion and emission formation) and the amount of double bounds (this parameter influences the ignition delay and reactivity). The saturation pressure, which dominates the evaporation process, is not considered because: a) the saturation pressure differs little for the different oils and b) little to no temperature dependent data is available.

The previously stated studies and work are necessary to perform more specific and reliable research on diesel injections. To obtain more trust and experience with the basics, experiments were performed on the optically accessible combustion vessel at the Technical University of Eindhoven in cooperation with the local engine research group. Measurements were performed for a specific configuration, called '*Spray A*', determined by an international group that is working on the standardization of such experiments and diagnostics: 'the Engine Combustion

Network'. Apart from the obtained experiments, the purpose was to supply data for this specific configuration, as other institutions also intend to do. The resulting comparison allows to investigate the influence of the experimental setup.
The measurements involved the liquid length, spray penetration, ignition delay and flame lift off length. The comparison with other institutes reveals that the differences in the theoretically identical injectors (especially the nozzle diameter) have a strong influence on the results. After a mathematical correction for the diameter of the nozzle holes, the results were within the standard deviations.
Finally, the proposed spray model was successfully applied to '*Spray A*'. In a final part of this PhD, injections were measured in an inert and cold atmosphere (up to 150°*C*) for diesel, biodiesel, animals fat, palm and rapeseed oil. Several input parameters such as engine speed, fuel & vessel temperature and vessel pressure were varied. Since a volumetric pump is used for the injection, the behavior of the injection pressure is strongly dependent on the engine speed and fuel properties. As such, the injection pressure rises with bulk modulus, viscosity and engine speed. The moment of start of injection advances with increasing bulk modulus and a higher fuel density increases the injection duration.
For inert injection, the penetration for the different fuels is very similar to diesel at the start, but as the injection proceeds, the penetration of the oils becomes faster, due to the higher inertia of the bigger droplets.
The spray angle was found to be little dependent on the fuel in addition to the structure of the jet and especially at lower temperatures. At low temperatures, the viscosity is high and strongly temperature dependent. As a consequence, the atomization differs significantly: a poor atomization was visible through the high concentration of fuel at the spray axis and noticeable big droplets at the border of the spray. For higher temperatures (>60°*C*) and so under more engine realistic conditions, this phenomenon was much less visible in the shadowgraph images.

This PhD has given the foundations for further research which can focus on the evaporation and combustion of injections with straight vegetable oils and animal fats. All necessary tools are proposed:

- a flexible optically accessible setup for diesel injection with controllable boundary conditions.
- a transient spray model, already validated for fossil diesel
- a proposal for surrogate oils
- measurement of oil injection in a cold inert atmosphere of which the insights will be useful for the evaporating and reacting conditions.

1
Problem and goal statement

"The use of plant oil as fuel may seem insignificant today. But such products can in time become just as important as kerosene and these coal-tar-products of today."

- Rudolf Diesel (1912)-

The chapter is organized as follows: A background and motivation for this research project is given prior to stating the research goal & methodology. Finally the outline of this work is summarized.

1.1 Current situation & motivation

The energy consumption is already a topic of intense debate for several decennia in lots of different areas. An important area is undoubtedly the transportation sector since about 26.6% of the energy is consumed by this sector (cfr. Fig. 1.1).

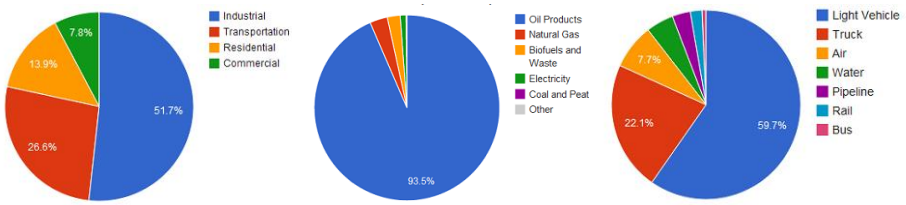

Figure 1.1: World energy consumption by sector, 2012 (left), world energy consumption by source, 2009 (middle), energy consumption by transportation, 2009 (right) (EIA data) [1]

The compression ignition combustion engine is still the most important power source for the heavy duty, railway, marine transport, agricultural machinery and stationary applications (referred to as medium speed diesel engines: MSDE). The shrinking crude oil resources, increasing energy demand, strict emission regulations and concern about the environment (e.g. greenhouse effect) are the main motivation to search for alternative fuels and energy conversion methods.
According to the European directive 2003/30/EG, 25% of the fuel used by the road transport should be renewable fuel by 2030.

As a result, research institutes and manufacturers are encouraged to contribute to this relevant research topic.
Several potential solutions have been proposed for the different applications. The current research project focuses on the use of straight oils as a diesel fuel in medium speed diesel engines. Throughout the text, the term 'diesel' will refer to fossil oil derived diesel fuel.

The main reason for the choice of straight oils as diesel fuel is threefold. First of all, straight oils originate from animal fat or vegetable crops. Animal fats are usually a waste product and can for this reason be (partially) recuperated. In the case of vegetable oil, they do not contribute to greenhouse gas emissions, since the CO_2 formed during combustion has been previously fixed by plants, which act as "carbon sink", creating a closed carbon cycle. In practice, the CO_2 net production on the overall cycle will not be exactly zero, as some energy is used in the harvesting process. Nevertheless the CO_2 production is lower than when fossil fuels are used.

Secondly, engine tests have revealed that similar performance as for diesel can be achieved. This is discussed in more detail in chapter 6.
Furthermore, these fuels are cheaper than e.g. biodiesel. Biodiesel is derived from straight oils and requires an additional chemical process and energy, increasing the production cost.

Last but not least, the gain of interest in research in medium speed diesel engines and its applications is also stimulated by the fact that emission regulations have become more and more severe for this sector. The regulation for emissions have always lagged behind the light duty ones: the first European emission legislation for off-road applications (guideline 97/68/EC) was implemented in 1999 (stage I) and between 2001 & 2004 (stage II). Marine, locomotive, aero and stationary applications were even not yet included. Stage III was implemented in 2006 (2004/26/EC) and included the emission limitation for MSDE. For passenger cars and light duty vehicles emission limitations were implemented about a decade earlier by guideline 91/441/EEC in 1993 (Euro I).

There are some challenges to overcome for the use of crude oils as diesel fuel. The viscosity is one of them which, due to the molecular structure of the oils (i.e. triglycerides), is typically 10 to 100 times higher than for conventional diesel (cfr. section 6.5), which is disadvantageous for the injection performance. Some solutions have been already proposed such as the earlier mentioned conversion to biodiesel. Others have emulsified the oils with less viscous fuels such as diesel and ethanol [2, 3]. Another solution is preheating of the fuel till acceptable viscosity levels are reached [4]. This would imply a heating mechanism and is only affordable for bigger engines on which space and weight is less of an issue, such as for stationary and marine application.
Several constructors or companies already have engines running with this principle. In a short time window, these systems work well. However a serious lack of understanding exists about the formation of emissions and the opinion differs between authors that have published results from their tests. A brief overview of the current knowledge is given in the following section.

1.2 Behavior of oils and fats as diesel fuel

Literature studies [5] have already shown that the triglyceride molecules are less stable than diesel both in terms of short and long term behavior. Concerning the long term stability, traces of free glycerol and free fatty acids (FFA) increase the acidity of the fuel and make the fuel more aggressive for the engine parts that are not protected against corrosion.

The injection temperature of the oil is found to give significant differences in ignition delay, rate of heat release and emission formation. The temperature has an important influence on the physical properties, especially on the viscosity. In the range of 300 to 360K the viscosity decrease is huge, influencing the atomization and mixing characteristics. Unheated oil fuel shows a longer ignition delay with a slow diffusion combustion stage [3, 4], both due to physical (atomization quality, and evaporation properties) and chemical properties. Several investigators used an engine setup with indirect injection (prechambers) in order to be less dependent on the atomization quality [4, 6].
Some basic fuel properties are given in table 1.1 for commonly used oils and are compared to diesel.

oil	**IV**	**CN**	**LHV**	ρ **(293**K**)**	μ **(311**K**)**	**CP**	**FP**
jatropha	104	40-50	39774	903	49.9	283	500
sunflower	110-143	37.1	39575	918	37.1	281	547
soybean	117-143	37.9	39623	914	32.6	269	527
palm	35-61	42	36553	915-950	63.6	300	435
peanut	80-106	41.8	39782	914	39.6	286	544
rapeseed	94-120	37.6	39709	920	37.0	269	519
diesel	-	47	45343	850	2.7	258	325

Table 1.1: Some fuel properties of common oils [6–9], with IV, the iodine value which is a measure for the unsaturation or oxidation stability; CN, the cetane number; LHV, the lower heating value; CP, the cloud point; FP, the flammability point

In general the following conclusions from a comparison with diesel can be made:

- the energy content is about 8-14% lower
- the flash point is very high
- the sulphur content is very low [10]
- the acidity is higher [10]
- the cloud point is higher
- the cetane number is slightly lower

An important difference between vegetable oils and animal fats is that animal fats tend to contain more ash constituent like silicon, phosphorus, sodium and potassium which all encourage the formation of particulate matter [11]. Phosphorus

appears generally in the form of phospholipides and should also be avoided since they provoke polymerization. Furthermore, phospholipids are important surface-active compounds and react with metals to form phosphorus soaps [12]. Phospholipids are also known to act as soot precursors. Other impurities involve metals and ions, mostly originating from processing and pretreatment. Animal fats, however contain systematically more impurities than vegetable oils originating from DNA and bones.
It is expected (due to their small amounts) that they will not have a significant contribution to the instantaneous spray and combustion process. However, the metals and ions, whether bonded in e.g. phytonutrients or not, will form oxides in the high temperature environment, causing long term abrasive wear damage to the engine [13].

One of the most reported engine failures when operating with crude oils is the clogging due to carbon deposits [3, 14, 15]. Bacon *et al.* [16] explained that the small thermal stability (especially the case for linolenic (C18:3) and linoleic (C18:2) acids) is the driving force for the deposits. Triple bonds are most prone to oxidation [17]. Relative rates of fatty acid oxidation are:

- Stearic acid (C18:0) : 1
- Oleic acid (C18:1) : 10
- Linoleic acid (C18:2) : 100
- Linolenic acid (C18:3): 150

This instability results in thermal as well as oxidative polymerization. The thermal polymerization (for temperatures > $370K$) involves the chain growth by carbon-carbon bonds. For this mechanism double C-bonds in the molecule are necessary. In the case of oxidative polymerization, also C-O bonds can be formed. During this process highly-active peroxides tend to form, which have a catalytic property to form a higher concentration of fatty acid radicals. The results are polymers with lots of branches and a high molecular weight. The double bonds are also responsible for the formation of volatile and combustible products when the oils are heated. Since these processes are promoted by molecules with double bonds it is important to keep the iodine value limited (max. 120 for the biodiesel standard En 14214 - 2003), which is a measure for the amount of double bonds or oxidation stability. On the other hand, these volatile components will shorten the ignition delay and increase the combustion speed during the premixed combustion phase [18].

Usually only qualitative conclusions are made from engine tests. Generally, the conclusions can be summarized as follows:
Emission trends are in general very similar to those found for biodiesel engine

tests [19, 20]. The oxygenated property of the fuel reduces the UHC, soot and CO emission, while higher combustion temperatures might increase the NOx-emission [4, 6, 11, 20]. The preheating temperature of the oil was found to give significant differences in ignition delay, rate of heat release and emission formation.
Again, some inconsistency exists among different authors. As an example, Babu and Devaradjane [6] reported higher particulate emissions (up to 140%) for palm oil, while this was not the case for rapeseed oil. Lower NOx emission is sometimes reported at low loads due to lower cylinder pressures. The results depend upon the engine settings, boundary conditions and used oil [20]. Most reports lack necessary details about this information and reasons for the differences are not mentioned.
Another potential reason for the general soot reduction is the absence of pure aromatics and sulphur [19]. However, phytonutrients are big complex structures with aromatic structures and might be important for emission prediction (especially soot) in spite of their small presence in the oils. No research so far has looked into this.
Hemmerlein *et al.* [7] were one of the few that also investigated the aromatic hydrocarbon, PAH, formaldehyde and keton emissions: although diesel fuel has a considerable content of aromatics (more than 20%) and rapeseed oil contains none (or very small amounts), emissions of aromatic hydrocarbons were significantly higher with rapeseed oil. This result was found regardless the engine type and operating point. However the reason for this observation could not directly be identified.

Carbon monoxide emissions within the whole engine operating range can be up to 100% higher compared to diesel fuel [7]. With rapeseed oil, Hemmerlein *et al.* measured also an increase in hydrocarbon emissions (ppm C3) for most of their tested engines. The increase depends on the operating range of the engines and can amount up to 290% compared to diesel fuel due to slower combustion and lower maximum temperatures in the combustion chamber. They also noted that particulate matter and PAH-emissions are dependent on the engine type: direct injected engines tend to have a higher emission than prechamber ones. Emissions of nitrogen oxides were found to be up to 25% lower.
As a result of the lower energy content compared to diesel (approx. 10%), the specific brake fuel consumption is higher. Nevertheless, slightly higher efficiencies at higher loads are obtained which was explained by Labeckas and Slavinskas [19] as the more complete combustion of the fuel-rich zones caused by the oxygenated nature of the oils.

A summary of the effects of pure bio-oils on the engine performance for both long

and short terms consequences, generally accepted, is given in table 1.2. It should be mentioned that some authors found different results in their experiments. This does not imply that they were wrong, but those results might be influenced by the type of biofuel and/or setup changes.

	low load	**high load**
brake thermal efficiency	+	+
CO	-/+	-/+
UHC	-/+	+
NOx	++	–
durability	–	–
aromatics	–	–
aldehydes/ketons	–	–
PAH	–	–
soot (mass)	-/+	++
soot (size)	-/+	++

Table 1.2: Overview of the engine performance when using crude oils. (+: slightly better than diesel, -: slightly worse than diesel, ++: better than diesel, –: worse than diesel).

Long term operation has often led to failure, mainly due to clogging, cavitation damage, premature cracking of the injectors, deposits and corrosion of fueling components [7, 13–15]. With concentrations up to 20*vol%* of crude oil in diesel fuel, it is reported that no significant long term issues should appear [21]. Apart from the high viscosity which promotes clogging, clogging and agglomeration might be encouraged by impurities in the fuel, such as AlCl and phospholipids [13]. Corrosion is found to be an important issue as well due to the high acidity and water content in these fuels [14]. For cost reasons, the preliminary treatment is usually poor, resulting in lots of metal particles that are not removed by the engine filter, resulting in excessive wear of moving engine parts (piston, combustion chamber, injector, fuel pump,...). Some results of the long term consequences are shown in Fig. 1.2 [13].

1.3 Research goal & methodology

This research thesis is part of a longer term project. The goal of this project is to **develop a tool to predict the engine performance of medium speed diesel en-**

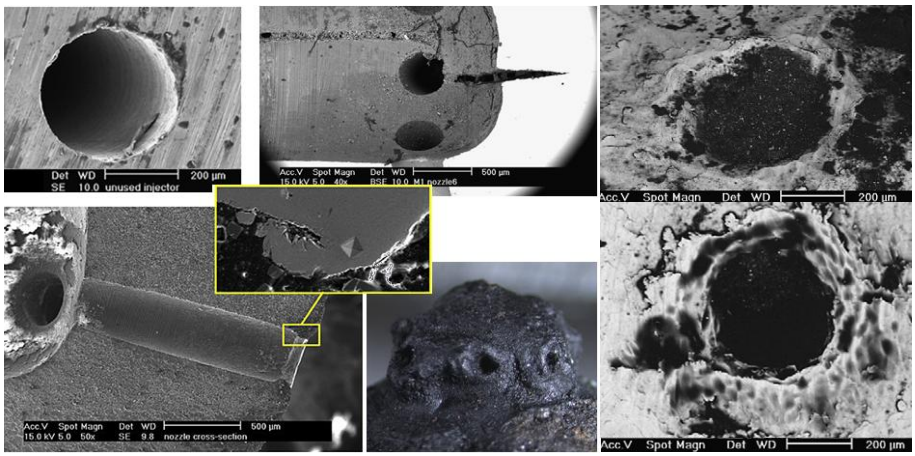

Figure 1.2: New injector hole (top left), nozzle failure due to crack, filled with organic material (top center), clogged and plastic deformed nozzle holes (of failed injector nozzles (left), compared against a new one (right) [13]

gines, using straight oils as an alternative fuel for diesel. In this way, the engines could be tuned in a better way in terms of emissions and fuel consumption.
Little is known about the behavior of straight oils under engine conditions (cfr. also section 6.5). This means that a better fundamental understanding is required prior to adapting existing spray models. This can be gained by knowledge of the in-cylinder processes through optical studies.
In the framework of this goal, an optically accessible test rig was built throughout the PhD period, equipped with optical spray and combustion diagnostics. Since no experience was available within the research group on this topic and experimental methods, knowledge was gained at another research facility for about 2 months. A lot of attention is paid to the determination of the boundary conditions. It is shown that the knowledge of these boundary conditions has a significant impact on the experimental results and knowing the conditions is necessary for a comparison between results obtained by different institutes.
A phenomenological spray model was reconstructed from literature as a prediction tool and some initial modifications for the straight oils were implemented and investigated. The results of the thesis work have led to several suggestions for future work.

1.4 Outline

Chapter 2 gives a brief overview of the current knowledge of fuel sprays under engine conditions. The different spray parameters are identified and described

in chapter 3, as well as the different optical diagnostics that are realized or are commonly used in this research field. The processing method for the obtained results of these imaging techniques is also included. The specifications and design issues for the experimental setup used during this work are included in chapter 4. The modeling strategy for the applied spray modeling is carefully selected in chapter 5. Chapter 6 introduces the use of surrogate fuels for diesel and biodiesel for modeling purposes and better understanding of the spray formation. The influence of the surrogate choice on the modeling performance is investigated and suggestions are made for surrogates for straight oils. Chapter 7 and 8 finally summarize the performed experimental results; chapter 7 focuses on heavy duty diesel spray experiments in the framework of an internationally established network and comparison of results with other research institutes. This measurement set was performed at the research facilities of the Technical University of Eindhoven together with ir. Maarten Meijer. This joint work resulted in a journal paper [22] and input for an international workshop. In chapter 8, the conclusions concerning cold spray measurements in our own setup are summarized. So far, this research is incomplete and still has a long way to go; some suggestions for future work are listed in chapter 9.

2
Diesel fuel sprays

"When you want to know how things really work, study them when they're coming apart."

- William Gibson -

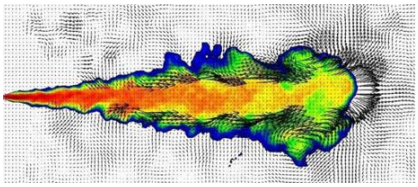

The chapter is organized as follows: first, an overview of existing conceptual models is given. Next, a more extended discussion is held about the different parts of a vaporizing spray. The different spray parameters are defined and the influence of some boundary conditions is described.

2.1 Introduction

The diesel injection process can basically be divided in 3 parts as denoted by the red boxes in Fig. 2.1: the fuel flow in the injector (Nozzle flow), the atomization & evaporation process (Atomization & vaporization) and the spray combustion (Combustion).
Each of these parts can be further divided in the different mechanisms that contribute to the considered spray part. The most important ones are indicated by the green boxes in Fig. 2.1. This structure will be used along this chapter for the description of the diesel spray process.
To give a more general view of the diesel spray process, first, an overview is given of the most accepted conceptual diesel spray models. Next, the different processes in Fig. 2.1 are discussed.
This work concentrates on the inert spray rather than the combustion process. For this reason the combustion topics are partially faded in the figure and will not be discussed in more detail. Nevertheless, since the combustion behavior will influence the spray atomization, it is important to understand all the basic physics, as known so far. So, the combustion process will be handled in the overview of the conceptual models. The conceptual models give a good general understanding of diesel spray combustion and will serve as a basis for all further discussions.

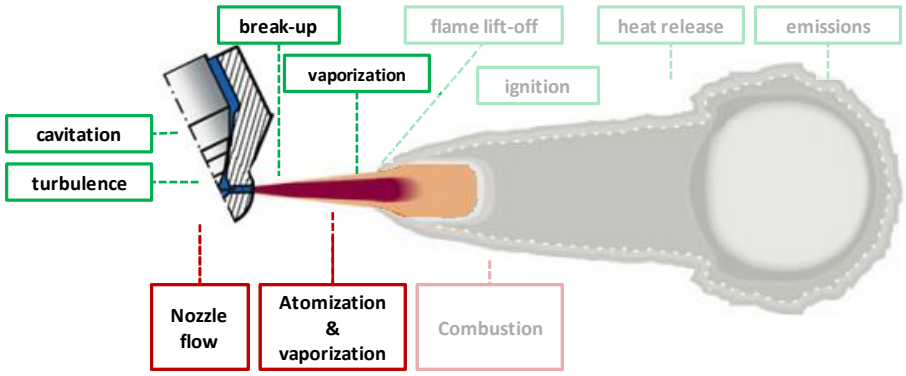

Figure 2.1: Schematic overview of the processes involved in diesel sprays

2.2 Conceptual diesel spray models

2.2.1 Model of Dec

One of the popular models for a quasi-steady state diesel spray combustion was introduced by Dec [23] in 1997. The concept is based on experimental findings

using a heavy duty common-rail injection system, validated with various optical imaging techniques. Dec's model consists of 2 steps of oxidation for both premixed and diffusive combustion: a partial oxidation in a rich premixed reaction and the combustion of a rich mixture of the partially oxidized products in an almost stoichiometric diffusive flame. Dec also made attempts to describe the process development from the moment of the start of injection until steady state [23, 24]. This idea is reproduced in Fig. 2.2.

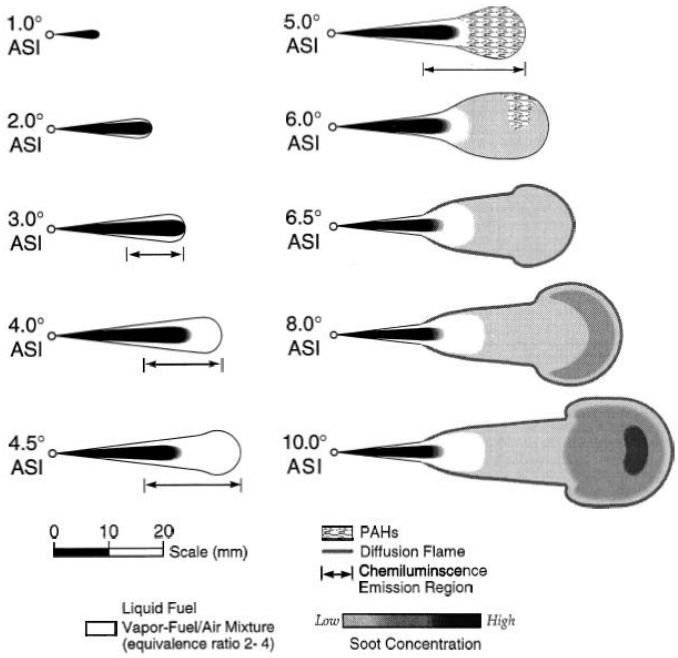

Figure 2.2: Schematic overview of the processes involved in diesel sprays, according to Dec [23, 24]

At the injector, only liquid fuel is found. Downstream, air is entrained and fuel vaporizes. Initially, liquid fuel (droplets, ligaments, and/or an intact liquid core) covers the cross section (1.0° after start of injection (ASI)). Then, vapor starts to develop and grows thicker as the jet continues to penetrate due to the better air entrainment (2.0° ASI), till all fuel is vaporized (3.0° ASI) and a stable liquid length is established. The distance from the injector to the position at which all fuel is vaporized is defined as the liquid length (LL).
Around 3.5° ASI chemiluminescence without detected heat release (known as the cool flame ignition) occurs somewhat downstream the liquid length. The chemiluminescent region of the jet is indicated in Fig. 2.2 by the arrow. Dec could however

not confirm whether the chemiluminescence occurs at the surface or more volumetrically through the vapor-fuel/air mixture in the leading portion of the jet.
By 4.5° ASI, the leading portion contains a "relatively uniform" fuel-air mixture with equivalence ratios ranging from about 2 to 4. After 4.5 to 5.0° ASI, autoignition occurs volumetrically by the fuel breakdown and PAH formation (defined as the hot flame ignition). During this process, the first heat release can be detected.
In the next stage, the heat release reveals a rapid rise, indicating the combustion of a fuel-rich mixture.
Between 5.5 and 6.5° ASI, a diffusion flame forms at the jet periphery between the surrounding air and the products of the fuel-rich premixed burn, containing still unconsumed fuel. The thin diffusion flame front covers the complete spray tip and extends back towards the injector to a point just upstream the liquid length. This position at which a stable flame front starts, is referred to as the flame lift-off. At the same time, soot occurs as very small particles throughout large portions of the cross section, downstream of the fuel jet.
By 6.5° ASI, soot is found throughout the cross-section of the downstream region of the jet and the soot particles become larger in a thin layer around the jet periphery. The soot concentration continues to increase throughout the cross section of the sooting region, with the greatest increase in concentration being towards the leading edge where the head vortex is forming.
From about 8.0° ASI, the diffusion flame remains as a thin reaction zone at the jet periphery, and the larger soot particles produced by this flame become distributed inward from the periphery for a few millimeters.
The soot concentration becomes higher throughout the head vortex (as indicated by the red and yellow colors in Fig. 2.3), and the soot particles in the head vortex have grown much larger. From this point, the mixing controlled combustion is considered to be in a steady state situation. Soot oxidation and NOx formation occur in the same conditions, i.e. where the temperature is high and there is available oxygen and/or OH. For prompt NO, calculations and experiments have shown that little NO is produced at equivalence ratios above 1.8. Besides, the conditions at the premixed flame front are not conducive to NO production since little oxygen is present and the adiabatic temperature is rather low ($< 1600K$). However, HCN production might still occur in this rich combustion, and if it does, it is likely that this bonded nitrogen would later be released as NO at the diffusion flame.
The remaining fuel burns as a diffusion flame at the jet periphery. At the diffusion flame, temperatures will be high and combustion is nearly stoichiometric since there is a source of oxygen. These conditions are nearly ideal for thermal NO production (indicated by the green line, indicated as *Thermal NO Production Zone* in Fig. 2.3).

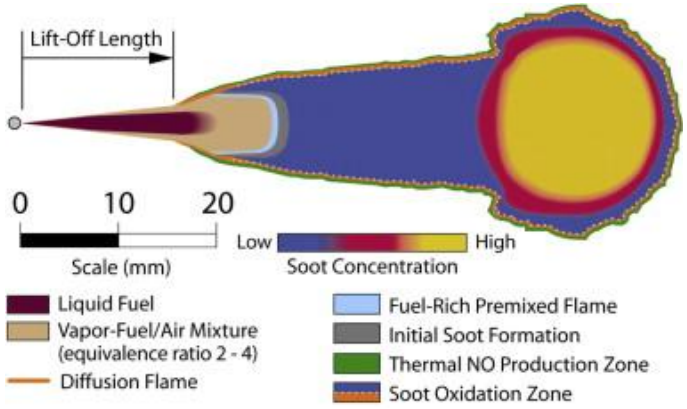

Figure 2.3: Representation of the diesel spray combustion processes, according to Dec [23]

2.2.2 Model of Siebers and Pickett

Siebers and Pickett [25, 26] extended the model of Dec with oxygenated fuels and noticed that the fuel composition plays an important role on the different zones, especially on the sooting areas (cfr. Fig. 2.4, where TEOP stands for 1,1,3,3-tetraethoxy-propane ($C_{11}H_{24}O_4$) and HMN for 2,2,4,4,6,8,8-heptamethyl-nonane ($C_{16}H_{34}$). They concluded from their experiments that the soot formation area happens much more downstream for the oxygenated fuels instead of near the edges of the jet as is indicated by the green area of Fig. 2.4.
They also found that the soot distribution is not coincident with the lift-off length or fuel rich flame.
Furthermore the different areas in the flame combustion are similar to the model of Dec: the blue area in Fig. 2.4, indicated as *fuel-lean partially premixed reaction*, represents the premixed flame, where the flame is fuel-rich partially premixed towards the center and fuel-lean premixed near the spray border. The initial soot or soot precursor formation exists more downstream in a small area for hydrocarbon fuels while for oxygenated fuels this area, due to the bonded oxygen, is significantly larger. Finally, the diffusion flame (orange area, indicated by *diffusion flame*) surrounds the combusting spray.
At the baseline operating conditions, the most upstream soot formation occurs at the edges of the jet for the hydrocarbon fuels, while for oxygenated fuels, the soot formation is confined to the jet central region. When conditions are varied to produce enhanced fuel-air mixing upstream of the lift-off length in the hydrocarbon fuel jets, the initial soot formation shifts towards the fuel jet center and eventually no soot is formed.
For all experimental conditions, the observed location of soot formation relative

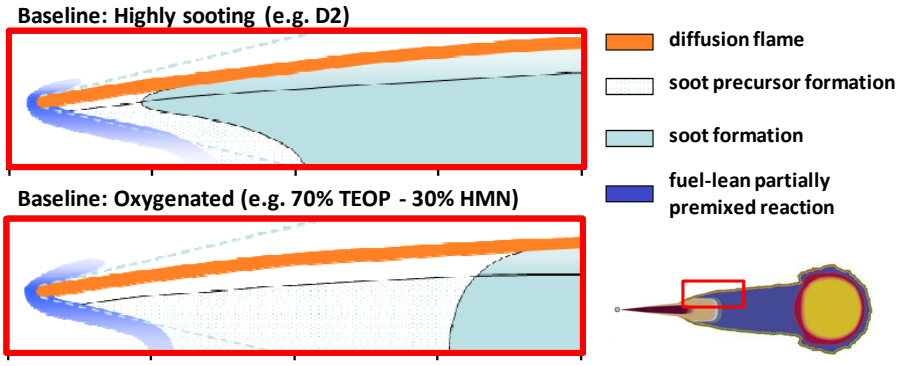

Figure 2.4: Representation of the diesel spray combustion processes, according to Siebers and Pickett [25]; with D2, diesel #2; TEOP, 1,1,3,3-tetraethoxy-propane ($C_{11}H_{24}O_4$) and HMN, 2,2,4,4,6,8,8-heptamethyl-nonane ($C_{16}H_{34}$)

to the heat-release location (flame lift-off) suggests that soot formation occurs in a mixture of combustion products originating from partially premixed reactions and the diffusion flame. The soot precursor formation rates also depend strongly on the fuel type in the region between the lift-off length and the first soot formation.

2.2.3 Model of Kosaka *et al.*

Another view on the combustion process was proposed by Kosaka *et al.* [27] as reproduced in Fig. 2.5. Their concept is based on laser imaging techniques in a rapid compression machine. Some important differences are noticed compared to Dec's model. Kosaka *et al.* [27] observed a liquid length more upstream of the flame lift-off. Furthermore they do not show the diffuse flame at the head of the jet and no specific description of the fuel-rich premixed flame is given. They show that larger soot particles are located downstream the flame head region due to particle growth. Correlated with the particle number density, the authors found that the number of particles was reduced downstream due to agglomeration.
In the early stage of the ignition process formaldehyde is formed in the leading portion of the spray, which is an indication for the cool flame ignition. This ignition stage is quickly followed by hot flame ignition as a result of the fast consumption of formaldehyde and heat release is detected. These ignition regions strongly depend on the ambient conditions and on the negative temperature coefficient (NTC) effect of the fuel: when the temperature is within the NTC temperature range, the mixture tends to ignite in the spray center while ignition more likely occurs in the periphery of the spray flame for temperatures out of this NTC range. The ignition regions will finally merge.
In the early soot formation process the soot precursor is formed in the whole lead-

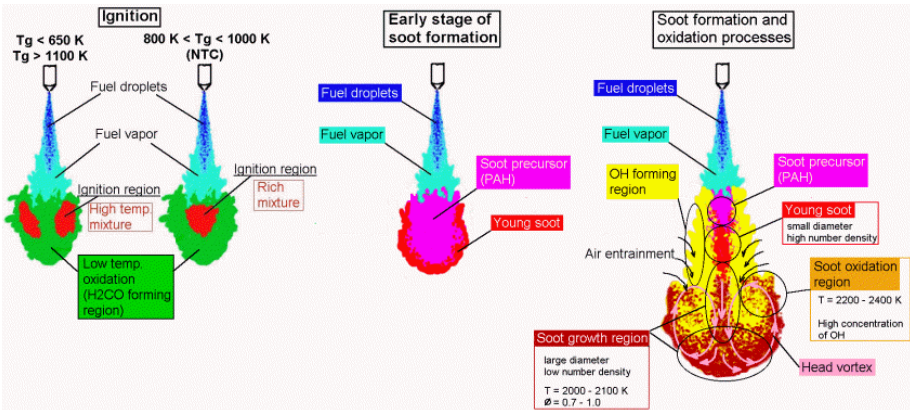

Figure 2.5: Representation of the diesel spray combustion processes, according to Kosaka et al. [25]

ing portion of the spray flame immediately after the hot ignition. The soot precursor located in the periphery of the spray flame is converted to a soot particle at first. During the diffusion combustion, the soot precursors are formed through the central fuel rich area and surrounded by the adjacent fuel lean region where the OH-radicals are formed.
The young soot particles grow by surface growth and are coagulated during convection to the spray head. In this process the size of soot particles increases and the number density of particles decreases. At the spray tip the soot particles are pushed aside to the spray periphery by the motion of the head vortices.
Finally, the soot particles are convected to the upstream side of the head vortices and re-entrained into the lean side of flame, where the concentration of OH is high, and are oxidized rapidly.

2.2.4 Model of Bruneaux

Bruneaux [28, 29] studied the mixture fields of diesel spray combustion by tracer LIF and summarized his conclusions in a conceptual model as represented by Fig. 2.6. The jet mixture consists of 2 distinctive zones: the stationary mixing zone upstream of the spray, where air entrainment due to shear turbulence dominates the dynamics, and the stagnation zone at the tip where the jet pushes away the dense surrounding gases. The latter is characterized by a lower mixing rate since small scales of turbulence are missing. Mixing is strong in the stationary zone and it was found that the local mixing rate remains constant despite an increase in the injection pressure.

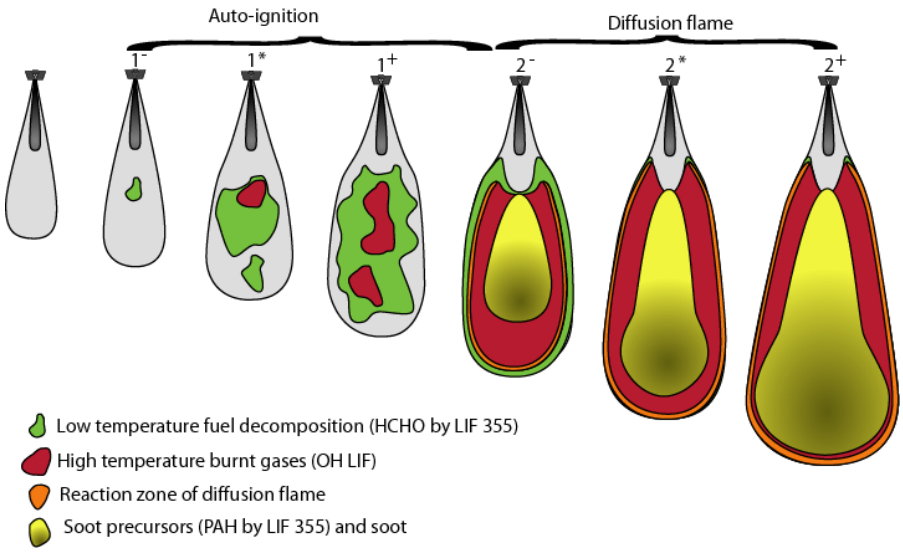

Figure 2.6: Schematic overview of the processes involved in diesel sprays [28]

2.2.5 Model of Musculus *et al.*

Musculus *et al.* [30] extended Dec's model. The extension applies to both early and late injection conditions, though the spatial extent of some features (e.g., liquid fuel penetration) and the timing of some events (e.g., ignition) will shift depending on operating conditions and fuel injection timing. One of the extension features is the indication of the formation of formaldehyde at the early stage of combustion as indicated by the purple areas in Fig. 2.7. The appearance of formaldehyde during the early stages of combustion is consistent with the chemical kinetics modeling results for both fuel-rich and fuel-lean reactions.

The premixed burn occurs within 1-2° after chemiluminescence is first detected, and no clear distinction between first-and second-stage ignition is discernible in the heat release rate.

The portions of the jet that first ignite are fuel-rich and soot precursors (red, indicated by *Soot or Soot Precursors (PAH)*) appear during the premixed burn, followed by soot formation (also red and indicated by *Soot or Soot Precursors (PAH)*) a short time later. The time-scales of second-stage ignition, OH^*-formation, and soot precursor formation are very short because of the rapid temperature increase. OH^* (green, indicated by *Second-Stage Ignition of Intermediate Stoichiometry or Diffusion Flame (OH)*) may appear in isolated spots at the periphery of the spray close to the same timing as soot precursor formation (see Fig. 2.7 at 6° ASI), indicating nearly simultaneous combustion of fuel-rich and intermediate stoichiometry regions of the jet. Within a short time after ignition, the OH^* layer grows to form

a diffusion flame on the spray periphery.
The zone of first-stage combustion products (mostly formaldehyde) persists upstream of the lifted diffusion flame.
During the processes of second-stage ignition, the liquid length decreases somewhat, likely due to local temperature rise at the onset of combustion, including a temperature increase because of compression heating from the premixed burn.

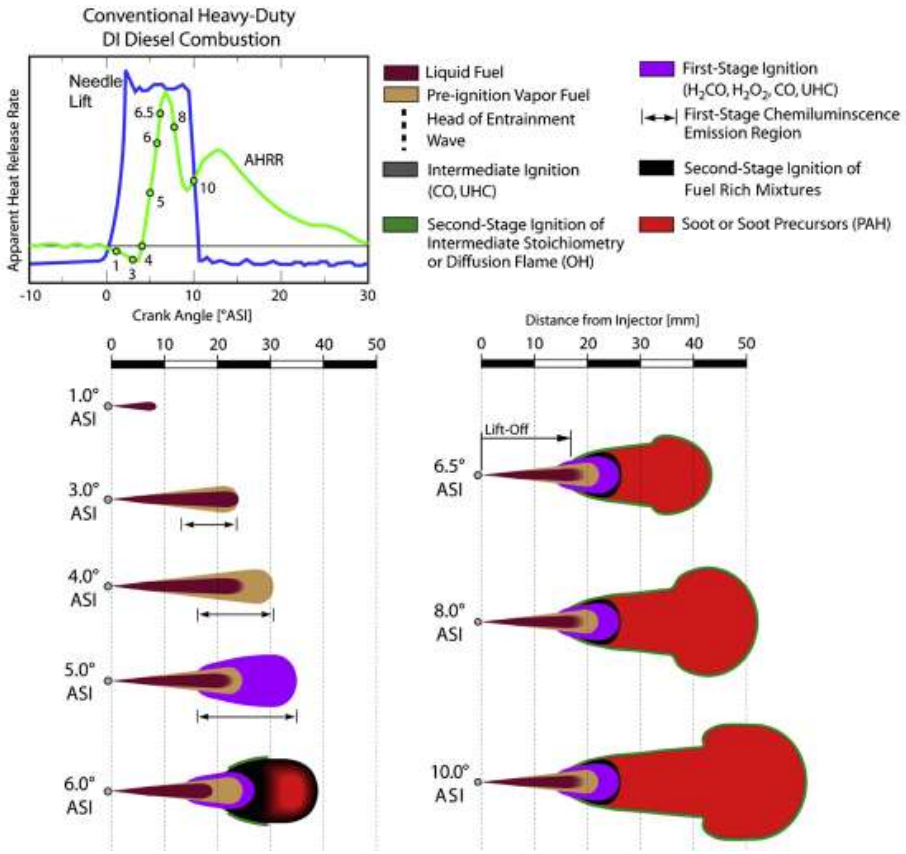

Figure 2.7: Schematic overview of the processes involved in diesel sprays according to Musculus et al. [30]

From the conceptual models described above a good understanding of the diesel combustion process already exists, however they still have a lot of shortcomings and lack explanation for the observed behavior such as: how soot may fail to oxidize and become particulate matter and the interaction between multiple plumes or wall.

2.3 Nozzle flow

The nozzle flow refers to all the influences from the injection system till the exit of the nozzle hole. Knowledge of this flow behavior is important since this flow will significantly affect the onset of the atomization process.
It is a complex flow and depends on tolerances, clearances and roughness of the injector parts, which makes modeling with high accuracy extremely difficult [31]. Due to the narrow nozzle holes and high pressure differences, phenomena such as turbulence and cavitation can occur, strongly depending on the shape and size of the nozzle.

Most of the research reported in literature is performed on a common-rail injection system, as this enables a better control of the injection pressure. In this work a pump-line-nozzle system is used and one might expect that the variable injection pressure will affect the nozzle flow and for this the further spray development. However, Blessing *et al.* [32] concluded from their experimental research that the main difference between these two injection systems is located at the start of injection.

In the next sections 3 phenomena that occur in the nozzle and will affect the further spray development are described: cavitation, turbulence and needle lift & vibration.

2.3.1 Cavitation

Cavitation is the formation of vapor cavities in a liquid due to a sudden and local pressure drop. The process is also known as nucleation. These vapor bubbles collapse inside the nozzle or at the nozzle outlet, depending on the nozzle and the cavitation number K, as discussed further. The pressure drop causes the local tension $(P_v - P)$ to exceed the tensile strength of the liquid, $P_v - P_{cr}$, with P_{cr} the critical pressure, resulting in the following criterion for cavitation [33, 34]

$$Cavitation \Longleftrightarrow P_v + \left(\mu \frac{\delta u}{\delta y}\right) - P > P_v + \left(\mu \frac{\delta u}{\delta y}\right) - P_{cr} \tag{2.1}$$

where P is the local pressure, P_v the vapor pressure and $\mu \frac{\delta u}{\delta y}$ gives the influence of the viscous stresses [33].
Cavitation is often considered to be the main reason for the primary break-up of diesel sprays [35–38]. The transient behavior of the exit velocity due to the occurrence of cavitation bubbles increases the turbulence and surface perturbations [36, 39]. Other authors [40, 41] conclude that the collapsing of cavitating bubbles directly results in disintegration of the jet and a shortening of the break-up length.

For most experimental set-ups, it is not possible to look into the nozzle and to investigate the different cavitation patterns. Therefore, a cavitation parameter is defined based on external parameters, derived from the 1D law of Nurick [42] (cfr. Eq. 2.2). Under cavitation conditions, the discharge coefficient C_d, which represents the losses in the nozzle, is given by the ratio of the actual mass flow and the theoretical mass flow:

$$C_d = \frac{\dot{m}}{\dot{m}_{th}} = \frac{A_0 C_c \sqrt{2\rho_l (P_1 - P_v)}}{A_0 \sqrt{2\rho_l (P_1 - P_a)}} = \frac{C_c \sqrt{P_1 - P_v}}{\sqrt{P_1 - P_a}} = C_c \sqrt{K} \tag{2.2}$$

where C_c is the Nurick contraction coefficient, A_0 the theoretical cross section; P_1 is the pressure at the nozzle inlet, P_a the ambient pressure and K the cavitation number.

While the theoretical mass flow $\dot{m}_{th}$ depends on the pressure drop $(P_1 - P_a)$ across the nozzle, the actual mass flow $\dot{m}$ does not increase if the pressure difference across the nozzle is raised for a fixed injection pressure. From the model of Nurick, it can be concluded that the cavitating nozzle is choked, or thus, the mass flow is independent of the ambient pressure P_a. Equation 2.2 shows that in cavitating conditions, C_d is proportional to $\sqrt{K}$. However, in non choking conditions, the discharge coefficient C_d depends on the Reynolds number, but is independent of K, because the mass flow is not choked. K_{crit} is defined as the experimentally determined point in which the discharge coefficient becomes independent of the pressure difference across the nozzle. This results in the following criterion for cavitation: if $K<K_{crit}$, the mass flow is choked and cavitation occurs as visualized in Fig. 2.8 [42].

It is important to notice that the value K_{crit} is not a fixed parameter for a particular injector. Other commonly used parameters to describe the influence of cavitation

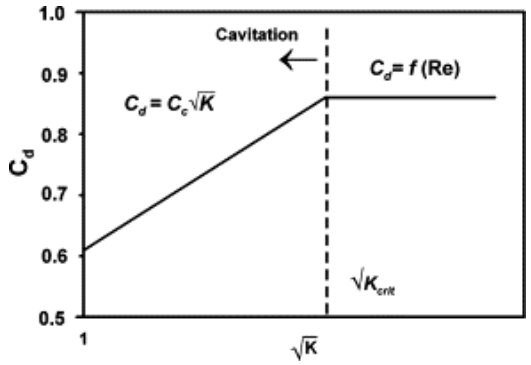

Figure 2.8: One dimensional criterion for cavitation following the model of Nurick [42]

are the velocity coefficient C_v (Eq. 2.3) which describes the velocity change at the

nozzle outlet, the area coefficient C_a (Eq. 2.4) which describes the flow area change at the nozzle outlet and C_ρ (Eq. 2.5) which describes the flow density change at the nozzle exit.

$$C_v = \frac{v_{0,\text{eff}}}{v_{0,th}} \tag{2.3}$$

$$C_a = \frac{A_{0,\text{eff}}}{A_{0,th}} \tag{2.4}$$

$$C_\rho = \frac{\rho_{0,\text{eff}}}{\rho_{0,th}} \tag{2.5}$$

$$C_d = C_v C_a \tag{2.6}$$

with $v_{0,\text{eff}}$, $A_{0,\text{eff}}$ and $\rho_{0,\text{eff}}$ the effective outlet velocity, the effective nozzle outlet cross section and effective fuel density respectively.

Many authors report [36, 41, 43, 44] that the mass momentum flux increases proportionally to the pressure drop (cfr. left of Fig. 2.9), even for choking conditions. So, as the mass flow stagnates (cfr. right of Fig. 2.9), the outlet velocity increases for choking conditions. All cavitation mechanisms can be divided in 2 categories:

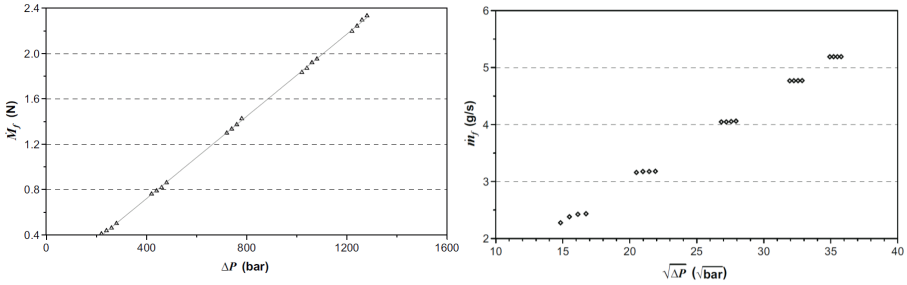

Figure 2.9: Influence cavitation on the mass flow rate and momentum flux [43]

geometrical & string or vortex cavitation as displayed in Fig. 2.10. For geometrical cavitation, the low pressure is induced by the in-nozzle geometry, while string or vortex cavitation occurs by the formation of vortical structures with low internal pressures.

Geometrical cavitation

Geometrical cavitation means that cavitation is induced by the reduction in static pressure by an abrupt change in geometry of the flow passage, e.g. when the needle starts to lift or at the entry of the nozzle holes: the liquid is accelerated, pressure is reduced and vapor bubbles are formed.
Geometrical cavitation is the most important and most reported type of cavitation.

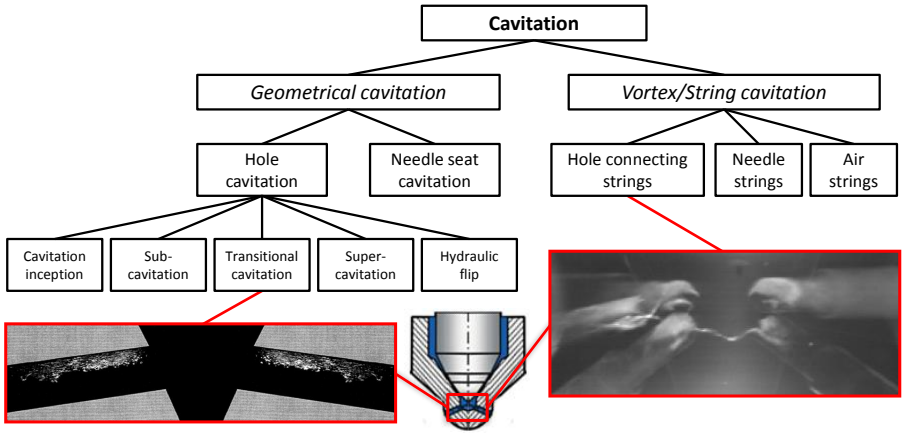

Figure 2.10: Overview of different cavitation types [45, 46]

These are briefly discussed in the following.

At the corners of the inlet, the strong curvature of the flow causes a separated flow and a recirculation zone is formed. The presence of this recirculation zone decreases the flow section of the liquid, causing the static pressure in the throat section to fall further. The cross section for the liquid with the minimal static pressure, and thus the maximum speed is called the 'vena contracta' as represented in Fig. 2.11.
Several classifications for the geometrical cavitation exist of which the classification according to the cavitation length L_{cav} is the most common. The cavitation length is the length of the part of the hole where cavitation bubbles are present (cfr. Fig. 2.11). This length is maximal if L_{cav} equals the total hole length L_{hole}. The classification can be subdivided in (see also Fig. 2.10):

- Cavitation inception: occurrence of the first cavitation bubbles at the inlet. $L_{cav} \sim 0$.
- Sub-cavitation and transitional cavitation regime: the cavitation zone grows $0 < L_{cav} < L_{nozzle}$.
- Supercavitation: the cavitation zone reaches the outlet: $L_{cav} = L_{nozzle}$.
- Hydraulic flip: no more cavitation is present.

The last type, hydraulic flip, is the last regime that could be reached: air from the combustion chamber enters the recirculation zone, the pressure inside the injector hole increases and cavitation disappears. This has an important influence on the spray development: the spray has a laminar appearance and is entirely liquid while choking does not occur. This flow regime has to be avoided: the break-up of the

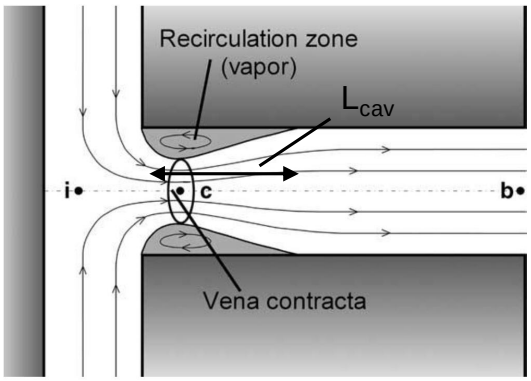

Figure 2.11: Schematical representation of geometrical hole cavitation with indication of the 'vena contracta' [43]

spray is inhibited, resulting in a very narrow spray angle and consequently an insufficient fuel-air mixing.
Hydraulic flip is reported in literature for simplified nozzles without needle, but does not occur in real nozzles, where the presence of the needle induces more turbulence, causing the separation zone to reattach before the hole outlet [37].

Comparison has shown that nozzles which promote cavitation (e.g. small L/D, sharp edges, cylinder-shaped hole) significantly increase the spray cone angle [42, 47–49]. As the cavitation length L_{cav}, increases, there is a further increase of the spray angle. The spray angle reaches its maximum value when the cavitation length L_{cav} is almost equal to the nozzle length L_{nozzle} [50]. The widest angle is detected at the critical cavitation number $K = K_{crit}$, which implies choking or supercavitation.
Gavaises & Andriotis [51] showed that the full spray angle increases a lot (up to 30°) in the transition from non-cavitating flow to supercavitation.
Another nozzle characteristic that influences the cavitation phenomenon is the hole conicity k, defined as

$$k = \frac{D_{in} - D_{out}}{D_{out}} \tag{2.7}$$

where D_{in} and D_{out} are in- and outlet hole diameters.
A constant outlet diameter and increasing inlet diameter results in a smoother decrease in cross section towards the exit which suppresses or reduces cavitation [40, 42, 52].

Vortex/String cavitation

The origin of hole strings or hole connecting strings is found in the interaction of the upstream flow with cross flow between the injector holes. Due to the presence of different pre-existing hole cavitation structures in the different holes, the flow rate is not equal through all these holes. This is the reason for the cross flow between adjacent holes. Due to the interaction with the upstream flow, vortical structures between the nozzle holes are present. The low pressure (still higher than the vapor pressure) in this vortex sucks out the pre-existing hole cavitation bubbles and forms a hole string that could link two holes together by a hole connecting string. So, in contrast to geometrical cavitation, cavitation strings do not form due to a local pressure drop, but rather represent a mechanism of vapor transport [53]. Cavitation strings develop in a transient way and disappear in the different holes repeatedly during one injection. This causes a difference in fuel flow and spray formation through the different holes (hole-to-hole variations). Whereas geometrical cavitation is beneficial for the atomization, it is clear that the spray-to-spray and hole-to-hole variations due to string cavitation are highly undesirable.

If the viscosity difference between two fuels is high enough, it is possible that, under certain conditions, supercavitation occurs for the low viscous fuel and not for the high viscous one. In that case, a difference in outlet velocity is more pronounced: C_v increases for the fuel with supercavitation regime, causing a higher fuel velocity at the outlet of the orifice, resulting in a higher penetration rate at start of injection.
The longer the cavitation length inside the nozzle, the smaller the influence of viscosity on friction along the nozzle wall because fuel vapor will reduce the contact between liquid fuel and orifice wall. For cases where both fuels show supercavitation inside the nozzle, the previously mentioned effect of viscosity on friction in the nozzle is negligible, when comparing the two fuels with each other. However, if supercavitation occurs for one fuel, whereas for the other fuel there is only incipient cavitation, this influences the difference in fuel velocity at the nozzle exit.

2.3.2 Nozzle turbulence

Turbulence appears when the fuel is squished into the nozzle and through the narrow openings (e.g. between the needle and needle seat) and when the flow suddenly changes direction. The inertia of the liquid prevents the streamlines from following the physical boundaries of the nozzle, resulting in a chaotic flow.
Initial perturbations on the jet surface are induced by the radial velocity components of the turbulent fluctuations in the jet, originating from the shear stress along the nozzle wall and possible cavitation effects [54]. Tatchel *et al.* [31] demonstrated the relative importance of turbulence/cavitation induced and aerodynamic induced break-up, shown in Fig. 2.12, which shows the local distributions of the

turbulent and aerodynamic break-up rates in a section across the spray axis. The maximum of the turbulence/cavitation induced break-up intensity is observed very close to the nozzle exit as expected.

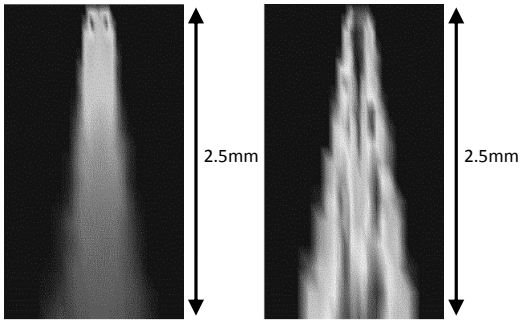

Figure 2.12: Influence of turbulence (right) on the spray atomization [31]

However some authors such as Karrholm *et al.* [55] believe that the influence of the turbulence is relatively weak compared to cavitation and so do not take turbulence inside the nozzle into account. Optical measurements in combination with transparent nozzles in real size geometry [35, 49, 56, 57] have shown that due to the turbulent and often cavitating flow the disintegration of high-pressure diesel sprays begins already inside the nozzle holes, and that the jet leaving the nozzle hole consists of a very dense spray of ligaments and droplets instead of a single liquid core.

The influence of viscosity is most pronounced for turbulent (non-cavitating) conditions: in cavitating conditions, liquid flow detaches from the wall and therefore liquid viscosity plays a minor role [58]. So, the discharge coefficient is practically unaffected by viscosity in the supercavitation regime (and thus, the influence of the density is dominant).

2.3.3 Needle vibration & lift

An important but almost untouched topic is the influence of the needle vibration, lift and misalignments. The reason is basically because of the difficulty to predict the behavior since that depends on the unique manufacturing defects. Powell *et al.* [59, 60] performed a high-speed X-ray imaging technique to visualize the needle motion and compared this for several 'theoretically' identical nozzles. A significant difference was found in both needle lift profile and radial vibration as shown in Fig. 2.13. How this needle behavior influences the spray is not yet clear since it is difficult to isolate the different nozzle flow features.

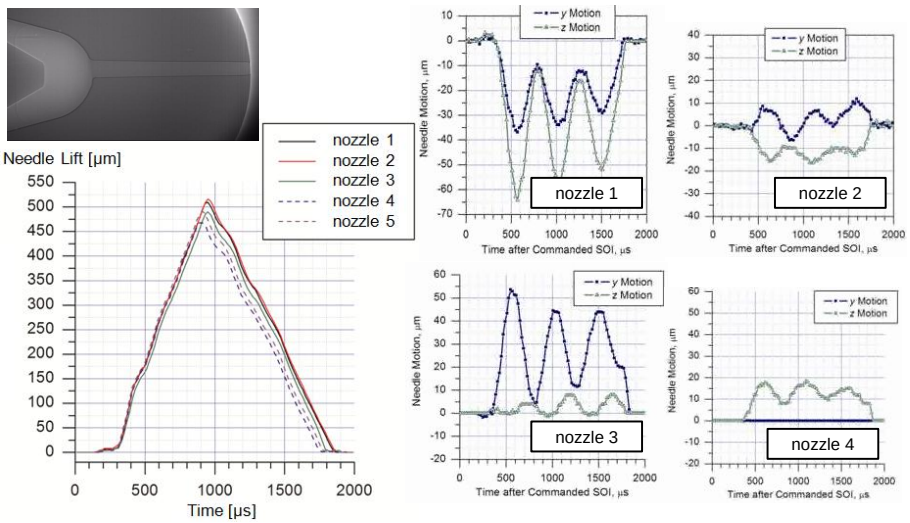

Figure 2.13: Comparison of needle motion behavior of 'theoretically' identical nozzles. Left: the needle lift profile. Right: radial nozzle vibration profiles for the different nozzles in 2 perpendicular directions [59, 60]

2.4 Atomization & Vaporization

The atomization process is usually divided into 3 main processes: primary break-up, secondary break-up and dispersion of the droplets. Finally, the droplets are vaporized.

2.4.1 Primary break-up

The primary break-up of the spray jet is the atomization process that occurs close to the nozzle and is a difficult zone to analyze [61, 62].
The three main mechanisms reported in literature, responsible for the disintegration of the jet are the aerodynamic-induced atomization, the jet turbulence-induced atomization and the cavitation-induced atomization [63, 64]. Modern technologies such as micro-visualisation allow researchers to investigate the spray areas near the nozzle. As an example, Manin *et al.* [65] used a microscopic lens and a resolution of 166px/mm to capture the details of the spray at the nozzle down to 2mm. Crua *et al.* [66] was even able to obtain a resolution of about 1650px/mm with an acquisition rate of 100kHz.

Some inconsistency exists in literature concerning the nature of the injected jet. Some [49, 56] claim that the disintegration of the jet already starts inside the nozzle and that droplets or ligaments are injected rather than a solid liquid jet. Others

showed that the injected liquid does not break up instantly after injection and the unbroken portion is referred to as the liquid break-up length [35, 61]: measurements of electrical conductivity in the spray confirmed that there is an intact core of essentially unbroken liquid in the vicinity of the nozzle exit [61]. These 2 interpretations have led to different modeling strategies such as the 'blob'-model, which considers the injection of droplets with a diameters size of the nozzle hole [61, 67–69] and the 'WAVE' breakup-model [63, 67, 68, 70], in which the liquid core is disintegrated by the aerodynamic drag.

The first break-up process is usually considered as the disintegration by instabilities caused by aerodynamic shear forces (i.e. Kelvin-Helmholtz instabilities) and depends on the interaction of the jet structure with the ambient gas, jet internal turbulence and cavitation inside the nozzle holes [54, 63]. The instabilities occur at the surface of 2 fluida, due to velocity differences between the fluida.
The Kelvin-Helmholtz theory predicts the onset of the instabilities and the droplet size when break-up occurs. The primary break-up is usually described in terms of break-up time. At the break-up time, the jet will have typically penetrated about 20-100 nozzle diameters into the combustion chamber [71].

A further potential primary break-up mechanism is the relaxation of the velocity profile [49]. However, this phenomenon is more applicable for not fully turbulent nozzle flows. In the case of fully developed turbulent pipe flow (large L/D ratios, no cavitation), the velocity profile may change at the moment the jet enters the combustion chamber.
The most important primary break-up mechanisms are illustrated in Fig. 2.14.

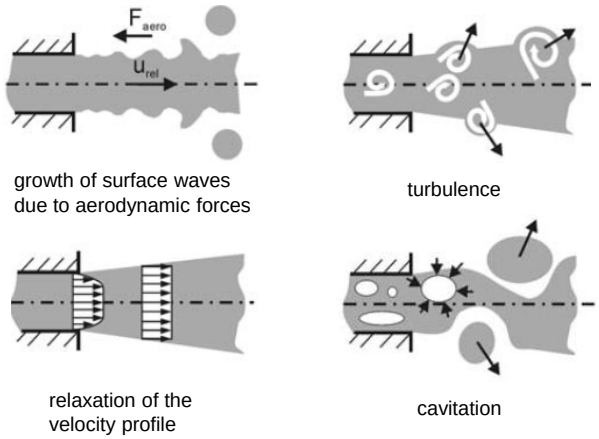

Figure 2.14: The 4 most important primary break-up mechanisms: aerodynamic forces, turbulence, velocity relaxation and cavitation [66]

2.4.2 Secondary break-up

The quality of the atomization is usually characterized by the spray angle, droplet size distribution or sauter mean diameter (SMD). Once spherical droplets are created during primary atomization, secondary atomization starts and its governing mechanisms are common for any type of spray: it only depends on the initial droplet sizes, relative velocity between the drop and ambient gas and the physical properties of the system (pressure, temperature, viscosity, surface tension,...). These parameters determine the break-up mechanism under which a droplet will further disintegrate [54]. The dependency can be represented by the dimensionless Weber number (*We*) (Eq. 2.8) and the Ohnesorge number (*Oh*) (Eq. 2.9) [54, 61, 63, 64, 72, 73].

$$We = \frac{\rho v^2 l}{\sigma} \tag{2.8}$$

$$Oh = \frac{\mu}{\sqrt{\rho \sigma l}} \tag{2.9}$$

with l the characteristic length, σ the surface tension, ρ the liquid density, μ the dynamic viscosity and v the liquid velocity.
The relation between *We* and SMD is usually expressed with correlations such as the one of Elkotb [74]:

$$\text{SMD} = 3.8\nu^{0.335} \left(\sigma \rho_L\right)^{0.737} \rho_a^{0.06} \delta P^{-0.54} \tag{2.10}$$

with ν the kinematic viscosity.
For straight vegetable oils and animal fats, the Ohnesorge number can be 10 times higher than for diesel: the secondary break-up therefore is delayed caused by the high viscosity and surface tension [75]. Reddemann *et al.* [76] mentioned that for a wide range of Ohnesorge numbers (Oh<0.1) the liquid viscosity has little influence on secondary break-up and the surface tension becomes the most important parameter.
Important to mention is that this theory can be counteracted by the coalescence and collision of the droplets, especially in the dense spray region. This phenomenon is studied in detail by Crua *et al.* [77]. They noticed that the droplets near the nozzle are generally smaller than further downstream the nozzle (20-25*mm* downstream). Collision was considered as the main cause. More further downstream, the droplets (or *SMD*) again become smaller due to the evaporation rather than further breakup.
The importance of the collision-related processes is illustrated in Fig. 2.15, comparing the spray penetration and *SMD* predictions with and without the collision model, along with experimental data [62]. The penetration shows a small change but the *SMD* is more strongly affected.

Due to the high density of the ambient gas, the droplets will experience drag forces. This drag corresponds to a momentum transfer from the droplets to the ambient gas, decelerating the droplets [78]. A higher chamber gas density causes an increased deceleration of the droplets and as a result, faster droplets will push the slower ones outside more rapidly. This stronger dispersion of the droplets results in wider spray angles. This is expressed by different authors [79, 80] using the relationship $tan(\theta) \sim \rho_a^x$, with x between 0.17 and 0.20 in most publications. The spray angle is also influenced by the fuel density: an increase in fuel density results in a decreased deceleration of the spray. Therefore, less droplets are pushed aside and spray angles are smaller [78].

The effect of the injection pressure on the spray angle has been studied by e.g. Naber and Siebers [79]. In their experiments, they used three different nozzles and the results showed no significant effect of injection pressure ranging from 75 to 160*MPa*. This was confirmed by Arregle *et al.* [81] and Desantes *et al.* [80]. The latter stated that increasing the injection pressure has an influence on the spray angle through cavitation only. So as long as the cavitation regime does not change, the spray angle is independent of the injection pressure. Dernotte *et al.* [78], on the other hand, conducted non-vaporizing experiments and observed an increase in spray angle when the injection pressure increased in the range between 30 and 150*MPa*.

2.4.3 Mixing & dispersion

Much further away from the nozzle, the droplets drift away from each other and it was seen by several researchers that each droplet can be considered (or modelled) as an isolated droplet [64]. Coalescence and collision is usually neglected in this region since this is more of importance more nearby the nozzle [62, 69].
Neglecting collisions and coalescence would simplify the situation enormously. On the other hand, the droplets get a lot smaller by the secondary break-up and evaporation. This means that the small inertia of the droplets causes them to be more sensitive to the air motion and turbulence in the combustion chamber. Further downstream their velocity is decreased to the order of the in-cylinder air motion. As a conclusion, this final stage of the spray is even more difficult due to the fact the turbulence in the cylinder should be known or modelled as well.

The complete spray atomization is usually characterized by the spray angle θ. As will be discussed in section 3.3, no consistency exists in literature concerning a proper definition. Most definitions are based on high speed spray images. Apart from the correct value of the spray angle, many authors found similar trends of the

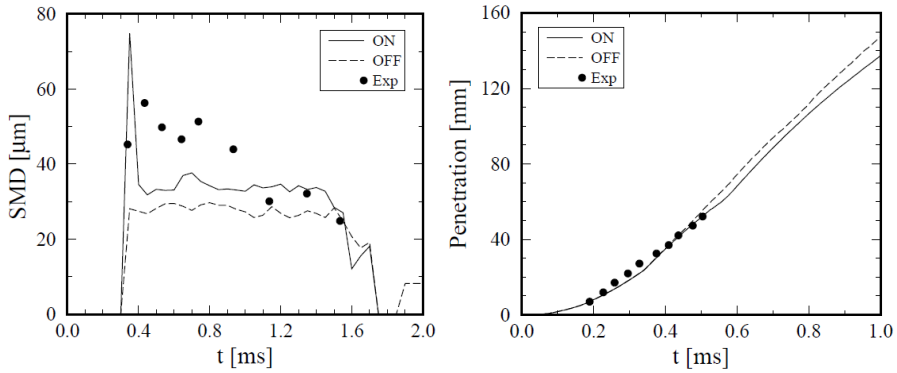

Figure 2.15: Influence of the collision model on the SMD (left) and spray penetration (right) [62]

influencing factors. Reitz & Diwakar [61] found that the spray angle (or quality of the atomization) is proportional to $\sqrt{\rho_a/\rho_f}$. It is agreed that larger cone angles lead to a smaller minimum drop size [61, 82], and a better dispersion as a logical consequence. Several authors report that the spray angle changes during the injection: a wide spray angle is found at the beginning of the injection but narrows with the injection duration to a steady state value [82]. The steady state value was also noticed in the experiments conducted in this work, even for PLN systems. The transition to the steady state local spray angle takes less than $1ms$. The approach of the steady state value can happen with or without overshoot, but researchers have not yet reached any consensus about this behavior [79, 83].
At the end of injection, a small peak in spray angle can be observed for every axial position. This is probably caused by the descent of the injector needle [79].
Since the spray angle is related to the atomization quality, fuel parameters such as viscosity and surface tension will have an impact. The injection pressure will also play an important role. High injection pressures correspond with high velocities which promote the shear stresses and instability growth and as such the atomization [84, 85]. The injection pressure is reported to influence the penetration, with $S(t)$ being proportional to $\Delta P^{0.25}$, with ΔP the pressure difference accross the nozzle [79, 81].

The influence of the aspect ratio (the ratio between the hole length L and the hole exit diameter D) on the spray angle was investigated by Varde *et al.* [85] and found that the spray angle varies with the orifice aspect ratio: for low aspect ratios, the angle was increasing with increasing injection pressure. At an aspect ratio of 4, the dependency of the angle on the injection pressure was negligible. For higher aspect ratios, the angle decreased with increasing injection pressure. The latter in-

dicates that the cavitation influence is decreased, resulting in a less atomized spray. High viscosity suppresses also the instabilities required for the fuel jet to break-up and thus delays atomization resulting in reduced angles [86].
Surface tension effects were studied by Hiroyasu *et al.* [87]. The fuel in their research was chosen in such way that they had the same viscosity. For the same injection pressure (and viscosity), the *SMD* increased with an increase in surface tension, but the effect became smaller for higher injection pressures.
An increase in fuel density, on the other hand, provoked the instabilities in the fuel jet required for atomization.

Important as well is the fuel temperature. The storage temperature and injected fuel temperature is reported to differ significantly [88] as will also be confirmed in chapter 4. This knowledge is important in order to know whether the droplets are in a superheated condition or not, since flash-boiling effects might already start within the nozzle hole while not expected. The consequences are similar to the ones of cavitation, except for the fact that these vapor bubbles do not implode and so do not provoke the atomization [64].
Ra & Reitz [88] also concluded that the initial droplet size mainly affects the early stages of evaporation of single multi-component droplets. The evaporation constants during the later stages of the drop life time are independent of the initial drop temperature.

Dernotte *et al.* [78] concluded that increasing viscosity leads to a longer penetration during the fully developed zone, while penetration was similar during the transient zone. Furthermore this effect of viscosity seems to be less pronounced for higher ambient densities. The penetration in the transient region is slower by the friction inside the nozzle caused by the higher viscosity and this reduces the injection velocity. The bigger droplets on the other hand, result in higher penetration for the fully developed zone.

The fuel density has different effects on the droplet velocity. On the one hand a low density leads to a high outlet velocity, following the Bernoulli law. On the other hand it results in stronger droplet deceleration due to aerodynamic forces [76]. For their non-vaporizing CR experiments, Dernotte *et al.* [78] observed an increase in penetration for the more dense fuels. This effect was only observed in the fully developed zone, while in the initial stages of the injection the penetration did not show any dependence on fuel density for all operating conditions. Furthermore, it can be seen that the influence of density is less significant for higher injection pressures and ambient density.

The effect of the density on the *SMD* is not very clear: near the nozzle shear

stresses are higher and the atomization might be better, causing smaller droplets. However, collision and coalescence processes might be stronger due to the stronger deceleration of the droplets. This causes the SMD to increase at positions further downstream the spray.

2.4.4 Evaporation

Siebers & Naber [79] and others [30, 89] have shown experimentally that for current diesel technology, the atomization process is quick enough so that the thermodynamic equilibrium is reached very rapidly and dominates the droplet's vaporization: mixing is the limiting factor rather than atomization.
To determine which is the limiting factor, Siebers [90] investigated the influence of the orifice diameter and the injection pressure on liquid length. If the mixing controlled model is assumed, a comparison between the energy supply rate and the rate of required energy is needed; the rate of energy supplied or gas entrainment rate is proportional to the orifice diameter while the rate of energy needed or fuel mass flow rate is proportional to the square of the orifice diameter d_0. So the spray length needed to entrain the appropriate amount of air to vaporize the fuel (i.e. the liquid length) should be proportional to the orifice diameter. Using the local interphase controlled evaporation model, one should look at the lifetime of a droplet in contact with a gas containing more than enough energy to evaporate the droplet. The orifice diameter was found not to be a main parameter determining the *SMD* for injections at high P_{inj}, while the lifetime of a droplet is mainly dependent on his diameter.
Siebers gave the following numerical example based on results he found in literature: a factor of five increase in orifice diameter results in a 50% increase in the mean droplet diameter. This would result in a factor of two increase in the droplet lifetime and about a 50% increase in the droplet penetration distance (i.e. liquid length) based on models for droplet evaporation. A 50% increase in liquid length is significantly less than the factor of five increase in liquid length predicted in the mixing controlled limit for a factor of five increase in orifice diameter. The experiments showed a linear relation between liquid length and orifice diameter, indicating that the mixing control model is valid for diesel injections. So, vaporization in a diesel spray is controlled by air entrainment processes. This is true for current and proposed future engine technology conditions. The conclusion does not, however, say that atomization and individual droplet vaporization processes are not important, only that they are not the rate-limiting steps in the fuel vaporization process.

The mixing-limited hypothesis idea makes it possible to drastically simplify some spray models as will be discussed in chapter 7. As a result, for high injection pres-

sures (P_{inj}> 70MPa) the droplet size distribution and spray cone angle barely, if at all, changes with altered injection pressure [87].
Vaporization in a reacting diesel spray, is controlled by air entrainment into the spray. Atomization and local interphase transport processes, such as droplet evaporation, do not limit the rate of evaporation [90].
Siebers [90] showed that the liquid length decreases only slightly linear with the fuel temperature. The effect of fuel temperature is most significant at the low gas temperature-density condition. On a relative basis, the reduction in liquid length for each condition over the 60°C change in fuel temperature is approximately 12%.

Vaporization is related to heat transfer and so to the heat conduction within the droplet and the heat convection from the gas to the droplet. The Biot number ($Bi = h.l/k$, with l the characteric length, h the convection coefficient, k heat conductivity) plays herein an important role which relates the resistance to heat conduction within the droplet to the resistance to heat convection from the gas to the droplet. For Biot numbers much less than unity, the assumption of a uniform temperature within the droplet is justified. In the other case, convective heat transfer dominates [71].
Karrholm and Nordin [91] have shown that the relative velocity is the most important parameter for the evaporation rate.
The same conclusion as for the spray angle can be made concerning the liquid length: no clear definition is found but the trends for high pressure diesel injections are in accordance with the literature [92].
While the liquid length decreases with increasing ambient temperature, the inert spray penetration is barely influenced. As a result, due to combustion the steady state liquid length, established prior to start of ignition, is slightly shortened [93].
The injection pressure has the opposite effect: the spray penetration increases while for the high injection pressures, the liquid length does not change significantly [23, 31, 90]. The last indicates that the change in fuel flow rate that occurs with a change in injection pressure must cause exactly the same change in the overall fuel evaporation rate [31]. This is also the reason why under these conditions the vaporization process can be considered as limited by the fuel-air mixing rate.
Furthermore, during injection a steady state liquid length is established with small fluctuations related to turbulence [90]. Pickett *et al.* [92] also noted this but pointed out that the timing at which the steady state liquid length is reached, is delayed when the injection pressure decreases.
The liquid length scales linearly with the orifice diameter: doubling the orifice diameter quadruples the fuel injected, but only doubles the entrained gas. This means a factor of two longer spray entrainment length is required before the energy needed to vaporize the fuel can be supplied, resulting in a factor of two longer liquid length [90]. The same author showed however that the orifice aspect ratio

(*L/D*) barely influences the liquid length. The most notable effect occurs at the low temperature-density condition with the longest liquid lengths. For this condition, the tips with aspect ratios of 4.2 and 8.0 have liquid lengths 5% and 8% longer than the shortest aspect ratio tip, respectively [90].

Another important boundary condition is the ambient gas density, actually more important than the ambient pressure. The ambient gas density has a significantly larger effect on spray penetration and a smaller effect on spray dispersion [79, 82]. The range for the penetration dependence on ambient gas density reported in the more recent investigations is $\rho_a^{-0.23}$ to $\rho_a^{-0.5}$ with one exception. That exception occurs early during the injection period, where Hiroyasu and co-workers have shown that penetration depends linearly on time, but has no dependence on gas density [79]. The most widely cited penetration data and correlations are those of Hiroyasu and Dent, both of which have a density dependence of $\rho_a^{-0.25}$.

The effect of the ambient density on liquid length was found to be strongly non-linear [90, 93]. The increasing gas density causes a decrease in liquid length but this effect decreases for higher densities. This trend was observed for all temperatures. In the early stages of injection, the spray behavior is different. Hiroyasu & Arai [35] found that during the early stages of the injection the penetration is a linear function of time and is not affected by the density of the ambient gas.
The spray angle on the other hand increases with an increase in the ratio of ambient gas and fuel densities with a factor of about $\left(\frac{\rho_a}{\rho_f}\right)^{0.19}$, according to Naber and Siebers [79]. Varde *et al.* [85] proposed 0.33 for the exponent.
The effect on the liquid length is similar to the effect of the ambient temperature; the strong non-linear decrease for both an increase in ambient temperature and density is shown in Fig. 2.16.
Decreasing the fuel volatility, on the other hand, increases the liquid length since more energy is required to vaporize the fuel. In the case of multi-component fuels the liquid length is more controlled by its lower volatility fraction [90]. The lower volatility usually comes together with a higher viscosity and surface tension, which are regarded to have the largest contribution to the change in SMD [84].

2.5 Conclusions

The intensive study of diesel sprays since decades has led to already a lot of understanding and several conceptual models has been derived from these results and observations.
The most widely accepted conceptual models for high pressure diesel sprays has

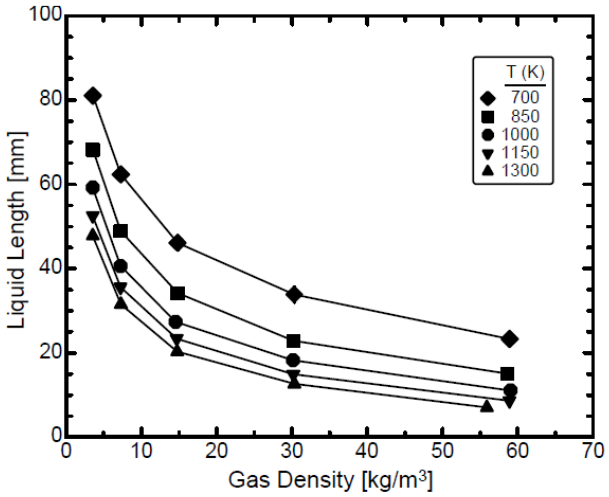

Figure 2.16: Liquid length as a function of gas density for five gas temperatures [90].

been described above, pointing out the most important features of the diesel spray and combustion. Next, the vaporizing spray has been considered in more detail, revealing the mechanisms for the sub-processes and the influencing parameters.

The behavior of some important spray charactization parameters: the liquid length (*LL*), spray angle (θ) and penetration, are qualitatively summarized in table 2.1. Relations on which no consensus exists in literature are indicated with '?'.

	T_a	ρ_a	D	L/D	P_{inj}	T_b	μ_f	σ_f	ρ_f
LL	↓	↓	↑	↗	-	↑	↑	↑	-
θ	↓	↑	↓	↓	↗	-	↑	↓	↓
penetration	-	↓	↑	↘	↑	↘	↑	↑	↑
SMD	↓	?	↘	↓	↓	↓	↑	↑	↘

Table 2.1: Behavior of some spray characteristics (liquid length LL, spray angle θ, penetration and sauter mean diameter SMD) on the boundary conditions: the ambient temperature T_a, ambient gas density ρ_a, orifice diameter D, injection pressure P_{inj}, boiling point T_b (measure for the fuel volatility), fuel viscosity μ, fuel surface tension σ_f, fuel density ρ_f, with ↓: decrease, ↑: increase, ↘: slight decrease, ↗: slight increase, -: no effect, ?: no consensus in literature

3
Spray Diagnostics

"A fool is a man who never tried an experiment in his life."

- Erasmus Darwin -

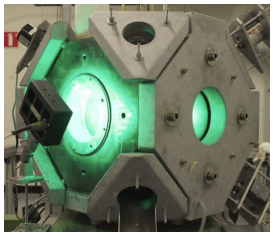

The chapter is organized as follows: the different spray and combustion parameters that were used in this work are defined. For each parameter, the applied diagnostics are described.

3.1 Introduction

The definition of the spray parameters in this chapter are related to the experimental work. A visual representation of the parameters, discussed in the text, which describe the spray are already presented in Fig. 3.1.
Only the optical diagnostics applied in this work are discussed in detail.

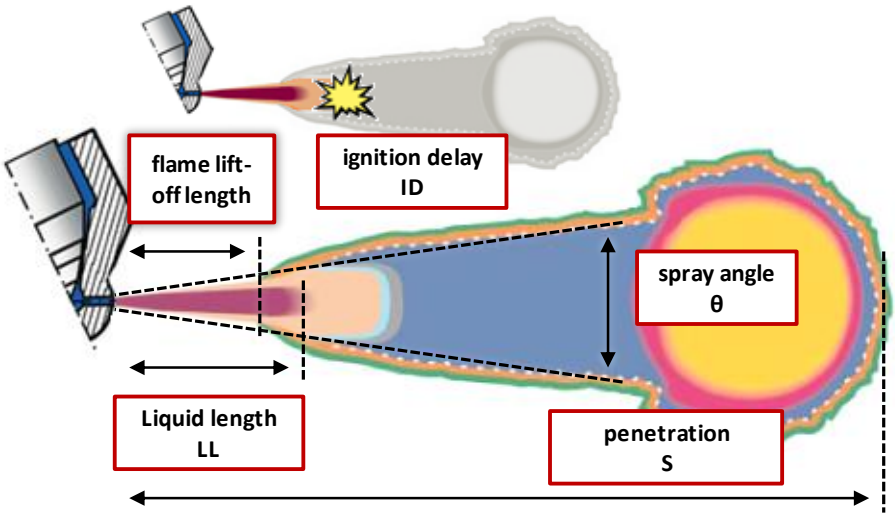

Figure 3.1: Visual representation of the measured spray parameters

3.2 Liquid length

3.2.1 Definition

The liquid length (LL) definition is based on the normalized pixel intensity of the acquired image. The determination of the average liquid length is based on the measurement of the light extinction through the liquid core. The reference level is the background of the image when there is no liquid injection. A mean image of the background, I_{BG} is created by averaging a number of individual frames taken right before start of injection (SOI). Next, each image during the injection can be divided by the background image, in order to obtain the normalized intensity of the image. The logarithm of the normalized intensity gives the extinction factor τ in the whole visualization field:

$$\tau(x,y) = -log\left(\frac{I(x,y)}{I_{BG}(x,y)}\right) \tag{3.1}$$

For the steady LL the evolution of τ along the spray axis is considered to be a measure for the liquid length. τ is computed on a time-averaged image, during the steady-state period of the injection. Several individual measurements are used to obtain an ensemble average together with shot-to-shot standard deviation.
This technique suffers from beam steering near the liquid spray tip, due to the refractive index gradient created by the vaporized fuel. Therefore the exact liquid length is not measured precisely. As a compromise, the decay of the extinction factor along the spray axis is therefore linearly fitted. The location where this linear fit intercepts zero, is defined as the liquid length as demonstrated in Fig. 3.2.

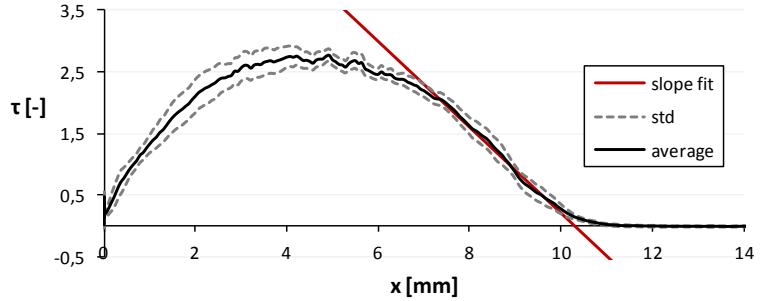

Figure 3.2: Image processing method for the averaged liquid length: the extinction factor τ is plotted along the spray axis. The liquid length is defined as the intersection of the linear fit of the decaying profile and the horizontal axis

3.2.2 Diffused back illumination (DBI)

A commonly used method to visualize the liquid phase in diesel sprays makes use of a light extinction method. In the case of an evaporating spray a diagnostic is required to filter away the gas phase. Diffused back illumination is such a technique and makes use of a diffuse light source. The setup configuration is presented in Fig 3.3. The details of the combustion chambers that are used in this work are discussed in chapter 4.
A diffuse light source ensures that multiple light beams go through each point of the measurement section. When a liquid droplet is present in that point, light will barely pass, both through external and internal reflection. The result is a dark spot on the projection screen. The deflection direction of the beams depend upon the density gradient and since multiple beams go through the same point, the brightness on the projection screen will differ less than is the case for diagnostics as schlieren and shadowgraphy, as explained later.
An advantage of DBI is that the incident illumination without the spray provides an intensity reference that can be used to determine the global extinction. Although

beam-steering still occurs for any single ray, the integration of multiple rays onto a single pixel has the effect of smoothing the effects of beam steering on the 2D results. The setup for the diagnostic can be dimensioned theoretically and the cal-

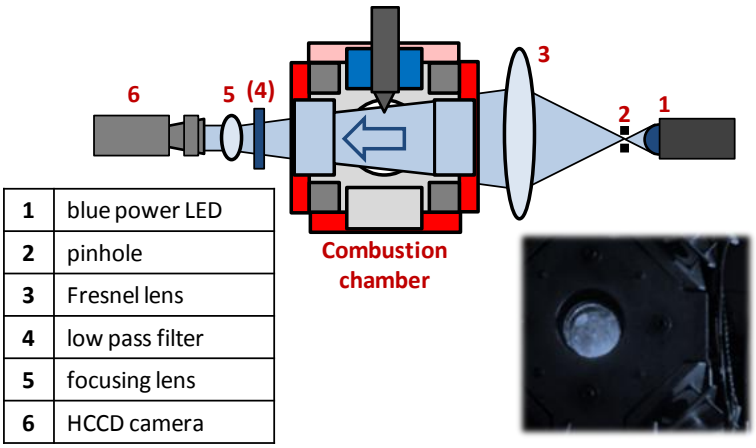

1	blue power LED
2	pinhole
3	Fresnel lens
4	low pass filter
5	focusing lens
6	HCCD camera

Figure 3.3: configuration of the implemented diffused back illumation setup

culations can be found in the work of Ghandi and Heim [94]. The setup makes use of a fresnel lens to direct as much light rays as possible towards the camera while maintaining homogeneous diffused light. The camera is placed in the direction of the light source. For this reason this diagnostic is categorized under the line-of-sight methods.

3.2.3 Mie-scattering

Another way to visualize the liquid phase is based on elastic scattering of light. Since scattered light is captured, this method is not a line-of-sight technique; the camera is positioned under an angle with the light source. In this research application there is an optical limitation since the optical access is perpendicular. If the light source would have been placed under an angle according to the window, some part of the image would not be seen and a lot of light would be lost through the scattering on the window. This technique is less prone to light inhomogeneities and for that reason, no diffusor or fresnel lens is required.

Accordingly, Mie scattering theory has no droplet size limitations and converges to the limit of geometric optics for large and smaller particles than the wavelength of the incident light. However mie-scattering theory is complex and for this reason it is only preferred for particles with similar wavelength to the scattered light, such as atomized droplets.

Mie-scattering becomes difficult when reacting sprays are investigated: soot particles might be big enough to scatter light with an intensity that can interfere with the signal from the liquid phase. According to Musculus *et al.* [95] it can be assumed that the light is extinguished by rather small soot particles (around 30-50*nm* in diameter, according to measurements by Bougie [96]) and is dominated by absorption, rather than scattering.

The schematic of the optical setup is given in Fig. 3.4. It should be pointed out that it is preferred to have the camera directly in front of the window perpendicular to the light source. In this way the maximum light intensity is achieved since less light is lost due to the limited collection angle as is the case in the represented configuration. Nevertheless, this configuration is useful when simultaneous measurement techniques are implemented with a limited number of cameras.

1	green power LED	**3**	planar mirror	**5**	HCCD camera
2	biconvex lens	**4**	quartz window	**6**	pulsed array LED

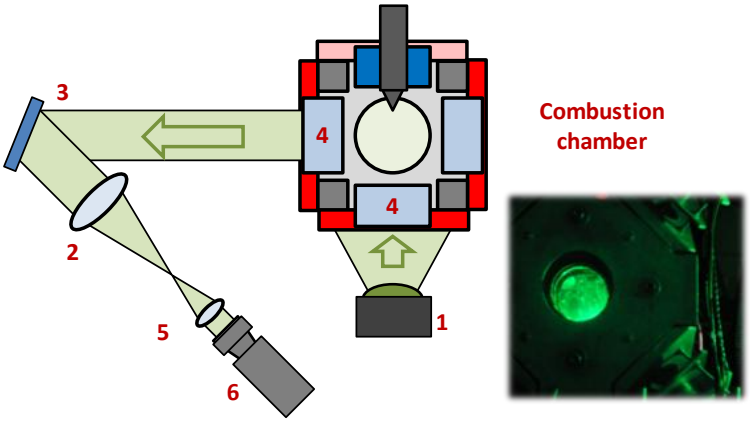

Figure 3.4: Configuration of the implemented Mie-scattering setup

3.3 Spray angle

3.3.1 Definition

The spray angle was already briefly discussed in section 2.4 and is in this section handled in more detail with the focus on how the spray angle can be obtained from optical diagnostics.
Several definitions for the spray angle are reported in literature. Hiroyasu and Arai [35] defined it as the maximum angle of a cone which was fixed at the nozzle

exit. Somers *et al*. [47] defined two types of spray angle. The local spray angle [47, 79] is the angle at a certain axial position. The second definition is the use of a macroscopic cone angle based on the contours of the spray and at a further distance from the injector [48]. Others define the spray angle θ_A as the acute angle of an equivalent isosceles triangle of which the triangle has the same area and height as the entire spray or only the upstream half of it, or an isosceles triangle combined with a semicircular top. The information on the spray angle which is obtained from only the upstream half of the spray or at a so-called standard distance is often used for correlating spray penetration with models [47, 48]. Varde *et al*. [85] took the average angle for the fully developed spray measured when the penetration of the spray plume in the chamber was at least 80mm from the injection point.
It can be concluded that no consistency or standarized spray angle exists in literature and care should be taken when comparing experiments, since the quantitative values can differ significantly among the different methods.
Furthermore, the sensitivity of the image processing can strongly depend on the used processing method. From each spray experiment in this work, the spray angle was calculated in 2 different ways which were found to be robust enough:

- averaged local spray angle
- Siebers angle

Averaged local spray angle

The full local spray angle θ_{loc} is defined at every position along the spray axis as the angle between the spray axis and the outer boundary of the spray [97], defined by the image processing: after the noise filtering and binarization, the spray boundary is determined with standard matlab functions. The local angle θ_{loc} is calculated according to Eq. 3.2. The parameters are defined in Fig. 3.5.

$$\theta_{loc} = 2.tan^{-1}\left(\frac{a}{b_{loc}/2}\right) \tag{3.2}$$

with

$$\begin{aligned} a &= x_{end} - x_0 \\ x_{start} &= x_0 + startDelay \end{aligned}$$

x_0 is the invisible part of the spray due to the thimble, which provides the possibility to investigate only 1 spray of a multi-hole nozzle as will be discussed in section 4.3.2, and is set to be 6.2mm, based on the CAD drawings. The parameter $startDelay$ involves the length of the spray zone in which the spray is still very short which would lead to an excessively fluctuating spray angle. As a default this

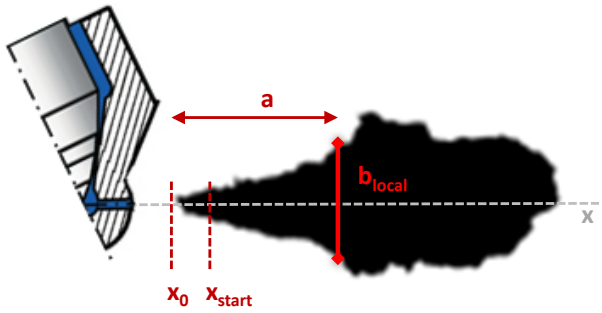

Figure 3.5: Definition of the parameters used in the determination of the local spray angle

value was put to 10*pixels*. In essence, the spray angle calculations start at 10*pixels* downstream the visual start of injection.
The local spray angles are found to be noisy and sensitive to the threshold of the image processing. A moving averaging operation is performed to smooth the data according to Eq. 3.3 with the moving average parameter *window* uneven and taken equal to 7. This is demonstrated in fig. 3.6.

$$\theta_{ma}(j) = \frac{1}{window} \sum_{i=-floor\left(\frac{window}{2}\right)}^{floor\left(\frac{window}{2}\right)} \theta_{loc}(j+i) \tag{3.3}$$

Finally, the local spray angles of each image are averaged to get the robust averaged local spray angle $\theta_{av,loc}$.

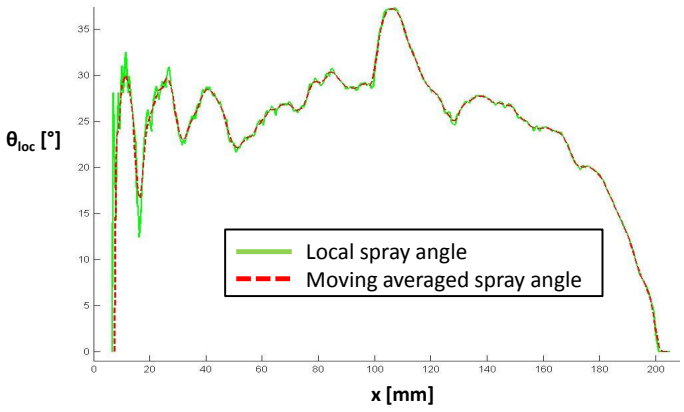

Figure 3.6: Time resolved local spray angle of a single experiment

Siebers angle

This angle definition is based on the definition proposed by Siebers [97] and has gained a lot of interest since this value is less sensitive to the used postprocessing technique and thresholding. This definition is even proposed as standardized spray angle by the Engine Combustion Network (ECN), a recently established network to share and standarize spray data. More details about the ECN are given in section 7.1. Since the first part of the spray is not visible, the expression was modified to Eq. 3.4 and is visualized in Fig. 3.7. From this expression it is noticable that only the first half of the spray is used for the angle calculation: the head of the spray experiences to much irregularities and vortices due to its transient behavior.

$$\theta_{Siebers} = 2 \cdot tan^{-1}\left(\frac{(A - a \cdot w)/2}{(a/2)^2}\right) \tag{3.4}$$

To demonstrate the important difference of the used definition, both definitions

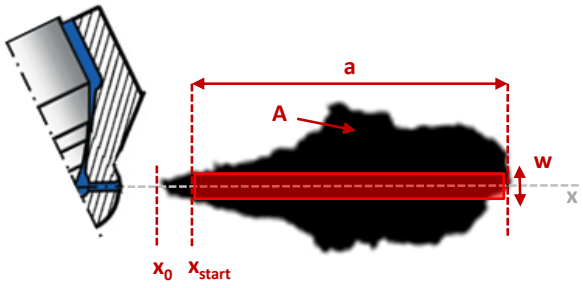

Figure 3.7: Definition of the parameters used in the determination of the Siebers spray angle

for a single cold spray experiment are plotted in Fig. 3.8. In all experiments, the Siebers angle $\theta_{Siebers}$ was about 2° higher than the averaged local spray angle $\theta_{av,loc}$. This difference might be important for modeling, in which the spray angle is usually used as an input. This discussion is continued in chapter 5.

3.3.2 Schlieren diagnostic

A commonly used optical diagnostic in several research areas to visualize density changes in a fluid is the schlieren technique. Although the theoretical principle is relatively easy, the setup is usually difficult to align and for proper measurements and the optics can be expensive. Once a change in density occurs in a fluidum, the light refractive index will change. As a result, the incoming light will change direction relative to the surface of the density change: the light beams are deflected with an angle α towards the area with the highest density. The refractive index n

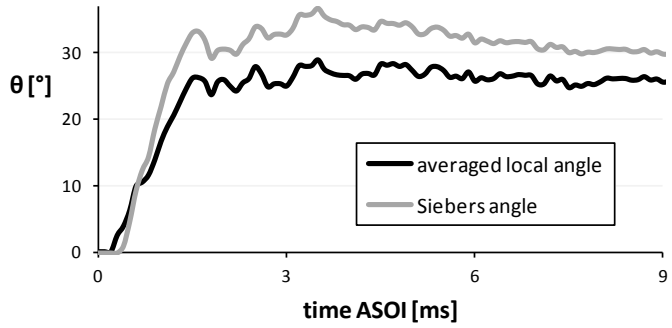

Figure 3.8: The time resolved spray angle for a single experiment determined in two different ways: averaged local spray angle (black) & Siebers angle (grey)

is directly correlated with the density ρ by the Gladstone-Dale equation, with K the Gladstone-Dale constant [98, 99]:

$$n - 1 = K.\rho \tag{3.5}$$

$$\frac{\triangle n}{\triangle \rho} = K \tag{3.6}$$

In Merzkirch *et al*. [100] the values for K can be found for several gases.

The principle of schlieren is shown in Fig. 3.9. In a medium with homogeneous density, an initial parallel light beam can be focused in one point (point *FP* in Fig. 3.9). When a density change occurs, the beams that go through this area will be deflected and would not be focused anymore in point *FP*. The position of this focus point will depend on the magnitude of the density gradient. The principle of the schlieren technique is to block the light that is not focused in the focus point *FP* by the use of a so called 'knife edge' or schlieren stop. Lots of different 'knife edges' can be used, depending on the application and which gradient needs to be visualized. For example, if all gradients need to be displayed perpendicular to the line of sight, a pin hole can be used. If only the positive gradients in one direction should be visualized, a razor-like schlieren stop is preferable. In order to have some knowledge about the magnitude of the density gradients, graded filters can be used in such way that the deflected light by strong gradients is completely blocked while the light originating from small to medium gradients is gradually blocked. Applying an offset from the focus point perpendicular to the line of sight also allows to decide which magnitude of gradients should be blocked or not. For more details about the knife-edge choice, the reader is referred to Settles [99].

The interpretation of the recorded schlieren images is however not straightforward. Apart from distorsion by the optical components (astigmatism, coma, impurities,

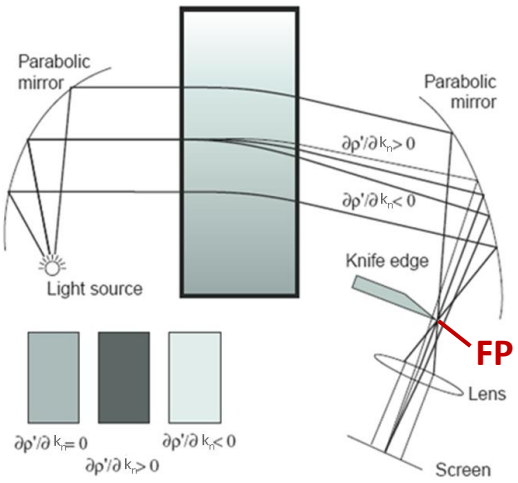

Figure 3.9: Schematic of the schlieren principle

...) [15], misalignments and inhomogeneous light distribution of the initial parallel light beam, the schlieren image is usually the 2D projection of a 3D phenomenon. This means that the measured deflection of each beam is the result of the integration of the density gradients along the line of sight in the test section. Where it is in theory possible to obtain quantitative results from schlieren, it is in reality very difficult and will strongly depend on the nature of the investigated phenomenon. In the case of the complex spray atomization and combustion process quantitative results for the density field with the schlieren diagnostic is not attempted.

A schlieren image of a vaporizing spray reveals both the gas and liquid phase of the spray. The liquid phase visualization is however dominated by light extinction rather than the schlieren effect. From the schlieren image only, it is not possible to make the distinction between the gas and liquid phase. In order to do so, other or simultaneous diagnostics are necessary (cfr. section 3.7).
The practical implementation of the schlieren setup used throughout this work is given in Fig. 3.10. A pulsed high power LED is used as the light source. LED light is very homogeneous and has a high luminosity-power ratio. The pulse mode capability makes it possible to deliver an even higher intensity during the gating time of the camera. Highly intense and short light pulses help to ensure sharp images with a high contrast. The light is focused through a pinhole which is positioned in the focal point of an achromatic biconvex lens. The focal length of these lenses is preferably large in order to be less sensitive to light noise. A focal length of 8 times the lens diameter ($f/8$) has been found to be a good trade-off between image quality and space. The astigmatism problem, which is a distorsion based on the

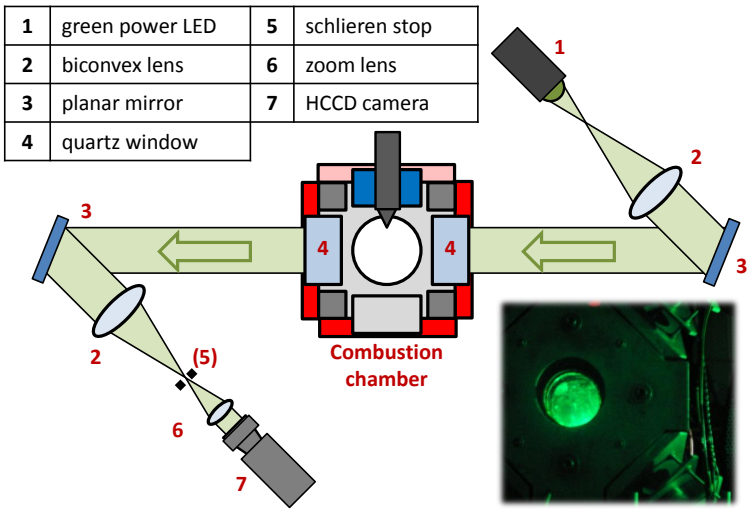

Figure 3.10: Configuration of the implemented schlieren/focused shadowgraph setup

different refractive indices of colors, is minimized by the use of the achromatic version of the lenses. To avoid distorsions introduced by the lens boundary, the lens diameter is taken slightly bigger than the optical aperture of the test section.
A second achromatic biconvex lens is positioned behind the test section to focus the beam again in one point. In this point, the 'knife edge' can be positioned to block some of the light. Important to mention is that the second lens is placed as close as possible to the test section in order to have the maximal collection angle: if the distance is too long, light might be permanently lost.
The optical mirrors are necessary, due to the limitation of space and have no further optical function. Finally, a high speed camera is positioned as close as possible to the 'knife edge'. For each desired magnification m of a projection of the test section image, as defined in Eq. 3.7, a unique image plane exists. In the current application the length s would become unrealistically long if the image plane is sized equal to the camera sensor size. The path length s can be shortened by the use of an extra focusing lens in front of the camera. The focal length of the required focusing lens f_3 can be calculated with Eq. 3.8 [99].

$$m = \frac{f_2}{|s|} = \frac{\text{sensor width}}{\text{real image width}} \tag{3.7}$$

$$f_3 = \frac{m\left(f_2{}^2 - sg\right)}{f_2 - ms} \tag{3.8}$$

with g as small as practically possible. With $m = 0.148$ (for the PCO Dimax high speed camera and real size image 150mm), $f_2 = 1200mm$, $g = 30mm$, $s = 400mm$ (as practical restriction), the required focal length f_3 of the lens becomes $185mm$.

In the case of a reacting spray, an optical filter can be used to avoid light disturbance, originating from the combustion. Since emitted light from soot becomes important above $600nm$, a $600nm$ small band-pass filter is used. In such way the light from the schlieren light source ($530nm$) is not affected by the combustion.

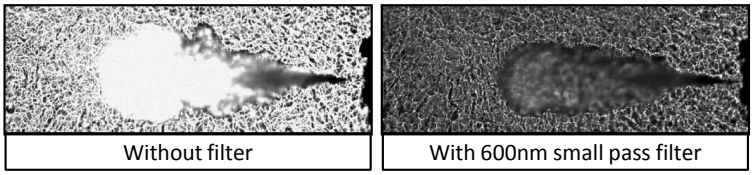

Figure 3.11: Influence of the combustion on the schlieren images. Left: without optical filter, right: with 600nm small band-pass filter

3.3.3 (Focused) shadowgraph diagnostic

The shadowgraph technique is based on exactly the same principles as for the schlieren technique. As for the schlieren technique, both liquid and vapor phase are visualized. The only difference is the absence of the 'knife edge': all light is captured by the camera. This has the fundamental consequence that this imaging technique does not display the density gradient, but the change of the density gradient, as expressed in Eq. 3.9.

$$\delta I = k\left(\frac{\delta^2\rho}{\delta x^2} + \frac{\delta^2\rho}{\delta y^2}\right) \tag{3.9}$$

with k a constant that depends on the medium (similar to the Gladstone-Dale constant K). The principle is depicted in Fig. 3.12: if the density gradient is equal in the whole test section, all light beams will deflect over the same angle α and the screen will still have the same homogeneous intensity, but shifted over the distance AA'.
The same remark as for the schlieren technique needs to be made: the complexity of the multi-dimensional behavior of the spray process makes it impossible to give quantitative information about the density field.
The same configuration as in Fig. 3.10 is used. Note that the collection angle becomes even more important for shadowgraphy, since the lost light traces will act as schlieren effects in the recordings.

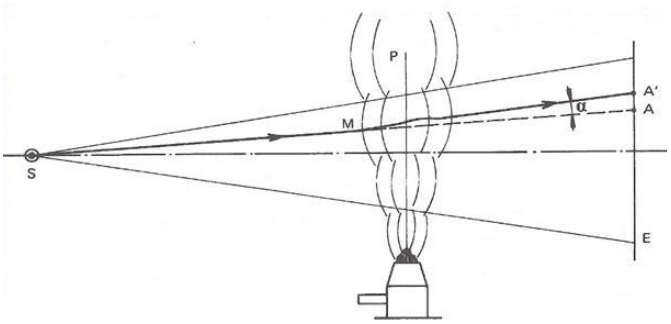

Figure 3.12: Principle of the shadowgraph diagnostic

Although the schlieren and shadowgraph technique are based upon the same optical principles, some differences exist that make one of the techniques more suitable for specific applications:

- Schlieren is more sensitive to density gradients and the sensitivity can be adjusted by the choice and position of the 'knife-edge'.
- For small collection angles, the shadowgraph images can suffer more from schlieren effects.
- The schlieren diagnostic might suffer more from inhomogeneous light blocking (more light is blocked near the image edge than in the center) if the focal point is not properly tuned.
- With shadowgraphy it is not possible to select a desired direction of the density gradient.
- The contrast variation is stronger for shadowgraphy. The contrast in the schlieren images can be improved by the use of graded filters as 'knife edge'.
- The resulting image intensity is higher for shadowgraphy since no light is blocked.

3.4 Spray penetration length

As for the liquid length and spray angle, a conventional definition for the spray penetration length or, as it is also called, the vapor length, is not given in literature. Siebers [79] defined the penetration length by the radius r of an arc starting at point (x_0, y_0). The total width of the arc is equal to half of the spray angle and is positioned symmetrically around the spray centre line. The spray center line is the line that connects point (x_0, y_0) with the spray mass centre point (y_C, x_C) and is deflected from the horizontal line by angle α. This is demonstrated in Fig. 3.13.

This definition is proposed by the ECN and will be further used throughout this work.

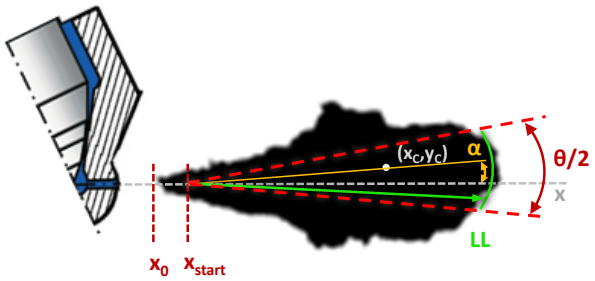

Figure 3.13: Definition of the spray penetration obtained with schlieren or shadowgraphy

The proposed diagnostic in the literature are the shadowgraph and schlieren image technique as explained in resp. sections 3.3.2 and 3.3.3.

3.5 Ignition delay

3.5.1 Definition

The ignition delay is defined as the start of combustion or otherwise, the start of heat release. The auto-ignition of a diesel spray happens in 2 stages: the cold flame and hot flame phase. During the cold flame, the chemical reaction starts but without heat release. The ignition delay is determined as the moment at which heat release is detected. The practical definition depends on the diagnostic: in the optical spray measurements ignition delay is based on the moment a certain amount of pixels is detected from the strong illumination of the flame. The OH-radical is an indicator of combustion [101–103] and has a maximum emitted light wavelength of 310nm. Other possible tracers or combustion radical are shown in table 3.1. During the cool flame, mainly CH_2O- and HCO-radicals are formed which also emit light (in the range $450-500nm$) but less severe [104, 105]. This is the motivation to relate the start of combustion to the moment when the detected spot becomes much brighter. At the initial stage of combustion no soot formation is yet formed in this area.

3.5.2 Chemiluminescence

The measurement of ignition delay is based on the natural light emitted from the combustion. Figure 3.14 represents the general optical setup. The emitted light from the combustion is directly captured by a HCCD camera after being intensified by an image intensifier. For the ignition delay measurements, all initial light from

Species	Wavelength [*nm*]
OH^*	306-315
NH^*	336
CN^*	359-386
CH^*	390, 432
C_2^*	469-473, 510-516
CH_2O^*	395, 423
CO^*	205-245
CO_2^*	broadband

Table 3.1: Flame emission wavelengths for the most common combustion radicals [106, 107]

the start of combustion needs to be detected. Since soot formation at this early stage can be neglected, no optical filter is used. In order to avoid overexposed light from the soot production in a later combustion stage, which can damage the intensifier, the intensifier is deactivated after a predefined amount of images. This amount of predefined images is determined experimentally with low gain and/or exposure time setting for the intensifier. A good indicator of combustion is the OH-radical, usually represented as OH^*.

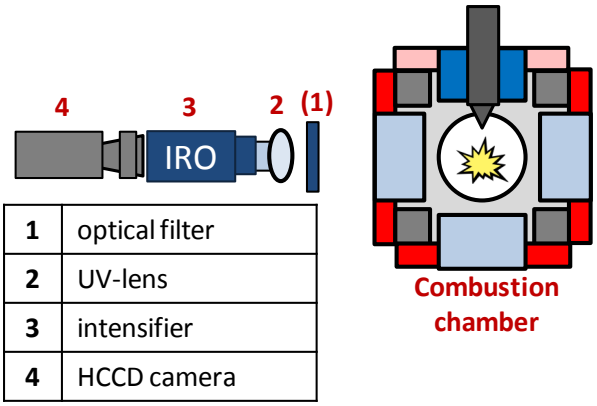

Figure 3.14: Configuration of the setup for flame lift-off length and ignition delay measurements. For the ignition delay measurements, the optical filter (1) is not used.

3.5.3 Pressure based

Due to the heat release of the combustion, the pressure in the vessel rises. With a sensitive pressure sensor, the ignition delay can be defined based on this pressure rise. The hot flame ignition is defined as the moment at which the first pressure spikes appear. This definition was validated by a simultaneous optical diagnostic with a sensitive photodiode by Sandia National Laboratories [108] as shown in Fig. 3.15. In this case the ignition delay is defined as the moment the pressure increase becomes more than $0.015 MPa$.

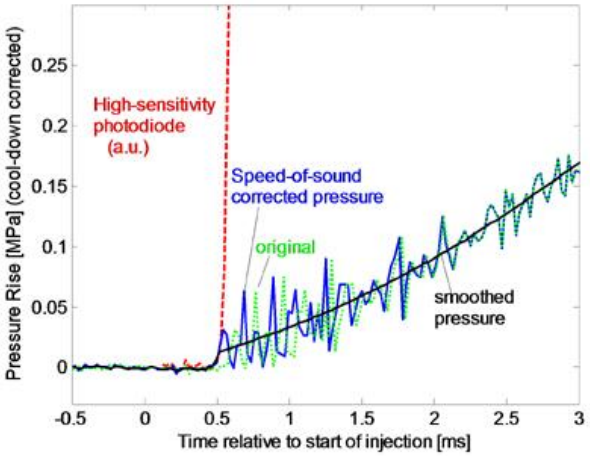

Figure 3.15: Validation of the pressure based diagnostic for the ignition delay [108]

3.6 Flame lift-off length

3.6.1 Definition

The flame lift-off length of a combusting spray is defined as the distance between the nozzle and location where the flame front initiates and stabilizes during an injection event. The majority of researchers use a definition related to the intensity to define the lift-off length. Traditionally the flame lift-off length is defined as the position at which 50% of the maximum intensity from the 'knee' value is reached. The intensity profile is obtained along the spray axis [109]. An example of an obtained intensity profile is shown in Fig. 3.16.

3.6.2 Chemiluminescence

The same optical diagnostic and setup as described in section 3.5.2 can be used. The only important difference is the use of an optical filter to isolate the light

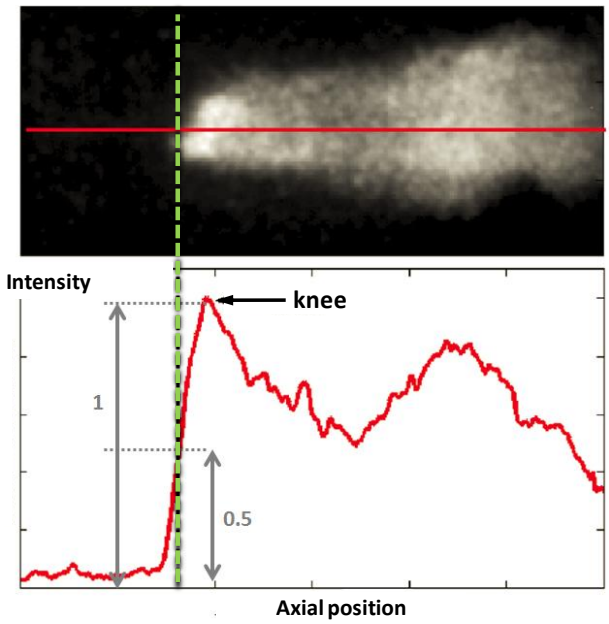

Figure 3.16: Definition for the flame lift-off length, based on the image intensity

emission from the OH-radicals (310*nm* ±10*nm*), as combustion indicator. The light from the soot is much more intense and distributed in a broad range (but most intensively for wavelengths higher than 600*nm*) which would overexpose the images. The light at 310*nm* is dominated by the OH^*, so one can be confident by using a small band pass filter (bandwidth of 10*nm*) that the captured light originates from OH^*. The high-speed camera can now be exposed to the combusting flame during the whole injection event.

3.7 Simultaneous measurements

It is preferred to obtain as much information as possible from each experiment. The main motivation for this is the fact that every spray suffers from cycle-to-cycle variation and some understanding might be lost when averaging is applied. There is no single optical technique from which we can obtain all spray relevant parameters, however a simultaneous combination of techniques can be applied.

It is very difficult to get quantitative information about the liquid and gas phase mass distribution in the spray. Several attempts are taken to subtract images that measure the liquid phase (e.g. diffused back illumination or mie-scattering) and both liquid & gas phase (e.g. with schlieren or shadowgraphy). The ideal way

is to record 2 imaging techniques at the same time. In this way, the data comes from the same experiment and uncertainties concerning the variation between 2 experiments can be neglected. One of the possibilities using only 1 high speed camera was implemented by Parrish and Zink [110]. A schematic overview with the triggering scheme is shown in Fig. 3.17. While the shutter time of the camera

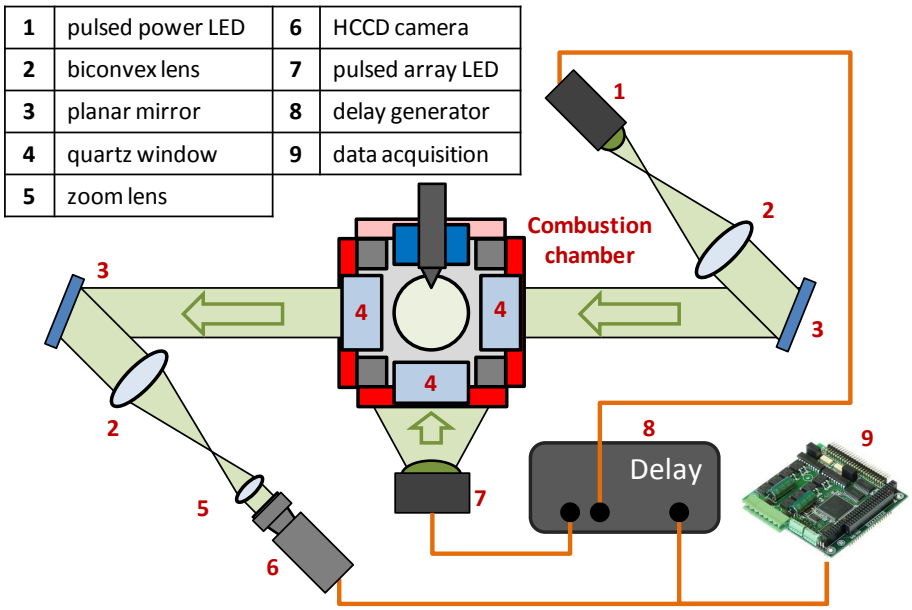

Figure 3.17: Configuration of the implemented simultaneous shadowgraph and mie-scattering diagnostics

equals the recording frequency, a delay generator is used to activate the LED's at the correct time: at the rising edge of the delayed pulse, the shadowgraph light source (1) is activated. The LED array (7) for the mie-scattering diagnostics is then activated at the falling edge. The delay and pulse width are set in such way the shadowgraph image is captured by the camera at the end of the shutter time at each 2 frames while a mie-scattering image is taken at the beginning of each 2 frames. This is clarified in Fig. 3.18. The minimum pulse time for the LEDs is $5\mu s$. The purple signal is the signal measured by a photo diode that was placed at the place of the HCCD camera. The rising edge of the yellow signal corresponds to the moment a new image is recorded. The shutter time was set equal to the time between to image triggers.

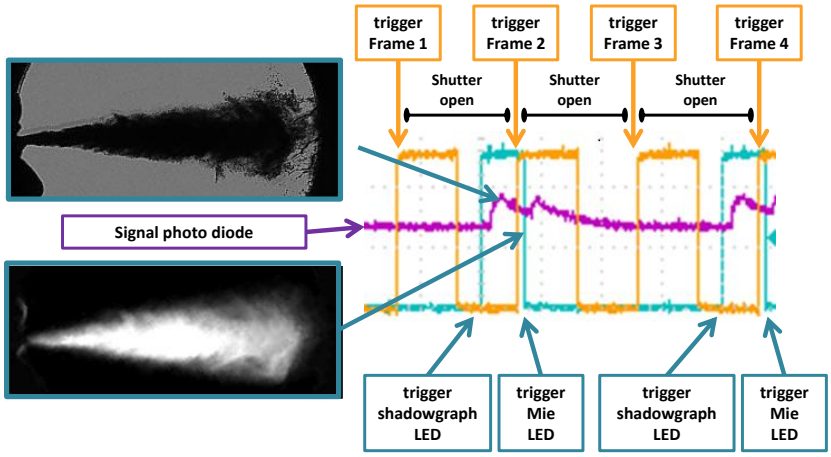

Figure 3.18: Triggering schematic for the simultaneous shadowgraph and mie-scattering diagnostics

3.8 Image processing

Each measuring technique has its own image processing file(s). Nevertheless, the overall procedure is similar for all techniques. The main steps of the image processing are

- grid size determination
- background normalization and subtraction
- noise filtering
- desired spray information
- averaging

3.8.1 Grid size determination

The size of the grid is determined by the use of a grid insertion with known dimensions. For better accuracy and contrast, the average image of several grid images is taken. This becomes an issue when an image intensifier is used with a high gain factor setting since photon noise becomes high. This is demonstrated in Fig. 3.19. This grid can also be used to focus on and to evaluate the image distorsion. With the flat windows, distorsion due to the optical components in the setup is considered negligible. If distorsion or inhomogeneity of the light would occur, all components should be realigned properly.

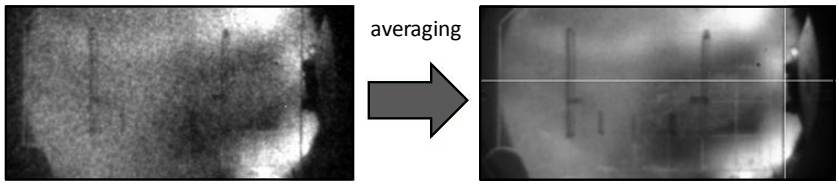

Figure 3.19: Original single grid image acquired with the intensifier(left), averaged grid image (right). The white cross at the right indicates the tip of the nozzle

3.8.2 Background normalization and subtraction

In optical spray measurements, the intensity I is not only depending on the camera settings, but also on the optical components and the density conditions in the combustion chamber. An average intensity I_{av} is calculated in an a priori selected part of the background. This calculated value is added to a chosen threshold value I_{offset}. The main idea for this last operation is to get rid of some of the noise. The offset value used in the experiments was fixed to $0.08(2^y)$ based on experience. The operation can be translated to Eq. 3.10.

$$I_{\text{norm}} = 1 - \frac{1}{2^y - (I_{av} + I_{\text{offset}})}\left[(2^y - I) - (I_{av} + I_{\text{offset}})\right] \tag{3.10}$$

with I_{norm} the normalized intensity for a y-bit image. Finally, every image is subtracted from the background image. For a quiescent ambient this is a sufficient way to cancel the background noise. For turbulent ambient conditions this is less effective, but the same strategy can be used for two succeeding images. If the frame rate is too low (or the turbulence level too high) additional filtering operations will be necessary, which is discussed in next section.
The background normalization and subtraction operation is visualized in Fig. 3.20.

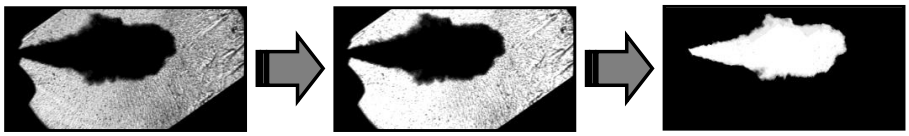

Figure 3.20: Background normalization and subtraction

3.8.3 Noise filtering and binarization

For some diagnostics a binarization of the image is necessary. This operation requires a threshold and it is known that this value can influence the results significantly if not chosen properly. One of the key problems is noise. A sequence

of noise canceling operations are performed in matlab (*imfill*, *imdilate*, *imdilude*, *imerode*). In the case of highly turbulent ambient conditions, an extra image smoothing operation is done via L_0 gradient minimization as described by Xu *et al.* [111]. This was the case for the spray penetration measurements discussed in section 7.2.2. After the binarization, the largest white area is assumed to be the spray and all others are considered as noise and are deleted.
The result of the noise filtering and binarization process of a cold inert spray is shown in Fig. 3.21.

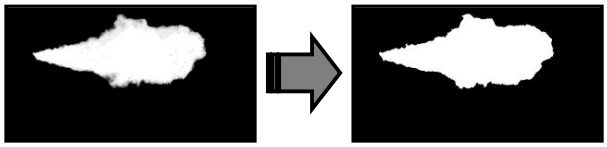

Figure 3.21: Result of the filtering and binarization

3.8.4 Desired spray information

In the current stage the image is processed enough to obtain the desired information (e.g. Fig. 3.22). The used algorithms depend strongly on the diagnostic and desired parameters.

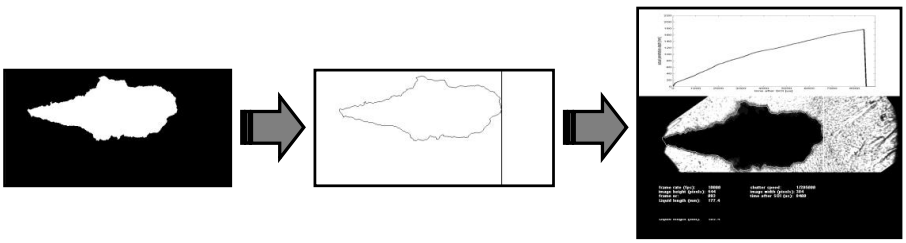

Figure 3.22: Example of acquiring quantitative spray information

3.8.5 Averaging

If all images are processed, experiments under the same conditions can be clustered in order to average the experiments. Averaging allows us to determine the reproducibility and noise suppression on the calculated parameters. However, information might get lost as demonstrated in Fig. 3.23. The average spray penetration and cone angle is represented well in the average spray, the head vortices and the wavy spray boundary are faded away. On the other hand, lots of simplified spray models make use of the assumption that the spray is conically shaped in the

steady region and spherically shaped at the transient region (spray head) [89]. This corresponds with the averaged spray images.

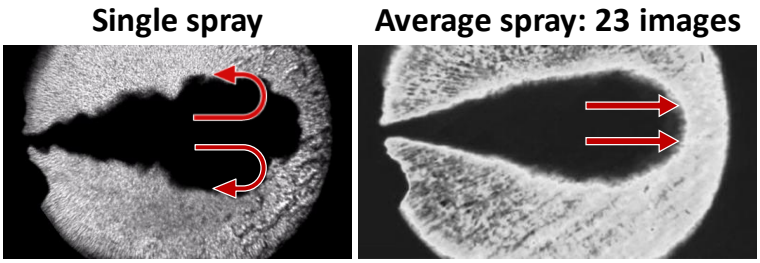

Figure 3.23: Loss of air entrainment and head vortices due to the averaging operation

3.9 Summary

The different spray parameters measured in this work have been defined, together with their diagnostic. The measured parameters with their optical diagnostic are summarized in table 3.2.

Spray parameter	**Diagnostic**
spray angle	schlieren
	schadowgraphy
spray penetration	schlieren
	schadowgraphy
liquid length	diffused back-illumination
	mie-scattering
ignition delay	intensified chemiluminescence
	pressure based
flame lift-off	OH^*-chemiluminescence

Table 3.2: Measured spray parameters with their corresponding diagnostics

4

Experimental setup for optical spray measurements

"No amount of experimentation can ever prove me right; a single experiment can prove me wrong."

- Albert Einstein -

The chapter is organized as follows: the design of the two setups used in this work is discussed. Next, the boundary conditions for the spray measurements are determined based on measurements on the target engine type. The boundary conditions, acquired through a pre-combustion method, are validated both on repeatability as well as on homogeneity.

4.1 Introduction & motivation

From prior discussions, it should be clear that a detailed understanding of the spray and combustion process is necessary when good engine performance on different fuels is desired. The combustion and emission formation is complex and depend on several parameters other than the fuel as well. Parameters might also interact with each other, resulting in unexpected results. This vague statement, simply since no clear answers yet exist, can be seen in the conclusions made by several different researchers for engine tests with different fuels. The inconsistency is a result of the lack of knowledge of the involved processes and usually the change in engine settings is not given or motivated.
Attempts are made to understand the processes by the use of optical investigation of the spray (combustion) in test rigs such as optical research engines, rapid compression machines and constant volume vessels. Optical research engines are preferred to closer meet the conditions as they exist in the production engine. However difficult optical access, the moving parts and lubrication issues make such setups hard to operate. Constant volume combustion chambers are usually preferred due to the possibility of optical access in different directions. Further, accurate and more homogeneous determination of the boundary conditions allow to do a more fundamental spray study. These are the main reasons for the choice of such type of experimental setup. During this work, 2 such setups were used: the Eindhoven high pressure cell (EHPC) and the Ghent University Combustion Chamber I (GUCCI).

Since the main focus is the use of viscous fuels in medium speed diesel engines, the design of the GUCCI-setup differs from most of the existing combustion chambers: the larger injected fuel mass requires a bigger internal volume and the viscous fuels need to be heated to lower the viscosity. A list of known constant volume combustion chambers for the application of medium speed diesel engines is given in table 4.1. The implementation and issues of the one developped in this work are discussed in the following sections.

institute	**country**	**volume [l]**	**ref**
Norwegian University of Technology	Norway	5	[112]
Helsinki University	Finland	4	[113]
Kyushu University	Japan	6.2	[114]
Wartsila	Switzerland	29.5	[115]

Table 4.1: Combustion chambers for medium speed diesel engines, known by the author

4.2 Eindhoven High Pressure Cell (EHPC)

In this section a brief overview is given of the constant volume combustion chamber which is designed and used in Eindhoven. The reader is referred to Frijters [116, 117] for more details. The combustion chamber was baptized as the Eindhoven High Pressure Cell (EHPC) and the initial ideas were used to design the constant volume combustion chamber of Ghent (cfr. Fig 4.1).
Furthermore, spray measurements in both inert and reacting atmosphere were carried out during this PhD in collaboration with TU/e and are discussed in detail in chapter 7.

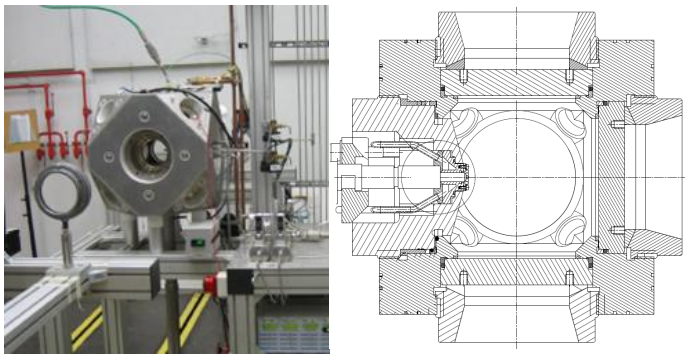

Figure 4.1: The practical realisation (left) and a drawing of a cross section (right)

The EHPC is an optically accessible constant volume combustion chamber where elevated temperatures and pressures can be created by the pre-combustion method (cfr. section 4.5).
This method involves the combustion of a predetermined gas mixture to create the desired ambient conditions for spray measurements [118] . The gas mixture is formed by acetylene (C_2H_2), argon (Ar), nitrogen (N_2) and oxygen (O_2), based on the partial pressure method. A 4-component gas mixture allows to choose 4 independent properties at the time of injection: density, amount of oxygen, temperature and heat capacity. This method is discussed in more detail in section 4.5 and appendix A. A common rail injection system up to $280MPa$ is implemented. The constant volume high pressure combustion vessel is optically accessible through three $50mm$ thick sapphire windows with a diameter of $100mm$. The inner combustion chamber walls are electrically heated to $453K$. Multiple spark plugs are utilized in combination with high capacity coils to provide consistent ignition of fuel-lean mixtures. A mixing fan stirs the gases during filling and throughout the complete experiment to minimize mixture density and temperature non-uniformities.
The gases to create the mixture for the pre-combustion, are supplied by Bronkhorst thermal mass flow controllers (MFC's). The communication with the MFC soft-

ware is established with a Matlab filling program. The nominal gas flow of each controller is calibrated for each gas.
All sensors and control signals are handled by the TUeDACS/3, an in-house designed data-acquisition system. Information concerning the sensors and data acquisition is listed in table 4.2.
The exhaust and inlet for the gases and combustion products are realised by standard poppet valves which are pneumatically controlled with nitrogen gas. The vessel is secured against overpressure by a bursting disk at the bottom. The features inside the combustion chamber are indicated in Fig. 4.2.

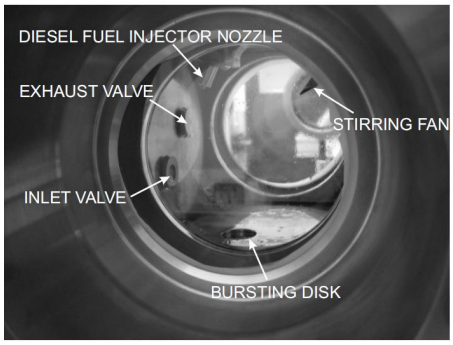

Figure 4.2: The inner chamber parts (image from Frijters [116])

vessel specifications	
window aperture	100mm
window thickness	50mm
chamber volume	1260cm^3
injector mounting	side window
injector tip protrusion	5mm
mixing fan location	upper corner near injector
fan speed	approx. 1900rpm
spark plug position (2x)	opposite diagonal corners
max. vacuum	1-2kPa
inner body temperature	453K
sensors & acquisition	
high speed camera	Phantom V7.3
absolute pressure	Druck PMP 4070 (0-7MPa)
relative chamber pressure	Kistler 7061 (0-20MPa), cooled

Table 4.2: Sensors and data-acquisition equipment of the EHPC-setup from the Technical University of Eindhoven

4.3 Ghent University Combustion Chamber I (GUCCI)

4.3.1 Setup overview

Experiments have been conducted in a constant volume combustion chamber, baptized in 2008 as the 'Ghent University Combustion Chamber I' (GUCCI). An overview of the progress of the setup until the end of this thesis work is shown in Fig. 4.3. The first injection synchronized with the camera and sensors at atmospheric conditions dates from March 2010. The pressurizing of the chamber (up to 8MPa) had to wait till April 2011 after the experimental room was built and equipped with a gas supply system. After the fine tuning of the operation and measuring procedures, a controlled pre-combustion was established in September 2012.

The setup is schematically presented in Fig. 4.4. The chamber has an internal cubical shape with an internal volume of 4.1$liter$ ($160^3 mm^3$) and a maximum oper-

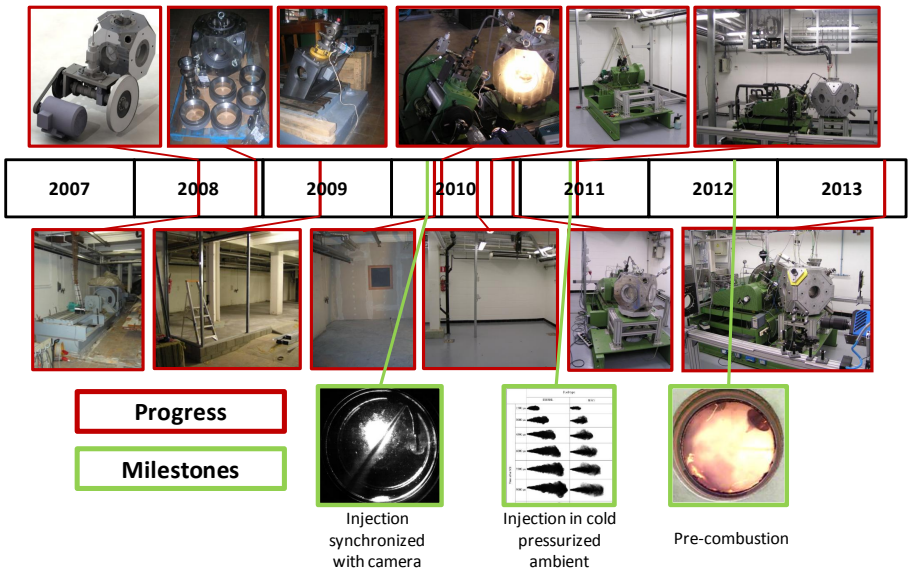

Figure 4.3: The progress of the GUCCI-setup with some milestones

ating pressure of 35*MPa*. For the experiments throughout this work, the maximum pressure is limited by a bursting disk of 17*MPa* (±10%). Optical access is assured by quartz windows with a diameter of 150*mm* and a thickness of 78*mm*. The fuel injector is located at the top of the chamber in such way that the investigated spray propagates along the cube's space diagonal. The injected fuel temperature is set independently from the wall temperature by controlling the temperature of cooling oil, circulating through the injector. The control of the injector temperature is discussed in section 4.6.2. All cell walls, except for the upper, can be electrically heated. The maximum temperature is limited to 420*K* to prevent the formation of cokes from fuel leftovers. The wall heating has mainly two reasons: to avoid water condensation on the windows and to keep the gas temperature as homogeneous as possible when a mixture is burned. The hot and pressurized atmosphere is created in a similar way as was done in the EHPC. The maximum pressure of the gas mixture prior to combustion in this work is limited to 4*MPa*, with combustion peak pressures limited to 16*MPa*.

A compressor wheel from an automotive turbocharger, driven by a speed controlled BLDC motor, is used as a mixing fan to assure a good mixing during the filling of the gases. The performance and influence of this fan is discussed in section 4.6.4.

Two spark plugs mounted at opposite sides are used to ignite the gas mixture and are triggered together with the pressure sensors and fast K-type thermocouples.

The triggering sequence is discussed in section 4.3.8. The used sensors and acquisition apparatus are listed in section 4.3.6.

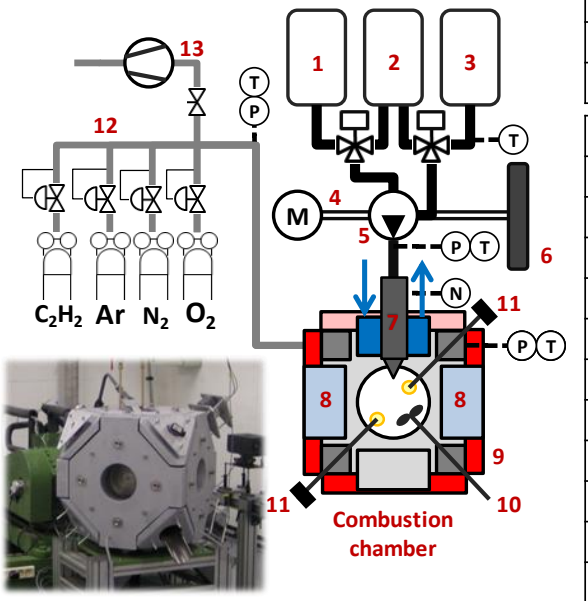

P	pressure sensor
T	temperature sensor
N	needle lift sensor

1	diesel tank
2	mix tank
3	bio-fuel tank
4	motor with camshaft
5	actuated injection pump
6	flywheel
7	Injector with cooling
8	quartz window
9	heating resistors
10	mixing fan
11	spark plug
12	PID controller gas supply
13	vacuum pump

Figure 4.4: Configuration of the constant volume combustion vessel GUCCI

4.3.2 Injection system

The GUCCI-setup is equipped with a pump-line-nozzle injection system as used on the ABC diesel engines: a volumetric injection pump is driven by a camshaft (cfr. numbers 4-7 in Fig. 4.4). The only modification compared to the engines is that one bend in the injection pipe is missing. The use of such system has some issues or difficulties. First of all, the injection pressure will depend on the fuel and temperature. It is not possible to vary the injection pressure or profile as an independent parameter. At the moment of injection a high force is required for the cam to lift the pump plunger. The energy required to minimize the speed dip during injection is stored in a flywheel in order to limit the size of the electric motor which drives the cam shaft. The flywheel was theoretically designed based on the energy required to have a limited speed dip (<3%) [119]. This flywheel with an inertia of $1.4 kgm^2$, showed however undesired high deceleration at the moment of injection as seen on the left side of Fig. 4.5. Speed reductions up to 25% were detected. A new design, based on the speed dip in the experiments resulted in a flywheel of

$33 kgm^2$. The highest speed dip was expected at full load, lowest speed ($400 rpm$) and fuel with the highest bulk modulus & viscosity. The dip of the velocity was not more than 1.5% of the camshaft speed for oils at $298K$ and 1% for diesel at $298K$ [120].

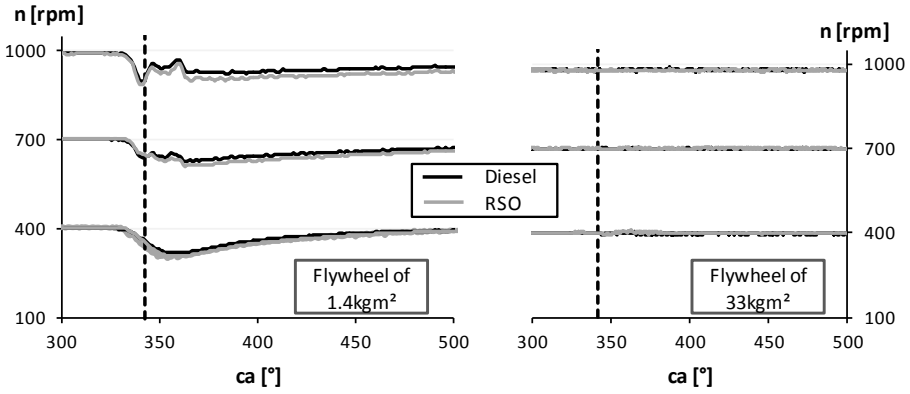

Figure 4.5: The speed variation during injection for rapeseed oil (RSO) (grey line) and diesel (black lines) for different engine speeds (400, 700, 1000rpm), with the vertical dashed line the moment of start of injection

This modification had also an important impact on the injection pressure; injection pressures with the modified flywheel were significantly higher, the pressure rise was faster and the pressure peak is shifted to the left (cfr. Fig. 4.6).

Since the injected volume depends on the injection pump displacement, only multi-hole nozzles can be investigated. A thimble is mounted on the nozzle to isolate one of the sprays. The construction of the thimble was done in such way that the part of the spray, diverted by the thimble, has as little contact as possible (cfr. Fig. 4.7) in order to limit the interaction between the thimble and the breakup & air-entrainment. The influence of the thimble on the spray has been studied with the measurement techniques available: the influence on the injection pressure and spray momentum were compared in the cases with and without thimble. No significant difference in injection pressure or spray momentum could be detected. Optical investigation was however not possible since the sprays almost immediately collide with the windows and the obstruction of the different sprays along the line of sight make optical access impossible.
So, it could not be confirmed with optical measurements that the thimble does not affect the spray, although no influence on the injection conditions were found.

This type of injection system was chosen over a common-rail for 2 reasons:

- The research project is in cooperation with Anglo Belgian Corperation (ABC),

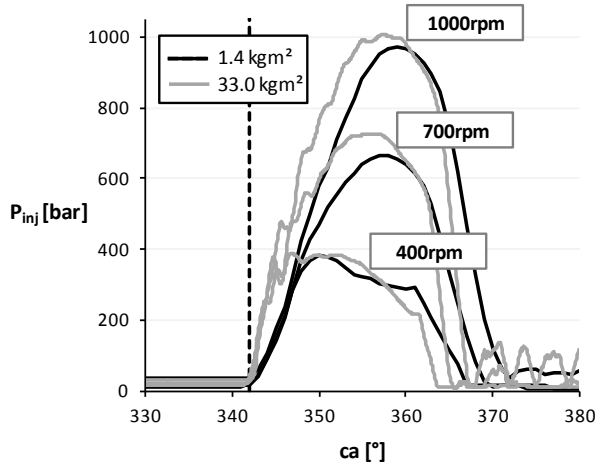

Figure 4.6: Influence of the re-designed flywheel on the injection pressure for diesel at 3 different speeds (400, 700, 1000rpm). The black lines represents results with the old flywheel (1.4kgm^2, measurement accuracy = 1°ca), the grey line the results with the new one (33kgm^2, measurement accuracy = 0.1°ca). , with the vertical dashed line the moment of start of injection

a medium speed diesel engine manufacturer in Ghent. Their engines are so far all equiped with pump-line-nozzle systems. In order to allow a comparison in the future between the optical spray measurement and engine tests, it is necessary to keep as many parameters as possible comparable.

- No common-rail systems are available on the market for highly viscous fuels. The accurate clearances in these injectors put a limit to these systems, so far.

4.3.3 Fuel circuit

The fuel supplying circuit is designed in such way that a quick switch can be made between 2 fuels and that the fuel tank and pipes can be heated. This implementation is necessary for the use of highly viscous fuels. The temperature is controlled by a Gefran1600 controller. Details of the circuit are shown in Fig. 4.8.
One of the fuel tanks (*biofuel tank* in Fig. 4.8) is designed as an au-bain-marie system; the electrical heaters (4x500W) heat up a thermal oil that surrounds the main fuel tank. This prevents the fuel to locally overheat which could cause chemical changes. The other tank (*rinse tank*) directly heats up the fuel and is for this reason not used for experiments but rather to rinse the whole circuit to prevent solidification of the viscous fuels. This rinsing procedure is executed with heated diesel. For the rinsing itself, the fuel is drawn from the (heated) *rinse tank* and returned

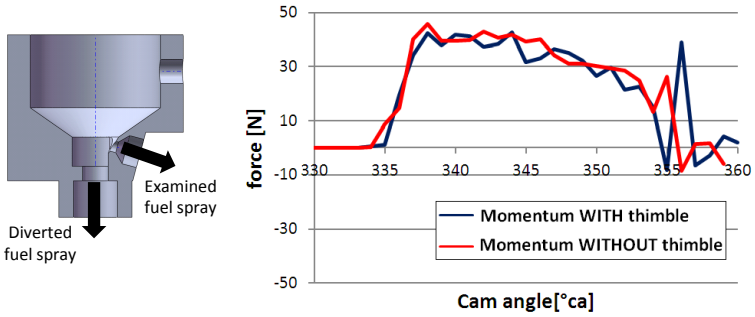

Figure 4.7: Construction of the thimble to isolate the examined fuel spray (left), influence on the spray momentum (red lines) and injection pressure right (black lines) with (solid lines) and without (dashed lines) thimble

to the *mix tank*. For the switch to the (preheated) bio-fuel, the fuel is drawn from the *biofuel tank* and returned to the *mix tank* until the only remaining fuel in the circuit is the bio-fuel. In that case the fuel is returned back to the bio-fuel tank.

4.3.4 Gas filling

The gas supply circuit to pressurize the combustion chamber is able to handle 6 different gases. In this work, only 4 gases will be used: acethylene (C_2H_2), argon (Ar), nitrogen (N_2) and oxygen (O_2). The motivation for this choice can be found in section 4.4. A schematical representation of the whole circuit is given in Fig. 4.9. Each gas is controlled by a proportional valve (*R1-6* in Fig. 4.9) and protected by a non-return valve (*N1-6*). The selection and stand alone PID control of these valves is realized with a Gefran2500 controller and the implementation is shown in Fig. 4.10. For safety reasons, electromagnetic valves (S) and manual valves ($M1-M6$) are installed in the supply tubes.

The filling for a certain gas mixture composition (cfr. section 4.4) is based on the method of partial pressures. During the filling procedure, the pressures are monitored by the piezo-resistive sensor, installed just before the chamber shut-off valve (*S3*). This implies that the chamber needs to be in contact with a part of the gas supply system (*S3* open) in order to know the absolute pressure in the chamber. This is necessary since the absolute pressure sensor cannot withstand the combustion pressures and temperatures. The filling procedure is summarized below and will clarify the scheme of Fig. 4.9:

- The combustion chamber is evacuated (90% vacuum), rinsed with pressurized air and again evacuated (90% vacuum). As a result, $0.01MPa$ of air remains in the chamber. A correction will be done for the supply of N_2

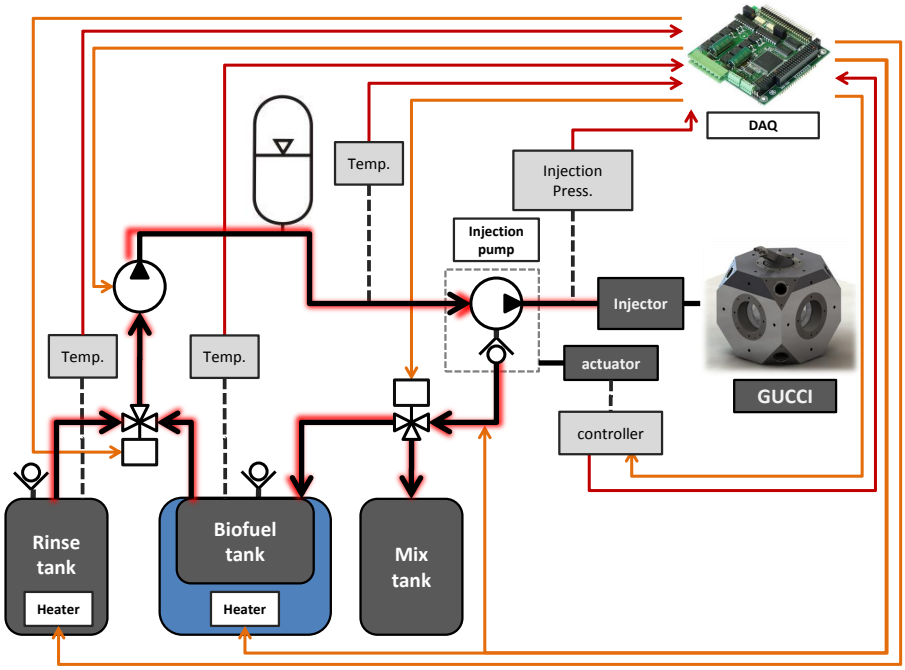

Figure 4.8: Fuel circuit: the black arrows represent the fuel flow; the orange arrows, the electrical output signals from the data acquisition (DAQ); the red arrow the electrical input signal to the DAQ.

and O_2, assuming the remaining gas composition consists of $79vol\%$ N_2 and $21vol\%$ O_2

- The chamber is sealed by closing valves *S3* and *S4*
- The gas pipes are evacuated (95% vacuum) through *S1*
- The first gas is filled in the pipes till the desired pressure is reached: the data-acquisition sends the pressure level to a PID-controller (Gefran2500). This controller, while monitoring the piezo-resistive sensor, sends the desired control signal to the driver of the proportional valve *R*. When the desired pressure is reached, the corresponding *R*-valve closes.
- *S3* is opened and the gas can flow into the chamber until the desired pressure level is reached, again controlled by the PID-controller
- The chamber is again sealed (*S3* and the corresponding *R* close). For the other gases the procedure starts again from the evacuation of the gas pipes.

The measured accuracy of the gas filling, obtained with the PID control, is given in table 4.3.

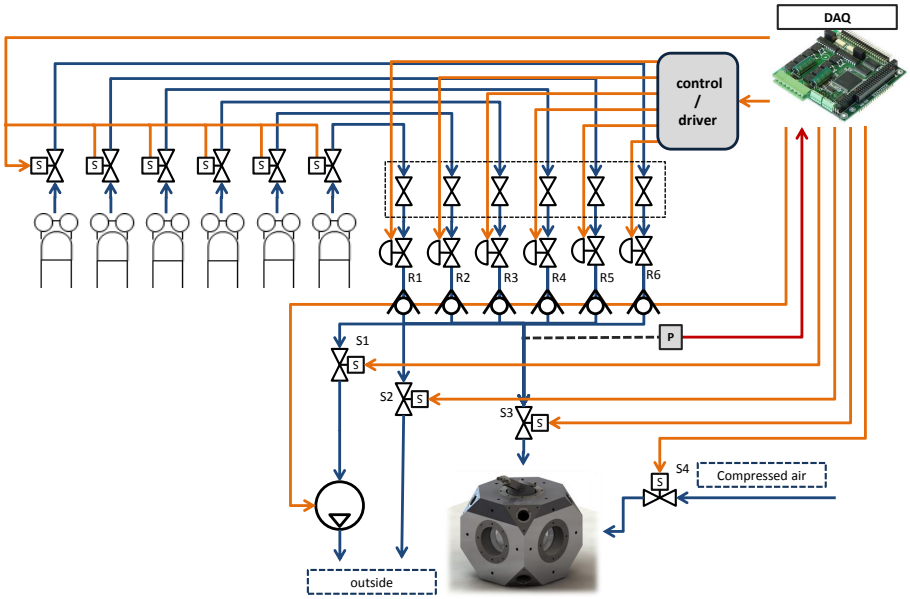

Figure 4.9: Gas supply circuit: the blue arrows represent the gas flow; the orange arrows, the electrical output signals from the data acquisition (DAQ); the red arrow the electrical input signal to the DAQ. G1-6, M1-6, R1-6, N1-6 are resp. the 6 gas bottles, manual shut-off valves, proportional valves and non-return valves. The S-valves are safety valves on the gas bottles

std	**[*bar* ‖ %]**
partial pressure C_2H_2	4.1e-3 ‖ 0.85
partial pressure C_2H_2	5.6e-3 ‖ 0.62
partial pressure C_2H_2	5.6e-3 ‖ 0.07
partial pressure C_2H_2	21.1e-3 ‖ 0.88

Table 4.3: Measured accuracy of the gas filling, based on 40 experiments

4.3.5 Injector cooling

The fuel temperature is an important parameter and needs to be controlled. The performance and strategy of the fuel temperature control is considered in section 4.6.2. Here, the hardware and control loop is discussed and schematically presented in Fig. 4.11.

A thermal oil *Mobiltherm* is used as the cooling fluid. Due to the high heat capacity and small temperature differences, the flow rate is high enough to consider that

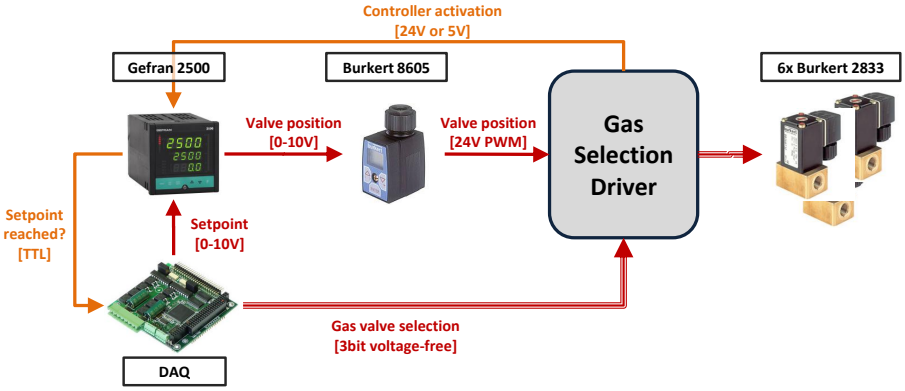

Figure 4.10: Stand alone PID control implementation for the proportional gas valves

the in- and output temperature of the injector block is equal. The temperature of the oil is measured at the output of the injector block. This temperature signal is used as control signal for the PID controller (Gefran1600). If cooling is required, 2 solenoid valves and a fan are activated. This allows the oil to flow through a heat exchanger with forced air cooling. To heat up the oil, the solenoid valves & fan are deactivated and an electrical heating wire wrapped along a parallel tube is activated.

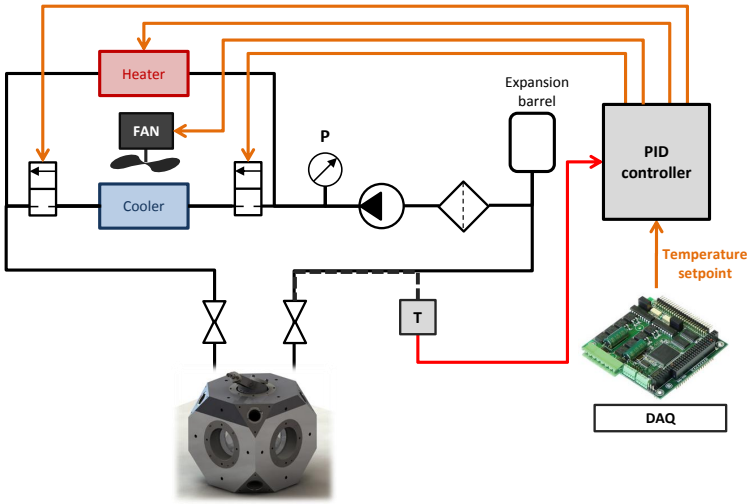

Figure 4.11: Implementation of the injector cooling circuit. The orange lines represent the data signals sent from the DAQ while the red lines are signals received by the DAQ

4.3.6 Sensors & data-acquisition

All sensors that are used throughout this work are listed in table 4.4.

sensors	
relative chamber pressure	cooled QC34D (AVL)
absolute chamber pressure	4075A100 (Kistler)
ambient conditions	ATAL
cam encoder	2614A (Kistler)
needle lift	Wolff analog Hall effect sensor
fast temperatures (chamber)	50μm K-thermocouple
fast temperatures (injector)	0.5mm K-thermocouple (grounded hot junction)
slow temperatures	1.5mm K-thermocouple (insulated hot junction)
spray momentum	force sensor 9217 (Kistler)
absolute injection pressure	4067A2000 (Kistler)
acquisition	
data acquisition system	NI cDAQ 9178
control software	Labview 8.6
processing software	Matlab
fast thermocouples acquisition	M-series PXI-6251 & SCXI-1102C module

Table 4.4: Sensors and data-acquisition equipment of the GUCCI-setup

4.3.7 Setup control strategy

The whole setup is controlled by a Labview interface program. The program is not discussed in detail here, but an overview of the control strategy is required to understand the triggering and operation sequence. A lot of different components and sensors need to be measured and controlled which lead to the need of understanding how the communication is realized. It is important to know that when a button is pushed in the program, it takes a certain time till the operation is actually performed. Taking this issue into account, some subsystems are implemented as stand alone systems. These subsystems are activated and deactivated by the Labview-DAQ system. The subsystems involve:

- pressure control for the gas supply system (as discussed in section 4.3.4)

- temperature control of the chamber using a Gefran1600 controller
- temperature control of the injector cooling circuit (as discussed in section 4.3.5)
- temperature control of the fuel tanks (as discussed in section 4.3.3)
- pneumatic actuator control for the activation of the injection pump (as will be discussed in section 4.3.8)

The program itself consists of several blocks (or parts) as schematically explained in Fig. 4.12.

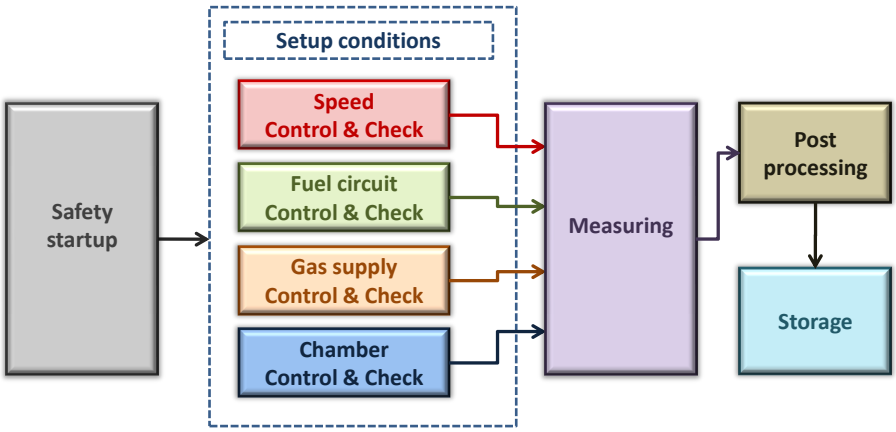

Figure 4.12: Schematical representation of the labview program

The program starts in a mode in which a signal is given for a couple of seconds to indicate the setup is activated and to allow people to exit the experimental area (block *Safety startup*). During this sequence, no systems can be activated. After this startup safety procedure, the right settings for the setup can be chosen. This involves 4 different parts: the speed of the cam shaft to simulate the engine speed (*Speed Control & Check*), the control of the fueling circuit & fuel temperature (*Fuel Circuit Control & Check*), the gas composition & filling for the pre-combustion (*Gas supply Control & Check*) and the chamber condition (temperature, fan, spark timing) (*Chamber Control & Check*). As long as one of these separated blocks is not finished, measurements are not possible. This also involves some safety checks, such as, no activation of the injection pump can be done without activation of the fuel circulation pump.

When a fast and timed measurement is activated, no additional signals or sensors are controlled or monitored; the labview only sends commands to the data acquisition, required for the triggered measurement signals: activation of the actuator, reading of the high speed sensor signals, trigger-train for the camera and LEDs and

ignition of the spark plugs. A master-slave programming strategy is implemented in order to obtain correct synchronization.
After the successful measurement, basic post-processing such as the transformation of the voltage signals into the correct units (pressure [MPa], force [N],...) is realised (*Post processing*) and finally, the data is stored in a txt-file (*Storage*).

4.3.8 Triggering

Apart from reliable and accurate sensors, triggering and simultaneous measuring is required for trustworthy measurements. Due to the use of a cam driven injection system, precise triggering is not straightforward.

The fast responding measurements (needle lift, spray momentum, injection & chamber pressure) are captured at each rising edge of the cam encoder signal. The top dead center signal (TDC) is chosen to be the maximum cam lift. Figure 4.14 gives an overview of the procedure and electrical signals when the measurement button is pressed (*START* in Fig. 4.14) in the Labview program.

First, all piezo-electrical sensors are reset automatically. In this way, the zero-level of the chamber pressure sensor is equal to the pressure that was measured just before closing the chamber (after the filling of the gases).
Next, several pre-combustion experiments are required without injection in order to determine the time needed between triggering of the spark plugs and obtaining the right conditions for the start of injection. This time is an input for the program and is translated to an amount of cam angles, based on the measured cam shaft speed. This calculation is done just after the moment of pressing the measurement button. From the cam drawings one knows that the mechanical cam lift starts at $50°ca$ BTDC and ends at $50°ca$ ATDC, with actual injection between 25 and $20°ca$ BTDC [120]. Assuming the physical time of injection is $21°ca$ BTDC, which is the case for diesel at 1000rpm and nominal load (cfr. section 4.4), the moment of triggering of the spark plugs can be calculated (*Trig*).
Then, the system waits till the reference (TDC) is detected. The spark plugs are triggered according to the calculated position. A few sparks are generated close to each other to ensure ignition. At the moment the last TDC-signal is seen by the data-acquisition, all fast responding sensors are triggered as well as the light source(s) and high speed camera. Both HCCD camera and light source(s) can be triggered at each cam angle signal or at a certain specified frequency. In the latter case, only the first rising edge will trigger the camera and light source(s) and all succeeding pulses will be ignored.
At the $50°ca$ position the pneumatic actuator is activated to load the fuel injection pump. The practical realization of the actuator is shown in Fig. 4.13 and details

can be found in Galle & Lagast [15]. The actuator has 260°*ca* time to react and is sent out before cam lift for the actual injection. Tests have shown that even in the worst case (highest speed) the pneumatic actuator responds well in the available time window.
The injection occurs and at 50°*ca* ATDC the actuator retracts to the zero load position, preventing a second injection. To give the spray (combustion) enough time to develop after the end of injection, the measurement is stopped after a certain amount of cam angles. This amount of cam angles can depend upon the targets of the measurement, but as a default the measurements are stopped 50°*ca* BTDC (= at the mechanical start of the 'second injection').

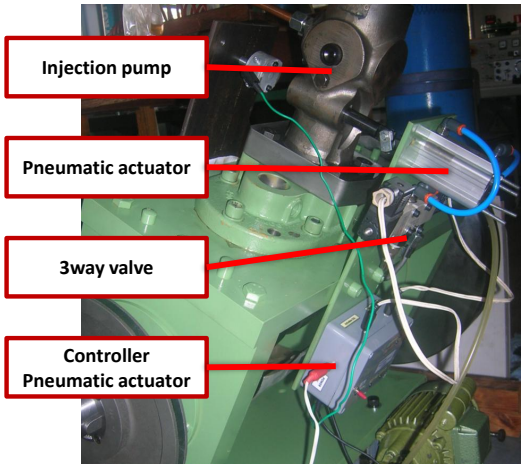

Figure 4.13: Practical implementation of the pneumatic actuator on the injection pump

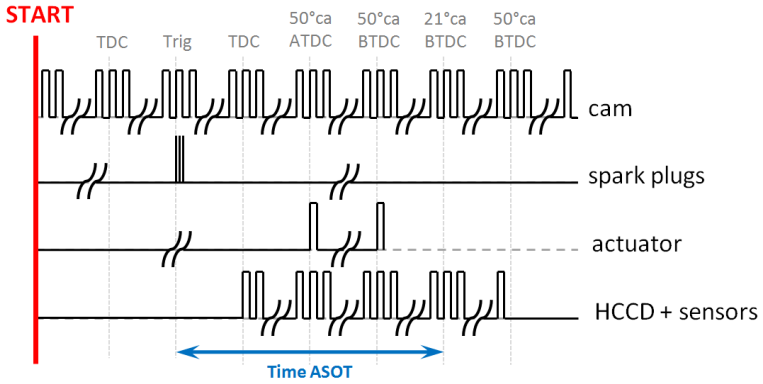

Figure 4.14: Triggering strategy for the GUCCI-setup

4.4 Boundary conditions

Performing accurate and reliable measurements requires a lot of experience and patience. As the setup was mostly developed during the PhD, this thesis is limited to spray measurements in cold ambients. However the boundary conditions for hot ambient conditions were evaluated as well. In this section the future boundary conditions are chosen as a function of the engine that will be studied as a first target: the ABC 6DZC engine (Fig. 4.15). This engine type is the most distributed among the ABC engines and an engine setup is available to have the ability to compare engine test bench results with experiments in the constant volume combustion vessel. The most relevant specifications of the engine are given in table 4.5.

Figure 4.15: The ABC 6DZC engine, target engine type for this research

The moment of start of injection depends on the speed, fuel type and temperature as will be demonstrated later on in chapter 8. For comparison purposes, the boundary conditions are taken for diesel at nominal speed ($1000 rpm$) and full load, which is the most relevant situation for such engine applications. At these conditions the injection duration is approximately 48°ca. The compression process is considered as a polytropic process. The polytropic exponent γ is found to be 1.356 (6DZC, 100%, 1000rpm, no EGR) based on a linear fitting on the $log(P)/log(V)$ diagram of engine measurements between the closing of the inlet valve (IVC) and moment of start of injection (SOI).
The pressure at start of injection is obtained from the engine measurements (P/α-diagram). The variable cylinder volume and temperature can be determined by:

$$\frac{V_{IVC}}{V_{SOI}} = \frac{1+\frac{CR-1}{2}\left[\left(1+\frac{1}{R}\right)-\left(\cos(\theta_{IVC})+\frac{1}{R}\sqrt{1-R^2\sin(\theta_{IVC})^2}\right)\right]}{1+\frac{CR-1}{2}\left[\left(1+\frac{1}{R}\right)-\left(\cos(\theta_{SOI})+\frac{1}{R}\sqrt{1-R^2\sin(\theta_{SOI})^2}\right)\right]} \tag{4.1}$$

ABC 6DZ(C)	
cycle	4-stroke, 6 in-line
bore	$256mm$
stroke	$310mm$
compression ratio (CR)	12.1
brake mean effective pressure	$1.88MPa$ (at $1000rpm$)
power	$170-250kW/cyl$
relative boost pressure	$0.21MPa \pm 0.2$
ratio of crank radius to connecting rod length (R)	0.25
inlet air temperature	$338K \pm 8$
start of injection (SOI)	21°BTDC
inlet valve closing (IVC)	40°ABDC

Table 4.5: Specs of the ABC 6DZ(C) engine, as a target for spray measurements in the optically accessible combustion chamber

and

$$T_{SOI} = T_{IVC}\left(\frac{P_{SOI}}{P_{IVC}}\right)^{\gamma-1} \tag{4.2}$$

With Z_{SOI} and Z_{IVC}, resp. the compressibility factor at the moment of start of injection in the GUCCI setup and inlet valve closing. In terms of spray characterization, the density is a more meaningful parameter than pressure; it is the density that provides the resistance and enhances the breakup rather than the pressure (cfr. chapter 2: Diesel fuel sprays). From the corrected ideal gas law, assuming a gas mixture with the properties of air ($R = 287J/kgK$), the density at SOI is calculated as:

$$\rho_{SOI} = \frac{P_{SOI}}{Z_{SOI}.R_{SOI}.T_{SOI}} \tag{4.3}$$

In the engine, the moment of start of injection is relatively early (approx. $21°ca$) and compression is still going on. From needle lift measurements, the injection duration is approximately $48°ca$ ($\sim 4ms$ at $1000rpm$, full load). The start of injection for medium speed diesel engines is earlier and the injection takes longer compared to common rail heavy duty engines (e.g. '*spray A*' [108] as discussed in chapter 7): $21°ca$ BTDC vs. $6-15°ca$ BTDC with an average injection duration of $4ms$ vs. $\sim 1.5ms$. This results in a wider range of ambient conditions during injection and makes it hard to choose a single condition for experiments in the constant

volume vessel. The measured cylinder pressure is displayed in Fig. 4.16 by the solid blue curve. The pressure trace during injection is located between the 2 vertical green dashed lines. In the GUCCI-setup the ambient condition is constant, so no influence of the further compression and start of combustion can be simulated. The condition at the moment of start of injection would underestimate the mean ambient density and temperature during injection and thus was not withheld as the appropriate test condition. A more relevant condition needs to be chosen to study a vaporizing spray.
A reasonable approach is averaging the injection profile during the injection time, weighted with the mass flow rate. In such way the contribution at the highest injection rates is more important than the start and end of injection. The mass flow rate and spray momentum profiles are similar to the one of the injection pressure. As a consequence, the measured cylinder pressure during injection is weighted with the injection pressure according to Eq. 4.5 ($\theta = 0°$ represents the TDC). The injection pressure profile is measured during the experiments in the injection line. The injection pressure is then shifted in time using a correction for the speed of sound c according to Eq. 4.4 in which L, n, B and ρ represent resp. the length between the pressure sensor and the nozzle $[m]$, the engine speed $[rpm]$, the bulk modulus $[Pa]$ and density $[kg/m^3]$ of diesel at the fuel temperature.

$$\begin{aligned} \triangle ca_{shift} &= 6n\frac{L}{c} \\ c &= \sqrt{\frac{B}{\rho}} \end{aligned} \tag{4.4}$$

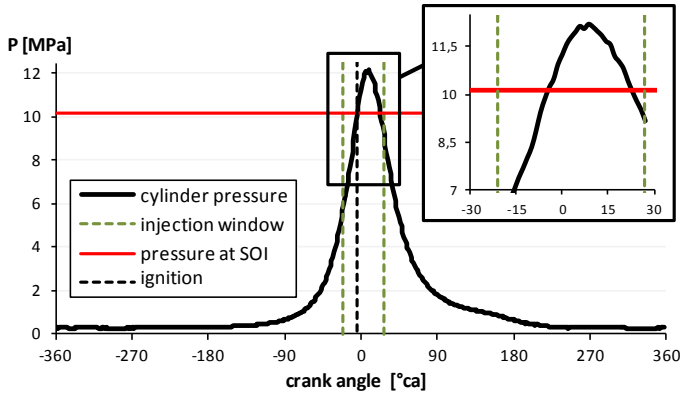

Figure 4.16: Determination of the pressure at start of injection in the GUCCI-setup based on an engine test on a 6DZC at full load at 1000rpm.

$$P_{SOI} = \frac{\sum_{\theta=-21°}^{27°} \sqrt{P_{inj}}(\theta) P_{cyl}(\theta)}{\sum_{\theta=21°}^{27°} \sqrt{P_{inj}}(\theta)} \tag{4.5}$$

Equation 4.5 results in a pressure P_{SOI} of $9.87MPa$ (horizontal red line in Fig. 4.16). On the other hand, also a good understanding of the start of combustion is required when investigating reacting sprays. For this reason, the previous approach for determining the appropriate vaporizing spray conditions might not be successful. From heat release data, the ignition delay for the investigated ABC engine was found to be $17°ca$, which corresponds to a start of combustion at 4° BTDC. The corresponding cylinder pressure is $10.25MPa$, based on the experiments indicated by the vertical black dashed line in Fig. 4.16.

Both approaches, conditions based on ID and weighted average of cylinder pressure, are totally different, but surprisingly, both conditions give similar results.
For $P_{IVC} = 0.33MPa$, $\theta_{IVC} = 220°ca\ ATDC$, $\theta_{SOI} = 5°ca\ BTDC$, the bulk temperature and bulk density were respectively $850K$ and $35kg/m^3$. The temperature at SOI is calculated with equation 4.2.
After iteration to determine the compressibility factor Z_{SOI} at a temperature T_{SOI} of $850K$, Z_{IVC} ($340K$, $0.33MPa$) = 1 and Z_{SOI} is 1.0247 [121].

4.5 Pre-combustion

4.5.1 Introduction

The pre-burn or pre-combustion method has been evaluated in the past as a reliable method to create engine-like conditions in a constant volume combustion chamber for optical spray measurements and is widely used [90, 112, 117]. This method is used to create the desired hot and pressurized ambient by igniting a carefully chosen gas mixture. The ignition is realised by two spark plugs placed oppositely with high capacity coils. A piezo-electric pressure sensor monitors the cooling down process by measuring the bulk pressure. The piezo-resistive sensor that monitors the gas filling is used as the absolute reference signal. Only 4 gases are used for the initial gas mixture, allowing us to define 4 properties at start of injection. The most important ambient gas properties which will influence the spray (and combustion) are:

- amount of oxygen [$vol\%$]: influences the oxidation process
- temperature at SOI: influences the evaporation process
- density at SOI: influences the spray break-up process
- heat capacity at injection: influences the evaporation process

Other properties such as viscosity and heat conductivity are not directly matched but are checked nevertheless. The main motivation is that those parameters are usually not included in simplified spray and combustion models, since the influence is not significant [89].

Apart from the gas mixture properties prior to pre-combustion, one needs to take the impact of the pre-combustion on the combustion chamber into account; peak pressure & temperature, the minimum & maximum allowed concentration of the fuel to have a combustible mixture.

The demands lead to a set of 4 equations 4.6-4.9 resp. the mass conservation, the expression for the amount of oxygen left after the pre-combustion, the energy conservation and the expression for a matched heat capacity. The derivation is given in more detail in appendix A.

$$\rho_u V_{chamber} = m_{u,C_2H_2} + m_{u,O_2} + m_{u,N_2} + m_{u,Ar} \tag{4.6}$$

$$\begin{aligned} 0 \quad = \quad & \frac{1}{M_{C_2H_2}}\left[\frac{5}{2} + \frac{1}{2} vol\%_{b,O_2}\right] m_{u,C_2H_2} \\ & + \frac{1}{M_{O_2}}\left[vol\%_{b,O_2} - 1\right] m_{u,O_2} \\ & + \frac{1}{M_{N_2}}\left[vol\%_{b,O_2}\right] m_{u,N_2} \\ & + \frac{1}{M_{Ar}}\left[vol\%_{b,O_2}\right] m_{u,Ar_2} \end{aligned} \tag{4.7}$$

$$\begin{aligned} 0 \quad = \quad & [u_{u,C_2H_2}(T_u) + \frac{5}{2}\left(\frac{M_{O_2}}{M_{C_2H_2}}\right) u_{b,O_2}(T_b) - 2\left(\frac{M_{CO_2}}{M_{C_2H_2}}\right) u_{b,CO_2}(T_b) \\ & - \left(\frac{M_{H_2O}}{M_{C_2H_2}}\right) u_{H_2O}(T_b)] m_{u,C_2H_2} \\ & + \left[u_{O_2}(T_u) - u_{O_2}(T_b)\right] m_{u,O_2} \\ & + \left[u_{N_2}(T_u) - u_{N_2}(T_b)\right] m_{u,N_2} \\ & + \left[u_{Ar}(T_u) - u_{Ar}(T_b)\right] m_{u,Ar} \end{aligned} \tag{4.8}$$

$$
\begin{aligned}
0 \quad = \quad & \frac{1}{M_{C_2H_2}}[2.c_{pCO_2}(T_{SOI}) + c_{p_{H_2O}}(T_{SOI}) - \frac{5}{2}c_{pCO_2}(T_{SOI}) \\
& -\left(2+1-\frac{5}{2}\right)c_{p_{mix}}(T_{SOI})]m_{u,C_2H_2} \\
& +\frac{1}{M_{O_2}}\left[c_{pO_2}(T_{SOI}) - c_{p_{mix}}(T_{SOI})\right]m_{u,O_2} \\
& +\frac{1}{M_{N_2}}\left[c_{p_{N_2}}(T_{SOI}) - c_{p_{mix}}(T_{SOI})\right]m_{u,N_2} \\
& +\frac{1}{M_{Ar}}\left[c_{p_{Ar}}(T_{SOI}) - c_{p_{mix}}(T_{SOI})\right]m_{u,Ar}
\end{aligned} \tag{4.9}
$$

The solution returns the mass to be filled of each gas. The masses are transformed to pressures using the ideal gas law (cfr. appendix A). The final settings for the gas filling for an inert atmosphere is given in table 4.6. The peak pressures for adiabatic combustion were estimated to be $16MPa$ for the inert atmosphere. From the experiments it will be seen that the measured peak pressure is lower than expected, which would allow us to go to more extreme situations without damaging the windows. For safety reasons, this risk was not taken. A second remark involves the concentration of C_2H_2 in the gas mixture. The flammability limits are between 2-2.5$vol\%$ and 75% at ambient conditions and should be checked for the considered mixture. It was found that the minimum concentration for C_2H_2 in the mixture had to be equal or bigger than $2.7vol\%$ in order to ignite which is a result of the temperature and pressure dependency of the flammability limits. One of the reasons could have been the gas leakage or inhomogeneity in the chamber, resulting in a too lean mixture near the spark plugs. This was the main reason to fill the chamber with an excess of C_2H_2 (about 10%).

gas	**part. pressure [MPa]**	**#mol**	**cum. pressure [MPa]**	vol%
C_2H_2	0.104	0.129	0.104	2.7
Ar	0.189	0.234	0.292	4.8
N_2	3.393	4.213	3.685	87.3
O_2	0.201	0.249	3.886	5.2

Table 4.6: Pressure settings for the filling gases prior to pre-combustion in order to create an inert atmosphere

Only 4 independent parameters could be controlled by the composition of the gas mixture. Viscosity and heat conductivity of the ambient gas could not be directly controlled. The error was estimated and is given in table 4.7. The target condition refers to the property of air (without EGR) under the conditions at start

of injection. As can be seen, deviations are small and deemed acceptable.

Property	Target	at SOI	Theoretical error [%]
heat conductivity [W/mK]	0.0545	0.0529	3.0
dynamic viscosity [mPa.s]	3.51e-2	3.48e-2	1.0

Table 4.7: Comparison between the target and realized values for the additional gas properties heat conductivity and dynamic viscosity for an inert ambient.

4.6 Evaluation of the boundary conditions in the GUCCI-setup

4.6.1 Introduction

Sprays are very sensitive to the boundary conditions. Furthermore, the boundary conditions in diesel engines are challenging: high injection pressures, high ambient pressures and temperatures, complex fuel composition and moving engine parts. All these factors make it not only hard to reach these conditions to perform optical experiments, but make it also necessary to have a good knowledge about the accuracy and reproducibility of these boundary conditions.
In this section important boundaries such as injected fuel temperature, ambient temperature and ambient velocity field are determined. Two factors are investigated: the repeatability and homogeneity. The latter is important since most simplified spray models consider homogeneous boundary conditions such as constant ambient and fuel temperature.

4.6.2 Fuel temperature

Spray models that start modeling at the nozzle exit, require the fuel temperature at the nozzle exit. Many researchers, using similar experimental setups, take the temperature of the injector or fuel temperature in the injector prior to the pre-combustion without further motivation. The properties of fuels with higher viscosity are more sensitive to temperature (see also chapter 8). The importance of this effect was also noticed in spray measurements [13, 120].
Therefore, in this section, a validation study is performed to make a statement for the injected fuel temperature possible.

First, the regime fuel temperature inside the injector, prior to pre-combustion is required. By modifying the temperature of the cooling (thermal) oil of the injector, the fuel temperature can be controlled independently from the chamber wall

temperature. Figure 4.17 shows the injector cooling implementation in the injector block of the setup. The complete cooling circuit was handled in section 4.3.5.
Only the lower part of the injector can be cooled. All fuel injected at full load ($\sim 2cm^3$) is already contained in the injector between the positions $x = 7mm$ and $140mm$. A dummy injector, perforated along the injector axis for a 0.5mm ther-

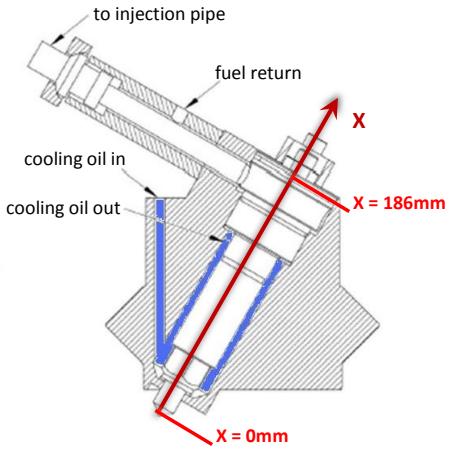

Figure 4.17: Implementation of the injector cooling. The blue area represents the area taken by the cooling oil

mocouple, is used to measure the fuel temperature inside the injector at different places along the axis for several combinations of ambient and cooling temperature (resp. T_a and T_c). No fuel is contained in the injector during these measurements. It is assumed that the measured temperature is the same as the fuel temperature at that place since the whole system is in steady state. Due to the length of the injector, it is unavoidable to have a temperature gradient along the injector axis. However, the experiments showed that even in the worst case measured scenario ($T_c = 70°C$, $T_a = 145°C$) the temperature difference is limited to approximately $10°C$.
A correlation of the form $T_f = f\{T_a, T_c\}$ could be found, based on the least squares method. The results of some of the measurements are displayed in Fig. 4.18. The grey area represents the local volume in the injector occupied with fuel, while the black line represents the cumulative volume. The area between the blue dashed lines indicates the area that is directly in contact with the thermal cooling oil. Note that the fuel temperature for locations above position $x = 140mm$ is dominated by the chamber temperature since the cooling oil can not reach that area. The influence of the fan was found to be negligible. The temperature is averaged along the injector axis weighted with the volume fraction at each position x.
The form of the correlation (Eq. 4.10) is chosen in such way that a minimal number

of parameters is required, while still having a good agreement with the experiments (= high R^2). The corresponding coefficients are shown in table 4.8.
For each combination of the desired ambient and fuel temperature in the experiments the temperature of the thermal cooling oil is calculated and set according to Eq. 4.10. The predictions were compared with experiments and the correlation revealed an accuracy of better than $1.5°C$. These errors are within the accuracy of the thermocouple, from which one can conclude that this method is accurate enough to determine the fuel temperature.

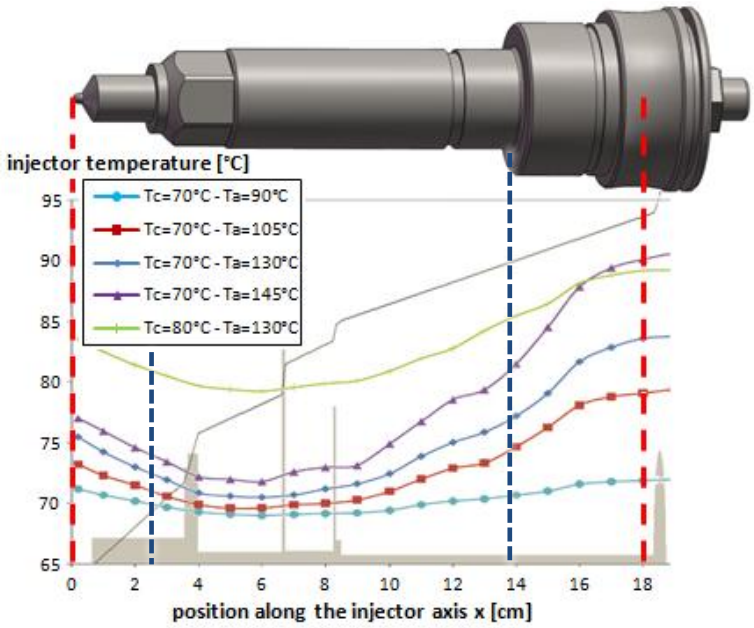

Figure 4.18: Results of the fuel temperature inside the injector for different combinations of ambient (T_a) and injector cooling (T_c) temperatures. The grey area represents the local volume in the injector occupied with fuel, while the black line represents the cumulative volume.

$$T_f = a_0 + a_1 T_a + a_2 T_c + a_3 T_a T_c + a_4 T_a^2 + a_5 T_c^3 \tag{4.10}$$

The next step is the investigation of the influence of the pre-combustion process on the fuel temperature. It has been reported in literature [122] that the pre-combustion causes the injector tip temperature to rise prior to injection. This temperature increase might cause heating of the fuel. Injector temperature measurements during pre-combustion are conducted with and without thimble. The results of 2 different axial positions are displayed in Fig. 4.19: $0mm$ (= bottom of

a_0	4.318	a_3	-1.04E-3
a_1	0.131	a_4	3.10E-3
a_2	0.690	a_5	-7.20E-6

Table 4.8: Coefficients involved in correlation 4.10 for the injected fuel temperature

the sac volume) and 10mm.
The influence of the thimble is clearly seen. Without thimble (dashed lines) the temperature of the nozzle is increasing significantly (more than 25°C) and is not yet stable at the desired moment at SOI (about 2s after ignition). Introducing the thimble lowers the increase and a more or less stabilized temperature at start of injection is obtained.
As mentioned earlier, the fuel is located between $x = 7mm$ and $x = 140mm$. This means that about 10% of the injected fuel is below $x = 10mm$. As a conclusion, the influence of the pre-combustion on the mean fuel temperature is negligible.

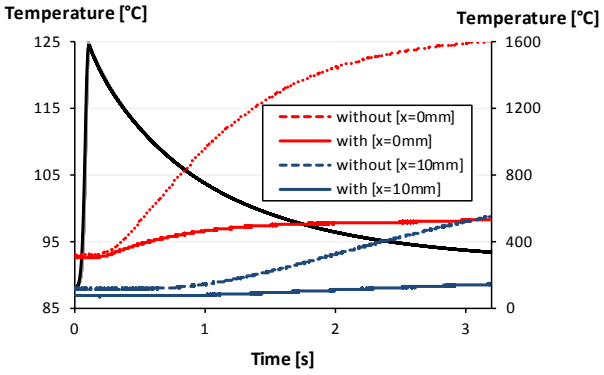

Figure 4.19: Influence of the pre-combustion on the nozzle, with (blue curves) and without (red curves) thimble. The dashed lines represent the temperature at the bottom of the sac volume, while the full lines represent the nozzle temperature at position $x = 10mm$. The black curve is the bulk temperature during the pre-combustion process (temperature scale at the right side).

Finally, as noticed in Fig. 4.19, the tip temperature of the injector rises. If the fuel is heating up during injection by passing the hot nozzle, the modeling results might differ from the experiments. The temperature rise of the fuel is estimated by the use of a basic 0D heat transport problem according to Eq. 4.11 with the worst case scenario.

$$\dot{m} c_p \frac{\delta T_f}{\delta x} = hA\left(T_w - T_f\right) \tag{4.11}$$

For simplicity, the convection coefficient h is taken as a constant along the injector position. With the initial fuel temperature T_{f0} at position $10mm$ upstream the injector, the equation results in:

$$T_f(x) = T_w + \left(T_{f0} - T_w\right) e^{hA(0.010-x)/\dot{m}c_p} \tag{4.12}$$

With

$$\begin{aligned} h &= Nu.k/D \text{ (order of } 6000W/m^2K) \\ Nu &= 0.023Re^{0.8}Pr^{0.4} \text{ (order of 150)} \end{aligned}$$

with Re in the order of 10000 to 30000 (depending on the engine speed, the fuel velocity is between 10 to $30m/s$ inside the sac volume). Assuming the wall temperature to be equal to the measured temperature in the sac volume ($T_w = 96.5°C$), the resulting temperature increase is less than $0.1°C$ before the entrance of the nozzle holes. The temperature increase inside the nozzle holes is determined in a similar way ($h \simeq 15000W/m^2K$, $Nu \simeq 280$, $Re \simeq 20000$, $T_w = 540K$). Fuel properties of diesel were taken: $k = 0.125W/mK$, $c_p = 2000J/kgK$ and $\mu = 2.4mPas$.
As a global result, the fuel temperature rise is less than $0.1°C$ and thus can be neglected.

The pre-combustion increases slightly the nozzle tip temperature but the injected fuel temperature is not affected by this temperature rise. One can conclude that the fuel temperature can be determined accurately enough through Eq. 4.10.

4.6.3 Ambient temperature

The pre-combustion process generates initially a higher pressure (and temperature) than required for the start of injection. Due to heat transfer to the wall, the pressure (and temperature) level lowers until the desired injection conditions are reached. Two questions need to be answered: 'Is the timing for the injection after pre-combustion constant?' and 'Is the temperature homogeneous?' or 'What is the difference between the bulk and core temperature?'.
The performance of the pre-combustion strongly depends upon the mixing of gases. The mixing fan dominates this process [123]. Experiments with both activated and deactivated fan during the pre-combustion were conducted and are shown in Fig. 4.20. The solid lines represent the average pressure development with and without mixing fan. The bright area around these curves is the standard deviation. It is concluded that the moment of start of injection is much more repeatable for the case with activated fan. With a fan speed of $3000rpm$ the variation on the moment of start of injection is less than 1%. The pressure trace without the fan was found to be sensitive to time at start of ignition and the level of gas leakage. The following conclusions can be drawn from these experiments:

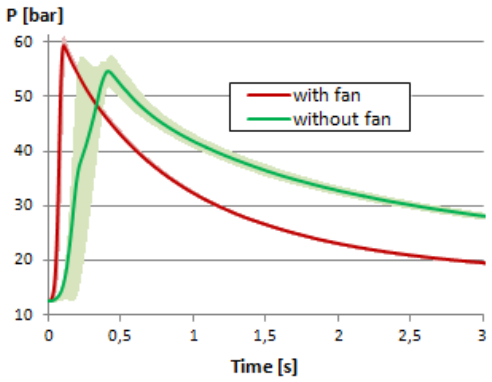

Figure 4.20: Influence of the fan on the pre-combustion process. The activated fan performed at maximum speed (3000rpm) The bright area around the pressure profiles represent the standard deviation

- the higher the fan speed, the higher the peak pressure
- the higher the fan speed, the faster the combustion (the more the theoretical adiabatic combustion is reached)
- the higher the fan speed, the lower the variation in the cooling-down process
- the higher the fan speed, the faster the temperature decrease (the higher the convective heat transfer to the walls)

The homogeneity of the chamber temperature was investigated with fast responding thermocouples (cfr. table 4.4). The thermocouples were inserted at different positions in the chamber along one of the window sides as shown in Fig. 4.21. Temperature measurements were taken 20mm distance from the wall to the core of the chamber. The measurement results are given in Fig. 4.22. The gas mixture composition (i.e. the boundary conditions) were chosen in such way the peak temperature was limited in order to keep the thermocouple lifetime acceptable. K-type thermocouples consist of a junction with 90% nickel/10% chromium and a junction of 95% nickel/2% manganese/2% aluminium/1% silicon and are designed to operate in a range of 273-1300K (continuously) or 100-1600K (short period), with a melting point of about 1700K. The measurements were performed in order to have a better understanding about the combustion behavior inside the vessel.
The upper part of Fig. 4.22 represent the schlieren images at 10kHz (upper row) and color images with a regular camera (lower row) for the indicated time instants.

No significant temperature distribution is noticed within the measurement cube. However, this easy measuring technique suffers from the fact that it is intrusive

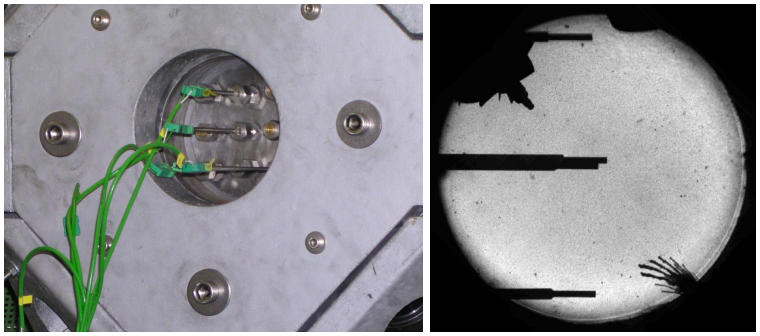

Figure 4.21: Practical implementation of the fast responding thermocouples for simultaneous measurements at different positions

and is only able to measure in discrete points. So limited information is available. From these measurements it is interesting to note that a significant amount of time is required to achieve stable temperature measurements. From the schlieren images it can be estimated that a more or less stable environment is established about 1 second after start of spark trigger. The temperature fluctuation might be mainly the result of vibration of the fine thermocouple wires due to the combustion turbulence. The junction is situated fairly close to the shaft of the thermocouple, which is made of an insulating material. The shaft will be much colder during the combustion and when the junction hits the shaft, significantly lower temperatures are registered. After more than 2 seconds, the temperature measurements are stabilized and become useful for the calculation of the ratio of core and bulk temperature.

In a next step, a more realistic set of boundary conditions was applied, taking the minimum ignitability of the mixture of the preburn gases into account (cfr. table 4.9). The maximum bulk temperature measured was around $1700K$ (cfr. Fig. 4.23). This is around the melting temperature of the thermocouples, and was noticed by the strongly reduced lifetime of the sensors. Two thermocouples were placed simultaneously in the chamber: one near the wall ($5mm$), far away from the spark plug and one in the middle. The bulk temperature was calculated based on the chamber pressure trace with the ideal gas law using a compressibility factor of 1.0247. The thermocouple, $5mm$ away from the wall measured lower temperature. This was especially clearly seen in the later stage of the cooling down (later than $2s$). A difference in temperature rise is detected as well which is consistent with the position of the thermocouples. The core thermocouple was spaced away further than the thermocouple near the wall (about $140mm$ vs $50mm$), so the flame front is first detected by the thermocouple near the wall. Heat transfer through the wall causes a less steep temperature gradient compared to the core measurement.

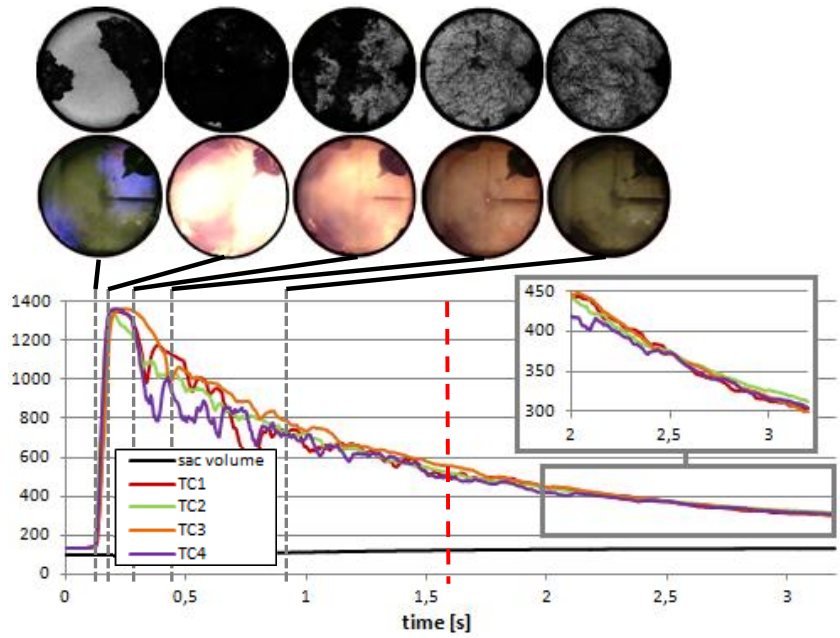

Figure 4.22: Temperature measurements during the pre-combustion with fast responding thermocouples at different places in the combustion chamber

Peak temperature results are not reliable since the maximum range was exceeded, so the quantitative results can not be trusted. During the early cooling down period, the average core temperature is slightly higher but very unstable, due to the combustion turbulence and the probable thermocouple vibration. When the temperatures become stable, the heat transfer becomes visible, by the lower measured temperatures near the wall.
The resulting T_c/T_b-ratio is 1.038 with a standard deviation of less than 3% and was calculated by averaging the ratios in a measurement window from 1.8-2.4s. As a consequence, injecting in a range of 797K and 842K would lead to acceptable accuracy (a bulk temperature of 819K corresponds with a core temperature of 850K). Translated to time this results in an acceptable time window of 2.14s to 2.4s.

4.6.4 Velocity field

For simplicity, most models and experimental validations consider the ambient velocity negligible compared to the injection velocity. This might be true at the nozzle exit, but the spray tip velocity decreases approximately exponentially. Figure 4.24 shows a typical velocity decrease along the spray axis. Validation of the

$T_{chamber}$	$400K$	C_2H_2	$0.099MPa$
ρ	$25kg/m^3$	Ar	$0.169MPa$
T_{SOI}	850K	N_2	$2.471MPa$
f	0.41	O_2	$0.224MPa$

Table 4.9: Boundary conditions for the T_c/T_b-ratio

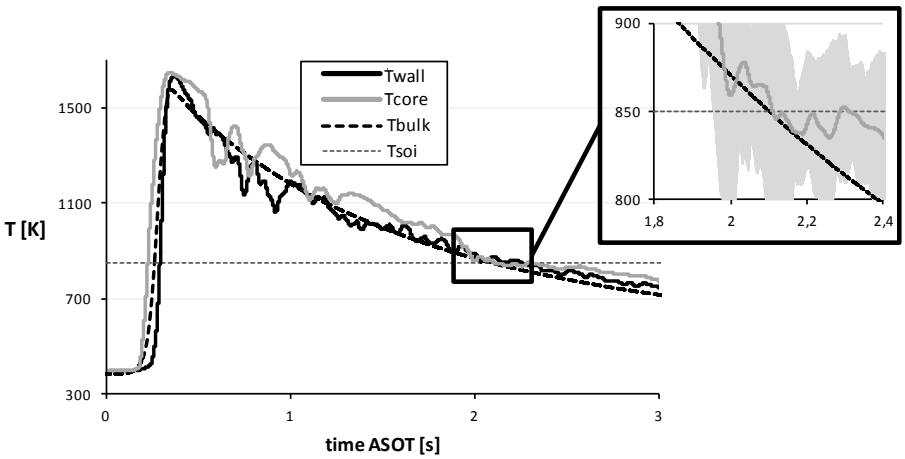

Figure 4.23: Temperature measurements to determine the T_c/T_b-ratio at the moment of start of injection. The red line represents the average temperature measured 5mm away from the wall at the lower corner of the vessel, the green line is the average core temperature. The light green area corresponds with the standard deviation of the core temperature measurements. The black dashed line is the bulk temperature converted from the pressure measurements

ambient velocity is necessary, in order to conclude whether this velocity field can be neglected or has a significant influence on the spray tip.
The validation has been qualitatively performed by high speed schlieren and shadowgraphy imaging during the whole measuring period: from the moment of spark ignition until the end of the expected fuel injection.
During the pre-combustion, gradients are too strong for the schlieren technique, resulting in an almost completely black image (cfr. Fig. 4.25, right column at $90ms$ and $120ms$ ASOT).
As was noticed in Fig. 4.20 the pre-combustion process takes longer when the fan is not activated and the velocity field (and density/temperature field) is less homogeneous. The bottom line images of Fig. 4.25 shows an image of a stabilized velocity field. Note that this moment is significantly before the desired time at

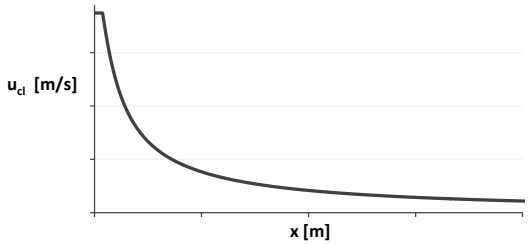

Figure 4.24: Typical decrease of axial spray velocity u along the spray axis x

injection (>1.5s ASOT). However, the velocity field at start of injection is of our interest.

It was found that the schlieren technique is more desired since more details of the ambient gases are revealed. This has been made clear in Fig. 4.26 in which the schlieren and shadow images are compared at the desired moment at start of injection. These high speed schlieren images qualitatively show that a more or less homogeneous flow field exists at the moment of injection. For a quantitative idea of this flow, methods such as particle image velocimetry (PIV) and phase doppler techniques, have shown in literature [124] valuable results for this application. However these techniques require expensive equipment and additional modifications to the setup, such as a seeding mechanism. This was not realizable during this PhD period. Recently, a method based on the optical density in the schlieren method has been developed by the German company Goldlucke Ingenieurleistungen, so no additional equipment other than the high speed schlieren setup is required. The method is known as the Optical Flow Method (OFM) [125]. The main assumption of this method is that the intensity of a structure in succeeding images is considered not to change. This means if in 2 images a pixel changes intensity, this pixel is moving at a certain velocity. The method requires 3 images in order to generate 1 image with the velocity field. This allows the method to make a prediction of the trajectory of the structures. For details of the principles, realization and validation, the reader is refered to the work of Lorentz *et al.* [125]. A result of a stabilized velocity field is shown in Fig. 4.27. The velocities are mainly between 0.5 and 2.5m/s. It should be mentioned that this is the 2D result of a 3D phenomenon. This implies that the velocity component along the line of sight is lost, resulting in an underestimation of the velocity. The highest velocities exist near the fan and bottom of the chamber (the image is rotated over 135°, the fan is physically in the upper left corner of the image).

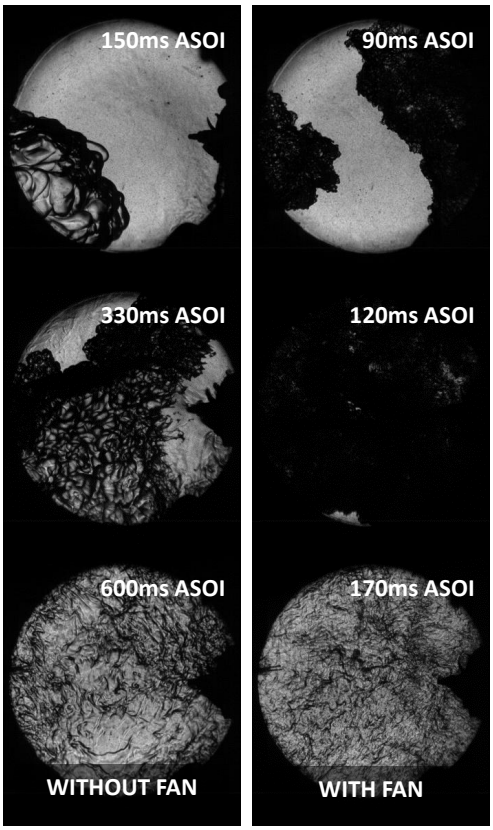

Figure 4.25: Schlieren images of the pre-combustion process with (right column) and without fan (left column) at 3 different moments: 150*ms,* 330*ms and* 600*ms after start of trigger*

4.7 Summary & conclusion

Two different optically accessible constant volume combustion chambers were described: the Eindhoven High Pressure Cell (EHPC) and the Ghent University Combustion Chamber I (GUCCI). The latter was developed during this PhD work. The most important subsystems and choices were motivated.
In order to obtain relevant spray measurements, the boundary conditions were chosen and motivated. The resulting boundary conditions are summarized in table 4.10. A pre-combustion method is implemented to reach these conditions, a mixture of 4 gases (C_2H_2, Ar, N_2 and O_2) was calculated for both inert and oxidizing ambient mixture. The 4 gases allow to choose 4 independent desired ambient properties: amount of oxygen, ambient heat capacity, density and temperature.

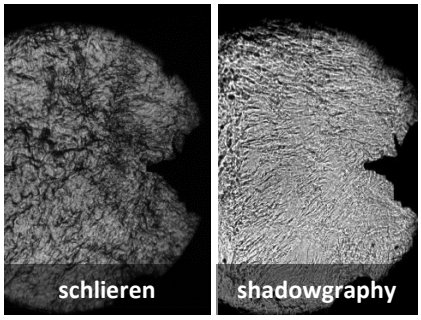

Figure 4.26: Comparison of the performance of schlieren (left) and shadowgraphy (right) for a qualitative investigation of the stabilized flow field after pre-combustion

T_u [K]	400
T_{SOI} [K]	850
ρ_{SOI} $[kg/m^3]$	35.0

Table 4.10: Summary of the proposed boundary conditions for the initial spray measurements

Properties such as heat conductivity and viscosity were not matched, however the error on these parameters were evaluated and found to be acceptable.

The boundary conditions (fuel temperature, ambient temperature and ambient velocity field) were evaluated since they will dominate the accuracy and usability of the quantitative spray measuments. Here, both mean values and homogeneity were investigated:

Values:

- the nozzle tip temperature increases slightly when the thimble is used, but is constant during injection. This is not the case if the thimble is absent

- the pre-combustion has no significant influence on the fuel temperature prior to injection

- the ambient velocities at SOI are below $3m/s$

- the fuel temperature can be chosen independently of the chamber wall temperature with good accuracy by controlling the injector cooling temperature ($< 1.5K$).

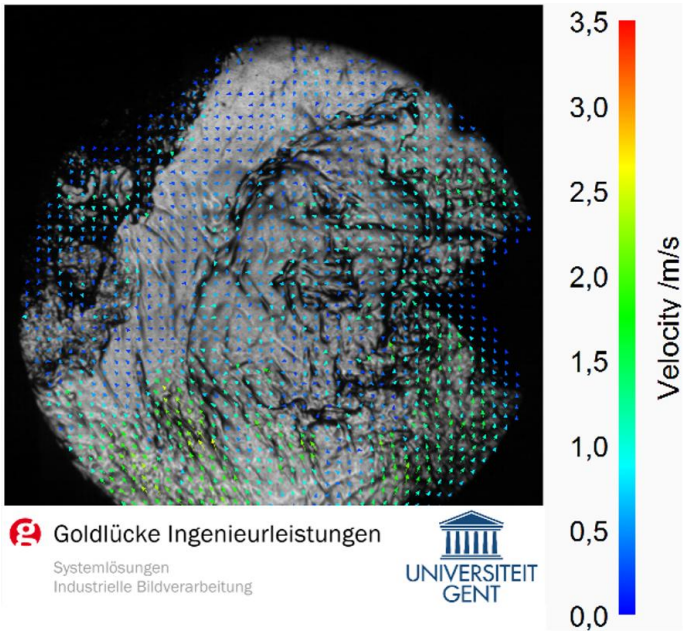

Figure 4.27: Schlieren image of a stabilized velocity field after pre-combustion at maximum fan speed with the use of the Optical Flow method (processed by Goldlucke Ingenieurleistungen)

- activation of the fan during the pre-combustion reduces the standard deviation on the time of SOI.

Homogeneity:

- the velocity field after pre-combustion with activated fan is much more homogeneous, with slightly higher velocities at the bottom of the chamber
- the thermal boundary layer of the ambient at SOI is below $20mm$. The core/bulk-ratio was found to be 1.038 $\pm 3\%$. This can be compared to other but smaller combustion vessels in which a ratio between 1.03 and 1.08 is found (cfr. Fig. 4.28) [126]. This corresponds with an injection at a bulk temperature between $797K$ and $842K$. It should be pointed out that the smaller this ratio is, the more homogeneous the temperature is inside the vessel.

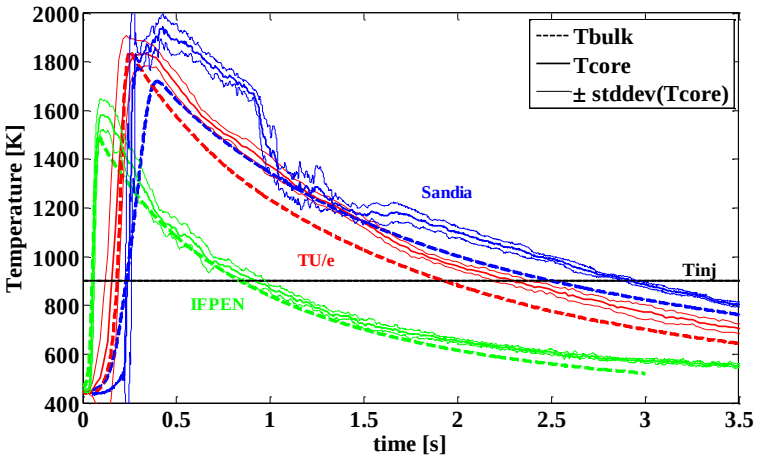

Figure 4.28: Core and bulk temperature measurements obtained by other research institutes: Sandia National Laboratories (blue), TU/e (red) and IFPen (green) [126]

5

Prediction of vaporizing sprays

"The way you learn anything is that something fails, and you figure out how not to have it fail again."

- Robert S. Arrighi -

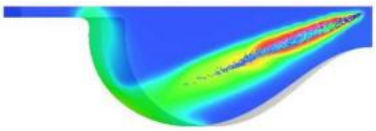

The chapter is organized as follows: attempts are undertaken to model vaporizing sprays of different fuel types using a model class appropriate for use as a submodel for powertrain simulations.
After the elucidation of the modeling targets and overview of modeling strategies, the choices considering the boundary conditions are clarified and linked with experiments. The third section deals with the chosen model strategy and gives an overview of the most common models. The fourth section describes the model of interest in more detail, together with the innovative features. Finally, a sensitivity analysis has been performed to better understand the model behavior.

5.1 Introduction

5.1.1 Spray and combustion modeling targets

It has been reported before in this work: the spray processes are complex and very sensitive to their boundary conditions. Therefore, lots of spray models or attempts exist, depending on their application. In some applications, certain simplification or hypotheses might be valid while for others this is not the case. The degree of simplifications depends on the purpose of the modeling as well. Basically, 3 important reasons exist why modeling or process prediction is used:

- **understanding** of a physical process (~ fundamental modeling): e.g. understanding the reaction or behavior of a spray in a turbulent environment and the influences of parameter changes
- **design and optimization** of systems (~ design modeling): e.g. design of a piston bowl taking the penetration length and air flow into account
- **tuning** of a system (~ applied modeling): e.g. to find (semi-)real-time the optimal injection timing for different operating conditions

The application in this work considers high pressure fuel sprays under engine-like conditions (high ambient temperatures and pressures). The final goal of the modeling work in this project is the prediction of the engine performance (power output, tailpipe emissions, efficiency) when using crude oils. This application can be considered as applied design modeling.
In order to accomplish this, spray models validated for diesel will be modified where necessary. In the following, the described models have been validated for diesel (or its surrogates).

5.1.2 Modeling strategy

One of the most difficult aspects of a high pressure, high temperature fuel spray is the determination of the boundary conditions. Real engines exhibit cycle-to-cycle variation, change of the ambient conditions (air composition, moisture, temperature, pressure), engine wear that affects temperature distribution, dimensions, leakage,... While the influence of some of these factors is negligible, others can have significant impact.
As is clear from previous chapters, the complexity and multiplicity of the physics involved are very challenging and in spite of the research efforts spent over the last decades, there is no phenomenon which can be considered as well understood. For each phenomenon, a set of adjustable constants is tuned to give the best fit on some chosen cases [70]. However, too many adjustable constants can lead to the fact that a certain model is only applicable for one certain engine or application. In this case the factors can vary over a wide range. This was e.g. noticed by

Chryssakis et al [54], who used a factor for the coupling of the nozzle effects to the primary atomization which can vary over a factor of 10 for different nozzles. Also Seykens *et al.* [127] found a wide range of values for the discharge coefficient in literature. This makes it very difficult to simulate the injected mass flow rate accurately on the basis of literature data.
All these uncertainties make the spray modeling complex and the use of a very complex model might not be better than a simplified one, depending on the application.

When considering modeling, one has a lot of choices to make in different areas: choice of the dimension, choice of the strategy, choice of interpretation of the phenomena, choice of physical phenomena to take into consideration, choice of submodels, etc.
In the literature there is not an unambiguous classification of the choice of the dimensions of the models. In this work, the distinction is made between 5 categories: heuristic models or correlations, thermodynamic models, phenomenological models, multi-dimensional models and combined models. These are briefly clarified below.

Heuristic models

Heuristic models or simply correlations are the simplest models and describe the parameters of interest by correlations based on experimental results. Mostly, the physics behind the correlations are rather poorly represented: the equations are usually the result of a fitting curve through the measured points and only the investigated parameters can be found in the expressions. In the best case, one has stated that a certain proportionality exists and tuned the correlation by the use of correction factors or terms [128].

Apart from the short resolving time, which makes them attractive in complex situations such as whole powertrain simulations, they are usually limited to a narrow range of operating conditions or are unique for only one (type of) engine(s) [70].

Thermodynamic models

Thermodynamical models are also very simplified and computationally efficient 0D-models: they use a simplified description of the combustion chamber and state that all gases are ideally mixed and neglect any flow field contribution to the spray formation and mixing.
The calculations to describe certain properties of the phenomenon are based on the thermodynamic fundamentals, in essence the conservation laws of mass, momentum and energy [64].

However, Ung & Assanis [66] stated that these models cannot be used to account for fuel spray evolution and spatial variation in mixture composition and temperature, which are essential to predict exhaust emissions and perform well if only a general indication of the engine performance is required [64].

Phenomenological models

Phenomenological models (sometimes indicated as multi-zone models) are at the turning point between CFD 2D/3D-models and look-up table models or pure 0D-models. The improvement of physical representative capability while keeping reasonable CPU performances in order to be embedded in a full engine simulator is a challenging and relevant topic in 0D- or quasi dimensional-model development [129].
Phenomenological models divide the combustion chamber (or spray) into numerous different zones that are characterized by different temperatures and compositions. Contrary to the thermodynamical models, a description of subprocesses is possible as well as the prediction of heat release and emissions. It should be noted that turbulence cannot be resolved because in these models there is still no flow field present in the computational domain. Since turbulence has a significant effect on heat release and emissions, the accuracy should be critically considered [64].

Multi-dimensional models

Multi-dimensional models, such as CFD-models, is the most advanced form of modeling with the highest resolving time. Although CFD models make use of fundamental equations, there are still some correlations involved based on experimental results (e.g. spray angle correlations in Fluent) and certain threshold values to activate a certain physical process such as *Re* and *We* for the break-up process.
Multi-dimensional modeling itself can also be classified based on different methods. These methods differ in how the different fluids or phases will be interpreted or tracked and resolved in the flow field of the computational domain.

The main problem of these models is the determination of the boundary conditions, which are usually strongly simplified.
Another problem by which this model strategy struggles is the grid size dependency (both time and spatial) [62, 130, 131]. Most spray models consider the whole spray as single droplets (Lagrangian particle tracking method [31, 69, 131]) or as continuous fluid in ambient gas (Eulerian approach [31, 62]). The grid-dependency of the Lagrangian approach is mainly the fact that the cell volume for the solution of the gas phase should be much larger than the maximum size of droplets contained in it, which is a problem for the spray area near the nozzle tip. According to the assumption made by the Eulerian formulation for the two-phase

flow, on the other hand, the grid size should be small enough to resolve the gas phase velocity distribution near the nozzle [70].
The main drawback of the Eulerian approach is that the equations are usually of partial-differential form, in contrast with the ordinary differential equations for the Lagrangian approach. Therefore they require more elaborate and expensive mesh-based solution methods which are prone to additional errors, notably numerical diffusion [62].

As a compromise, a combination of both the less grid-dependent Eulerian (near nozzle field) and Lagrangian (far field) is widely used as a CFD modeling strategy.

Combined models

A more efficient way to overcome the grid-dependence problem is the combination of simpler 1D- or phenomenological models for the computation of spray atomization and vaporization. In that case, the 1D or phenomenological models provide source terms (mass momentum and energy) that are used in the 3D model [70, 72].

Discussion

An important factor in the consideration of the modeling strategy is the trade-off between the resolving time, sensitivity and accuracy of the results.
The phenomenological models are the trade-off between very simple thermodynamical or 0D models and the computationally expensive CFD models, especially when the influence of the fuel properties and injection profile need to be validated as is the case in the considered project.

Furthermore, for high pressure, high temperature diesel fuel sprays, the following hypothesis are considered valid for diesel:

- Even under non-vaporizing conditions, the droplets almost immediately reach a dynamic equilibrium with the surrounding gas phase. Therefore, droplet sizes under realistic engine conditions are so small that atomization is no longer a limitation in the subsequent physical processes (evaporation and mixing) leading to combustion. This means that injection pressure has little, if any, influence on this parameter and so fuel-air mixing rate is the limiting factor [64, 132]. This hypothesis is also refered to as the ‘mixing limited’-hypothesis [133].
- Fuel is usually injected as a compressed liquid in a (near-)supercritical environment. This has a direct influence on the spray characteristics since in the supercritical state of a fluid, no distinction can be made between liquid and vapor. The mixing of the spray with the surrounding air becomes

a pure diffusion mechanism, indicating that the gas jet theory is applicable [134, 135].

- The initial spray can be considered to be axisymmetrical, since injection velocities (>100*m/s*) are sufficiently higher than the ambient flow field

Several investigations imply that many results from the literature concerning gas jets can be directly applied to sprays. The main difference between a turbulent gas jet and a spray is that, for a given nozzle geometry, the jet has a constant cone angle that depends neither on injection pressure nor on ambient density, while the diesel spray has a cone angle that depends on the operating conditions [136].

5.2 Phenomenological spray models

In this section some commonly used phenomenological diesel spray models are reviewed and compared.

5.2.1 Hiroyasu model

One of the oldest and most widely used phenomenological models is the one proposed by Hiroyasu *et al.* [64, 137] during the 80's. Important to note is that common rail systems were not yet available and maximum injection pressures were limited to 700*bar*. Nevertheless, this model is nowadays still used in commercial simulation software such as GT-Power. The model is able to predict the influences of parameters on the fuel consumption, NOx and soot emission such as the effect of intake air pressure, intake swirl ratio, nozzle diameter, intake air temperature, air entrainment and injection rate profile. All calculations were performed in a few hours' calculation time (with the pc's from 1993).
The model idea is schematically presented in Fig. 5.1.
The spray is divided in concentric cells which consist of an amount of liquid fuel, vaporized fuel, surrounding air and combustion processes.
A schematic diagram of the mass system in the package according to Hiroyasu *et al*. [137] is presented in the bottom half of Fig. 5.1.

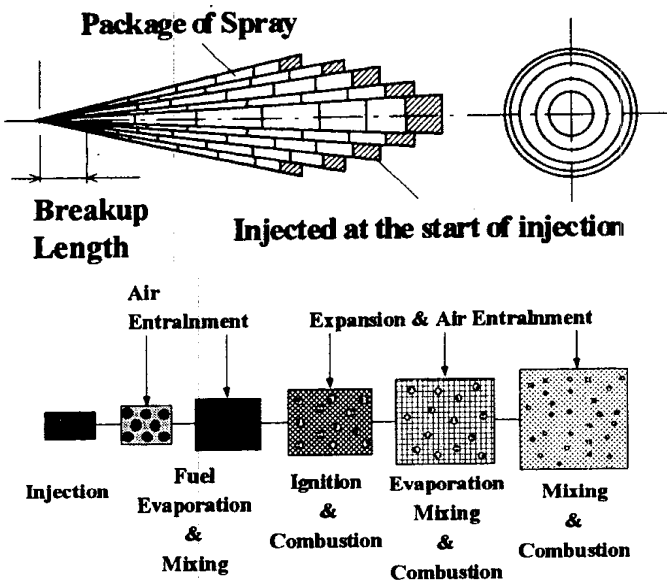

Figure 5.1: Schematic representation of the phenomenological model proposed by Hiroyasu et al. [137]

The model resolves the classic conservation equations for mass, momentum and energy. The cone angle is input of the model. With this information, the cross sectional area can be calculated. The amount of air entrainment is then determined from the momentum equation:

$$\dot{m}_f u_0 = \left(\dot{m}_f + \dot{m}_a\right) u \tag{5.1}$$

The penetration length S of the spray is determined by two correlations with only a limited amount of parameters: one for the spray in which the development time is smaller than a stated break-up time t_b, and one if breakup exists ($t>t_b$):

$$\text{for } t < t_b : S = 0.39\sqrt{\frac{2\Delta P}{\rho_f}}.t \tag{5.2}$$

$$\text{for } t \geq t_b : S = 2.95\left(\frac{2\Delta P}{\rho_a}\right)^{1/4}\sqrt{\alpha_0.t} \tag{5.3}$$

with ΔP the pressure difference between the injection and ambient pressure, ρ_f the fuel density, d_0 the exit nozzle hole diameter, ρ_a the ambient density, α_0 a tuning parameter and

$$t_b = 28.65\frac{\rho_f d_0}{\sqrt{\rho_a \Delta P}} \tag{5.4}$$

For each package, the Sauter Mean Diameter (SMD) is calculated. This diameter represents the average size of the droplets and is used to determine the vaporization.
An extension of the model was done by Stiesch & Merker [135]. They took into account that the injected fuel first has to overcome higher drag forces and will therefore penetrate slower into the cylinder than a fuel portion that is injected towards the end of the injection period. They implemented it by defining that the instantaneous zone velocity is not only a function of the radial position r but also of the axial position i:

$$v_{i,r} = C_1 . v_k \left(1 + \left(\frac{i-1}{i_{max}-1} \right)^{C_2} \frac{\Delta t_{inj}}{C_3} \right) \tag{5.5}$$

with C_x tuned parameters.

5.2.2 Sandia model

The Sandia model was developed by Naber and Siebers [79] at Sandia National Laboratories (USA). They use a very simplified model that predicts parameters such as penetration length.
Figure 5.2 shows a schematic of the conceptual spray model used in the analysis to develop the spray tip velocity relationship. The major assumptions made in the analysis are that :

- the spray has no velocity slip between the gas and liquid phases
- the whole system is at the same pressure P_a
- the constant injection velocity, density and temperature profiles are top hat
- the spray angle θ is constant and input to the model
- the fuel vapor is saturated and at thermodynamic equilibrium with the liquid fuel and entrained air

A correlation for the penetration *S(t)* was found by solving the fuel mass, momentum and energy conservation, resp. Eq. 5.6, Eq. 5.7 and Eq. 5.8 .

$$\rho_f A_f(0) U(0) = \rho_f A_f(x) U(x) = \dot{m} \tag{5.6}$$

$$\rho_f A_f(0) U(0)^2 = \rho_f A_f(x) U(x)^2 + \rho_a A_a(x) U(x)^2 \tag{5.7}$$

$$\begin{aligned} &\dot{m}(LL) h_f\left(T_f, P_a\right) + \dot{m}_a(LL) h_a(T_a, P_a) \\ &= \dot{m}(LL) h_f(T_s, P_a) + \dot{m}_a(LL) h_a(T_s, P_a - P_{sat}) \end{aligned} \tag{5.8}$$

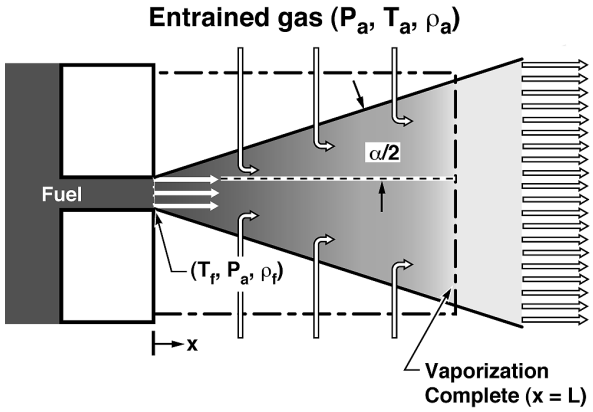

Figure 5.2: Schematic representation of the phenomenological model proposed Naber et al. [70, 97]

with LL the liquid length, $A_f(0)$ the cross section at the exit of the nozzle orifice $= C_a A_0$ (with A_0 the physical cross section at the exit of the nozzle orifice), $U(x)$ the axial spray velocity at position x and $U(0)$ the injection velocity:

$$U(0) = C_v \cdot \sqrt{2\frac{P_{inj}(t) - P_a}{\rho_f}}$$

For the spray penetration, only the fuel mass and momentum equation are solved; no distinction is made between fuel vapor and liquid. The (extra) energy equation is only used to calculate the liquid length LL.
A fourth equation defines the cross-sectional area of the spray occupied with entrained air ($A_a(x)$):

$$A_a(x) = A(x) - m.A_f(x) \tag{5.9}$$

with m 0 or 1, depending whether the fuel is neglected ($m = 0$) or not ($m = 1$). For simplification, m was set equal to 0 in the model. The spray velocity $U(x)$ is the result of this set of equations. Integration of the velocity $U(x)$ leads to the spray tip penetration $S(t)$:

$$S(t) = \sqrt{\frac{C_v\sqrt{2C_a}}{a.tan\left(\frac{\theta}{2}\right)}}\sqrt{\sqrt{\frac{P_f - P_a}{\rho_a}}d_0 t} \tag{5.10}$$

The expression for liquid length was found in a similar way:

$$LL = \frac{b}{a}\sqrt{\frac{\rho_f}{\rho_a}}\frac{\sqrt{C_a}d}{tan(\frac{\theta}{2})}\sqrt{\left(\frac{2}{B\left(T_a, P_a, T_f\right)} + 1\right)^2 - 1} \tag{5.11}$$

with

$$B = \frac{Z_a\left(T_{sat}, P_a - P_{sat}\right) P_{sat} M_f}{Z_f\left(T_{sat}, P_{sat}\right)\left(P_a - P_{sat}\right) M_a} = \frac{h_a\left(T_a, P_a\right) - h_a\left(T_{sat}, P_a - P_{sat}\right)}{h_f\left(T_{sat}\right) - h_f\left(T_f, P_a\right)} \tag{5.12}$$

and Z the compressibility factor, T_{sat} and P_{sat} resp. the saturation temperature and pressure of the fuel, h the enthalpy, a & b in the expression for the liquid length LL (Eq. 5.11) are tuning parameters defined in [97].

5.2.3 Versaevel model

Versaevel *et al*. [70] extended some shortcomings of the Sandia model, such as vapor phase information and influences of the finite nozzle, by introducing the void fraction m in order to account for vaporization upstream of the liquid length LL. The hypotheses of the Sandia model are still valid, so the schematical representation of the model in Fig. 5.2 is also still applicable.
Derivation of the model can be found in the work of Versaevel *et al*. [70]. The expression for the vapor fraction leads to Eq. 5.13

$$Y_{fg} = \frac{1}{\left(\frac{p_a}{p_{sat}(T)} - 1\right)\frac{M_a}{M_f} + 1} \tag{5.13}$$

From these basic parameters, the velocities along the spray axis, spray tip penetration length and liquid length follows in a similar way as for the Sandia model. The expression of the liquid length is given below to indicate the similarity with the Sandia model (with $B = 1/\Delta$). The last term (the only difference with the Sandia model) corrects for the effect of a finite nozzle size.

$$L = \frac{1}{4a}\sqrt{\frac{\rho_{f0}}{\rho_a(L)}}\frac{\sqrt{C_a}d}{tan\left(\frac{\theta}{2}\right)}\sqrt{\left(\frac{2}{B}+1\right)^2 - 1} - \frac{1}{2a}\frac{\sqrt{C_a}d}{tan\left(\frac{\theta}{2}\right)} \tag{5.14}$$

5.2.4 Valencia model

This model has been developed by Payri and coworkers over the last couple of years and has been published several times by the team [89, 132, 133, 136].

The model considers the spray as a symmetric cone in which the atomization is no longer a limitation in the subsequent physical processes. In essence, breakup is not considered. Instead, the spray angle is used as an input to take breakup and dispersion into account (similar to the Sandia and Versaevel model). The spray is further considered as a homogeneous mixed fluid of entrained gas, fuel liquid and vapor.
The main contribution to evaporation is the mixing with the hot surrounding air

(the so-called 'mixing limited'-hypothesis); the vapor and liquid fraction are in equilibrium (saturated situation) at any time.

Gaussian distributions are used for the conserved parameters axial velocity $u(x,r)$, fuel mass fraction $f(x,r)$ and spray enthalpy $h(x,r)$ (cfr.Eq. 5.15), with x the position along the spray axis and r along the radial of the spray (cfr. Fig. 5.3). This forms the main difference with the model of Versaevel or Sandia, that use uniform profiles. The assumption is based on experimental results [29, 138]. This strongly reduces the calculation efforts since only calculations are required for the parameters along the spray axis, while retaining the 2D character. The whole symmetric 2D spray can be reconstructed with the information on the spray axis and the use of the Gaussian profiles for the 3 conserved parameters.

$$\frac{u(x,r)}{u_{cl}} = \left[\frac{f(x,r)}{f_{cl}}\right]^{1/Sc} = \left[\frac{h(x,r)-h_{a,\infty}}{h_{cl}-h_{a,\infty}}\right]^{1/Pr} = exp\left[-k\left(\frac{r}{x}\right)^2\right] \tag{5.15}$$

with q_{cl} the peak value of parameter q for the Gaussian profile, which corresponds with the value of q on the spray axis. The parameter k is the shape factor of the Gaussian such that the velocity at $r = R$ equals 1% of the axial position. This results in:

$$k = \frac{1}{tan\left(\frac{\theta}{2}\right)^2} ln(100) \tag{5.16}$$

The parameters Sc and Pr represent respectively the Schmidt and Prandtl number. For vaporizing diesel sprays, it is motivated by Pastor *et al.* [132] that both a Schmidt and Prandtl number of 1 is valid.
The use of variable radial profiles is the biggest difference with the model of Versaevel or Sandia.
A schematic overview of the model is given in Fig.5.3.

5.2.5 Conclusions

The model of Hiroyasu is still used in commercial codes, however there are some important drawbacks. First, this model was originally developed for relatively low injection pressures (<700bar), which reflects in the consideration of droplets. Secondly, the 2D approach (radial and axial cells) suggests that the resolving efforts are still high.

The resolving time is improved in the Sandia model but no information is obtained about the fuel vapor/liquid distribution. As a consequence, this model can not be used for combustion and emission prediction without modification.
It was found by other authors [139], but also by Naber and Siebers themselves that the experimental liquid length values are a factor of around 2 to 3 higher than

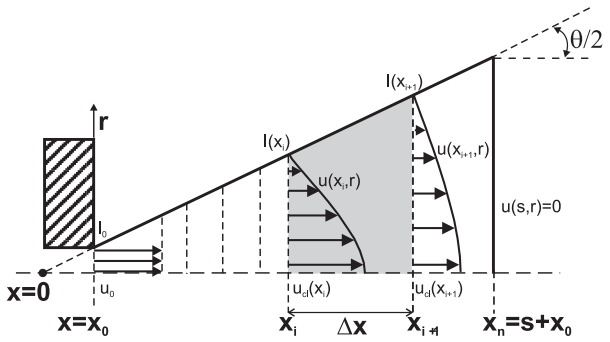

Figure 5.3: Schematic representation of the phenomenologic model proposed the Valencia group, with x_0 the nozzle outlet position [133]

the theoretical maximum liquid length derived by their entrainment calculations. Desantes *et al.* [139] pointed out that this was due to the consideration of cross-sectional average properties, which was not the case for the model of Valencia.

An important conclusion was drawn by Kurvers [140] that the thermodynamics in both Sandia and Versaevel models are fully equivalent, nevertheless there is some difference in the derivation. This confirms the earlier conjecture that the saturation thermodynamics can be decoupled from the process of spray penetration, which is purely governed by dynamics.

The 1D model strategy of Valencia group is found to be a good compromise between resolving efforts and accuracy (due to the more realistic radial distribution) for complete powertrain systems to investigate the influence of changing parameters, such as e.g. the fuel type or operating condition. This model concept will be further considered in this work, sligthly modified as motivated further on.

5.3 Model derivation

In this chapter, only the non-reacting vaporizing spray is considered. It is useful to model a non-reacting spray since Dec [23] noticed that the spray reaches its maximum liquid penetration length before the first heat release was detected. The model described in this chapter uses the combination of features and hypotheses from Payri and coworkers [89, 132, 133, 136] and from Musculus and Kattke [141].

Musculus and Kattke [141] adapted the model of Payri for a non-evaporative sprays with strongly reduced equations and with the use of another, but Gaussian-like radial profile. They proposed for the fuel fraction and axial velocity the profiles from Eq. 5.17 and Eq. 5.18 respectively.

$$f = f_{cl}\left(1-\zeta^{\alpha}\right)^2 \tag{5.17}$$

$$u = u_{cl}\left(1-\zeta^{\alpha}\right)^2 \tag{5.18}$$

with $\zeta = r/R$, with r the radial position, R the spray radius and α equal to 1.5 in order to approach the Gaussian profile. The advantage for the use of these type of profiles is the more realistic and smoother transient process from the injected (uniform) profile to the profile of the steady state part of the spray (cfr. Fig. 5.5).

5.3.1 Assumptions & hypotheses

The hypotheses and assumptions considered in this model are in essence equal to the ones of the Valencia group, but the most important ones are listed again below.

- Droplet sizes under realistic engine conditions are so small that atomization is no longer a limitation in the subsequent physical processes (evaporation and mixing) leading to combustion (this means that the injection pressure has little, if any, influence on this parameter, so fuel-air mixing rate is the limiting factor). The main contribution to evaporation is the mixing with the hot surrounding air (= 'mixing limited'-hypothesis); the vapor and liquid fraction are in equilibrium (saturated situation) at any time.
- The constant and homogeneous pressure in the whole spray equals the chamber pressure.
- Variable temperature along the spray axis and radial direction under saturated conditions.
- Gaussian-like distributions for the conserved parameters fuel mass fraction f, axial velocity u and enthalpy h (cfr. Eq. 5.17 and Eq. 5.18, with the same shape factor α for f, u and h).
- The whole spray is considered as a homogeneous mixture with a mixture density of ρ_{mix}
- Lewis number $Le = 1$ resulting in analogous equations for mass and energy conservation.
- The spray angle θ is constant and input to the model. Important to note is that the spray angle measured at early times of injection is not constant. This is reported by several authors [35, 47] for common-rail systems and has also been found for pump-line-nozzle systems. The behavior however

is strongly dependent on the definition of the spray angle. This is confirmed by experiments in the constant volume combustion chamber, conducted in this work, as shown in Fig. 5.4. The spray angle defined by Siebers shows significantly higher values and an overshoot in spray angle at early injection times.

- The ambient air is at rest (initial velocity = $0 m/s$): the movement of the ambient air is negligible as confirmed by the experimental evaluation of the boundary conditions in chapter 3.
- The thermal inertia differences between the fuel mixture components is ignored (at each time and each position the mixture is homogeneous).
- The injected jet is considered to be fully turbulent. This justifies the use of a uniform injection profile.

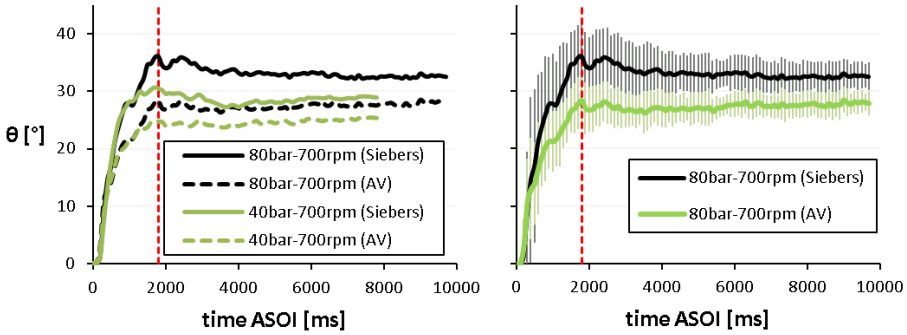

Figure 5.4: The spray angle for diesel defined in two different ways as mentioned in chapter 4: the Siebers angle (Siebers) and the averaged local spray angle (AV). The vertical lines in the right graph represent the standard deviation of the different experiments while the solid lines are the average value

5.3.2 Derivation

The model derivation is summarized in this section. A detailed derivation can be found in appendix B. The vaporizing spray model can be divided in three parts:

- the liquid core (core of only liquid, with vapor-liquid surroundings)
- the vaporizing spray (vapor-liquid equilibrium)
- the vaporized spray (only vapor)

Figure 5.5 gives a visual representation of the three parts which will be separately explained further on.

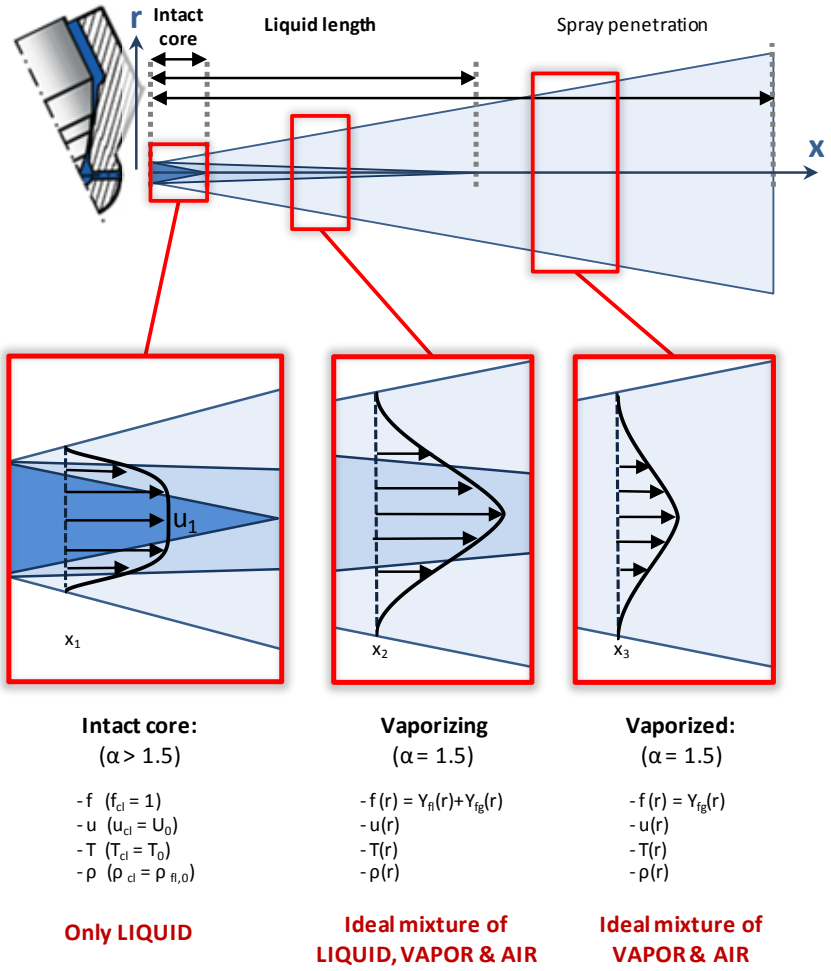

Figure 5.5: Schematic representation of the phenomenological model as proposed in this work, with the use of the radial profiles of Musculus et al. [141, 142]

The set of equations to be solved are the mass conservation for the fuel given by Eq. 5.24 and the spray momentum conservation equation Eq. 5.25. The conservation of energy gives the same result as the mass conservation since *Le* is taken equal to 1.
The conservation equations are of the form:

$$-\frac{\delta}{\delta x}\left[\int_0^\infty \rho\,(x,r,t)\,q\,(x,r,t)\,u\,(x,r,t)\,dV\right] = \frac{\delta}{\delta t}\left[\int_0^\infty \rho\,(x,r,t)\,q\,(x,r,t)\,dV\right] \tag{5.19}$$

With $q = f$ for the conservation of mass, $q = u$ for the conservation of momentum and $q = h$ for the conservation of energy. The radial distributions are defined as Gaussian-like:

$$\begin{aligned} f &= f_{cl}\left(1-\zeta^{\alpha}\right)^2 \\ &= \frac{(\alpha+1)(\alpha+2)}{\alpha^2}\overline{f}\left(1-\zeta^{\alpha}\right)^2 \end{aligned} \tag{5.20}$$

$$\begin{aligned} u &= u_{cl}\left(1-\zeta^{\alpha}\right)^2 \\ &= \frac{(\alpha+1)(\alpha+2)}{\alpha^2}\overline{u}\left(1-\zeta^{\alpha}\right)^2 \end{aligned} \tag{5.21}$$

$$\begin{aligned} h &= h_{cl}\left(1-\zeta^{\alpha}\right)^2 \\ &= \frac{(\alpha+1)(\alpha+2)}{\alpha^2}\overline{h}\left(1-\zeta^{\alpha}\right)^2 \end{aligned} \tag{5.22}$$

with $\zeta = r/R$ and $\overline{q}$:

$$\begin{aligned} \overline{q} &= \frac{\int q.dA}{dA} \\ &= \frac{\alpha^2}{(\alpha+1)(\alpha+2)}\, q_{cl} \end{aligned} \tag{5.23}$$

Discretization of Eq. 5.19 leads to the expressions Eq. 5.24 and Eq. 5.25.

$$A_f\left(\overline{u}_{i+1}^{j+1}\overline{f}_{i+1}^{j+1}\right) + B_f\overline{f}_{i+1}^{j+1} + C_f = 0 \tag{5.24}$$

with $\overline{u}$ and $\overline{f}$ the cross sectional average value of the axial spray velocity and the fuel fraction respectively.
This is the main difference compared to the model of the Valencia group where the equations are solved to the conservation parameters on the spray axis (u_{cl}, f_{cl}).
The advantage of this approach is the more smooth and realistic transition from the 'liquid core' to the steady state region of the spray. No concern about axial velocities u_{cl} and fuel fractions f_{cl} is required; the average values can only decrease since the same profiles are used for the entire spray. Figure 5.6 illustrates this statement. The average fuel fraction f_{av} and the axial fuel fraction f_{cl} are plotted along the spray axis x. The relation between f_{av} and t_{cl} is determined by the shape factor as was given in Eq. 5.23. This also implies that the shape factor α is completely determined by the fuel fraction and can be considered as a state parameter, calculated independently of the spray dynamics: α is not a tunable spray parameter.

$$A_u\left(\overline{u}_{i+1}^{j+1}\right)^2 + B_u\overline{u}_{i+1}^{j+1} + C_u = 0 \tag{5.25}$$

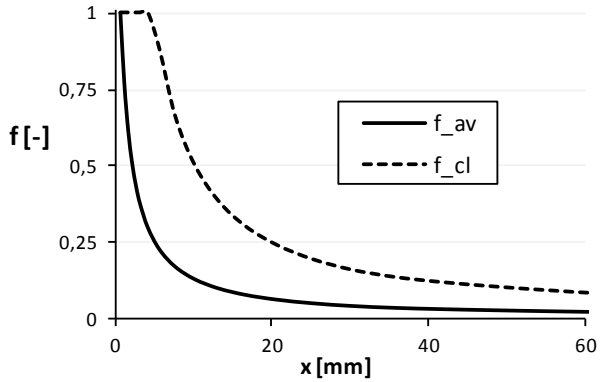

Figure 5.6: Illustration of the difference between f_{av} and f_{cl} along the spray axis x

The parameters A_u, B_u and C_u become as listed in table 5.1.

A_u	$2\pi {x_{i+1}}^2 F_{i+1}^{j+1}(2)$
B_u	$\pi \frac{\Delta x}{\Delta t} {x_{i+1}}^2 F_{i+1}^{j+1}(1)$
C_u	$\pi \frac{\Delta x}{\Delta t}\left({x_i}^2 {u_{cl}}_i^{j+1} F_i^{j+1}(1) - {x_{i+1}}^2 {u_{cl}}_{i+1}^{j} F_{i+1}^{j}(1) - x_i^2 {u_{cl}}_i^{j} F_i^{j}(1)\right)$ $-2\pi x_i^2 {u_{cl}}_i^{j+1} F_i^{j+1}(2)$
A_f	$2\pi {x_{i+1}}^2 F_{i+1}^{j+1}(2)$
B_f	$\pi \frac{\Delta x}{\Delta t} {x_{i+1}}^2 F_{i+1}^{j+1}(1)$
C_f	$\pi \frac{\Delta x}{\Delta t}\left({x_i}^2 {u_{cl}}_i^{j+1} F_i^{j+1}(1) - {x_{i+1}}^2 {u_{cl}}_{i+1}^{j} F_{i+1}^{j}(1) - {x_i}^2 {u_{cl}}_i^{j} F_i^{j}(1)\right)$ $-2\pi {x_i}^2 {u_{cl}}_i^{j+1} F_i^{j+1}(2)$

Table 5.1: Parameters for the equations of momentum and mass conservation

with

$$F_{i+1}^{j+1}(k) = \int_0^1 \rho\left(x_{i+1}, \zeta, t^{j+1}\right) \frac{(\alpha+1)(\alpha+2)}{\alpha^2} \left(1-\zeta^{\alpha}\right)^{2k} \zeta d\zeta \tag{5.26}$$

Liquid core

Near the nozzle it is reported by several authors [89] that a liquid core exists. This is considered as the length that is required to break-up the spray. Some models mention this as a 'break-up length' and the time needed, the 'break-up time' (e.g. t_b in the model of Hiroyasu in section 5.2.1). For modern high pressure diesel injections, the jet at the nozzle outlet can be considered as fully turbulent, so a uniform injection velocity and mass fraction profile can be assumed. Further

downstream, the profiles become Gaussian-like distributed as is confirmed by both modelers and experimentalists [124, 142]. In order to create a smooth transition, the proposed distribution is used. The uniform profile is approximated with the shape α approaching infinity while the Gaussian-like distribution is found for α equal to 1.5. As a result, the liquid core exists until an average value $\overline{f}$ (with $\alpha = 1.5$ and $f_{cl} = 1$) is reached, which corresponds to a corresponding average fuel fraction:

$$\begin{aligned} \overline{f} &= f_{cl}\,\frac{\alpha^2}{(\alpha+1)(\alpha+2)} \\ &= 1\,\frac{1.5^2}{(1.5+1)(1.5+2)} \qquad (5.27) \\ &= 0.257 \qquad (5.28) \end{aligned}$$

for $\overline{f}$ higher than 0.257, α is higher than 1.5, approaching infinity for $\overline{f} = 1$ and is found as the solution of Eq. 5.29.

$$(\overline{f}-1)\alpha^2 + 3\overline{f}\alpha + 2\overline{f} = 0 \qquad (5.29)$$

Figure 5.7 shows how the shape factor changes and the link between f_{cl} and $\overline{f}$ (or f_{av} as denoted in the figure). The dashed vertical line represents the end of the liquid core.

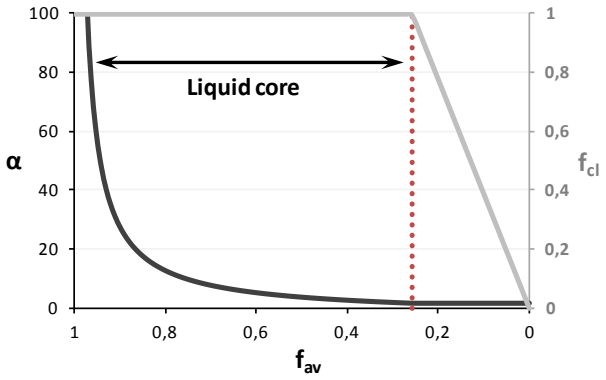

Figure 5.7: The shape factor α as a function of the fuel fraction f (black) and the relation between f_{cl} and f_{av} (= $\overline{f}$) (grey)

Vaporizing spray

In this part, the spray is considered as completely atomized, homogeneous and the Gaussian-like profile assumption with a constant shape factor of 1.5 is valid. The fuel fraction and velocity can be calculated as proposed by Eq. 5.24, Eq. 5.25

and table 5.1. The end of the 'vaporizing part' is determined by the hypothesis of thermal equilibrium of the spray. The vapor fraction (Eq.=5.30) will increase untill it reaches a value of 1. This is the point at which the liquid length is reached. The vapor fraction Y_{fv} is calculated by Eq. 5.30

$$\phi = \frac{1-f}{f}\frac{M_f}{M_a}\frac{P_{sat}}{P_a - P_{sat}} \tag{5.30}$$

with M_a, the molar weight of air and M_f, the molar weight of the fuel.
Due to the decoupling of the thermodynamics and the dynamics, the fuel fraction at total evaporation is independent of the spray characteristics.

Vaporized spray

The vaporized spray only exists of fuel vapor and entrained air. Also here, the same set of equations as for the vaporizing spray is resolved. The difference is in the calculation for the state parameters. The vapor fraction ϕ that was calculated for the vaporizing spray according to Eq. 5.30, is in this case taken to be 1 since all fuel is vaporized.

Finally, a schematical overview of the model is shown in Fig. 5.8, which is basically the adapted version of the one found in Pastor *et al.* [132].

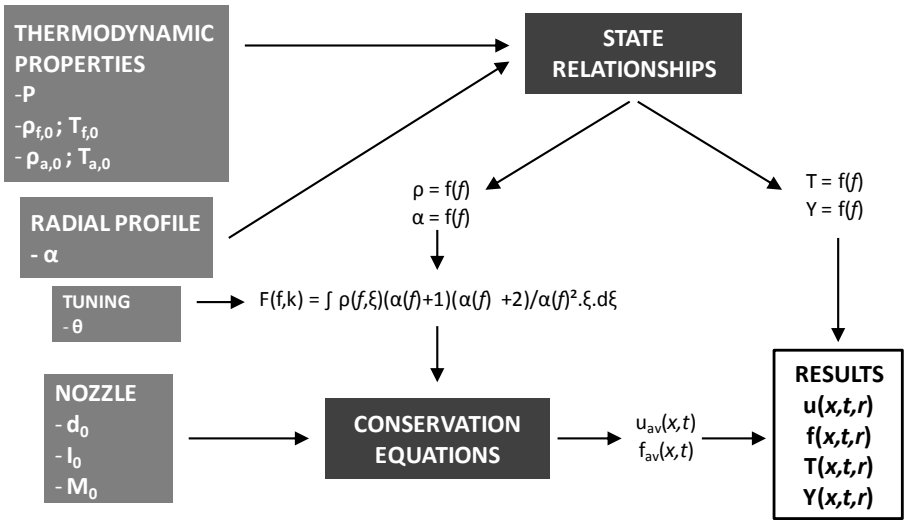

Figure 5.8: Schematical overview of the spray model implementation

5.4 Inputs and boundary conditions

5.4.1 Introduction

Apart from the modeling of the processes themselves, the choice of the boundary conditions has important issues as well. The most important challenge for the comparison between models and experiments is the translation of the boundary conditions from the experiments to the modeling inputs. Several reasons contribute to this problem:

- Not all parameters needed for the model input can be measured in experiments: e.g. injection pressure in the nozzle tip.
- Modeling simplifies a lot which sometimes cannot be achieved (enough) in the experiments: e.g. ambient velocity of $0 m/s$.
- There is no unambiguous definition or measuring method for certain parameters or the translation to the model is lacking: e.g. no standard definition exists for the spray angle.
- The model and measured parameters should match: e.g. there is no point to require the droplet size distribution as an input if this cannot be measured or validated in the experiments.

This section discusses the problems and proposals in terms of boundary conditions of the current application.

5.4.2 Ambient gas properties

The inputs to the spray for the ambient gas properties were taken as the average properties measured or set in the spray experiments. These involve ambient pressure and the gas mixture composition. From this information both ambient temperature and density can be derived as was discussed in chapter 3 and were calculated as described in chapter 4.
The variation or spacial distribution (such as ambient temperature distribution) and its influence on the model will be evaluated in section 5.6.

5.4.3 Spray angle

The initial spray angle is obtained from the image processing after averaging experiments under the same conditions. The image processing for the spray angle was discussed in detail in section 3.3. The average spray angle is used and the standard deviation provides a window in which the spray angle can be changed or tuned in the model to fit the modeled liquid length with the experiments. The strategy was also used by the Valencia group [89, 132].

The most reliable definition for the spray angle obtained from experiments is the Siebers angle since this is the angle of the steady state part of the spray. The model considers the spray as symmetrical cone where the angle can be considered as similar to the angle from the steady state part of the spray.

5.4.4 Injection velocity

The injection velocity could not be directly measured but is considered to be linked with the injection pressure according to Eq. 5.31.

$$v_{inj}(t) = C_d \sqrt{2\frac{P_{needle}(t) - P_a}{\rho_f}} \tag{5.31}$$

with P_a the ambient pressure, P_{needle} the pressure at the needle and C_d the discharge coefficient. The pressure P_{needle} can not be directly measured and should be estimated based on the pressure P_{inj}, measured in the injection pipe. According to simulations of the manufacturer of the injectors, the pressure difference between P_{inj} and P_{needle} should not be more than $2MPa$ at the highest mass rate. This corresponds with an error for the injection velocity of 4% at the theoretical needle opening (= $27.5MPa$) and 1% at peak pressures of $100MPa$, which is reasonable in terms of accuracy. For this reason, P_{inj} can be taken as the pressure at the needle.
The discharge coefficient C_d is taken to be constant and is tuned for one point in the injection profile.
A speed of sound correction is done to account for the pressure wave delay in the fuel with temperature T_f in the nozzle according to Eq. 5.32

$$c = \sqrt{\frac{B(T_f)}{\rho(T_f)}} \tag{5.32}$$

with $B(T_f)$ the bulk modulus at fuel temperature T_f.
The injection pressure profile is shifted over α crank angles, with a length L between the pressure sensor and nozzle:

$$\alpha = \frac{2\pi 60}{\text{rpm}} \frac{L}{\sqrt{\frac{B(T_f)}{\rho_f(T_f)}}} \tag{5.33}$$

with *rpm* the rotation speed of the camshaft. The time steps in the model are chosen to be a multiple of the time step of the experiments. This time step multiple depends on the maximum value of the injection velocity $v_{inj}(t)$ and the position step $\triangle x$ in such way that the CFL condition is fulfilled for the discretization in the calculations:

$$\triangle t < \frac{\triangle x}{\max\left(v_{inj}(t)\right)} \tag{5.34}$$

Finally, the velocity array model input $U_0(t)$ is constructed by interpolating between 2 values of the $v_{inj}(t)$ values with time step Δt.

5.5 Limitations

Using the spray angle as an input for the model is a strong limitation. A first estimation for the value is extracted from experiments, but is further tuned till the liquid length matches with experiments. A justification for this action is the high deviation of the spray angle in experiments (as mentioned in chapter 6) and the difficulty to find a standardized definition. The influence of the spray angle is tackled in section 5.6.

In experiments with injection of a viscous fuel, it is noticed that the fuel droplets are significantly bigger than for diesel or its surrogates. This might cause problems for the prediction of the viscous bio-fuels with the current model. Whether the Gaussian-like profile as proposed in the model is still valid for those fuels is not yet clear.

The fuel is considered as a homogeneous mixture. Real fuels consist of a range of different sized molecules which results in a unique behavior. This model requires a surrogate to approach the most important properties for this application. The choice of a single- or limited multi-component surrogate might lack matching several other properties. This discussion is continued in chapter 6.

5.6 Sensitivity analysis

5.6.1 Grid dependency

Modelers are very familiar with the influence of the grid size on the results. Even in this model a choice needs to be made concerning the spatial and time grid size. The performance of the model has been evaluated for a constant grid, as well as for a variable grid as is discussed more in detail in appendix B. A summary of the results of the analysis can be found in Fig. 5.9 for the fuel fraction f_{cl} for some different grid sizes, with a constant time step and constant injection velocity. The realized reduction of the resolving time in the case of the triangles ($x_{i+1} = x_i + dx$, $dx = 0.2mm$) and the black diamonds ($x_{i+1} = x_i + 2(x_i - x_{i-1})$) was in the order of more than 20, without significant change in values for the fuel fraction along the spray axis. The same conclusion could be made about the other parameters such as the velocity u_{cl}, temperature T_{cl} and mixture density ρ_{cl}. Further downstream, where the grid becomes coarse, some deflection might occur. This can be seen especially in the spray temperature at the left of Fig. 5.10. However, for the time

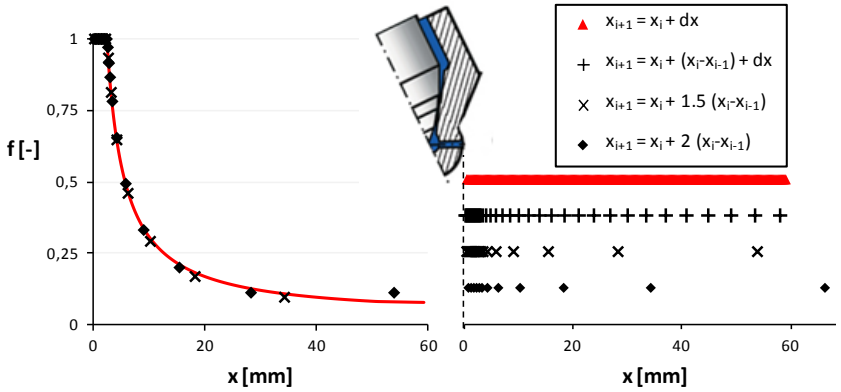

Figure 5.9: Evaluation of the grid dependency on the fuel fraction f (left). At the right the grid variation is shown.

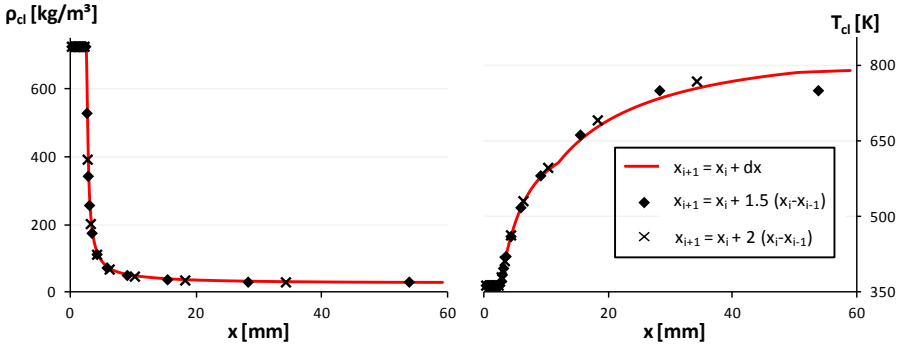

Figure 5.10: Grid dependency for the mixture density ρ_{cl} and temperature T_{cl}, for a constant time step and constant injection velocity

resolved spray penetration the performance of the model decreases if the spatial grid size increases as illustrated in Fig. 5.11. The symbols represent the discrete grid positions while the solid lines provide a qualitative result of the spray penetration by connecting the calculated points with a smooth line.
If the grid size increases too fast (as in $x_{i+1} = x_i + 1.5(x_i - x_{i-1})$ and $x_{i+1} = x_i + 2(x_i - x_{i-1})$) the spray penetration is underpredicted whereas the shape might differ as well. On the other hand, comparison with the small constant grid of $0.2mm$ and situation $x_{i+1} = x_i + (x_i - x_{i-1}) + dx$ confirms that the grid is allowed to increase along the spray axis.

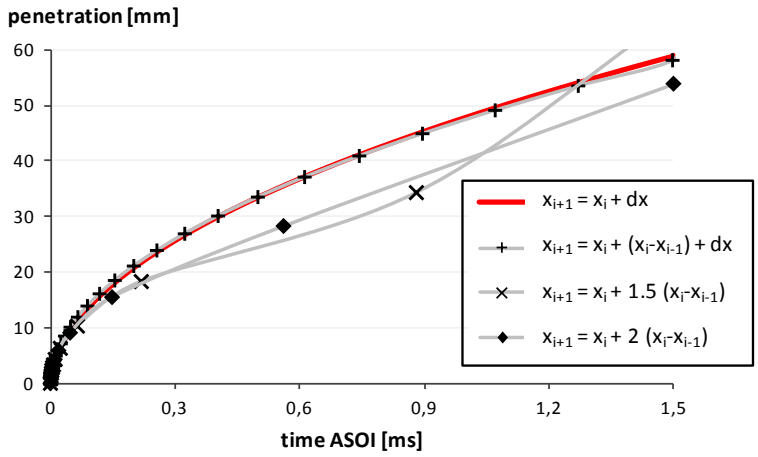

Figure 5.11: Grid dependency for the spray penetration, for a constant time step and constant injection velocity

5.6.2 Influence of the spray angle

Since the spray angle is the only tuning parameter, the model's sensitivity to its value is important to consider. For a change of 10% in the spray angle, a change of approximately 10% is found for the liquid length as demonstrated in Fig. 5.12. This is somewhat the interval for the standard deviation obtained with the experiments. Here, the test case as found in Payri *et al.* [132] is used.

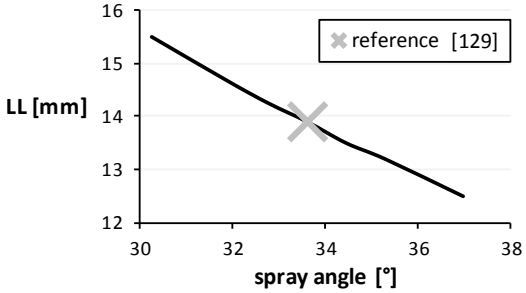

Figure 5.12: Sensitivity of the model for cetane with changing spray angle. The cross marker represents the reference case as used by Pastor et al. [132] (spray angle = 33.6°)

5.6.3 Variable ambient temperature

The ambient temperature is the driving force for evaporation and ignition. Since in real engines and experimental setups ambient temperature gradients exist, it is

important to investigate the sensitivity of the model to the local change in temperature. Temperature gradients due to active air motion, such as tumble and swirl as they exist in engines, are difficult to take into account for this simplified modeling strategy. Instead, the gradient caused by natural convection to the walls is considered: the thermal boundary layer. For the spray, this will be the worst case scenario: cold ambient temperatures near the nozzle and the core temperature downstream. The thermal boundary layer in either engines or constant volume combustion chambers is considered to be dominated by convection rather than conduction.
This is the main motivation to describe the thermal boundary layer as an exponential function [143] as described by Eq. 5.35 (with $T_{a0}(x)$ the ambient temperature at position x from the wall; δ, the thickness of the thermal boundary layer). The thickness δ is defined as the position at which 99% of the core temperature is reached (indicated by the factor 0.01 in Eq. 5.35).

$$T_{a0}(x) = T_{wall} + (T_{core} - T_{wall})\left(1 - e^{ln(0.01)x/\delta}\right) \tag{5.35}$$

The thickness of the thermal boundary layer is very hard to obtain in a real engine and no reliable data are published in literature. Several authors [122, 143], however, have made attempts to measure the temperature distribution in optically accessible combustion chambers with fast responding thermocouples. They all agree that the core-bulk temperature difference is about 2 to 8%.
The implementation of a changing ambient temperature is very time consuming for the resolving process since for every different ambient temperature the state relations need to be recalculated. Equation 5.35 was discretized in steps of $10K$, starting from a wall temperature of $600K$ which is a realistic temperature in diesel engines and $900K$ as the core temperature.

Simulations were performed with thermal boundary thicknesses ranging from 0 to $40mm$. Results with 0, 20 and $40mm$ are displayed in Fig. 5.13. The results for cetane (surrogate for diesel cfr. section 6.2) and methyl decanoate (MD) (surrogate for biodiesel cfr. section 6.3) are presented. The other fuels give similar results and for this reason are discarded from the graphs. The results show that the used model is not affected significantly by thermal boundary layers smaller than $30mm$ in terms of liquid length and spray penetration. For thicker boundary layers, the liquid length increases significantly while the spray penetration stays relatively similar. The latter is mainly the result from the fact that the spray penetration is dominated by the spray momentum and dispersion. The dispersion is included by the spray angle and was the same for each simulation case as was the spray momentum. A similar conclusion can be taken from Fig. 5.14 for the spray temperature on the spray axis T_{cl}. The influence is however slightly bigger than in the case of the fuel fraction since the ambient temperature has an important impact

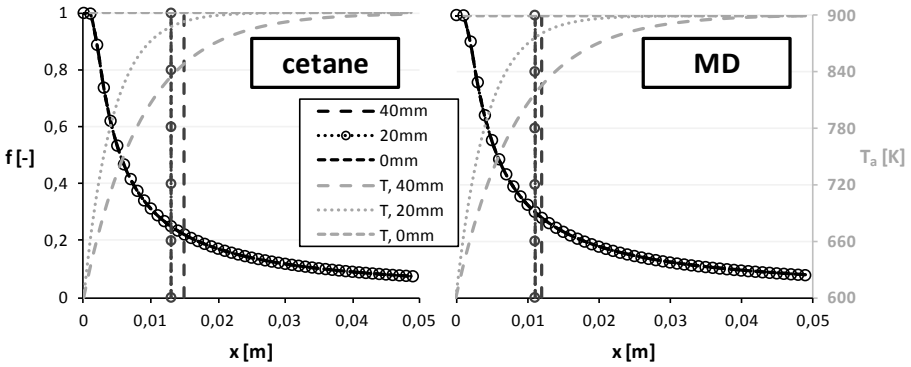

Figure 5.13: Behavior of axial fuel fraction f_{cl} on a thermal boundary layer with the described model. The vertical lines represent the corresponding liquid length

on the overall spray temperature. For boundary layers smaller than 30*mm* this effect is smaller than the measurement error or cyclic variation and can be ignored. As a conclusion, the calculation effort to account for temperature gradients in the

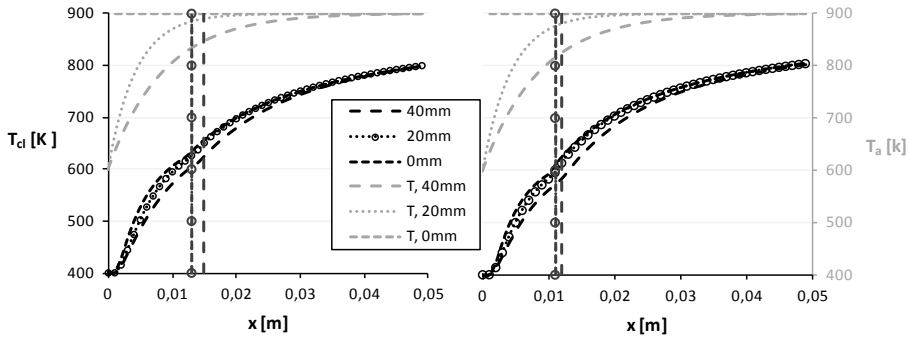

Figure 5.14: Behavior of axial spray temperature T_{cl} on a thermal boundary layer with the described model. The vertical lines represent the corresponding liquid length

combustion chamber in the case of a simplified model will not give more information. The spray angle has a much more significant influence on liquid length. The behavior of the model for the boundary layer is similar to the influence of the fuel temperature in the current form of the model: fuel temperature will dominate the atomization due more to the temperature dependence of the viscosity, bulk modulus and surface tension. However this atomization information is included in the spray angle, which is input for the model. Evaporation on the other hand, will be more dominated by the ambient temperature as was investigated in this section (cfr. Fig. 5.13).

5.6.4 Variable injection velocity

The fuel pressure delivered by a pump-line-nozzle system varies over time and results in a time varying fuel injection velocity. This is the motivation to study the effect of the model for variable injection pressures. As a validation of the model, 3 simple injection velocity profiles are applied as was done by Pastor *et al.* [132]. Figure 5.15 shows that the decreasing velocity is closest to the constant velocity profile; the penetration is dominated by the velocity of the intial droplets. According to the model, droplets (or fuel mass) are not able to overtake one another. As a result preceding fuel can only be pushed forward. This is also the case for the increasing profile. In reality this is not true: faster droplets will push the droplets away, but mostly along the radial direction. This effect is bigger for areas with stronger velocity difference. This is especially the case further downstream the nozzle and near the spray boundary. The best example of this phenomenon is the head vortex of the spray, where the droplet velocity becomes so slow that the resistance of the ambient gases easily makes the droplets change direction.

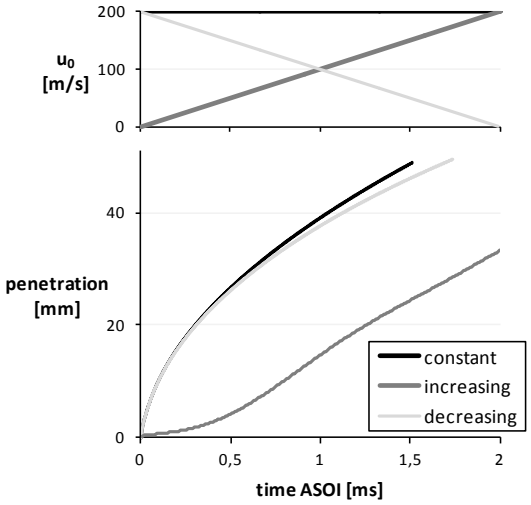

Figure 5.15: Penetration as a function of time (lower graph) for 3 different injection velocity profiles (upper graph) similar as by Pastor et al. [132]

The model can be tested for the experiments with the time varying injection pressure. A qualitative result of the model behavior on the experimentally obtained injection pressure is shown in Fig. 5.16. The boundary conditions for both cases were taken to be equal (even the spray angle θ), except for the injection velocity profiles which are represented at the top of the figure. The constant injection velocity (black line) is the average value of the time varying profile (grey line). There is

a significant difference in spray penetration development which can be explained as above. The slower injection speed at early injection timing slows down the initial penetration. Near the end of the injection, the penetration tends to decrease the penetration gap, due to the higher injection velocity at later time instants.

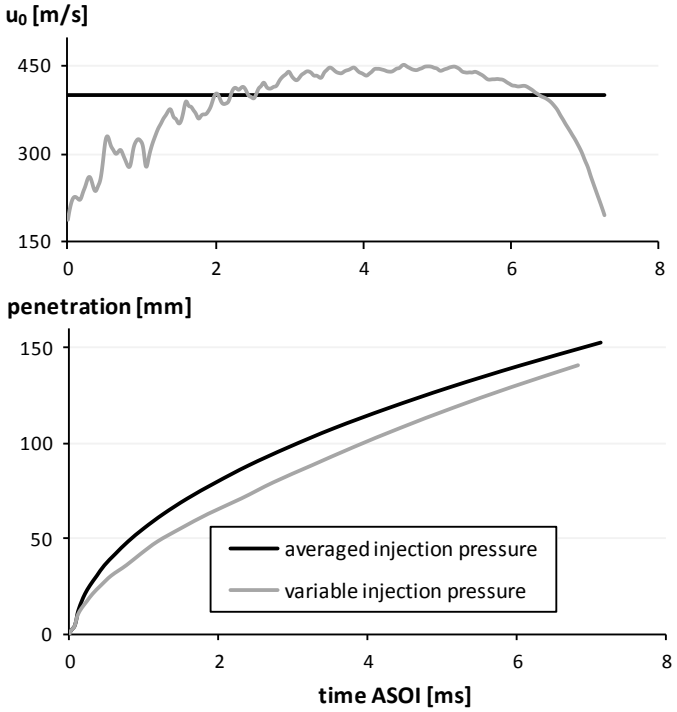

Figure 5.16: Qualitative influence of the injection velocity based on the experimentally measured injection pressure (black line) and its average (grey line)

5.7 Summary

Several strategies to model a certain phenomenon can be applied, depending on the application and modeling goals.
This research project focuses on the design and modification of a submodel for a complete power-train simulation. Phenomenological models seem to be a good trade-off between very simple thermodynamical or 0D-models and the expensive CFD models, while still providing enough details necessary to make the distinction between different fuels.
The most common phenomenological models are described. The strategy of the model of the Valencia group [132], using Gaussian-like profiles for the fuel frac-

tion f, axial velocity u and spray enthalpy h as proposed by Musculus & Kattke [141] seems to be the most valuable for this research goal. The model will be further validated in the next chapters.

6
Surrogate fuels

"A theory is something nobody believes, except the person who made it.
An experiment is something everybody believes, except the person who made it."

- Albert Einstein -

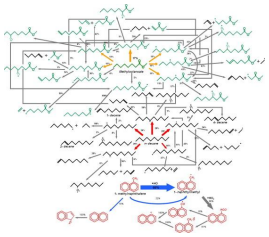

The chapter is organized as follows: the introduction of surrogates is motivated, followed by a brief overview of diesel and its commonly used surrogates. A similar approach is followed for bio-diesel. The behavior of the different properties of the surrogates are validated by using the spray model as described in chapter 5.
With the project goal in mind, an overview of straight oils and their performance as diesel fuel is given. Finally some comments concerning surrogates and potential target properties are made.

6.1 Introduction & Motivation

Real fuels are complex mixtures of different molecules. Furthermore, the composition can change with the origin and batch of the fuel. This makes it very difficult to model the injection and combustion process or to understand completely the spray dynamics. The main idea of the introduction of surrogate fuels is to approximate the real fuel for a certain application. The surrogate can be chosen to fulfill 2 different tasks:

1) The surrogate represents the fuel as a pure mixture of a small amount of known components and can be used in real experiments in order to better understand the processes.

2) The surrogate can be an artificial mixture of a small amount of molecules with spray relevant properties, tuned to match the real fuel. This latter is usually only used for modeling purposes to reduce the complexity and resolving time.

For the case of powertrain calculations, one is usually interested in the fuel consumption, power output and emission of soot, UHC, CO and NOx. The choice of the ideal surrogate should give the same results for these parameters as what would be obtained with the original fuel. The difficulty of this task has been mentioned by several researchers and before denoting a surrogate, the spray and combustion behavior need to be understood. When using real components as a surrogate, they are selected based on the available detailed property information. It is noteworthy that for most (spray relevant) properties no significant pressure dependence is found.
The advantage of choosing well-known molecules as a substitute for diesel is that the detailed chemical kinetics can be used in 3D simulations while this cannot be done in a reliable way when using a standard diesel fuel, since too many complex components are involved. Another motivation to use well-known molecules over a fictitious diesel fuel is that direct comparison between the modeling and experiments can be done with this surrogate. In this way, the physics of the spray process can be directly studied and understood.
In lots of simple spray combustion models only single-component surrogates are used. The big limitation of such choices is the small degree of freedom to match properties with diesel.

A lot of basic knowledge is already available from literature concerning the spray and combustion processes. Some important findings are summarized in the following sections which will be important for the choice of a certain surrogate (mixture).

6.2 Diesel & surrogates

Diesel is a mixture of hydrocarbons of which the composition depends on the place of origin, standards and production process and consequently has complex reaction kinetics. In general, the basic composition of diesel [144] consists of:

- iso-paraffins (25-50%): slightly branched containing only one or two methyl substitutions on a long C10-C24 chain

- cyclo-paraffins (20-40%): primarily 1-ring cyclo-hexanes with multiple alkyl side-chains; 2-ring and larger cyclo-paraffins are usually present at levels less than 5% of the total fuel.

- aromatics (15-40%): primarily 1-ring analogues, such as alkylbenzenes, with substituted 2-ring aromatics (naphthalenes). Naphtho-aromatics and larger 3-ring cyclo-paraffins and aromatics can also be present in diesel.

The wide range of hydrocarbon lengths (C10-C24) makes it hard to predict the evaporation process; a boiling range (190-300$^{\circ}C$) is usually defined instead of a single boiling point as is the case for single component fuels. Several experimental investigations [93, 145–148] have employed surrogate diesel fuels, but in the few studies where measured (surrogate and real diesel) and computed (surrogate only) results have been compared, the selection methodology for the surrogate composition and the measures taken to validate the chemical kinetic models are usually not discussed in detail, and the range of operating conditions used is often small [144].

Surrogates are selected based on one or a few chemical and physical properties, relevant for the spray and combustion process, which are matched to the target fuel. Important properties that are desired to meet those of diesel include chemical composition (determines strongly the combustion species and emissions), surface tension, viscosity, vapor/liquid equilibrium, distillation trajectory, molecular and thermal transport properties,... Moreover, most properties vary with temperature and pressure, suggesting that this dependency should fit as well. A surrogate that would cover all the chemical and physical properties of the fuel, would likely require more components than can be handled in current computational codes. For this reason the surrogate composition needs to be limited.

Surrogate fuels for spray combustion are usually single component liquids or mixtures of a few simple molecules. A common choice is n-heptane, preferred for its comparable cetane number (about 55), according to European and Japanese diesel standards [144]. Additionally, detailed chemical-kinetic mechanisms for low-, intermediate- and high-temperature n-heptane oxidation are available. Others are using hexadecane (or cetane, $C_{16}H_{34}$) or n-dodecane ($C_{12}H_{26}$) in order

to obtain a high density ratio, similar to diesel engine sprays [132]. Stralin and Wahlin [149] use n-dodecane for its high boiling temperature characteristics, comparable to diesel.

However, some difficulties exist in selecting a suitable surrogate fuel. For surrogates with comparable cetane number, the ignition position and combustion temperature might not match for a wide range of relevant diesel engine operation conditions and may differ since the first stage (low temperature) heat release will exhibit a different dependence on temperature and pressure. Key factors are the multi-component composition of diesel and different oxidation kinetics. For example, short molecules are more likely to vaporize first [114] and aromatic hydrocarbons are more likely to delay ignition [150]. The difference in hydrogen/-carbon (H/C) ratio, molecular structure and thus, local mixture fraction will reflect in differently predicted emission formation. The H/C-ratio can be readily matched with a single-component surrogate, however the similarity of the combustion behavior cannot be guaranteed. Dryer *et al.* [151] showed that the C/H ratio affects the flame temperature, heat of reaction, flame speed, and local air/fuel stoichiometric location.

Improvements can be made by using a multi-component surrogate. Puduppakkam *et al.* [152] matched properties of their surrogate mixture, such as, lower heating value, C/H ratio, distillation curve and ignition quality, to be in the target fuel range. From experiments, Pitz *et al.* [153] found that the ignition delay times are very similar for large n-alkanes (C7 - C16), indicating that the choice of the alkane length in the surrogate probably has a minor influence on the ignition delay. It should be noted that these shock tube experiments were performed at relatively low initial pressures (1.2-1.7MPa). The main motivation for Huber *et al.* [154] to incorporate iso-alkanes was the ability to better match the thermal conductivity of the surrogate fuel to that of diesel.

From experimental investigation one usually concludes that the emission prediction is insufficient. The main reason is that oxidation kinetics are strongly influenced by the relative amounts of aromatics, cyclo-paraffins and iso-paraffins. This was the main motivation for Gustavsson *et al*. [155] to add toluene to n-heptane. Iso-paraffins such as iso-cetane (= 2,2,4,4,6,8,8-heptamethylnonane) can be added, due to its low reactivity, to balance the ignition properties of high reactivity components, like n-alkanes [153]. Because of its use as a primary reference fuel, iso-cetane is readily available to experimentalists in high purity at relatively low cost.

Natelson *et al*. [156] modeled diesel by using a mixture of (1:1:1) n-decane, n-butylcyclohexane and butylbenzene to approach the average hydrocarbon compo-

sition and reactivity of the surrogate, while Peters *et al*. [157] proposed a mixture of 70*vol%* of n-decane and 30*vol%* methylnaphthalene for the same reason, as well as to improve combustion similarity, such as pollutant formation and density. Comparable ignition delay and heat release from experiments in an optical engine were found between the two-component reference fuel and diesel. This popular surrogate mixture has been baptized as IDEA (Integrated Diesel European Action) by several researchers [158, 159].

As a conclusion, while engine experiments with surrogates are capable of providing much insight, they may not accurately reflect the combustion behavior of real diesel fuel; choices only based on physical properties might not be appropriate to predict the chemical processes. A more detailed overview of diesel surrogates can be found in the work of Farrell *et al.* [144] and Battin-Leclerc [150].

Some commonly used diesel surrogates with the motivation for choosing them are summarized in table 6.1 and schematically visualized in Fig. 6.1.

Surrogate	Formula	Ratio	Motivation	Ref.
cetane	$C_{16}H_{34}$	1	C/H-ratio	[89]
n-heptane	C_7H_{16}	1	CN	[160]
heptadecane	$C_{17}H_{36}$	1	volatility	[97]
n-heptane : toluene	C_7H_{16} $C_6H_5CH_3$	var.	combustion, ignition	[155]
n-decane	$C_{10}H_{22}$	1	C/H-ratio	[155]
n-dodecane	$C_{12}H_{26}$	1	volatility	[144]
n-decane : n-butylcyclohexane : butylbenzene	$C_{10}H_{22}$: $C_{10}H_{20}$: $C_{10}H_{14}$	1:1:1	C/H-ratio	[156]
n-decane : 1-methylnaphthalene	$C_{10}H_{22}$: $C_{11}H_{10}$	var.	boiling range CN, C/H-ratio	[144, 157]
n-octane	C_8H_{18}	1	CN	[146]
1-methylnaphthalene	$C_{11}H_{10}$	1	density, volatility	[161]
iso-cetane : cetane	$C_{16}H_{34}$: $C_{16}H_{34}$:	var.	CN	[153]
1-methylnaphthalene : cetane	$C_{11}H_{10}$: $C_{16}H_{34}$	var.	CN	[153]
n-decylbenzene	$C_{16}H_{26}$	1	ignition, combustion	[144]
methylcyclohexane	$C_{16}H_{34}$	1	soot	[144]
n-decane : n-propylbenzene	$C_{10}H_{22}$ C_9H_{12}	4:1	soot ignition	[162]
n-decane : n-butylbenzene : n-butylcyclohexane	$C_{10}H_{22}$ $C_{10}H_{14}$ $C_{10}H_{20}$	1:1:1	boiling range, C/H-ratio, CN	[156]

Table 6.1: summary of commonly used diesel surrogates

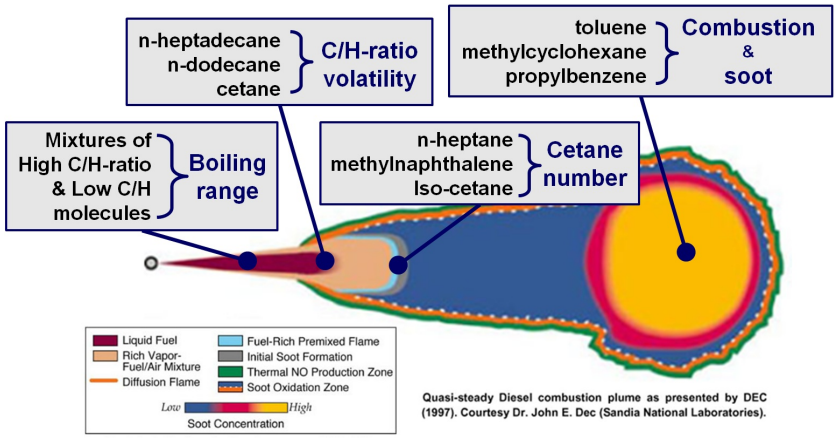

Figure 6.1: Commonly used surrogate components with indication of their specific influence in the spray

6.3 Bio-diesel & surrogates

Bio-diesel is a common alternative fuel for diesel and is already mixed with diesel in low percentages. Bio-diesel is the result of the transesterification of oils and fats (= triglyceride molecules). It is out of the scope of this work to provide an extensive overview of the origin, production and properties of bio-diesel. For that, the reader is referred to specialized literature such as [10].
Here, we focus on the link with surrogates and the motivation for their choice. As will become clear, several conclusions from this section will be important when considering surrogates for crude oils and fats.
Bio-diesel is composed of alkyl-esters of which the length depends on the oil or fat used in the transesterification process. The chemical reaction is schematically given in Fig. 6.2.
The chain length of the esters ranges from C12 (lauric acid) up to C24 (lignoceric). The abbreviations used throughout the text to indicate the most common fatty acids in oils are listed in table 6.2.

The alkyl-group is determined by the alkanol used during the transesterification process. Generally methanol up to butanol is used. The waste product from the process is glycerol ($C_3H_8O_3$) and can be found in small amounts in the fuel. Free fatty acids (FFA) as a result of the incomplete transesterification can also be contained in the fuel, but should be avoided in large amounts as it makes the fuel more acid and aggressive in terms of corrosion.

Bio-diesel contains oxygen molecules which will influence the combustion and

fatty acid	abbreviation	notation
lauric acid	La	C12:0
myristic acid	M	C14:0
palmitic acid	P	C16:0
stearic acid	S	C18:0
oleic acid	O	C18:1
linoleic acid	L	C18:2
linolenic acid	Ln	C18:3
arachidic acid	A	C20:0
eicosenoic acid	E	C20:1
benenic acid	B	C22:0
erucic acid	Er	C22:1
lignoceric acid	Lg	C24:0

Table 6.2: Most common fatty acid groups contained in bio-diesel with the notation Cxx:y, containing xx carbon atoms and y double bonds in each molecule

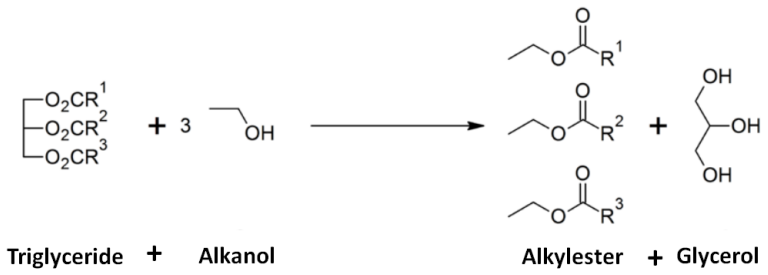

Figure 6.2: The transesterification process to produce bio-diesel (alkylester)

emission; Mueller *et al.* [163] pointed out the importance of the location and amount of oxygen in the fuel, especially concerning ignition delay and for the soot formation process. They state that the advantage of oxygen-bonds in the fuel is partially lost when ester-bonds (-O-(C=O)-) are present. In this case and especially at low temperatures, the oxygen is more inclined to directly form CO_2. In general, the fuel molecules that minimize soot formation are those where each oxygen atom is bonded to a different carbon atom. If not, the carbon chain is not broken and the radicals can form double carbon-carbon bonds at the place where

the oxygen atom has detached. Carbon chains with double bonds can more easily form acetylene (C_2H_2) and ethylene (C_2H_4) which are important soot precursors. Several studies show a linear decrease in engine-out soot with an increase in the mass fraction of oxygen in the fuel regardless of the type of oxygenate used where the reduction efficiency depends on the position of the oxygen atoms [164].

Other emissions such as NOx are also influenced by the nature of the fuel molecular structure. It was found by Gail *et al.* [165] that unsaturated methyl-esters produced higher NOx than fully saturated esters. Increasing the number of double bonds, quantified by the iodine number, was correlated with increasing emissions of NOx. Furthermore, the fatty acid chain length has an influence on the cetane number; the cetane number increases with fatty acid chain length, decreases with additional unsaturation in the fatty acid chain, and usually increases with alkoxy chain length. A sharp reduction in cetane number is noted between methyl oleate (CN = 59.3) and methyl linoleate (CN = 38.2). This is noteworthy because these acids can be predominant components in certain bio-diesels, e.g. methyl oleate in palm bio-diesel and methyl linoleate in soybean bio-diesel.

Several attempts have already been done in the past to take the properties of the bio-diesel into account. Due to the importance of the location and amount of oxygen, most authors [165–170] prefer esters as a surrogate. Common choices are methyl-butanoate ($C_5H_{10}O_2$, MB) [165, 167] and methyl-decanoate ($C_{11}H_{22}O_2$, MD) [166] or a mixture of both, since kinetic models are available and still reasonable in resolving time. The chain length of these surrogate fuels are significantly shorter than methyl-palmitate ($C_{17}H_{34}O_2$) up to methyl-arachidate ($C_{21}H_{42}O_2$), which are generally the main methyl-esters present in bio-diesel. This may lead to a lower reactivity than bio-diesel. According to Pitz *et al.* [170], this effect can be compensated for by adding a large n-alkane to MD or MB to increase the reactivity of the bio-diesel surrogate. However Gail and Thomson [165] suggest to use longer chain methyl esters since they found that methyl-butanoate does not reproduce well the negative temperature coefficient (NTC) behavior and early CO_2 formation of real bio-diesel fuels. Nevertheless, methyl-butanoate is potentially appropriate as a surrogate bio-diesel fuel for developing a better understanding of the reported bio-diesel soot suppression. Other bio-diesel surrogates that are proposed, involve mixtures of n-decane, 1-methyl-naphthalene and methyl-octanoate [168]. Golovitchev and Yang [169] used a mixture of methyl-butanoate, benzyl alcohol (C_4H_8O) and n-heptane (C_7H_{16}) as a surrogate for rapeseed methyl-ester (RME) to compensate for the C/O ratio. The vapor thermal properties were taken as those of the main methyl ester in RME which is methyl-oleate ($C_{19}H_{36}O_2$). The most common bio-diesel surrogates are summarized in table 6.3.

Surrogate	Formula	Ratio	Motivation	Ref.
methyl-butanoate	$C_5H_{10}O_2$	1	Combustion	[165, 167, 171]
methyl-decanoate	$C_{11}H_{22}O_2$	1	Combustion, better NTC	[166]
n-decane : 1-methyl-naphthalene : methyl-octanoate	$C_{10}H_{22}$: $C_{11}H_{10}$: $C_9H_{18}O_2$	var.	Volatility, ignition delay, combustion, C/O-ratio	[168]
methyl-butanoate : benzyl alcohol : n-heptane	$C_5H_{10}O_2$: C_4H_8O : C_7H_{16}	var.	Ignition delay, emissions, C/O-ratio	[169]

Table 6.3: summary of commonly used bio-diesel surrogates

Generally, some work has been done trying to model bio-diesel with acceptable results with the methyl ester kinetic model development to date, but there has been quite a limited focus on the specific role of the methyl ester functional group. As a result, these models occasionally over-predict the reactivity of methyl ester oxidation exhibiting shorter ignition delays and higher extinction limits of diffusion flames.

6.4 Surrogate spray prediction

Simplified spray models are very interesting due to their low required resolving time and simplicity. However this comes with a penalty: strong hypotheses and simplifications. As a consequence, the choice of the fuel properties might have a significant influence and needs to be considered when chosing the surrogate. The behavior of the different surrogates for diesel and bio-diesel is studied in this section using the earlier described spray model (cfr. chapter 5). The results use cetane as a reference as was done by the developers of the model [89, 132]. The boundary conditions for this numerical experiment are given in table 6.4. Taking into account the hypotheses of the model, the density, saturation pressure, critical condition and heat capacity (or enthalpy) are the fuel properties involved in the 1D-model.

θ	$33.6°$
D_0	$200\mu m$
x(0)	$\frac{D_0}{2.\tan(\theta/2)}$
$f_{cl}(0,0)$	1
$u_{cl}(0,0)$	$150m/s$
$T_f(0,0)$	$900K$
$T_a(0,0)$	$400K$
P_a	$8MPa$

Table 6.4: Initial conditions for the spray model, with D_0, the nozzle diameter

6.4.1 Surrogate properties

In order to understand the model behavior due to the used surrogate, the properties used in the model need to be compared. The data of the considered properties is obtained from the DIPPR database.
The critical pressure and temperature for the investigated surrogates are listed in table 6.5. Note that for every surrogate component both the critical pressure and temperature are exceeded by the ambient of $8MPa$ at $900K$ for the test case.

Some other important fuel properties are given in table 6.6 and are qualitatively compared with the target fuel (diesel and bio-diesel). The term "bio-diesel" refers to a general, unspecified bio-diesel, independent of the composition or origin.

The enthalpy difference between the different fuels was less than 20% (in most cases even less than 10%). As a consequence, these results provide no additional information and are not shown here.

The saturation pressure differs strongly among the surrogates, see Fig. 6.3 for the diesel surrogates and Fig. 6.4 for the bio-diesel surrogates. The saturation pressure mainly depends on the chain length and amount of double bonds: small molecules will evaporate faster than longer ones. This factor is expected to have a significant influence on the liquid length of the spray, since it is directly correlated with the vapor fraction:

$$Y_{fv} = (1-f)\,\frac{M_f}{M_a}\,\frac{P_{sat}}{P_a - P_{sat}} \tag{6.1}$$

With M_a, the molar mass of the ambient gases; M_f, the molar mass of the fuel; f the fuel fraction; P_a, the ambient pressure and P_{sat}, the saturation pressure of the mixture. Note that only the saturation pressure P_{sat} up to the critical point of the component should be considered; if the critical point is reached, only vapor exists and the saturation pressure is not used anymore in the calculations.

Component	T_c [K]	P_c [MPa]
cetane	723	1.40
heptane	540	2.74
octane	569	2.49
decane	617	2.11
heptadecane	736	1.34
toluene (tol)	592	4.11
methyl-naphthalene (MN)	772	3.60
methyl-butanoate (MB)	555	3.47
methyl-decanoate (MD)	687	1.94
methyl-oleate (MO)	764	1.28

Table 6.5: Critical condition for the used surrogate components for diesel (upper ones) and bio-diesel (lower ones)

The density for the different fuels differ less. The most significant difference is seen for methyl-naphthalene. However this component is mostly used in a mixture with other components.

6.4.2 Spray model results

The 1D model is implemented for different common diesel surrogates using the initial conditions as mentioned in table 6.4. Figure 6.5 presents the centerline spray velocity u_{cl} development as a function of the position on the spray axis and the centerline temperature T_{cl} as a function of the fuel fraction f. It should be noted that for most of these surrogates, the velocity development does not change significantly, while a strong difference is found for the liquid length. This can be explained by the difference in saturation pressure. The spray is assumed to be saturated at every position. The density of the fuel dominates the penetration (close to the nozzle, the fuel density; far from the nozzle the ambient density); spray angle, injection velocity and ambient conditions are taken the same in the different cases, which means that the momentum of the spray is driven by the spray density. A spray with low density will tend to decrease faster in speed than a higher density spray. As was noted and expected from section 6.4.1 penetration happens slightly faster for the surrogate mixture containing the higher density component methyl-naphthalene compared to the single component surrogate (100% decane).

surrogate	ρ **(293***K***)**	μ **(313***K***)**	**M**	**LHV**	**CN**	**H/C**
	[kg/m^3]	[mPa.s]	[g/mol]	[MJ/kg]	[-]	[-]
diesel #2	*830*	*2.5-4*	*200-233*	*45.0*	*50-55*	*2.0-2.2*
cetane	712	2.24	226.4	44.0	100	2.125
decane	730	0.70	142.3	44.2	76	2.200
heptane	684	0.34	100.2	44.6	53	2.286
heptadecane	777	2.65	240.5	43.9	105	2.118
toluene	867	0.46	92.1	40.5	0-4	1.143
MN	1020	2.08	142.2	39.4	0	0.909
octane	610	0.44	114.2	44.4	64	2.250
bio-diesel	*875-885*	*4.2-4.6*	*270-300*	*37.3-41.0*	*40-68*	*1.9-2.0*
MB	898	0.45	102.1	26.3	5	2.000
MD	872	1.45	186.3	34.1	52	2.000
MO	874	3.93	296.5	37.4	55-59	1.895

Table 6.6: Some fuel properties for the considered (bio)diesel surrogate components; with LHV, the lower heating value; CN, the cetane number; H/C, the hydrogen to carbon ratio

The same conclusion can be made for the heptane and heptane-toluene mixture. The temperature at each point of the spray is a complex function of the fuel fraction and fuel properties. This seems to result in a less significant difference than for the liquid length (*LL*) and fuel fraction at total evaporation (cfr. Fig. 6.6, with LL ranging from 5.8 to 15*mm* with the corresponding fuel fraction at total evaporation ranging from 0.46 to 0.25). A shorter liquid length is directly related to a higher fuel fraction due to the same spray angles.
Similar results are obtained for bio-diesel surrogates. Penetration is not significantly affected by the surrogate choice as shown in Fig. 6.7. The strong difference in vaporization properties however, show big differences in liquid length and the relation between the spray temperature and fuel fraction. Figure 6.8 summarizes again the liquid length, temperature and fuel fraction at the moment of total evaporation.

In chapter 5 it was found that the spray angle was an important tuning parameter. In the previous section, the spray angle was taken to be the same for each surrogate. This might actually not be entirely correct: the actual atomization (and for this reason the spray angle) will be influenced by the fuel properties as well.

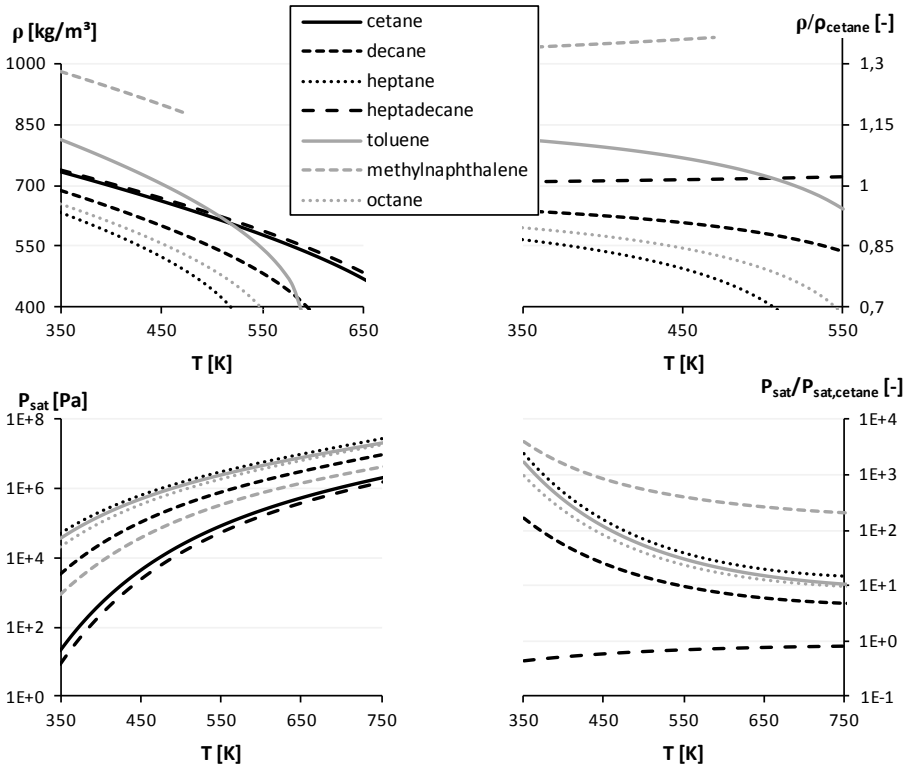

Figure 6.3: Liquid diesel surrogate properties density (upper) and saturation pressure (lower). Relative comparison to cetane is displayed at the right side

The spray angle was varied for each surrogate until the liquid length matched with the reference case cetane. From the results in Fig. 6.9, the difference in spray angle can be seen to be up to more than 50% compared to the reference surrogate. This suggests that only the surrogate heptadecane would be an acceptable alternative for a cetane spray in terms of liquid length. All the other surrogates give spray angle results that are outside the 10% standard deviation limits from experiments. Due to the model hypotheses, these results have significant consequences for the local mixture fraction and axial velocity, which deviate significantly from the cetane values and can be expected to affect the ignition, combustion progress and pollutant formation.

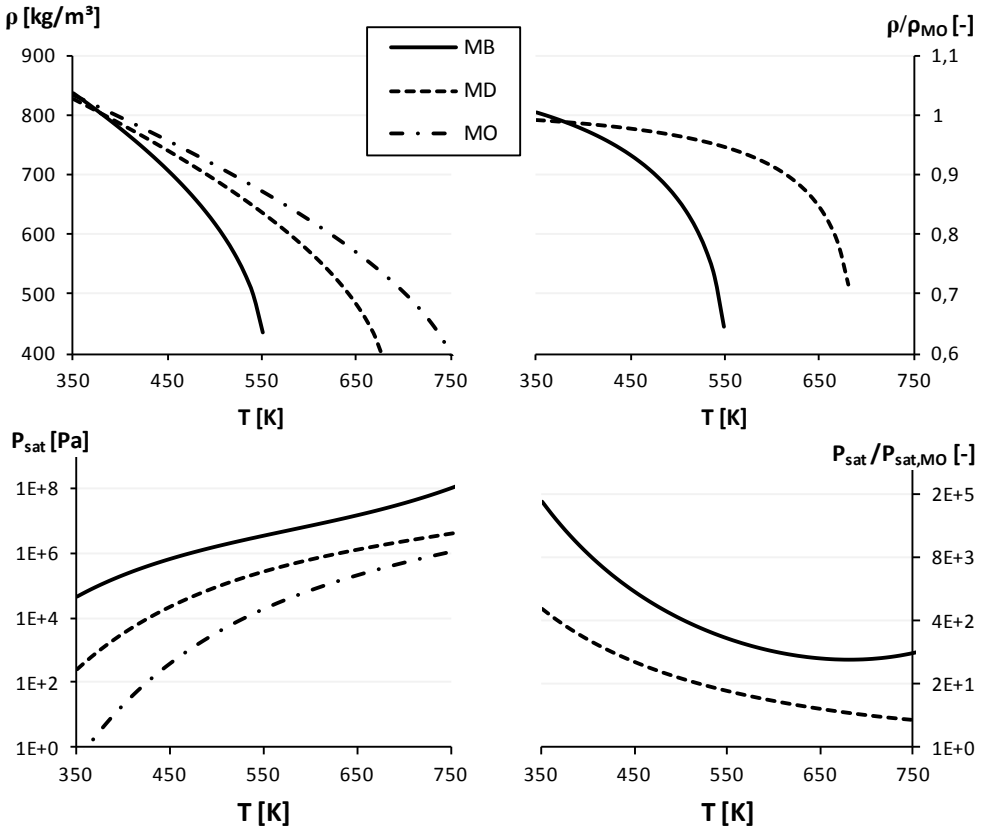

Figure 6.4: Liquid bio-diesel surrogate properties saturation pressure (left) and density (right). Relative comparison to methyl-oleate is shown by grey lines

6.5 Straight oils & fats

6.5.1 Composition

Similar to the diesel and bio-diesel chemical composition, oils and fats are composed of a wide variety of types of molecules. Nevertheless some consistency can be found:

- Fats and oils of animal and plant origin consist of 92-99% of triglycerides (also known as triacylglycerols).
- 0.1-2% of free fatty acids (FFA). A minor fraction consists of di- and monoglycerides.
- 1-4% are phytonutrients (vitamines, disease-preventing molecules,...) which are very complex molecules that usually contain aromatic structures, phos-

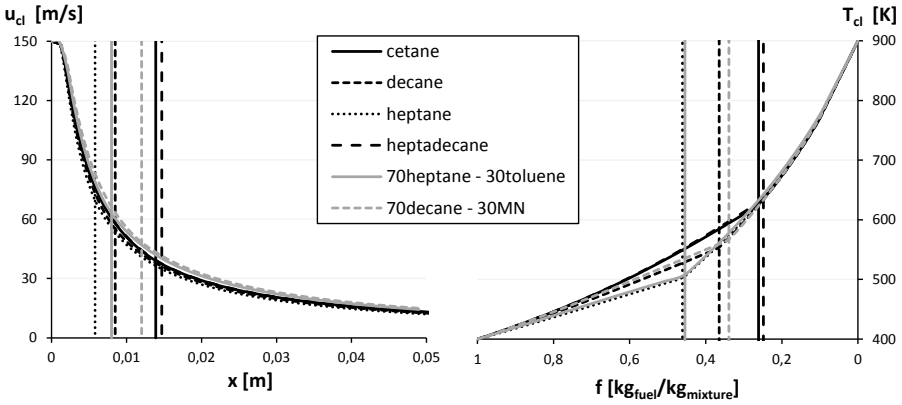

Figure 6.5: Evaporating 1D-model behavior for commonly used diesel surrogates

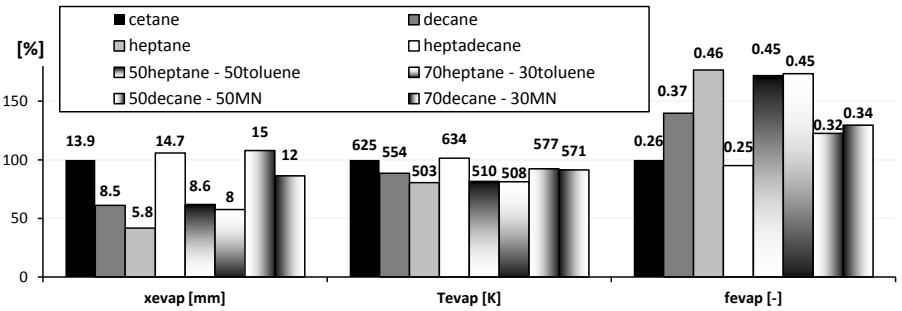

Figure 6.6: Summary of the comparison of the liquid length (x_{evap}), temperature (T_{evap}) and fuel fraction (f_{evap}) at total evaporation between the different surrogates for the same boundary conditions (the y-axis shows the percentage compared to cetane, the values on the bars represent the absolute value)

pholipids, sterols, tocopherols and metal ions such as Na, Ca, Cu, Fe, Pb, Zn, Ni, Hg, Co, Al,... [172].

Since straight oils and fats are the base products for the bio-diesel production, table 6.2 gives also the overview of the most important molecular structures of the fatty acids contained in the oils and fats. Detailed chemistry is out of the scope of this work, however some basic background is necessary in order to understand the behavior of oils in a combustion chamber. The reader will be referred to specialized literature where necessary.

As for diesel and bio-diesel, the composition of the same crop or animal specie differs from origin and batch. The average composition might be similar, but the deviation can be that important that the determination of the small amount of FFA,

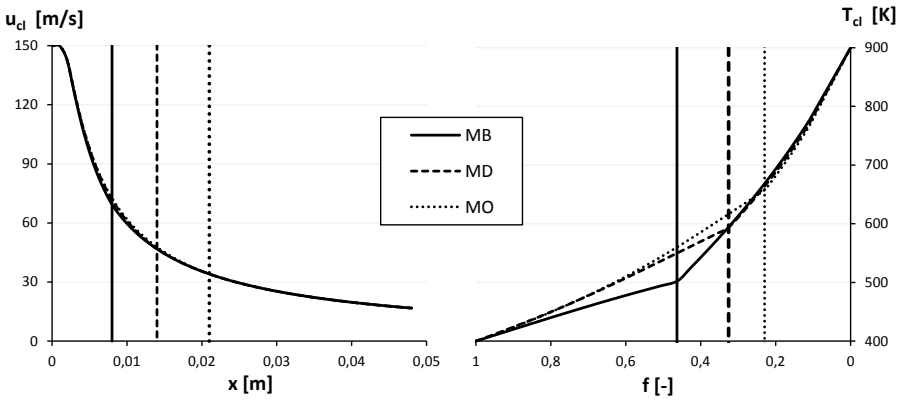

Figure 6.7: Evaporating 1D-model behavior for commonly used bio-diesel surrogates

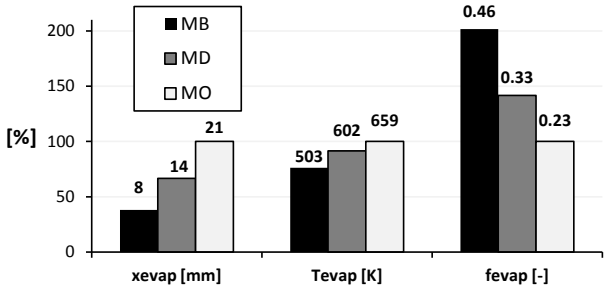

Figure 6.8: Summary of the comparison of the liquid length (x_{evap}), temperature (T_{evap}) and fuel fraction (f_{evap}) at total evaporation between the different bio-diesel surrogates (methyl-butanoate MB, methyl-decanoate MD and methyl-oleate MO) for the same boundary conditions (the y-axis shows the percentage compared to MO, the values on the boxes represent the absolute value)

phytonutrients, metals and others become insignificant in terms of spray and combustion behavior. Furthermore, literature specifies oils mostly in terms of the single fatty acid (FA) components as was listed in table 6.2. The average composition for some common oils is given in table 6.7 and can be obtained by the more standarized gas chromatography - mass spectroscopy (GC-MS) technique. This data however does not provide information concerning the triglyceride structures. Determination of the triglyceride composition requires more advanced and expensive measurement techniques. Details about the techniques and oil composition can be found in appendix C.

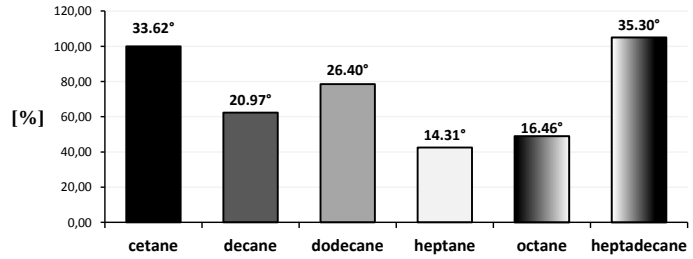

Figure 6.9: Tuned spray angle for similar liquid length (the y-axis shows the percentage difference compared to cetane, the values on the boxes represent the absolute tuned spray angle)

6.5.2 Surrogate requirements

From previous sections it is clear that oils and fats are also complex mixtures of molecules and that the use of surrogates is necessary in order to predict the in-cylinder processes.
Unfortunately, no surrogate fuels for straight oils are found in literature. This can probably be explained by the fact that such fuels only have potential for bigger engines and for these engines the emission regulations are lagging behind the ones for light- and heavy-duty engines (cfr. section 1.1). Lately, more and more interest is going to the use of these fuels as renewable alternatives for diesel.

Physical Differences

The choice of an oil surrogate should take into account the spray vaporization and combustion characteristics of the oil under engine conditions. Parameters to be looked at for the vaporization process are viscosity, surface tension, density, saturation pressure, heat capacity and heat conductivity. Combustion involves the heating value, ignition boundaries and cetane number.
As was demonstrated in section 6.4.2, the choice of the surrogate strongly depends on the modeling strategy and considered hypotheses & simplifications.
A big limitation for an oil surrogate is the lack of (temperature and pressure dependent) data and the detailed chemical reaction kinetics for the triglycerides.

Chemical Differences

The biggest (chemical) differences among the oils are the chain lengths of the different fatty acids and amount of double carbon-carbon bonds. The place of oxygen atoms can be considered the same since oils are for about 92 – 99% composed of triglycerides, which are ester structures.

FA	palm	olive	peanut	rapeseed	soybean	sunflower
C12:0	0.2	-	-	-	-	-
C14:0	1.1	-	-	0.1	0.1	-
C16:0	44.0	8.4	10.0	4.7	10.7	6.2
C16:1	0.1	0.7	-	-	0.3	0.2
C17:0	-	0.1	-	-	-	-
C17:1	-	0.1	-	-	-	-
C18:0	4.5	2.5	3.8	3.5	4	4.7
C18:1	39.2	78.0	54.4	58.2	23.8	20.4
C18:2	10.1	8.3	24.7	20.7	53.3	68.8
C18:3	0.4	0.8	-	10.4	7.6	-
C20:0	0.4	0.5	1.6	0.6	-	0.2
C20:1	-	0.3	1.1	1.3	0.2	-
C22:0	-	0.1	2.9	0.3	-	0.1
C22:1	-	-	-	0.2	-	-
C24:0	-	0.2	1.3	-	-	0.1

Table 6.7: Composition of some common vegetable oils in mol% [173].

Impurities

A small content $(1-4\%)$ of other components such as metal ions, sulphur, phospholipides, steroles, phenols etc... are contained in oils. A direct influence of these "impurities" on the spray and combustion can be neglected in a first approximation, but might be taken into account for engine durability and emissions. The emission models can for this reason be decoupled (as usually done in simplified modeling) from the combustion model. This is the motivation not to consider the impurities for the spray and combustion model. The emission models however require information from the combustion model but no feedback to the combustion model will be needed. Since combustion is not handled in this work, the influence of the impurities will be a subject of future work.

Oxygen Content in the Fuel

Like bio-diesel, pure oils have all fuel oxygen bonded in ester structures. This makes it reasonable to search for esters as surrogate components as is done for

bio-diesel. The bonds with the glycerol molecules are the key difference. In order to motivate the use of bio-diesel surrogates in terms of combustion, the breaking down of the triglycerides should be understood well. However, little is known in literature about the chemical kinetics during combustion.

In engine research, the measure for the oxygen-carbon ratio is usually defined through an equivalence ratio (ψ) (or air factor $\lambda = 1/\psi$) as ratio of the actual amount of air to fuel to the ratio air/fuel required for stoichiometric combustion [kg_{fuel}/kg_{air}]. However this is not a perfect measure when dealing with oxygenated fuels, because the fuel-bonded oxygen is not taken into account. This might result in actually more oxygen-rich areas when the fuel is combusted than was predicted. Mueller *et al.* [163] proposed an alternative parameter called oxygen ratio (Ω). The oxygen ratio is defined as the ratio of the amount of oxygen available in the reactants and the amount of oxygen required for stoichiometric combustion as given by Eq. 6.2. This parameter takes into account the oxygen content of the fuel.

$$\Omega = \frac{n_{O_{fuel}} + n_{O_{air}}}{n_{O_{stoich}}} \tag{6.2}$$

A conceptual explanation for the oxidation of oxygenated fuel in spray combustion is also given by Mueller *et al.*; the oxygen in the soot-forming regions at the centerline of the fuel jet will be higher for an oxygenated fuel compared to a non-oxygenated fuel at the same Ψ, which may enhance the soot reduction of the oxygenated fuels.

6.5.3 Surrogate Choice

In section 1.2 it was mentioned that the fuel type influences the engine performance. In order to make the distinction between the different fuel types, the surrogate should consist of a mixture of a limited amount of species to capture the most significant differences in properties for both vaporization and combustion.
Based on the earlier discussion in this chapter and the proposed model from chapter 5 in mind, the main requirements for the surrogate fuels will be:

- similar calorific value: the heat release during combustion will influence the temperature and therefore the whole spray process.
- properties with the most significant influence on the hypotheses and simplifications of the model, such as saturation pressure (cfr. section 6.4.2)
- similar parameters that have a big influence on the atomization and injection system (surface tension, bulk modulus and viscosity)
- similar amount of multiple bonds: the double bonds determine the fuel reactivity and have an impact on the emission formation (soot and NO_x)

- similar *oxygen ratio* Ω: the oxygen content is important for the combustion characteristics (flame lift-off, ignition delay, soot production,...)

Usually the choice of the surrogate is based on the availability of the detailed kinetic chemistry and temperature dependent properties (depending on the used modeling strategy). Knowledge of the chemical pathways is necessary to estimate local temperatures with acceptable accuracy in order to predict the emissions and heat release. Such calculations are useful for CFD. For simple 1D modeling these calculation efforts give usually no additional advantages due to the many strong hypotheses. Total oxidation with the assumption of frozen chemistry (= chemistry occurs much faster than the turbulent mixing) is often used. Desantes *et al.* [133] showed that the macroscopic properties could be captured well with this strategy. They however point out that local temperatures and species concentration are not properly calculated in the fuel-rich regions with their model.

The difficulty in searching for a surrogate will reflect in the way how the chemical composition of the oil is simplified. Proposals for bio-diesel and straight oil surrogates, based on the origin of the crop or composition are not found in literature for this application; the proposed surrogates for bio-diesel, such as MD and MB, are considered to be valid for each type of bio-diesel or the surrogate mixture was tuned for the investigated type (cfr. section 6.3).

A distinction between the fuels can be based on the chemical and/or physical differences. A chemical analysis is more interesting since the chemical composition also determines the physical properties of the fuel.
A common analysis involves gas chromatography - mass spectroscopy (GC-MS). This method is able to describe the oils in terms of their fatty acid composition. Chemical data about fatty acids are readily available (e.g. DIPPR 801 Database and [121]) so these could easily be used as surrogate components.
High Performance Liquid Chromatography (HPLC) is an analysis that is able to describe the oils in terms of their triglycerides, revealing more information about the fuel compared to a GC-MS analysis. The HPLC method is however more complex and less convenient than a GC-MS analysis. So, since it is easier and cheaper to obtain data from a GC-MS analysis, the oil surrogates in the following of the text will be based on data of a GC-MS analysis. More details of these analyzing methods can be found in appendix C.
Since the type of molecule is mostly the same in oils, the different properties are due to the double bonds and chain length. The difference between some common oils is demonstrated in Fig. 6.10.
The double bonds are dominated by the C18:y-acids. The influence of the bonds and chain length on the physical properties (mainly for determining the evaporation process) are shown in Fig. 6.11. One can see that the saturation pressure does

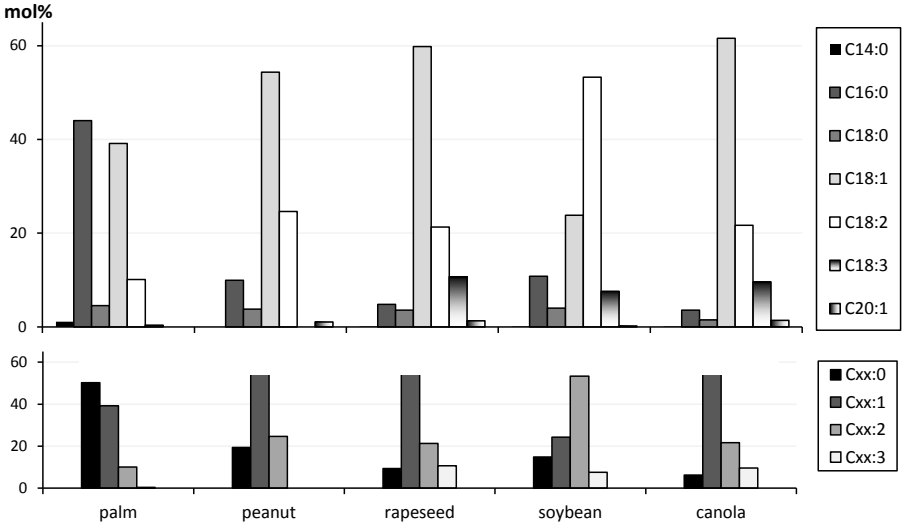

Figure 6.10: Composition of some common oils: (top) the fatty acid composition, (bottom) distribution of the double bounds, with is Cxx:y the fatty acid Cxx with y double bonds [mol%]

not differ a lot for the molecules with different amount of double bonds compared to the chain length. The effect of viscosity is more important: the viscosity decreases with the amount of double bonds. Knothe *et al.* [118] did a study on the dependence of the molecular structure of the viscosity; the kinematic viscosity increases with chain length of either the fatty acid or alcohol part in a fatty ester or in a n-alkane. The increase in kinematic viscosity over a certain number of carbons is smaller in n-alkanes than in fatty compounds. The kinematic viscosity of unsaturated fatty compounds strongly depends on the nature and number of double bonds. The position of the double bond affects viscosity less.
The viscosity of the fuel will affect the spray atomization. This is the main motivation to match the oil viscosity with the surrogate fuel. Furthermore, viscosity is a property which is easy to measure (cfr. appendix C). One difficulty is the temperature dependence of the viscosity, which makes matching hard when only a limited amount of surrogate components are used. In the discussed spray model, atomization is by-passed by the input of a spray angle, which is considered to be constant during injection. This fact justifies not making the surrogate mixture dependent on the viscosity, but rather to allow the measured fuel viscosity (or estimated from the acid composition) as an input to the model. Based on experiments in the future, the spray angle can be written as a function of this viscosity.

Saturation pressure was found to be very important for the considered hypotheses

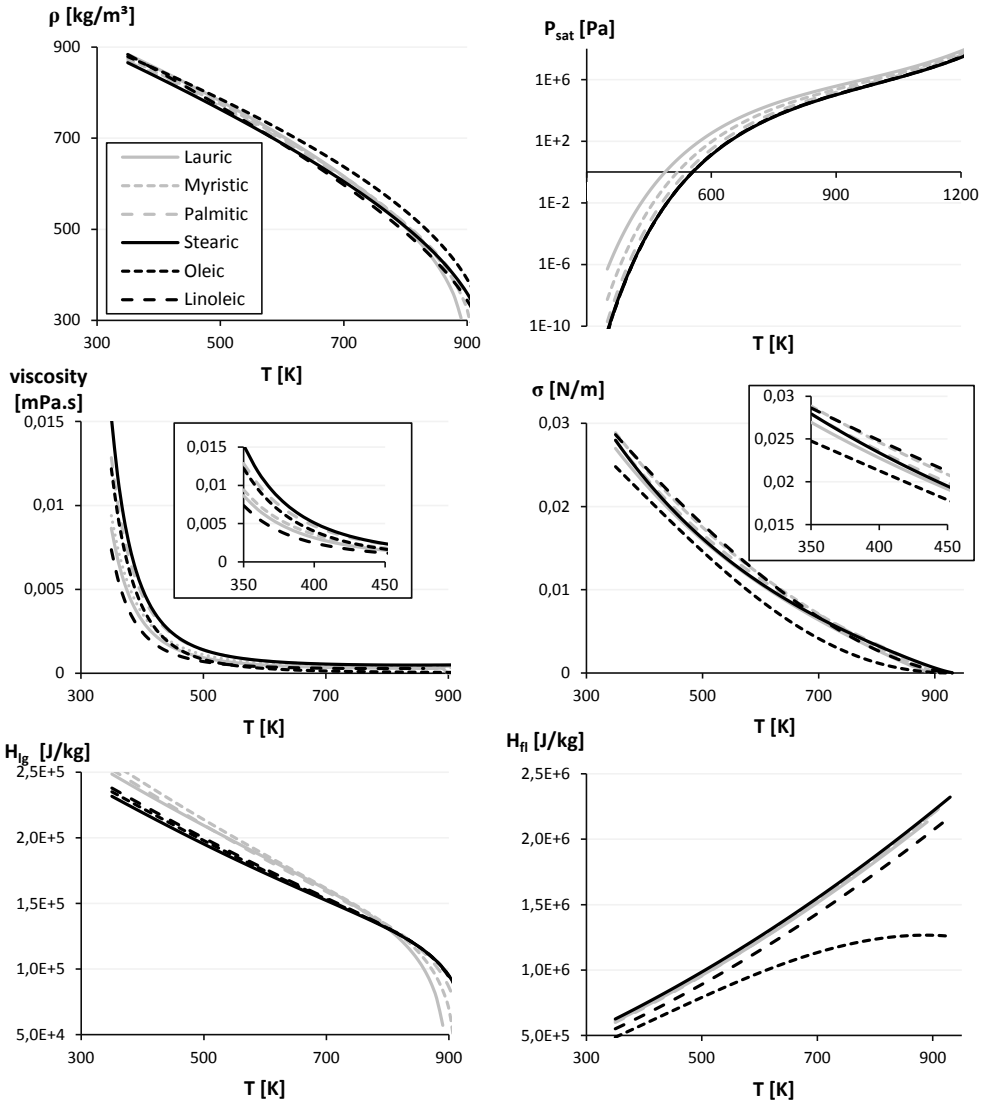

Figure 6.11: Physical properties for some triglycerides: (top, left to right) liquid density, saturation pressure, (middle, left to right) viscosity, surface tension, (bottom, left to rightliquid enthalpy, latent heat

in the model: the spray is considered saturated at each moment and position. The saturation pressure suffers from the same difficulty that this property is also temperature dependent. Furthermore, saturation pressure data is not readily available and measurements are more rare, expensive and time consuming [174]. A strong

link, however, exists between the saturation pressure and the viscosity, especially at higher temperatures. This is demonstrated in Fig. 6.12. The log(P_{sat})-log(μ) ratio shows a linear behavior. Viscosity data is much easier to measure and due to the relation with the saturation pressure it is acceptable to use the viscosity as a matching property for the surrogate as will be demonstrated in the following.

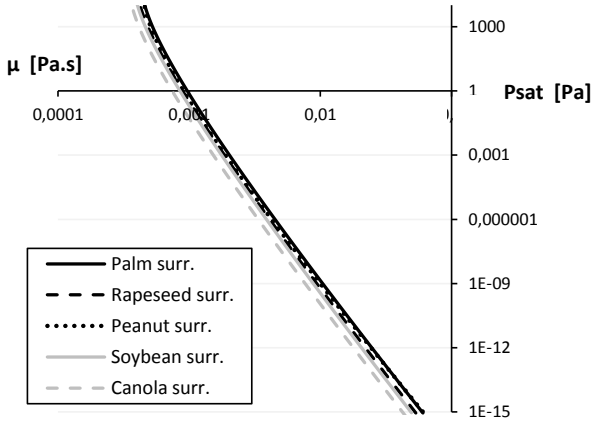

Figure 6.12: Logaritmic relation between viscosity and saturation pressure for different oils.

The amount of molecules with 3 double bonds is very limited. However they react faster in the combustion process, shortening the ignition delay [17]. For vaporizing sprays the molecules with 3 double bonds will not be taken into account directly but can be translated to molecules with 2 double bonds, based on the relative reactivity given in section 1.2 to reduce the complexity of the surrogate. A further motivation to discard these molecules (mainly C18:3) is because no extensive temperature dependent data is found in literature.

As a result from the current discussion, the following conclusion can be made:
Each oil is proposed to be written as the sum of 4 components. The molar fraction of each component is determined by a set of 4 equations:

(1) The viscosity of the surrogate is close to the oil (at the injection temperature)

(2) The amount of oxygen equals the amount in the real oil (determines the reactivity and emission formation)

(3) The amount of molecules with double bonds equals the amount in the real fuel (determines the oxidation reactivity and emission formation)

(4) The total mass fraction is equal to 1

The determination of surrogate mixture only demands the oil to be characterized by a GC-MS analysis and viscosity measurements. Especially the viscosity at fuel injection temperatures needs to be measured since this value can be used to include the viscosity dependency on the atomization in the spray model.

The final problem is the choice of the specific components:

Temperature dependent data are available for only a few triglycerides. The most relevant triglyceride in oils with double bond is linoleic acid triglyceride ($C_{57}H_{98}O_6$ or 3x C18:2), since linoleic is a fatty acid that is usually contained in the oils in large amounts. Enough data is available, making this triglyceride preferrable as a surrogate component. The fact that this molecule contains 2 double bonds will be advantageous for the prediction of ignition.

Another triglyceride that is commonly found in the oil and dominates the viscosity is also preferred. Stearic triglyceride (3x C18:0) is the triglyceride with the highest viscosity of which data is available.
Compensation for the fuel oxygen to carbon ratio is done by the addition of a triglyceride of another common fatty acid: palmitic triglyceride ($C_{51}H_{98}O_6$ or 3x C16:0) and a long n-alkane molecule: triacontane ($C_{30}H_{62}$).

Some important fuel properties for the surrogate components are given in table 6.8. Some common oils are added as well to allow qualitative comparison. The oils

surrogate	ρ **(293***K***)**	μ **(313***K***)**	**M**	**LHV**	**CN**	**H/C**
	[kg/m^3]	[mPa.s]	[g/mol]	[MJ/kg]	[-]	[-]
palm	918	39.6	810-855	39.5	42.0	1.95
rapeseed	912	37.0	926	39.7	37.6	1.81
peanut	903	39.6	835	39.8	41.8	1.82
soybean	914	32.6	874	39.5	37.9	1.79
triacontane	810	11.8	422.8	43.6	N/A	2.067
palmitic triglyc.	893	39.5	807.3	36.3	89.0	1.922
stearic triglyc.	891	52.6	891.5	37.4	85.0	1.930
linoleic triglyc.	912	25.6	879.4	35.6	33.5	1.72

Table 6.8: Some components; with LHV, the lower heating value; CN, the cetane number; H/C, the hydrogen to carbon ratio. Oil data from Sivaramakrishnan and Ravikumar [175], triglyceride data from Harnisch et al. [176]

from table 6.7 can be written as a function of the proposed surrogate components. Those results are shown in table 6.9 and visualized in Fig. 6.13. The upper part of the table represent the oil composition obtained by GC-MS analyses as well as the viscosity at the injected fuel temperature (= 353K). The lower part is the proposed surrogate composition in *mass%*. Details of the applied algorithm can be found in appendix D.
A remark should be made: the sum of the values might not be 100% since the values are based on analyses found in literature and some additional components (free fatty acids and other impurities) might have been contained in the oil up to 8%. In the algorithm, all values were converted so that the total contribution of the given components was 100%. The validation of the viscosity for the sur-

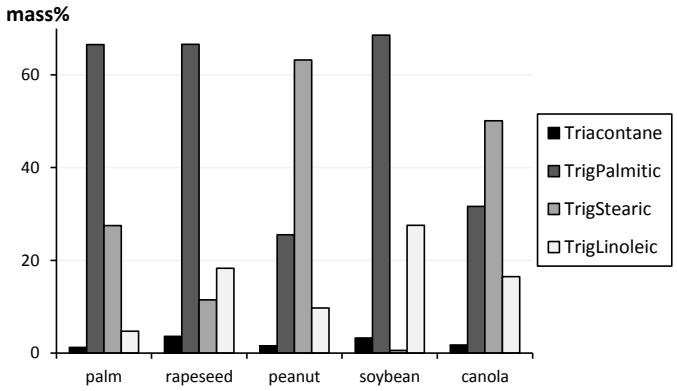

Figure 6.13: proposed surrogate composition [mass%]

rogates is performed in Fig. 6.14. The symbols represent the measurement data obtained from Defruyt and Van De Maele [120]. The graphs are split for the low and high temperature range, since the differences in viscosity become smaller as the temperature increases. The comparison is reasonable and makes distinction between different oils possible. Concerning the saturation pressure, few data can be found in literature and the data is limited to low temperatures. Although the saturation pressure was not matched as a target, the comparison with experiments show reasonable good agreement as well. An example for soybean oil is given in Fig. 6.15.

6.6 Model validation

The surrogates were implemented in the spray model of chapter 5. Since the differences in saturation pressure are small, only small differences in liquid length (LL) could be expected. This is confirmed by the results as shown in Fig. 6.16.

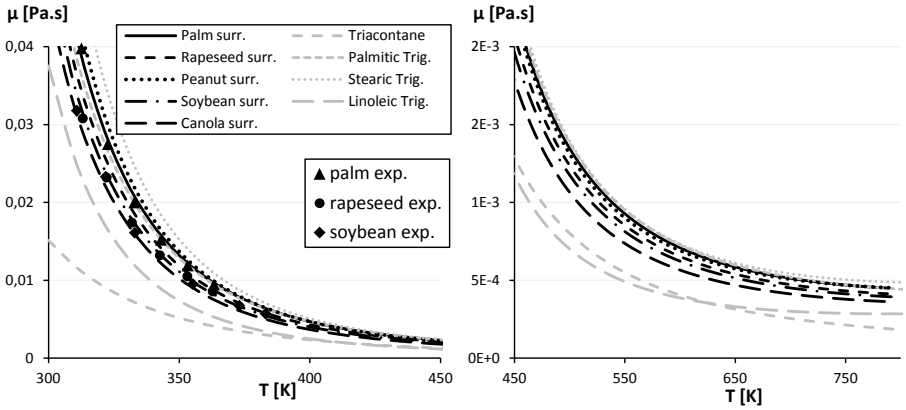

Figure 6.14: Proposed surrogate composition [mass%]. The symbols represent experiments with the corresponding oil.

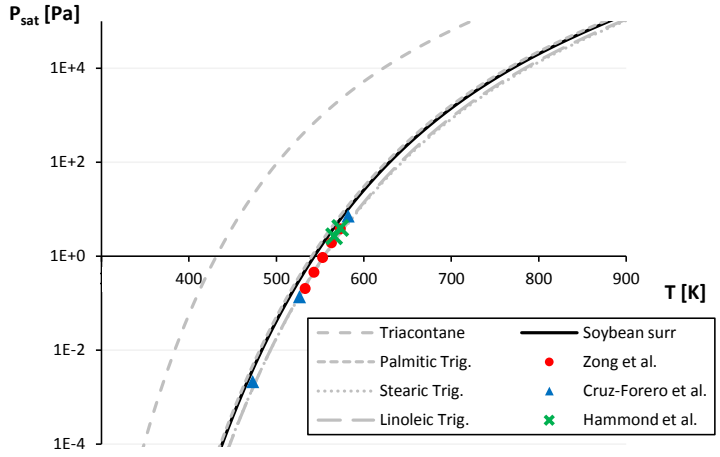

Figure 6.15: Evaluation of the saturation pressure for soybean. The symbols represent the experiments [177–179]

The figure shows the relative liquid length compared to the liquid length of palm oil. All results are within the 5% difference. So the differences are small and the trend can be considered due to the saturation pressure (or similarly: the viscosity). Note that the spray angle was kept the same for the different surrogates. No significant differences in spray penetration were found and are therefore not shown. This was also confirmed for cold inert spray experiments in the GUCCI-setup by Defruyt and Van de Maele [120] and from the discussion in chapter 8.

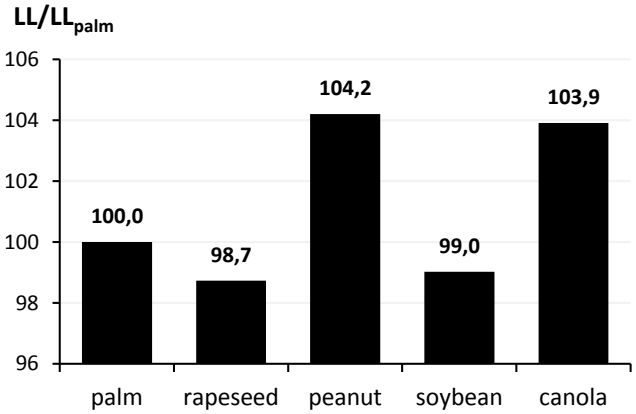

Figure 6.16: Relative liquid length (LL) [%] for the oils, with the LL of palm oil as a reference.

6.7 Conclusions

An overview is given of the current status of the diesel and bio-diesel. The importance of the influence of certain surrogate properties are pointed out in terms of the behavior in the spray model. The simplifications and hypothesis should be a crucial factor for the choice of the surrogate.
Crude oils are discussed as a function of their functionality as a diesel fuel. Little, if any, is known about surrogates and a proposal, based on known properties, composition and behavior is made as a mixture of 4 components:

(1) Triacontane ($C_{30}H_{62}$)

(2) Palmitic triglyceride ($C_{51}H_{98}O_6$ or 3x C16:0)

(3) Stearic triglyceride ($C_{57}H_{110}O_6$ or 3x C18:0)

(4) Linoleic triglyceride ($C_{57}H_{98}O_6$ or 3x C18:2)

The calculation of the surrogate mixture is possible by performing a frequently used GC-MS analysis on the considered crude oil for determination of the fatty acid composition. The viscosity at the temperature of the injector fuel is required as well and can be measured by simple methods.
The determination of the impurities is expected to only influence the emissions and are not futher considered in this work.
It should be clarified that this proposal could not be validated in experiments, since yet no vaporizing spray measurements could be done in the GUCCI-setup and this will be material for future work.

FA	**palm**	**rapeseed**	**peanut**	**soybean**
C12:0	0.2	0	0	0
C14:0	1.1	0.1	0	0.1
C16:0	44.0	4.7	10.0	10.8
C16:1	0.1	0	0	0.3
C17:0	0	0	0	0
C17:1	0	0	0	0
C18:0	4.5	3.5	3.8	4
C18:1	39.2	59.8	54.4	23.8
C18:2	10.1	21.3	24.7	53.3
C18:3	0.4	10.7	0	7.6
C20:0	0.4	0.6	1.6	0
C20:1	0	1.3	1.1	0.2
C22:0	0	0.3	2.9	00
C22:1	0	0.2	0	0
C24:0	0	0	1.3	0
$\mu(353K)$ $[mPa.s]$	11.9	10.5	12.4	9.5
surrogate				
triacontane	1.23	3.62	1.55	3.25
methyl decanoate	66.56	66.60	25.51	68.60
stearic triglyceride	27.50	11.50	63.22	0.60
linoleic triglyceride	4.71	18.28	9.72	27.55

Table 6.9: Simplification of some crude oils [mol%] and the proposed surrogate mixture [mass%]

7

Spray A investigated

"Experience is the past tense of experiment."

- Gregory Alan Elliot -

The chapter is organized as follows: a background and motivation for this spray measurement set introduces the discussion. The rest of the chapter is arranged in 2 parts.
The experimental part is an integral copy of the article SAE2013-01-1616 [22] which is published in the SAE Journal of Engines and was included in the second ECN workshop (september 2012, Heidelberg, Germany). The experiments were performed at the facilities of the Technical University of Eindhoven together with ir. Maarten Meijer. Both authors have contributed equally to the experiments and post-processing. The section is subdivided in the different measured spray parameters: liquid length, spray penetration, ignition delay and flame lift-off length. A comparison of the results with other institutes is done after corrections for the nozzle hole diameter.
In the numerical part, the model as described in chapter 5 is used to predict the experimental results.

7.1 Introduction

It was already pointed out in this work that spray measurements and the "translation" from experiments to modeling is not straightforward and still suffers from lack of understanding. This is one of the reasons the Engine Combustion Network (ECN) was established by Sandia National Laboratory (USA), IFP energies nouvelles (FR) and CMT motores termicos (SP) which involves the collaboration between various institutions to share experimental data, diagnostics, and computational results.
The main goal of this network is threefold:

- to establish an internet library of well-documented experiments that are appropriate for model validation and the advancement of scientific understanding of combustion at conditions specific to engines
- to provide a framework for collaborative comparisons of measured and modeled results
- to identify priorities for further experimental and computational research

Following this path, one tries to standardize spray diagnostics and definitions in such way that a comparison of experimental results between different research institutes can be made. Secondly, the modelers will be assured about the meaning of the quantitative results so they can use these to validate their modeling results.
Worldwide, several spray chamber facilities for high-temperature, high-pressure conditions have been developed. Because of the uniqueness of each facility, there are measurement uncertainties about their operation of which little is known so far. Some of the combustion chambers participating in ECN are shown in Fig. 7.1.

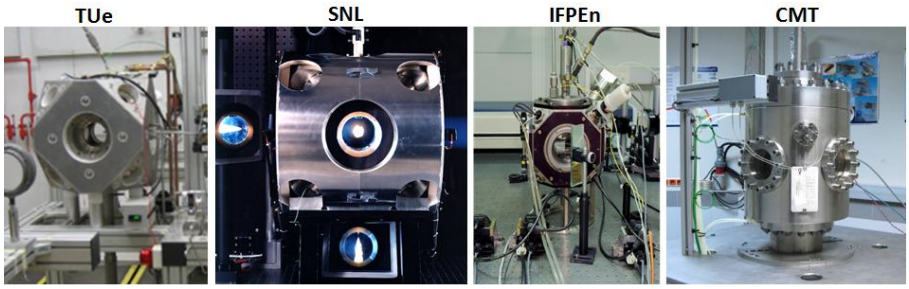

Figure 7.1: Some of the combustion vessels that are participating in ECN: (left-to-right) Technical University of Eindhoven (NL), Sandia National Laboratory (USA), IFP Energies nouvelles (FR), CMT motores termicos (SP)

In order to have comparable results and more knowledge about the setup uncertainties, the injection hardware and boundary conditions are specified and can be found on the ECN website (*http://www.sandia.gov/ecn/*). In this work '*spray A*' is

investigated. It involves a spray from a single hole, non-cavitating diesel injector. This configuration allows to investigate the most elementary spray. Multi-hole and cavitating sprays are also defined by ECN (resp. '*spray B*' and '*spray H*'), but are not considered in this work. The most important specifications are repeated in table 7.1. Note that the ambient properties are denoted as core properties (not bulk properties).

Spray A conditions	
ambient gas density	$22.8 kg/m^3$
ambient oxygen concentration	0 & $15 vol\%$
ambient gas temperature	$900 K$
ambient gas velocity	$< 1 m/s$
injection pressure	$150 MPa$
fuel	n-dodecane
fuel temperature	$363 K$
injection duration	$1.5 ms$
injected fuel mass	$3.5 mg$
nominal nozzle outlet diameter	$90 \mu m$
nozzle K factor	1.5
discharge coefficient	0.86
mini-sac volume	$0.2 mm^3$

Table 7.1: Most important boundary conditions and equipment for 'spray A'

In the framework of ECN, '*spray A*' measurements were performed in cooperation with the Technical University of Eindhoven on their constant volume combustion vessel (cfr. chapter 4). The original setup configuration (cfr. Frijters [116]) was adapted to meet the ECN specifications: an ECN injector was installed at a side window of the chamber (cfr. Fig 4.1). The nozzle was protected against temperature rise from the pre-combustion by a ceramic cover. This issue is discussed in detail by Meijer *et al.* [122] and is similar to the results that were obtained in the GUCCI-setup, described in section 4.6.2.
The ECN injector that was used during the measurements was injector n°677. This is an important detail since the actual nozzle hole diameters as well as the shape and eccentricity among the different ECN-injectors differ significantly as pointed out in the table of Fig. 7.2. The influence of the shape is however not fully under-

stood and is not considered in this study. Other institutes (e.g. Argonne National Laboratory, CMT Motores Termicos, Sandia National Laborary) are focusing on this issue by simulations and mass flow measurements using radiography measurements (cfr. ECN workshop 2 - 2012 - Heidelberg, Germany). The differences of the nozzle holes and the influence are summarized in Fig. 7.2 to demonstrate the significant impact that may arise in the measurements. In this study, only corrections for the nozzle diameter are performed for the comparison with other institutes. These corrections are based on earlier reported 0D models as will be mentioned further on in the text.

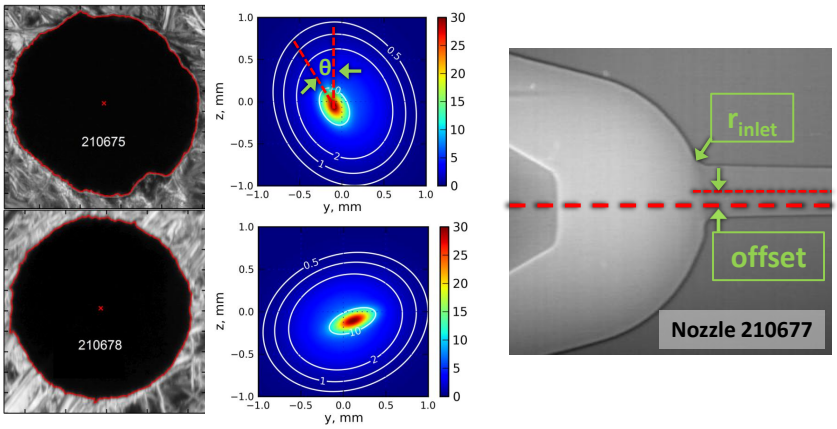

Injector #	D_{exit} [µm]	θ [°]	Offset [µm]	K-factor	r_{inlet} [µm]	C_a	C_d
Nominal	90	0	0	1.5	-	-	0.86
210370	90.8	-90	50	1.5	23	-	-
210675	89.4	9	53	1.3	25	0.98	0.90
210677	83.7	32	37	1.8	20	0.98	0.89
210678	88.6	36	39	1.8	19	0.98	0.89
210679	84.1	-22	22	1.8	17	0.98	0.91

Figure 7.2: Nozzle hole differences among the 'similar' ECN nozzle. top left: SEM images of the nozzle holes, top right: radiography images of the fuel mass distribution (data obtained from the ECN2 workshop, Sept. 2012, Heidelberg)

The main goal of the measurements was to provide the Engine Combustion Network a complete data set for '*spray A*' on the EHPC and to compare the results between the other research institutes. The different diagnostics will also be used for measurements in the GUCCI-setup. With the gathered experience during the ECN experiments, we can be sure that the measurements in our chamber are trustworthy.

7.2 Experimental 'Spray A'

This section gives an overview of the '*spray A*' results for the main basic spray diagnostics. The theory of the spray diagnostics can be found in chapter 3, while in the following only the technical specifications are given as applied for the measurements. All definitions used in processing of the measurement are according to the ECN proposals. The determination of the boundary conditions was done similarly as described in section 4.6 and is not repeated in this section. The ratio of core to bulk ambient temperature was found to be 1.08. This value is further used to determine the desired time of injection.

7.2.1 Liquid length

The liquid length (LL) is measured with the use of the diffused back-illumination imaging technique (cfr. section 3.2.2). The technical details are summarized in table 7.2.

light source	460nm power led
light pulse time	50ns
diffuser	50° square pattern
focal length Fresnel lens	152mm
acquisition rate	120kHz
camera lens	50mm/1.2

Table 7.2: Settings for the liquid length measurements

The liquid length was evaluated in two different ways: the development of the time resolved liquid length during one injection and the average liquid length during the steady state period of one injection. The time resolved LL is based on a background corrected instantaneous image. A threshold based contour is drawn around the binary image defined liquid area. The pixel at the maximum distance from the injector is defined as the time dependent liquid length. The results for the time resolved data are displayed in Fig 7.3. From these results it is found that a certain oscillation exists around a steady state value. The frequency of these oscillations, however, is not regular for the considered acquisition rate and no significant conclusion can be made on the origin. As a result, the fluctuation is considered as noise. The averaged value was found to be 10.3mm as shown in the lower part of Fig. 7.4.
The time averaged DBI method is based on the measurement of the light extinction through the liquid core. The reference level is the background of the image when

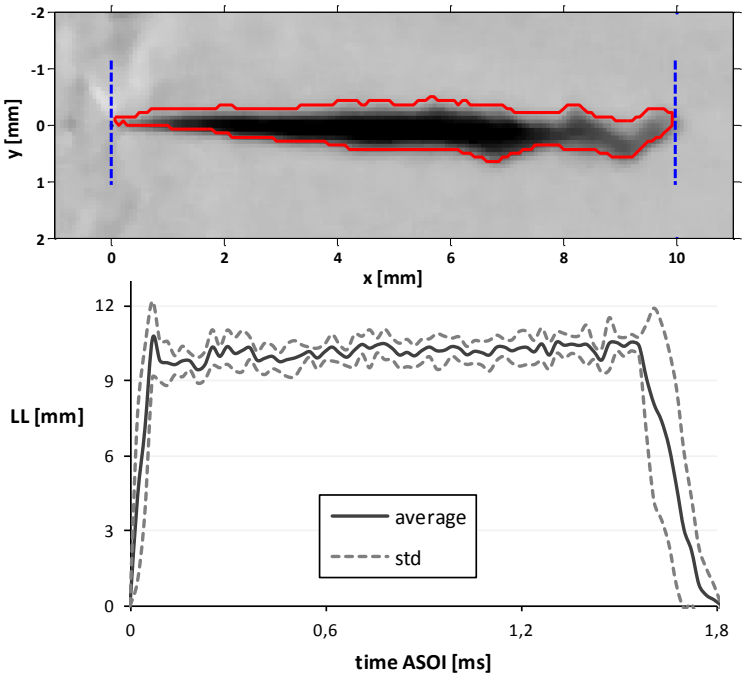

Figure 7.3: Top: background corrected single processed image frame, Bottom: time resolved result averaged over the experiments (thick solid red line) and standard deviation (thin solid black lines)

there is no liquid injection. A mean image of the background, I_{BG} is created by averaging 10 individual frames taken right before SOI. Next each image during the injection can be divided by the background image, in order to obtain the normalized intensity of the image. The logarithm of the normalized intensity gives the extinction factor τ in the whole visualization field:

$$\tau(x,y) = -log\left(\frac{I(x,y)}{I_{BG}(x,y)}\right) \tag{7.1}$$

For the steady LL the evolution of τ along the spray axis is considered to be a measure for the liquid length. To measure the steady-state liquid length, τ is computed on a time-averaged image, during the steady-state period of the injection (cfr. Fig 7.3). Ten individual measurements are used to obtain an ensemble average together with shot-to-shot standard deviation.
This technique suffers from beam steering near the liquid spray tip, due to the refractive index gradient created by the vaporized fuel. Therefore the exact liquid length is not measured precisely. The decay of the extinction factor along the spray axis is therefore linearly fitted. The location where this linear fit intercepts zero, is

defined as the liquid length. The followed method and the obtained LL for '*spray A*' conditions are shown in Fig. 7.4.

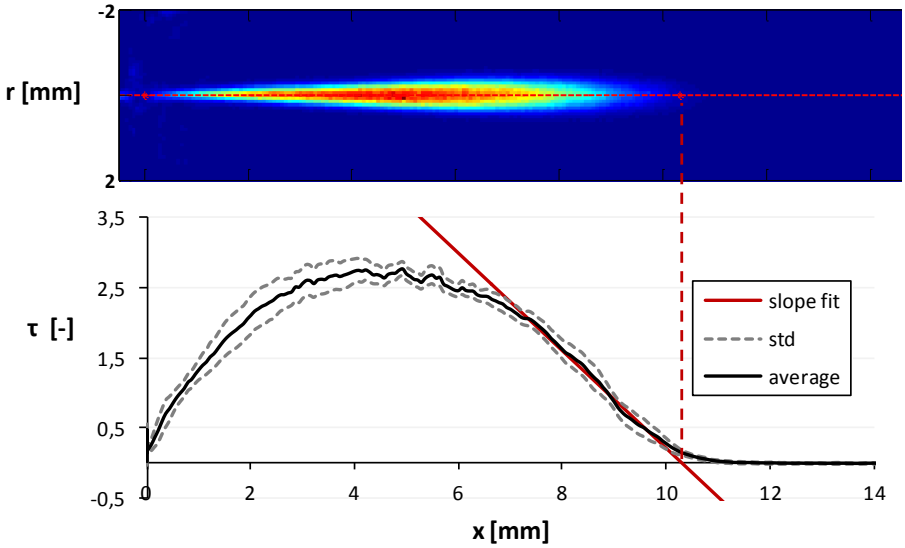

Figure 7.4: Image processing method for the averaged liquid length. The LL was found to be 10.3mm ±1.2mm. top: averaged intensity of the steady state part of the spray, bottom: averaged intensity along the spray axis

Besides the measurements executed at the TU/e, steady LL results are provided by the following ECN participants: Sandia, IFPEN and CMT. The data is officially published and can be taken from the ECN database. The obtained results are presented in Fig. 7.5. The error bars represent the standard deviation of the measurements. Differences between the used injectors are corrected for a fair comparison (red numbers). For these LL corrections the 0D liquid phase model from Siebers is used [90]. Siebers found that the liquid length is proportional with the hole diameter. It can be concluded that the obtained results for LL are encouraging since only minor differences are found among each participant and the applied nozzle-hole correction makes this even smaller. The deviations are within the measured standard deviations.

7.2.2 Penetration length

A focused shadowgraph setup is used to measure the gas phase penetration of both inert (0% O_2) and reacting sprays (15% O_2). A blue high power LED (460 ± 10*nm*) acted as a light-source. The parallel light beam was formed and again focused by two 100mm biconvex lenses. A small pass filter with 600*nm* cut-off frequency was used for the reacting spray to avoid overexposed light from the soot production.

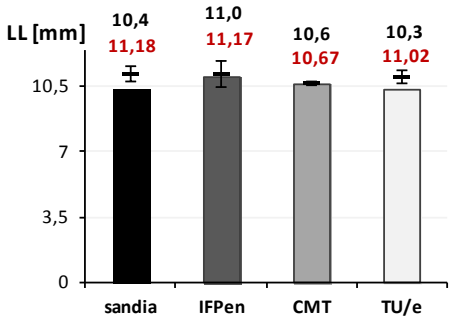

Figure 7.5: Comparison of the liquid length for nonreacting 'spray A' conditions. Showing the results from different institutes. The original values are shown in black at the top, the corrected values for the nozzle diameter [180] are shown in red below (data from ECN website).

Detailed settings for the optical setup are summarized in table 7.3. The same set-up with an additional spatial filter (schlieren stop) has also been used but it was concluded that the obtained results were similar but with more noise due to the background disturbances that became more intense with the schlieren set-up.

	Inert	**Reacting**
frame rate $[kHz]$	11	11
resolution $[mm/px]$	0.1143	0.1143
shutter time $[\mu s]$	80	80
small pass filter $[nm]$	none	600
focus lens	50mm/1.2	50mm/1.2

Table 7.3: Settings spray penetration measurements

The noise sensitivity for the penetration results was found reasonable since, based on experience and literature references, it is not easy to define the spray boundary from the background under these elevated ambient conditions. The fact that a relatively low measurement frequency was used for this work makes the disturbances by the frame to frame movements of the ambient background worse. Therefore, extra background noise correction was necessary. Applying the grain merge operation between 2 succeeding images leads to a more robust post-processing algorithm:

$$I_{corr} = \left(I_{raw}(i) - I_{raw}(i-1) + \text{offset}\right) . fullscale \tag{7.2}$$

With *fullscale*, equal to 4096 for a 12bit image. The offset was tuned and gave best results for a value of 0.4. Further image smoothing has been performed as developed by Xu et al. [111]. The results for the spray penetration of the inert and reacting spray are shown in figure 7.6. The vertical green line represents the (hot flame) start of ignition for the reacting spray as discussed in section 7.2.3. The start of combustion can be clearly observed by the nod in the curve as it was also shown in [79]. At that point, the density gradient becomes close to the one of the background, resulting in a virtual slowing down and decreasing penetration length.

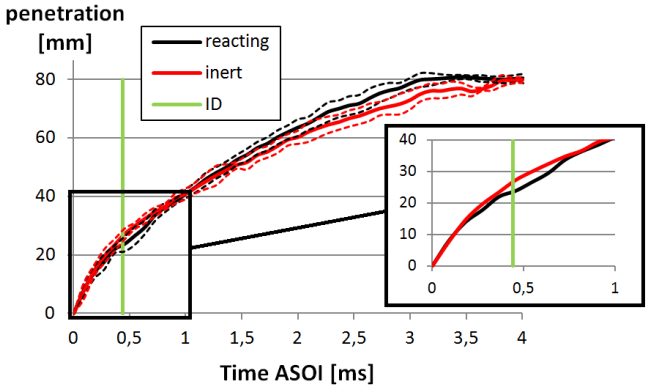

Figure 7.6: Spray penetration results for inert (red) and reacting (black) 'spray A'. The vertical green line represents start of combustion

The time resolved results from the different institutes are compared in figure 7.7 including the measurement deviations. It can be concluded that the results for vapor phase penetration data show variations (up to 8%) that fall within the expectations due to injector differences and measurement deviations. The spray penetration is found to scale linearly with the nozzle hole diameter as proposed by several 0D models [79, 111].

7.2.3 Ignition delay

An important parameter of spray combustion is the moment and location where the combustion process initiates. In this section, simultaneous measurements for the initial pre-ignition cool flame and the start of high temperature combustion ignition, are discussed. The ignition delay can be determined based on natural luminosity or the change in pressure of the ambient gas inside the vessel. Both methods are implemented and evaluated. The goal of the light based ignition delay measurements is to capture the first emission of light emitted at the pre-ignition

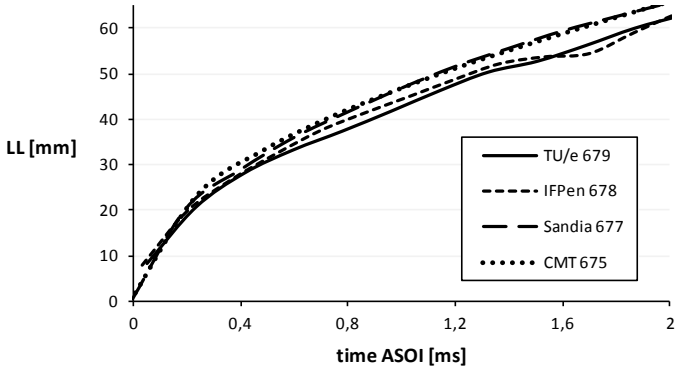

Figure 7.7: Comparison of the different spray penetration results from TU/e, IFPen, CMT and Sandia with the measurement deviation

cool flame start. The natural luminosity derived ignition delay is largely based on the intensified high speed recording set-up as was presented in section 3.5.2, without an optical filter. In this way the strong $HCHO^*$ and HCO^* emission in pre-ignition cool flames can be captured as well and used to identify the region where cool flame chemistry occurs prior to high temperature combustion [103, 181, 182]. The region of interest has been reduced to maximize the acquisition rate and resolution on the high speed camera CMOS chip. The used measurement settings are summarized in table 7.4. High intensity soot incandescence appears directly after the start of the high temperature combustion which will fully saturate the captured images if no measures are taken. In order not to damage the intensifier by overexposure from the highly intense luminosity from soot, the intensifier is deactivated about 40 images (or $4\mu s$) after triggering the injector (cfr.section 3.5.2).

frame rate [kHz]	41
resolution [mm/px]	0.2041
gating time [μs]	20
gain [%]	85
bandpass filter	none

Table 7.4: Settings for light intensity based ignition delay (ID) measurements.

As stated, in the combustion process, one can distinguish a cool and a hot flame stage ignition. The cool flame can only be measured by capturing the emitted light by natural luminosity because it is not notable in the recorded pressure (no de-

tectable heat release occurs). Some processed images for the natural luminosity measurements are shown in Fig. 7.8. The cool flame is defined as the moment at which the first light is detected.
The start of ignition is detected by the observation that the initial cool flames all merge together, the intensity of the luminosity goes up significantly and the flame front starts to expand. After applying a software based, median filter, the location of the ID for both cool and hot flame is defined as the mass center of the bright spot of light. The hot flame ID is used as the ignition delay of the fuel spray for further comparison with other institutes. It is recognized that this definition is, because of the used technique, somewhat arbitrary. For future work it is recommended to make a proper distinction between the pre-ignition cool flame and the hot flame ignition based on the detection of radical species such as HCHO* and HCO* (cool flame) and OH* (hot flame ignition).

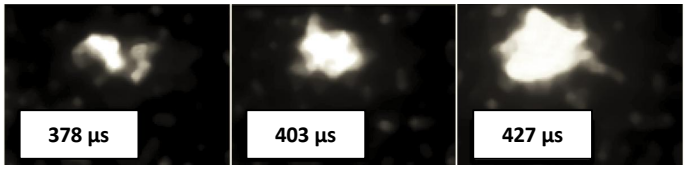

Figure 7.8: Succeeding time-resolved images of the initial stage of combustion. Indicating cool- and hot flame ignition. t = 378µs (cold flame ID), t = 403µs, t= 427µs (hot flame ID) = t_{ign}

For the pressure based ignition delay measurements a dedicated pressure sensor is installed inside the preburn combustion vessel. Normally the pressure history in the vessel is recorded with a single piezo-electric pressure sensor at $30kHz$ and therefore the settings of the pressure sensor amplifier are selected such that the whole pressure range during one measurement event (dictated by the pre-burn event) is covered. A second pressure sensor with higher sensitivity to pressure was kept in reset mode to continuously drain charge from the transducer until just prior to the spray event.
The followed post-processing method for the pressure based ID is based on applying a correction for the pre-burn pressure decline and speed of sound pressure delay. Again the followed approach and the filtering method are described in [103]. The correction for the speed of sound is based on the time t it will take for a pressure wave travelling at a speed of c over a distance D:

$$t = \frac{D}{c} \tag{7.3}$$

In contrast to the proposed triangulation theory in [103] the location D of the ig-

nition in this work is directly derived from the high speed images. The speed of sound is calculated with:

$$c = \sqrt{\frac{\gamma RT}{M}} \tag{7.4}$$

where γ is the ratio of specific heats, R the universal gas constant, T the bulk temperature and M the molecular weight of the ambient gas. Values for this particular set-up can be found in [117]. An example of the raw and processed data is shown in Fig. 7.9. It is noted that the raw unfiltered pressure data shows a very low noise level before ignition. Since both signals (raw vs. filtered) lead to the same result, one can argue that the whole filtering method is not strictly necessary to define the ignition delay according to ECN standards. For both the cool flame and the ignition delay, the time after start of actual injection (defined as start of activation plus hydraulic delay) and the axial position are summarized in table 7.5. Results are typically based on 10 individual measurements.

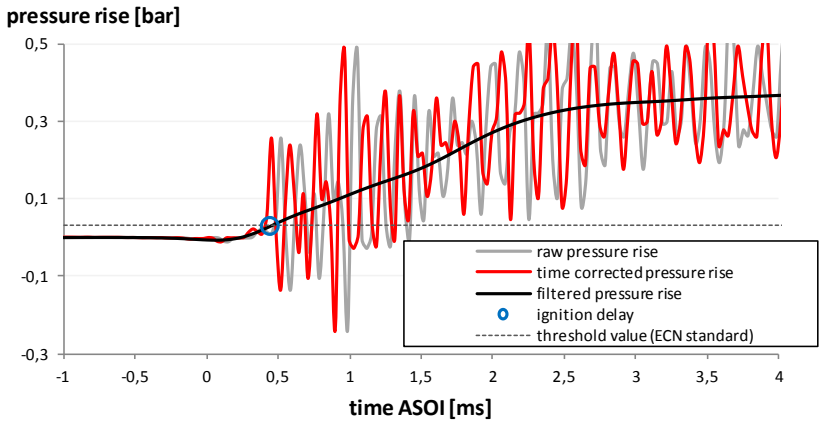

Figure 7.9: Pressure increase after ignition. The raw pressure signal is already corrected for preburn cool down pressure decay.

An ignition delay of 443μs is obtained, which is in line with the '*spray A*' results found by other institutes. A comparison of the ID is presented in Fig. 7.10. In order to have a more direct comparison a correction based on the linear dependence on the nozzle diameter is presented as well. This correlation was found by Payri *et al*. [180].

7.2.4 Flame lift-off length

An important and often studied characteristic of fuel spray combustion is the location where the flame front initiates and stabilizes during an injection event. The

	time [μs]	axial distance [mm]
cool flame ID		
average	394	16.0
std	34	1.7
hot flame ID		
average	443	17.6
std	34	1.24
ID pressure based		
average	408	-
std	38.5	-

Table 7.5: Results for the light- and pressure based ID measurements.

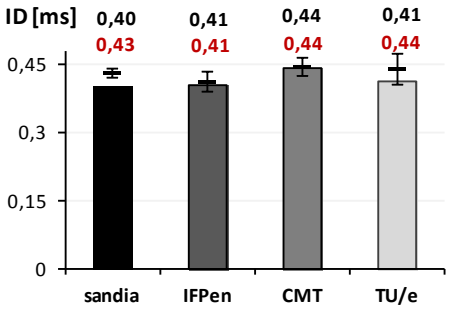

Figure 7.10: Comparison of the ignition delay (ID) based on the chemiluminescence between different institutes. The original values are shown in black at the top, the corrected values for the nozzle diameter are shown in red below.

distance from the injector of reaction zone stabilization after the time of auto-ignition is traditionally called the Flame Lift-Off Length (FLOL). The FLOL has a strong effect on diesel combustion. Flame lift-off allows fuel and air to premix upstream of the lift-off length, which affects the combustion and soot formation processes downstream [101].
A high speed imaging method as discussed in section 3.6.2 is implemented in order to obtain a time-resolved FLOL data. The detection of high temperature chemiluminescence from excited-state OH (OH*) indicates the location of the flame [183]. Normally OH* measurements are executed with a (single shot) ICCD camera and a relatively long exposure time (approx. 0.5*ms*). In this case the low intensity sig-

nals are intensified by a high speed intensified relay optic system (LaVision IRO) which is lens coupled to a high speed camera. A 310*nm* (10*nm* FWHM) optical bandpass filter is used for the experiments in order to capture the light emitted by the OH*-molecules and to block and avoid overexposure, primarily caused by soot incandescence as much as possible. The settings used for the camera and intensifier are shown in table 7.6.

frame rate [kHz]	21
resolution [mm/px]	0.2041
gating time [μs]	80
gain [%]	75
bandpass filter	310

Table 7.6: Settings flame lift-off length measurements

Post-processing of the FLOL recordings is done in 2 different ways. The first method is dedicated to making a direct comparison with the obtained measurement data from the other participating ECN institutes; Sandia, IFPEN and CMT. These institutes all used single shot ICCD cameras with a relatively long exposure time to capture the steady FLOL resulting in a "chip averaged" image [109, 122]. Therefore, for each TU/e experiment, a time-averaged image was generated by averaging the individual shots within the steady FLOL period of the injection. For direct CFD modeling validation, the time resolved evolution of the location of OH* will give a better insight in the evolution of the flame. For this method both the minimum and maximum location are of interest. In this case, the minimum distance can be regarded as the traditionally defined FLOL and the head of the flame as the maximum flame penetration. One conclusion drawn from the obtained images is that the used measurement approach suffers from internal reflections from the, uncoated and therefore (too) shiny, combustion vessel walls. The slight increase in intensity observed from the injector tip at 0*mm* up to approx. 15*mm* downstream reveals this effect on the intensity profiles. Although this is an undesired effect, it appears not to influence the obtained result since this "noise" is far below the used threshold value.

The obtained results for the time averaged FLOL measurements are summarized in Figure 7.11. The results from the other ECN participants who executed FLOL measurements are also shown here. This data has been taken from the Sandia website and results were discussed during the 2nd ECN workshop.
Pickett *et al.* [181] found that the FLOL depends on the nozzle-hole diameter to

the power 0.34. The nominal injector diameters from Fig. 7.2 are therefore used to correct the obtained results to make a fair comparison. This correction has been added to the results of Fig. 7.11 (indicated with the red values).

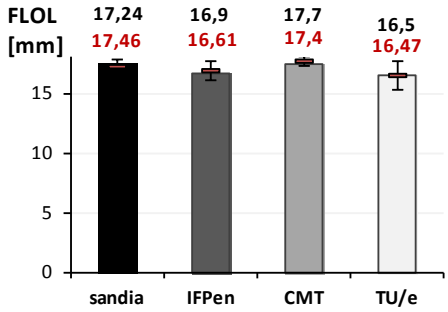

Figure 7.11: Comparison of the flame lift-off length (FLOL) between different institutes. The original values are shown in black at the top; the corrected values for the nozzle diameter [181] are shown in red below (data from the ECN2 workshop).

Post processing of the time resolved OH* images is done in a similar way as for the time averaged FLOL results. A post-processed single shot OH* image under '*spray A*' conditions is shown in Fig. 7.12 and a time resolved overview of the minimum and maximum FLOL is shown in Fig. 7.13. From Fig. 7.13 it can be observed how the upstream flame stabilizes till the end of injection while the down-stream flame at the head of the spray penetrates in axial direction. At the end of injection the upstream flame (FLOL) rapidly moves downstream and merges with the head of the spray till the flame quenches (black line). In some cases, but not always, it is noticed that at the end of injection the minimum FLOL not only moves downstream but splits and also moves back upstream to the injector tip. This phenomenon is presented in Fig. 7.13 by the red symbols. The reason why this upstream movement does not occur for every injection event is not well understood at this moment and cannot be explained based on the other available measured variables. Future work to investigate this more in detail is therefore recommended.

7.3 Numerical 'Spray A'

In this section, the inert '*Spray A*' is investigated numerically by the phenomenological model as described in chapter 5. The comparison with results of the Valencia group [89, 132] has already demonstrated the validity of the model which is now further validated for the '*spray A*' conditions.

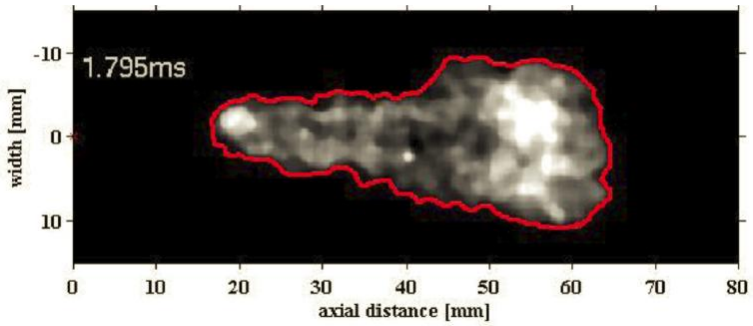

Figure 7.12: Post-processed single shot intensified OH image.*

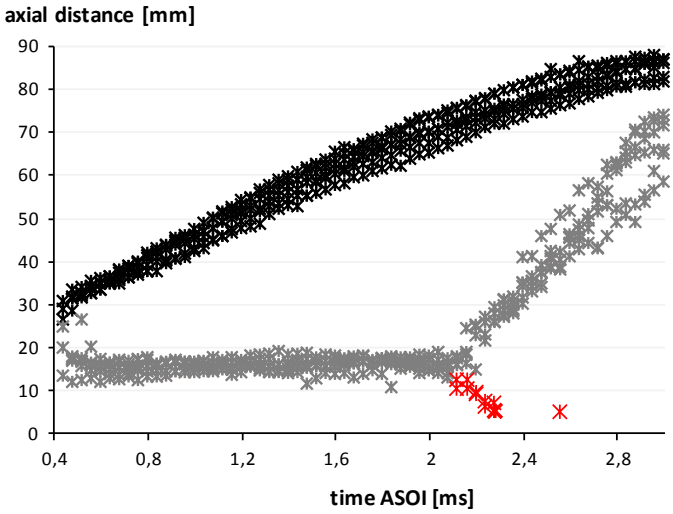

Figure 7.13: Time resolved FLOL and maximum flame penetration. The black symbols represent the tip of the flame and the grey symbols represent the flame lift-off length. The red symbols also represent the FLOL, but the flame travels towards the injector after end of injection. This was only seen in a couple of experiments

The fuel properties of n-dodecane and the initial boundary conditions were taken as specified for '*spray A*' (cfr. table 7.1) and supplied to the spray model.

Since injection velocity measurements are lacking, the velocity is estimated with the Bernouilly equation:

$$v = C_d \sqrt{\frac{2\left(P_{inj} - P_{a0}\right)}{\rho_{fl}}} \tag{7.5}$$

with ρ_{a0} the fuel density, P_{inj} the injection pressure, P_{a0} the ambient pressure

and C_d the discharge coefficient. This assumption results in a constant injection velocity of $553 m/s$.
From the discussion of the model in chapter 5, the spray angle is the tuning parameter that is used to fit the liquid length LL of the model to the experimental results ($LL = 10.3mm$). The experiments reveal a constant average spray angle of $18.6° \pm 1.1°$ for all performed experiments of the inert '*spray A*'. An angle input of 18° to the model gives the best results and is shown in Fig. 7.14 and in Fig. 7.15.

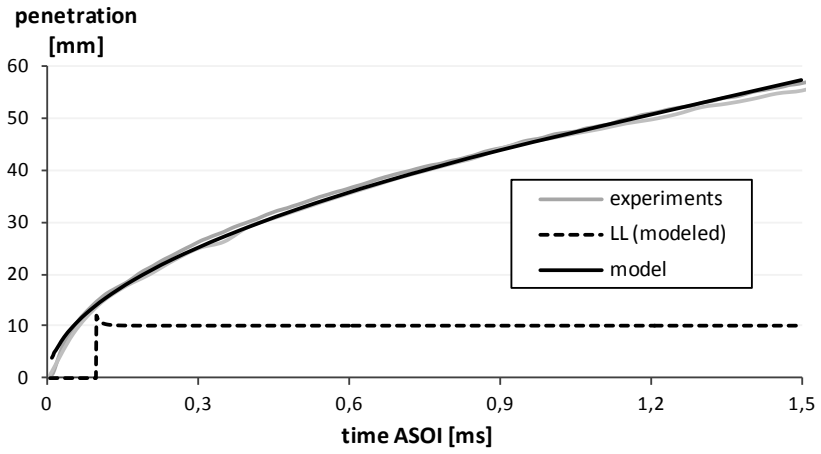

Figure 7.14: Comparison of the model result (black) with the experiments (grey). The modeled liquid length is represented by the dashed line.

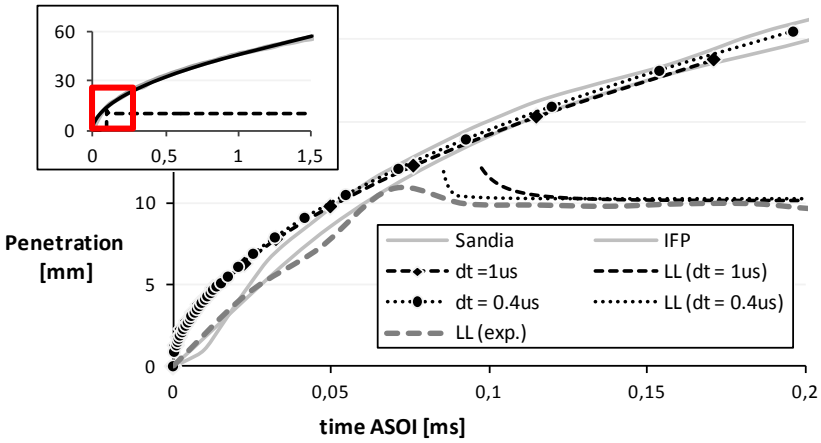

Figure 7.15: Zoomed view of the liquid length prediction

The model in Fig. 7.14 predicts the initial penetration well, but near the end of

injection, the model slightly overpredicts the experimental results. This is expected to be caused by the influence of the ambient velocities which become of the same order as the spray tip velocity. This causes more deflection of the axial velocity to the radial direction with a stronger head vortex as a consequence. The velocity deflection at the spray tip has been confirmed experimentally by IFPen [124]. Their PIV measurements of the spray velocity at 1.5*ms* after start of injection are shown in Fig. 7.16.

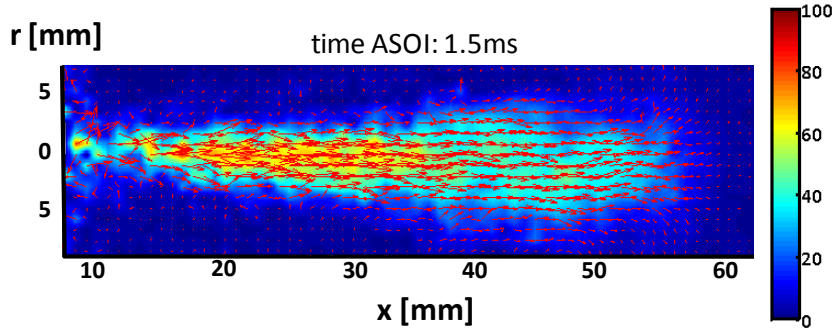

Figure 7.16: PIV measurements of the spray velocities, performed by IFPen [124]

Although the constant liquid length was tuned to fit the model, the transient behavior of the liquid length and the time instant at which the liquid length is detected for the first time. The experimental liquid length (grey dashed line in fig. 7.15), measured with the diffused back illumination technique (DBI) is initially longer and travels back towards the nozzle till a constant value is obtained.
The fact that a transient liquid length is predicted by the model is a direct result of the conservation of mass: if the velocity is increased in the considered cell, the fuel fraction will be smaller if the input boundary conditions are the same. This is clearly noticed for the axial velocity for a specified position on the spray axis (here $x = 15.3mm$) as a function of the time (cfr. Fig. 7.17). The vertical lines represent some interesting events in time: the time instant at which the penetration becomes 15.3*mm*, the time instant at which the first liquid length is detected and the time instant at which a steady liquid length is established.
Near the tip, the velocity and fuel fraction changes for each axial position with the time. Physically it can be explained by the high resistance from ambient gas that the fuel at the tip experiences. More upstream, the fuel experiences less resistance since the ambient is already in motion due to the previously injected mass. As time progresses a steady situation at the considered axial position is reached for the different parameters as well as the liquid length.
The transient situation is sensitive to the grid size as demonstrated in Fig. 7.15 in which 2 different timesteps were used ($\Delta t = 0.4\mu s$ and $\Delta t = 1\mu s$). The smaller the

time step, the shorter the transient behavior and the earlier the liquid length exists. The steady state liquid length value on the other hand is nearly not affected. The only small differences in the steady value origin from the interpolation due to the different grid size.

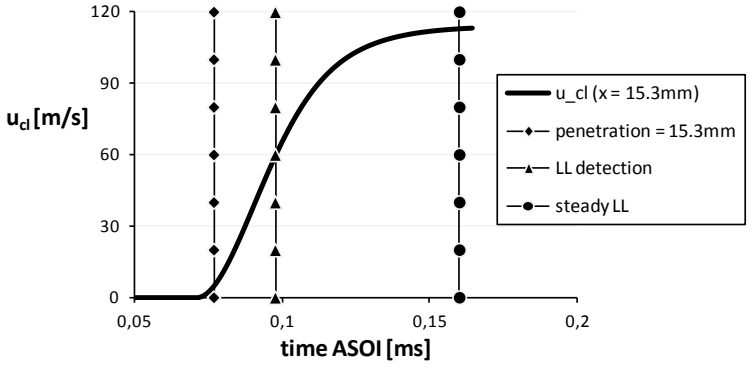

Figure 7.17: The axial velocity at specified position on the spray axis ($x = 15.3mm$) as a function of the time. The vertical lines represent the time instant at which the penetration becomes 15.3mm, the time instant at which the first liquid length is detected and the time instant at which a steady liquid length is established.

The important question arises whether the prediction of a transient liquid length and whether the timing of liquid length formation is important. The liquid length will contribute to place and timing of the ignition as it is an indicator for the atomization quality, so from this point of view it might be relevant. However, in the case of '*spray A*', the ignition delay is around $0.4ms$ in which a steady liquid length is already established. Furthermore, the experimental transient part of the liquid length is small and the average peak liquid length is very near the standard deviation range for the steady state value. As such, no further attention is given to this phenomenon which might only be interesting to investigate further when the ignition delay becomes of the same order as the liquid length formation, which is rather unlikely, especially with the focus on vegetable oils (with the cetane number of 30-45 compared to the cetane number of n-dodecane of 80 [184]).

7.4 Conclusions

7.4.1 Experimental '*Spray A*'

A complete set of basic spray diagnostics were carried out in the constant volume combustion chamber at the Technical University of Eindhoven together with ir. Maarten Meijer. Hardware and processing methods were applied as proposed by the Engine Combustion Network (ECN) for '*spray A*' (unless otherwise stated) to

have a direct and correct comparison between measurements from other participating institutes.

The evaluated parameters were liquid length, spray penetration, flame lift-off and ignition delay. Based on the executed measurements the following conclusions can be derived from this work:

- The flame lift-off, ignition delay, liquid length and spray penetration showed good agreement among the different institutes within the standard deviation boundaries.
- The nozzle holes for - theoretically identical - injectors differ among each other. Correction on the measurement results through the use of 0D models from literature lets the results converge even more when comparing between the different institutes.
- Difficulties for the processing of shadowgraph images concerning background movement can be significantly improved by using acquisition rates higher than $20kHz$.
- Although there are known differences in liquid penetration and spray shape because of nozzle or facility differences, the combustion (ignition delay and lift-off length) measurements show consistency between institutions, suggesting a certain insensitivity of the spray details to the ultimate combustion, at least at '*spray A*' conditions.
- The start of combustion is noted in the spray penetration data. However, a clear definition for ignition delay based on the spray penetration data is not yet proposed.

The results for the measured parameters for the reacting spray (penetration, liquid length (*LL*), ignition delay (*ID*) and flame lift-off (*FLOL*)) are summarized in Fig. 7.18. The corresponding grey lines represent the standard deviation boundaries

7.4.2 Numerical '*Spray A*'

The proposed spray model was validated for the inert '*Spray A*' conditions, with the following conclusions:

- The penetration was predicted well with the tuned spray angle within the range of measured spray angles.
- The transient behavior of the liquid length reaching a constant value was also fairly well predicted. The transient behavior was both explained in terms of the existing physics as well as in terms of the model behavior.

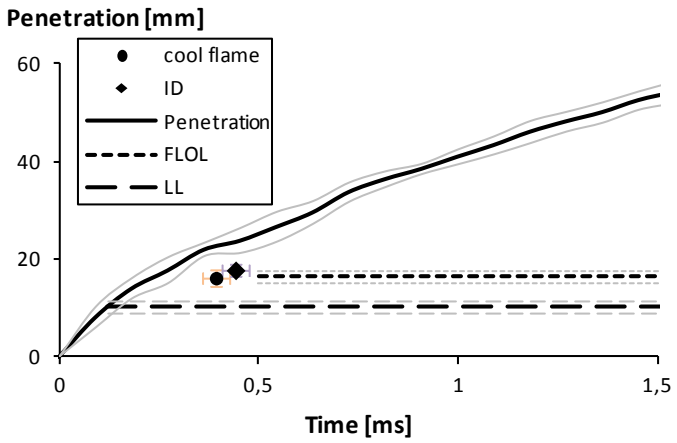

Figure 7.18: overview of the measured parameters for a reacting 'spray A': penetration, liquid length (LL), ignition delay (ID) and flame lift-off (FLOL). The grey lines represent the corresponding standard deviations.

- The transient behavior of the liquid length was found to be sensitive to the time grid size while the steady state value was not.
- For high penetrations (>60*mm*), the model slightly overpredicts the measurement values. It is assumed that this was due to the low velocities, making the spray sensitive to the surrounding velocity field. However at that time, the end of the combustion chamber will already be reached.

8

Medium speed diesel spray injections

"I have not failed. I've just found 10000 ways that won't work"

- Thomas A. Edison -

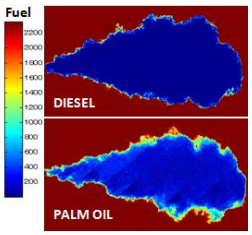

The chapter is organized as follows: Cold spray experiments and the behavior of different diesel fuels are reported. First, some fuel properties are compared for the different fuels. Next, the behavior of the injection pressure and needle displacement profiles are studied under different conditions. Finally, optical spray measurements are discussed for the fuels. This includes the penetration development, spray angle, tip velocity and some remarks concerning the spray structure. The chapter finishes with some conclusions and expectations for the combustion process and engine output.

8.1 Introduction

In this chapter, the behavior of some crude oil sprays is evaluated under cold inert, but pressurized ambients. The amount of tested oils is limited, but general conclusions can be drawn based on the results of the data set as will be mentioned in section 8.7. The different aspects of the spray that are investigated are schematically shown in Fig. 8.1. The vapor phase and combustion are shown in light gray since they are not yet considered in this study.

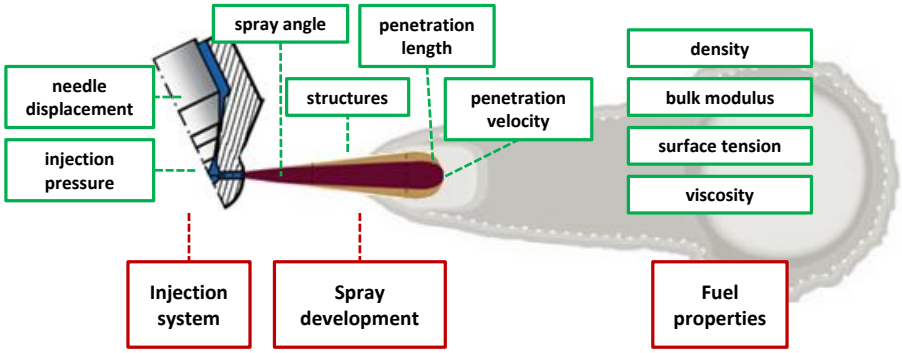

Figure 8.1: Overview of the parameters analyzed in this chapter: fuel properties, injection system, spray development

All experiments described in this chapter were obtained with the GUCCI-setup, partially by thesis students. Most of the results were published in 'Experimental investigation concerning the influence of fuel type and properties on the injection and atomization of liquid biofuels in an optical combustion chamber, Galle J., Van de Maele C., Piloto Rodriguez R., Denon Q., Verliefde A., Verhelst S., *Biomass and Bioenergy*, 2013'.

8.2 Experimental conditions

Several fuel properties and setup settings were varied to investigate their influence on the behavior of the injection system (section 8.4) and spray development (section 8.5). The varied settings are summarized in table 8.1. Some of the conditions are only very briefly reported in this work. The main reason is the lack of relevance of the considered condition, however they were tested as they might have given some useful information. As an example, spray experiments at atmospheric chamber pressure did almost not show any atomization and only a few data points could be gathered before impacting the wall. For this reason this condition was not further investigated. The poor atomization is shown in Fig. 8.2. From the image sequences it was clear that the mushroom-shaped spray tip (cfr. section 2.4.3) did

not exist or was not fully developed before hitting the wall. The arrows indicate the liquid flow direction of the spray tip.

Boundary condition	**value range**
fuel	diesel (D) / animal fat (AF) / palm- (PO) / rapeseed oil (RSO)/ rapeseed methyl ester (RME)
engine speed [*rpm*]	400 / 700 / 1000
injection pump setting [-]	half load / full load
fuel temperature [$°C$]	20 - 90
ambient temperature T_a [$°C$]	20 - 150
ambient pressure P_a [MPa]	0.1 / 4 / 6 / 8 (N_2 ambient)

Table 8.1: Measurement matrix for experiments in this work

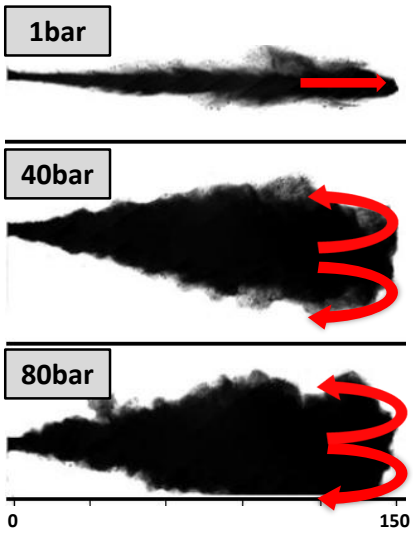

Figure 8.2: Difference in spray atomization under different ambient pressures. The arrows indicate the liquid flow direction of the spray tip.

8.3 Fuel properties

From chapter 2 it is understood that the fuel properties have a strong influence on the behavior of the spray.

The most important fuel properties (viscosity, surface tension, bulk modulus and density) were measured and are summarized in Fig. 8.3 and Fig. 8.4.
In this chapter, only the spray atomization at low temperatures is considered. One of the reasons is that the experimental setup was not yet able to deal with vaporizing sprays and secondly, the conclusions from non-vaporizing sprays might be able to help understanding the vaporizing sprays. After all, the spray part close to the nozzle is dominated by the fuel (density and temperature), rather than by the ambient [89].
Since this is a purely physical process, the chemical composition of the tested fuels is not included in this section. For the GC-MS analysis, the reader is referred to appendix C. The link between physical properties and chemical composition is handled in section 6.5.

The measurements for the viscosity, density and surface tension were conducted at the department of Applied Analytical and Physical Chemistry (prof. A. Verliefde) of the Faculty of Bioscience Engineering with the support of Quenten Denon. The measurement methods and equipment can be found in appendix C. For the bulk modulus (cfr. Fig. 8.4), no measurement equipment was available, so the data was gathered from the literature.
The rapeseed methyl ester (RME) was provided by Proviron Basic Chemicals NV (Oostende) together with a fuel analysis. That analysis was compared with the obtained results for RME in this section to validate the reliability of our measurements (cfr. Eq. 5.32).

8.3.1 Density

The measurements for animal fat (AF) and palm oil (PO) were started from 40°C as they start to solidify at lower temperatures.
RSO, AF and PO show the highest density, diesel has the lowest density and the values for biodiesel lie in between them. The density decreases linearly with temperature and the slope is the same for all tested fuels: -0.7mg/cm^3K (with R^2 > 0.9999).

8.3.2 Bulk modulus

The right equipment to directly measure the bulk modulus was not available. However, since the bulk modulus is important for the injection timing and the injection pressure profile (especially for PLN systems), values from literature are shown in Fig. 8.4.
The figure shows the results for 2 batches of diesel [185, 186], 2 batches of RME [186, 187], 2 batches RSO and PO and 1 for AF [188, 189]. The data of palm oil and rapeseed oil are very close to each other and almost not distinguish-

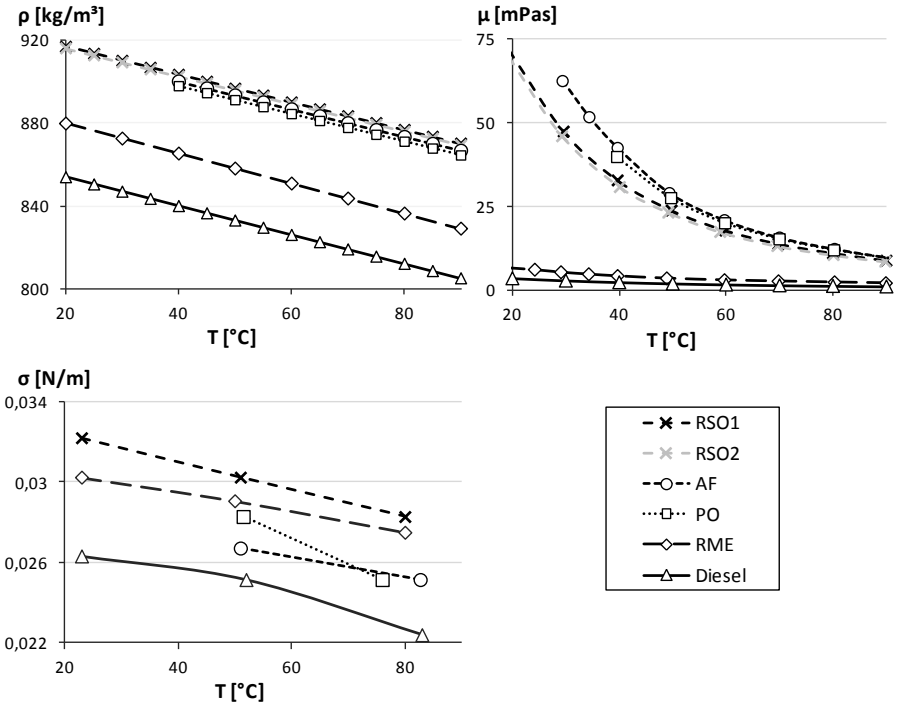

Figure 8.3: Measured physical fuel properties: density ρ, surface tension σ and dynamic viscosity μ

able on the figure. Interested to note is that McClements & Poveyt [189] reported speeds of sound obtained from different sources in literature for 13 crude oils at 20°C. They were all very similar (between 1460-1470m/s). As the density does not vary a lot for different crude oils, the bulk moduli are expected to be similar for the different oils.

The same trends as observed for the fuel density, can be repeated here. RSO and PO show the highest bulk modulus, diesel the lowest bulk modulus and the values of biodiesel lie in between them. Similar to the density, the bulk modulus shows an almost linear behavior with temperature. However, the slope of the curves are not exactly equal as was observed for the density. These data were obtained by different authors and even for two samples of diesel fuel, the slopes of both curves are significantly different but are between 7 and 10$MPa/^{\circ}C$.

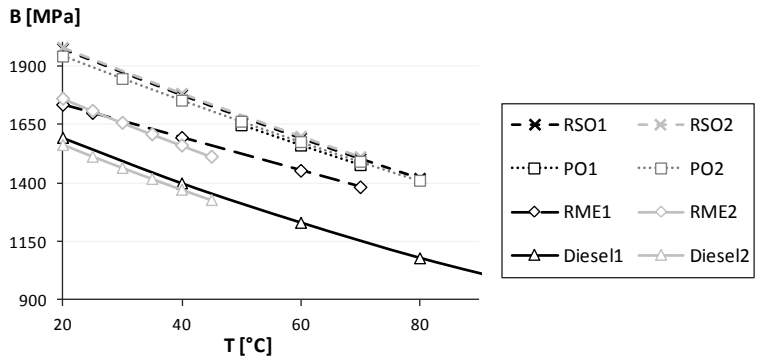

Figure 8.4: Temperature dependency of the bulk modulus, data obtained from literature

8.3.3 Surface tension

Again, measurements for PO and AF could not be conducted at low temperatures. Diesel has the lowest surface tension, RSO the highest. Furthermore, the surface tension of RME is higher than those of AF and PO.
For all fuels a linearly decreasing trend was noticed.

8.3.4 Dynamic viscosity

As was already mentioned in section 6.5, the exponential relation between the temperature and viscosity, results in strong viscosity differences at low temperatures (up to more than an order of magnitude). At higher temperatures, exceeding 80°C, the viscosity converges for the different oils, but is still up to 5 times higher than for diesel and biodiesel. Nevertheless the strong viscosity reduction of the oil with increasing temperature, the spray development might still differ from diesel.
The results show that a direct link between viscosity and surface tension is not obvious, as is usually considered in many simplifications used in literature: both decrease with temperature, but not with a similar relation with respect to temperature.

8.3.5 Fatty acid composition

The fatty acid composition is shown in table 8.2. This information is not used for the experiments described in this chapter, but can be useful as a reference when combusting sprays are investigated in future work.

Fatty acid	formula	RSO_1	RSO_2	PO	AF
Lauric	C12:0	0.0	0.0	0.1	0.2
Myristic	C14:0	0.1	0.0	1.0	2.1
Palmitic	C16:0	4.8	3.6	42.0	23.0
Stearic	C18:0	3.6	3.3	4.5	17.7
Oleic	C18:1	58.9	55.3	40.1	35.3
Linoleic	C18:2	20.2	19.1	11.1	12.8
Linolenic	C18:3	10.7	8.5	0.5	0.5
Arachidic	C20:0	0.6	0.2	0.3	0.0

Table 8.2: The fatty acid composition obtained from a GC-MS analysis.

8.4 Injection system

The parameters of the injection system that can be characterized with the GUCCI-setup are the cam angle-resolved needle displacement and injection pressure. These 2 parameters were studied by varying the boundary conditions as mentioned in table 8.1. The time-resolved information is acquired by measuring the time between each 2 cam angles.
The synchronized time-resolved development for both the injection pressure (P_{inj}) and needle lift (NL) is displayed in Fig. 8.5. In order to make the discussion more meaningful, some points are defined. These points and their definition are presented in table 8.3.
Some remarks should be mentioned. First, a partial needle lift occurs at low engine speed (<400rpm) as will be discussed later on. Secondly, the needle displacement exhibits strong oscillations after closing, caused by the elastic deformation of the needle/seat which acts as a mass-spring-damper system. Finally, the main full lift is 0.65mm, but maximum lifts higher than 0.65mm are obtained at the end of the needle lift, again due to elastic deformation of the system.
Later on it will be shown that the ambient pressure does not have any significant effect on most of the pressure profile and needle lift parameters (except for the partial lift at 400rpm). Therefore, the average values over 4/6/8MPa points are only indicative. The average standard deviation of the some measured parameters are shown in Fig. 8.8.
Although the pressure waves traveling inside the injection pipe, result in 'wavy' pressure profiles, it was observed that the variation in timing of the different events (NL_{start}, EOI,...) is very small. Most parameters expressed in $°ca$ have a standard

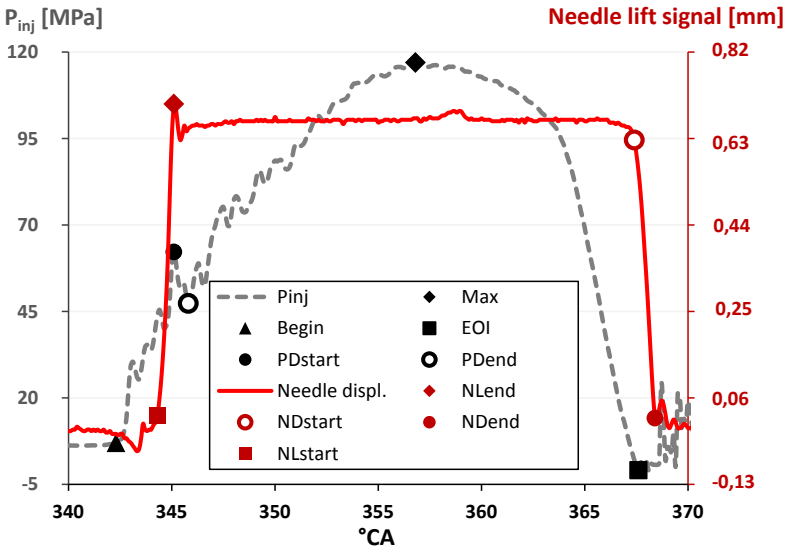

Figure 8.5: Synchronized time-resolved injector pressure profile and needle lift signal with the definitions to characterize the profiles

deviation below $0.1°ca$, which is the measurement interval. This is mostly related to the less reproducible injection profile at $400rpm$. The standard deviations at 700 and $1000rpm$ are significantly smaller. This is shown in Fig. 8.6 and Fig. 8.7. The upper graph in both figures represents the absolute standard deviation of the injection pressure (Fig. 8.6) and needle lift (Fig. 8.7) for the different parameters as defined in table 8.3. The lower graph shows the standard deviation of the position at which the defined parameter occurs in $°ca$.

Besides the timing, the absolute pressure at every moment in time is very reproducible too. The standard deviation on P_{max} is only around 0.3 to $0.4MPa$. Compared to the absolute values which are 80 to $120MPa$, this is less than 0.5%. Larger standard deviations can occur in a few cases. First of all, at $400rpm$, the standard deviation is larger in the first part of the injection. This is due to the needle displacement in this region, as will be discussed later in section 8.4.1.

The pressure waves after EOI are found to be significantly less reproducible (cfr. Fig. 8.8).

Finally, the percentage standard deviation can be somewhat higher before the actual injection. Keeping in mind the small absolute values of the initial pressure, this corresponds to standard deviations below $0.1MPa$.

Point	Definition
P_{init}	pressure in the pipe prior to injection
NL_{init}	needle lift prior to injection
P_{start}	start of pressure rise (P_{inj} = P_{init} + 1MPa)
NL_{start}	start of needle lift (NL = 4% of full lift)
NL_{end}	end of needle lift (NL = 96% of full lift)
PD_{start}	start of the pressure drop caused by the needle lift (manually selected)
PD_{end}	end of the pressure drop caused by the needle lift (manually selected)
P_{max}	point at maximum injection pressure
EOI	end of injection (P_{EOI} = $5MPa$)
ND_{start}	start of needle closing (NL = 96% of full lift)
ND_{end}	end of needle closing (NL = 4% of full lift)
SPD_{start}	start of pressure drop caused by partial needle lift (manually selected)
SPD_{end}	end of pressure drop caused by partial needle lift (manually selected)
MNL_{start}	start of the main needle lift (manually selected)

Table 8.3: Definitions of some important points on the needle lift and injection pressure profiles

8.4.1 Needle displacement

Needle lift

The fuel volume in the injection pipe and pump V is compressed until the injector needle lifts. This moment is determined by the forces acting on the needle and is defined as the point where the needle lift exceeds 4% of the full lift. The same definition holds for the closing of the injector. On the one hand there is the force of the spring (F_s), that keeps the injector needle on its seat, on the other hand there is the pressure of the fuel acting on the needle resulting in the force F_p. Once the needle opening pressure (NOP) is reached, F_p overcomes F_s and the needle starts to lift. The dynamics of the needle displacement can be expressed as follows:

$$m.a(t) = F_p(t) - F_s(t) - F_v(t) \tag{8.1}$$

where *a(t)* is the upward acceleration of the needle. F_s is proportional to the needle displacement. The viscous force F_v is proportional to the needle surface area A and

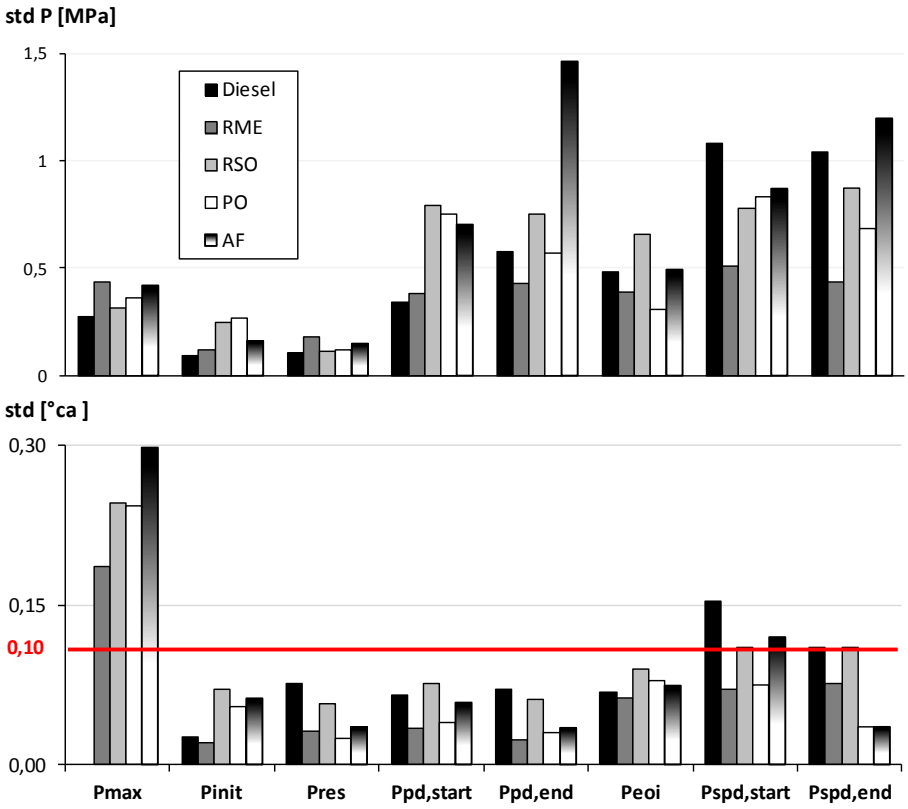

Figure 8.6: Averaged standard deviation (9 experiments) of the injection pressure points for the different fuels

the fuel viscosity μ:

$$F_v = \mu A \frac{dv(t)}{dy} \tag{8.2}$$

with $\frac{dv(t)}{dy}$ is the velocity gradient in the fuel surrounding the needle.

Equation 8.1 and Eq. 8.2 show that the inertia of the needle with mass m and the viscous forces of the fuel, slow down the needle displacement. This causes a significant delay between the moment when the *NOP* is reached and the moment when the needle actually starts to lift. During this period pressure build-up continues. Figure 8.9 shows NL_{start}, which is the cam position at the moment when the needle starts to lift, as a function of fuel temperature for different fuels.

The most important fuel properties affecting the moment of needle lift are the bulk modulus and the viscosity. A higher bulk modulus causes a higher injection

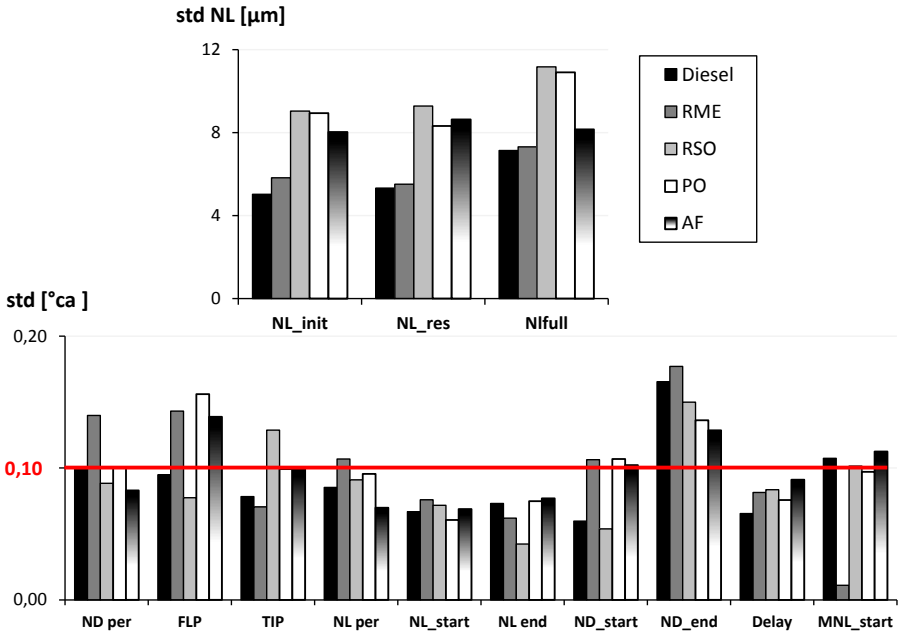

Figure 8.7: Averaged standard deviation (9 experiments) of the needle lift points for the different fuels

pressure, a larger F_p and thus an earlier start of needle lift. A higher viscosity increases the viscous forces and delays the start of needle lift. The effect of viscosity retarding the needle displacement was already observed for common rail (CR) injections [190, 191]. For CR injection systems, the injection pressure is constant at the needle, so there is barely any effect of the bulk modulus counteracting the effect of viscosity.

The needle lift is delayed and the needle rise is less steep when T_f increases, due to the decrease in B as is demonstrated in Fig. 8.10 for RSO. The differences are small but significant for all measurements. For the SVO's and AF, the changes in viscous forces are more important than for diesel and RME. The effects of the bulk modulus and viscosity counteract each other resulting in an NL_{start} which is less dependent on the fuel temperature.
In the high temperature range (70-90°C), where the viscosity is rather constant, the effect of the bulk modulus becomes more dominant: the needle lift is retarded and is less steep with increasing temperature.
One can conclude that at elevated temperatures (> 60°C) the higher bulk moduli of SVO and AF lead to an earlier start of needle lift of about 0.5°CA compared to diesel injections. This is noticed in the results of Fig. 8.11 where the needle lift is

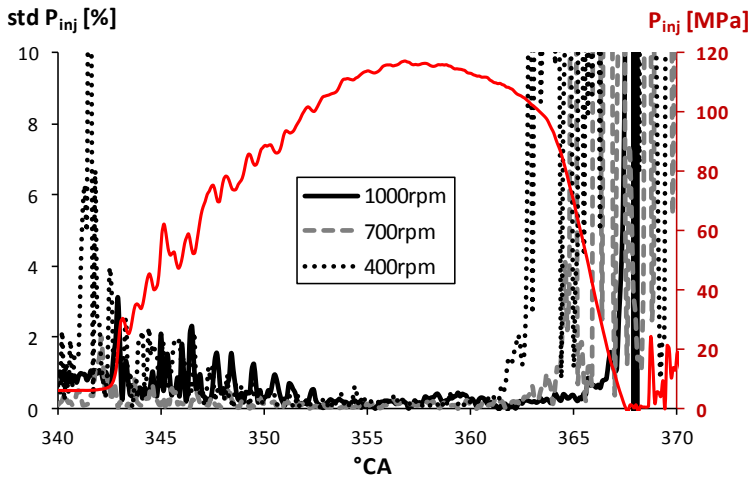

Figure 8.8: The standard deviation of the injection pressure for the different speeds. The red curve indicates the injection pressure profile at 1000rpm

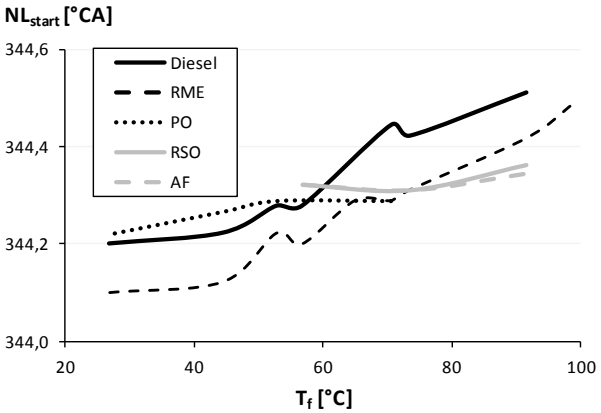

Figure 8.9: NL_{start} as a function of fuel temperature for different fuels. Average values of 9 experiments at engine speed set point of 1000rpm.

compared for the different fuels at a fuel temperature T_f of $90°C$.

At low engine speeds, the needle lift was observed to consist of two phases (cfr. Fig. 8.12). This can be explained as follows: on a degree cam angle based scale, the pressure buildup before needle lift is independent of the engine speed. Once the fuel pressure exceeds the *NOP*, the dynamics of the needle can be expressed using Eq. 8.1. If the needle starts to lift, a sudden pressure drop is induced. At 400*rpm*, this pressure drop, causes the pressure to fall below the *NOP* again. Thus, during

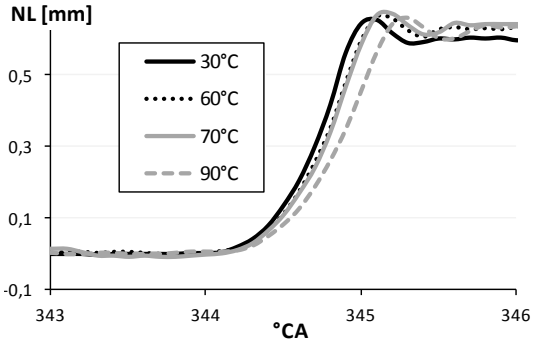

Figure 8.10: Dependency needle lift for RSO on the fuel temperature (T_f=30°C, 50°C,70°C, 90°C, T_a=140°C, engine speed = 1000rpm, P_a=8MPa)

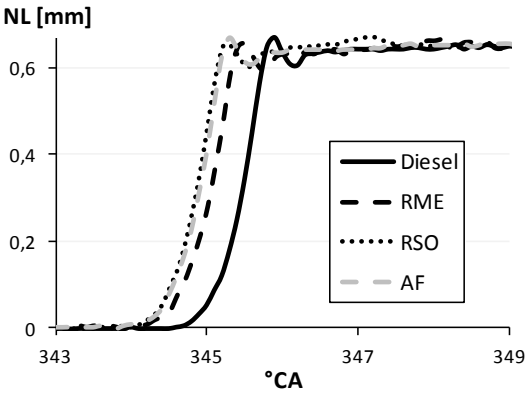

Figure 8.11: Comparison of needle lift as a function of °CA for diesel, RME, AF and RSO injections (T_c=90°C, T_a=140°C, T_f=91.5°C, engine speed = 1000rpm, P_a=6MPa)

a short period of time, the resulting force on the needle is directed downwards again. Due to the slower cam speed, the inertia force of the needle is lower. This allows the needle to drop again, but does not fully fall back on its seat. During this partial needle lift, a small amount of fuel is injected at low speed and is probably poorly atomized. The most important parameter affecting this partial needle lift at low engine speeds is the bulk modulus. First of all, B affects the pressure rise before and during the needle lift and determines the pressure at start of needle lift. Furthermore, the pressure rise together with the viscous forces will control the moment, the velocity and the height of the first partial lift.

For SVO and AF, an earlier start of needle lift is observed, similar as for the higher engine speeds. Furthermore, the pressure at start of needle lift is higher and the height of the partial lift is between 25 and 40% of full lift, compared to 8-20% for

diesel and RME (cfr. Fig. 8.12).

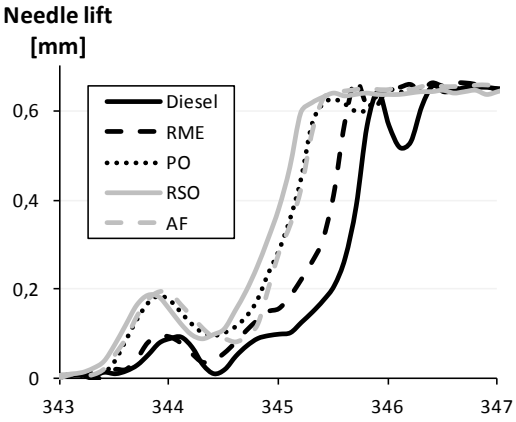

Figure 8.12: Needle lift at 400rpm engine speed as a function of °CA for diesel, RME, AF and RSO (T_c=70°C, T_a=140°C, T_f=74°C, P_a=6MPa)

There is a slight effect of temperature on the height of the partial lift (cfr. Fig. 8.12). The height decreases at higher temperatures because of the temperature dependent behavior of B. A more important parameter however, is the chamber pressure. The chamber pressure acts up on the needle tip, resulting in an extra upward force. At high engine speeds, these forces were negligible compared to the fast and high pressure buildup. At 400*rpm*, on the contrary, this affects the height of the partial lift significantly. For SVO and AF an increase of 10% of full lift was observed when the chamber pressure was increased from 4 to 8*MPa* for the case of RSO (cfr. Fig. 8.12).

Injection period

As we use a PLN system, in the ideal case the cam angle based (full load) injection duration should always be the same, independent of the engine speed and fuel.
This is because the full needle lift period *FLP* is mechanically determined by the injection pressure: if the pressure at the needle seat is higher than a pre-set value, the needle lifts. In the case of used ABC-injectors this pressure was set to 27.5*MPa*, regulated by a spring load. The needle lift period is defined as the time between opening and closing of the nozzle. In reality, the fuel compressibility, leakage, component expansion, the friction losses and the inertia of moving components provide changes in the duration.
The inertia of the moving components has a significant influence: as will be concluded in section 8.4.2, the higher the engine speed, the higher the injection pressure and the longer the injection duration expressed in °*CA*. On a time based scale

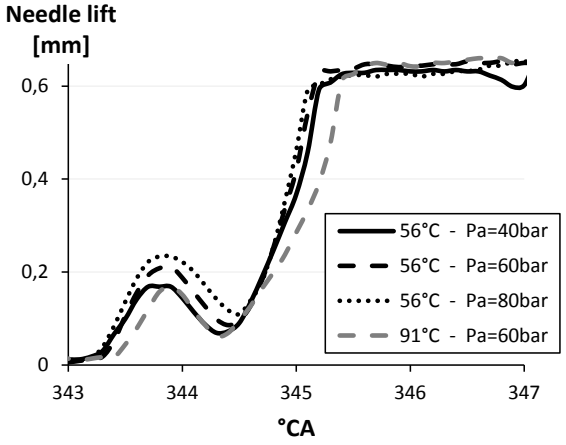

Figure 8.13: Needle lift at 400rpm engine speed as a function of °ca for rapeseed oil at different fuel temperatures and chamber pressures

however, the injection period decreases with increasing engine speed.

To express the volumetric flow rate through the nozzle orifices, the theoretical volume flow rate of the fuel is multiplied with a discharge coefficient C_d:

$$\dot{V} = C_d \dot{V}_{th} = C_d A \sqrt{2\frac{\Delta P}{\rho_f}} \tag{8.3}$$

with ρ the fuel density, A the orifice cross section and ΔP the pressure drop across the orifice and V the volume of fuel between the plunger of the pump and the injector needle.

Different authors [58, 78] stated that the discharge coefficient is independent of the fuel density for every constant ΔP.
The volume V_{th} is considered constant for a constant pump setting ($2000mm^3$ for the considered experiments), if leakages are neglected.
So from Eq. 8.3 the injection duration is directly proportional to the square root of the ratio of ρ to ΔP. For PLN systems, $\dot{V}$ is not constant during an injection because ΔP (and thus C_d) is not constant. These changes in ΔP cause only very small changes in ρ, so we can assume ρ to be approximately constant.

Using the simplification that ΔP is constant (which is actually only valid for CR systems), Eq. 8.3 expresses that the injection duration is directly proportional to $\sqrt{\rho}$. This simplified analysis shows that the fuel density is an important parameter affecting the injection duration and is confirmed by the experimental results: a lin-

ear relationship between the full lift period (*FLP*) and $\sqrt{\rho}$ is observed in Fig. 8.14. It can be concluded that the higher density of SVO and AF results in longer injections at lower volumetric flow rates, but higher mass flow rates. This effect can be slightly reinforced by the reduced leakages for SVO and AF, caused by their higher viscosity and resulting in a slightly higher injected fuel volume per injection [192].

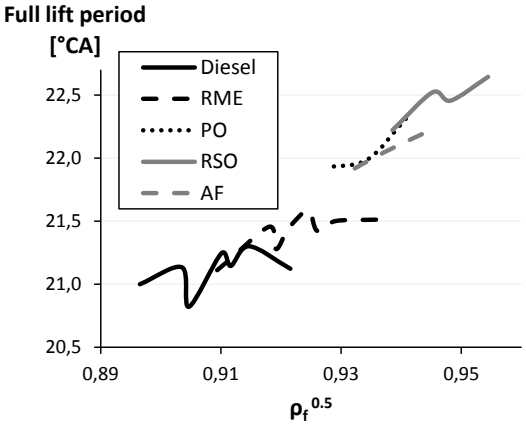

Figure 8.14: Fuel influence of the fuel on the relation between density and injection duration at 1000rpm

The duration of the needle lift period did not seem to vary a lot with temperature. The observed increase of 0.1°*ca* between 40 and 90°C is possibly the result of a decreasing bulk modulus but is within the experimental uncertainty. The differences between different fuels, however, are more clear. The needle lift period of diesel injections (1-1.1°ca) is longer than the one of RME injections (0.9°ca) at 1000*rpm* engine speed. For injections at 700*rpm* no significant difference was observed (1.3-1.5°ca) between these two fuels.
The needle lift period of SVO and AF injections is shorter (0.8°*ca* at 1000*rpm* and 1-1.1°*ca* at 700*rpm*). This can be related to the higher bulk modulus of SVO and AF, increasing F_p acting on the needle during lift. The viscous forces do not seem to have a significant effect on the needle lift period.

Needle drop

Once the decrease in volume induced by the pump plunger becomes lower than the volume flow rate of fuel through the nozzle orifices, pressure starts to fall. When the pressure falls below the *NOP*, F_s becomes higher than F_p and the needle starts to drop. The timing of the needle drop depends on the inertia of the needle.

The start of the needle drop ND_{start} is affected by the accumulated influences on the end of needle lift and the full lift period.
An increasing bulk modulus lowers NL_{end} and an increasing density increases the *FLP*. The latter is the dominant effect, when comparing different fuel temperatures or different fuels. SVO's and AF result in an earlier start of injection and a later end of injection compared to diesel injections.

The effect of fuel temperature on the needle drop period is not very clear. At 1000*rpm* the *ND* period seems to shorten when temperature rises. This could be caused by a decrease in viscous forces. However, the differences in average ND period were smaller than $0.1°CA$ and may not be considered as significant. At 700*rpm* no consistent trend with temperature is observed. Neither could any conclusions be drawn comparing the different fuels. The difficulty in the analysis was mainly due to the oscillatory behavior at the closing of the needle.
The influence of engine speed however, was significant: contrary to the *NL* period, the *ND* period shortens on a °CA based scale for the 700*rpm* experiments (0.7-0.8°CA) compared to the 1000*rpm* experiments (0.9-1.1°CA).

8.4.2 Injection pressure

Figure 8.15 illustrates the significant effect of fuel properties on the injection pressure profile. All these effects on the different phases of the injection process will be discussed in detail in this section.

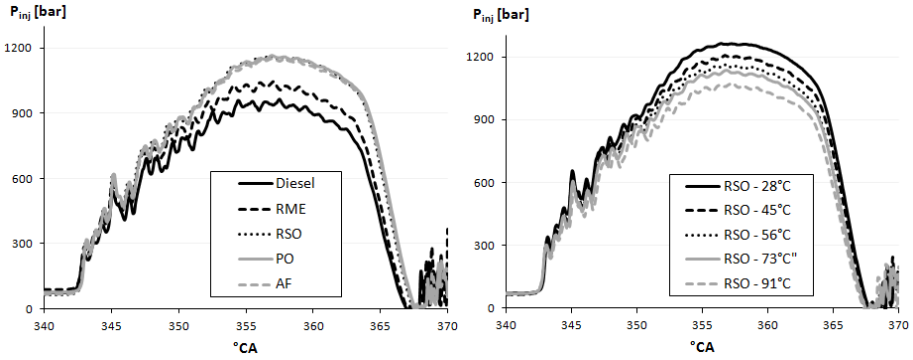

Figure 8.15: Influence on the injection pressure profile for different fuels (left) and different fuel temperature (right)

Pressure buildup

For a PLN injection, the movement of the injection pump plunger is cam shaft driven. Pressure is built up inside the pump, causing the delivery valve of the pump to open. As the cam shaft is rotating, the plunger moves upward and the

volume V is reduced. The increase of pressure related to this decrease in volume is mainly determined by the bulk modulus of the compressed fuel:

$$\frac{dP}{d\alpha} = -\frac{B(P,T)}{V}\frac{dV}{d\alpha} \tag{8.4}$$

where α is the cam angle and $\frac{dV}{d\alpha}$ the volume change which is determined by the geometry of the cam. The secondary parameters affecting the pressure are the expansion of the fuel pipe when pressure rises and the fuel leakages along the plunger, but these are neglected here.

The start of pressure buildup is defined by the parameter *Begin* (cfr. Table 8.3). The pressure sensor is mounted on the injection pipe about 400*mm* away of the plunger. For the different fuels and/or fuel temperatures, the velocity of sound varies from approximately 1300 to 1500*m/s*. As a result, the maximum difference in traveling time between the measured signal and pressure at the needle is very small. Even at 1000*rpm* these differences are less than 1°*CA*.

As expected from the discussion in section 8.4.1 and Eq. 8.1, a significant effect of the engine speed on *Begin*. The results for diesel are shown in Fig. 8.16 for the 3 different engine speeds (400, 700 and 1000*rpm*) was observed.

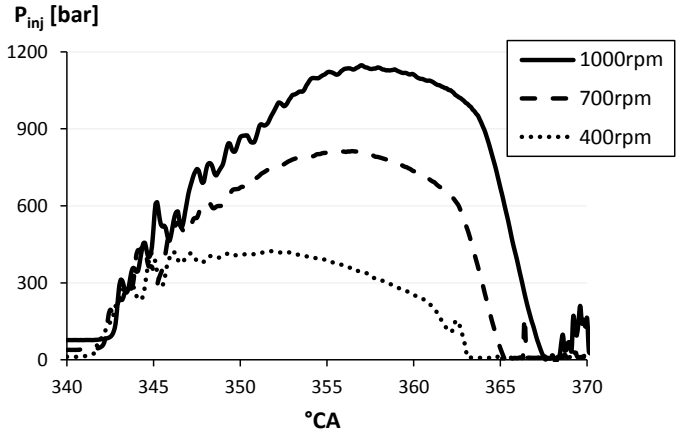

Figure 8.16: Injection pressure profiles of injections with palm oil at different engine speed setpoints. T_c = 60°C, T_a = 140°C, T_f = 65°C and P_a=6MPa

The pressure buildup is geometrically determined and thus P_{init}+1*MPa* is reached at the same cam position for every experiment with equal B. The traveling time of the pressure wave is equal on a time based scale and thus large differences are observed when traveling time is expressed on a °*CA*-based scale. Calculations of the traveling time made clear that this is exactly the cause of the observed differences

in the parameter *Begin* for experiments at different engine speeds.
After *Begin*, the pressure buildup continues. Many pressure waves travel back and forth along the injection pipe. They cause the wavy (but reproducible) injection pressure profile (cfr. section 8.4.2) which makes it more difficult to express the rate of pressure build-up (*RPB*). Here, *RPB [MPa/°CA]* is defined as the slope of the linear curve between *Begin* and PD_{start} (cfr. Fig. 8.5). Based on Eq. 8.4, the RPB is expected to be directly proportional to the bulk modulus. Furthermore, due to the proportial relationship between fuel temperature and bulk modulus, a linear dependence of the RPB and fuel temperature is expected to exist. This is confirmed in Fig. 8.17.

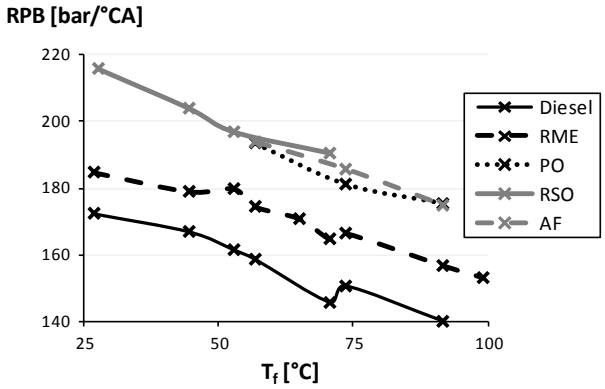

Figure 8.17: Rate of pressure buildup as function of fuel temperature for different fuels

Pressure oscillations

The pressure profile is quite wavy due to pressure waves traveling along the injection pipe and the injector. However, the exact same wave pattern is observed for different measurements at the same conditions. Small variations were observed between different fuels due to changes in the speed of sound c (cfr. Fig. 8.18). The frequency of the superposed oscillation is approximately $4kHz$ and is considered as a characteristic of the injection circuit: the wave travels back and forth in the injection pipe. However for such a complex system it is very difficult to actually predict these frequencies. Seykens *et al.* [127] found that the superposed oscillation in their common-rail system acts as a standing wave in a tube with one closed end where the rail acts as the open end and the nozzle as closed end. For the pump line nozzle system it is more difficult due the more complex construction of the internal pump volume taken by the fuel which varies in time during injection.
The largest dip in the pressure profile (between 345 and 346°CA in Fig. 8.15) is caused by the opening of the needle.

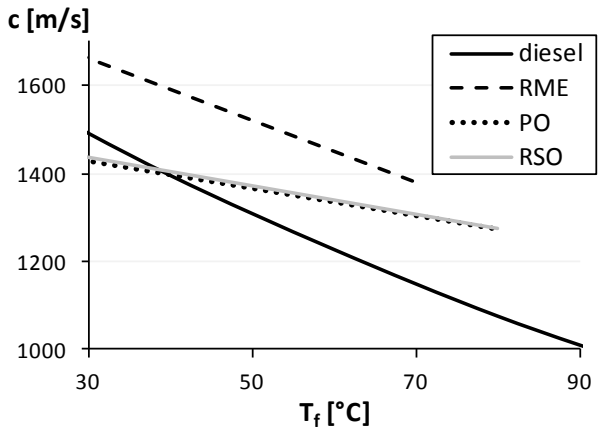

Figure 8.18: The temperature dependence of the speed of sound for the different fuels

The amplitude of the waves is attenuated due to the viscosity of the fuel [189, 193]. For the more viscous fuel, such as SVO's and AF, the injection pressure profile for the different curves are rather smooth at the top of the injection pressure profile. This is not the case for the less viscous fuels RME and diesel (cfr. left of Fig. 8.15). The same can be seen on the right of Fig. 8.15: the lower the fuel temperature and thus the higher the viscosity, the more smooth the injection pressure profile.

At the end of injection, after the closure of the needle, the pressure signal is strongly oscillating. Again this is caused by pressure waves. In this region the waves are not completely reproducible resulting in high standard deviations. However, the frequency seems to be quite constant for all measurements. The oscillatory region after the end of injection will not be studied in detail here.

Pressure drop

When the needle rises, fuel starts to leave the nozzle through the orifices and enters the chamber. The sudden decrease in pressure at the nozzle tip results in a pressure wave traveling upstream. When it arrives at the pressure sensor, a drop in the pressure profile is observed. The distance between the sensor and the needle tip is about $400mm$, the delay between the start of the needle lift and the start of the drop is $0.8°CA$ at $1000rpm$ and $0.6°CA$ at $700rpm$ engine speed. Both correspond to $280ms$, which is the time needed to travel to the sensor at the velocity of sound in the fuel. Although the differences are smaller than the standard deviation on the delay, it was possible to detect an increasing trend of the delay with increasing fuel temperature, due to the decrease in speed of sound of the fuel.

Maximum pressure

The pressure rises as long as the decrease in volume exceeds the volume flow rate of fuel. Once the decrease in volume becomes lower than the volume flow rate of fuel, pressure starts to fall. The transition between these two phases determines *MAX*. The maximum pressure reached during the injection is affected by different processes:

- The most important fuel parameter is the bulk modulus. This property defines the pressure rise related to the decrease in V. In this way, the needle lift was affected, but the point *MAX* at which the maximum pressure is observed, is not influenced. The maximum pressure P_{max} itself, on the other hand, will increase for higher B.
- The density of the fuel, determines the volumetric flow rate through the nozzle (cfr. Eq. 8.3). This parameter affects the point where P_{max} is reached and thus affects the mass of fuel inside V at *Max* and thus affects P_{max} itself. Because of the higher volume flow rate for diesel and RME, the maximum pressure was reached earlier.
- small effects of pressure waves can affect P_{max}. Especially at $400rpm$ where the relative importance of these waves is most significant.

The analyses show an approximately linear relationship between P_{max} and T_f and between $P_{max}$and B for all engine speeds and fuels. This can be seen in Fig. 8.19. Figure 8.19 presents the maximum pressures of all the $1000rpm$ measurements as a function of the fuel temperature and confirms the linear relationship with B.
If we compare diesel at $30°ca$ and the SVO's at $70°ca$, Fig. 8.3 predicts equal bulk moduli (at atmospheric pressure). However, comparing P_{max} for both cases, we still observe a difference above $10MPa$ as indicated on Fig. 8.19. Two possible theories can explain this behavior.
First of all, the higher viscosity for SVO's reduces leakages, this result in a small increase of P_{max} as was reported by Hassaneen [192]. Secondly, no sufficient data about the increase of the bulk moduli of the used fuels at elevated pressures is available.

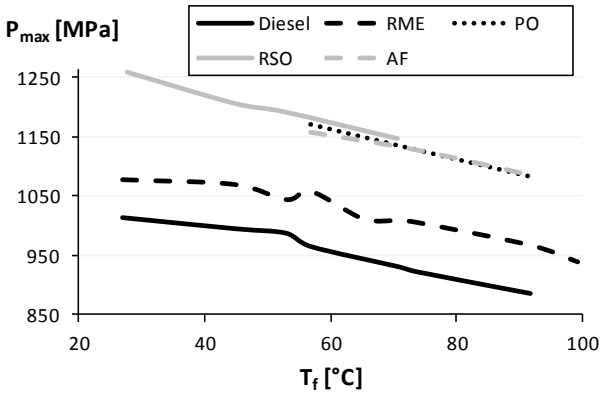

Figure 8.19: Maximum pressure reached during the injection as function of the fuel temperature T_f for injections at 1000rpm for the different fuels.

8.5 Spray development

As was discussed in chapter 3, spray measurements are difficult even with the current technology and standard deviations are rather high for the measured spray parameters [64, 79, 117]. The standard deviation for the performed experiments is about 4% for both the liquid length and Siebers spray angle. The typical development of the standard deviation is given in Fig. 8.20 for the liquid length (left) and the spray angle (right).

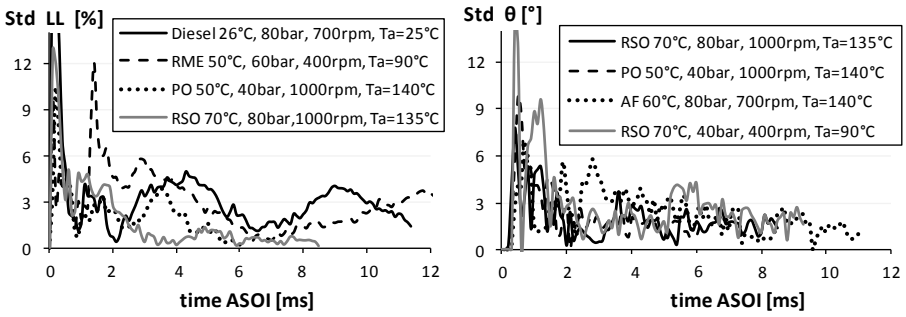

Figure 8.20: Typical obtained standard deviation for the liquid length (LL) and Siebers spray angle θ (cfr. section 3.3)

8.5.1 Spray angle

From section 2.4.2 it was suggested that $tan(\theta)$ was proportional with ρ_a^x, with x between 0.17 and 0.20 (for CR systems). The considered experiments were in

close agreement with the results of Desantes *et al.* [80] and a linear dependency to $\rho_a^{0.19}$ was found. Since the ambient temperature was restricted between 90 and 140°C only, the ambient density did not change a lot between these two temperatures for a fixed ambient pressure. Varying the fuel temperature did not alter the spray angle for diesel and RME. However, for RSO and RME, a decreasing spray angle was observed with increasing temperature (cfr. Fig. 8.21). The higher spray angles at higher fuel temperatures for the SVO could be related to the stronger decrease in viscosity, density and surface tension. In Fig. 8.21 measurements with diesel, RME and RSO at T_c = 60°C are shown for P_a = 4MPa and P_a = 8MPa, after moving average filtering (with a moving average parameter of 5) that was necessary because of the high noise levels. An increase of approximately 5° was observed between 4 and 8MPa.

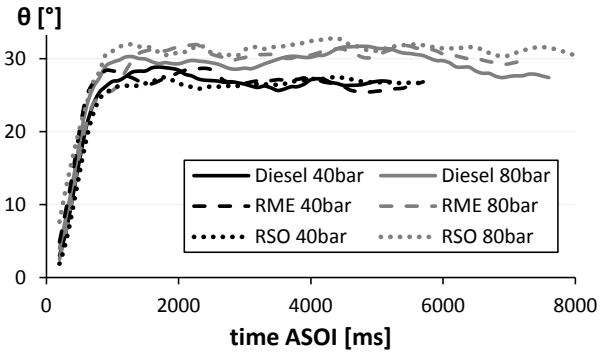

Figure 8.21: Influence of ambient pressure on the spray angle θ after moving average filtering. Injections with diesel, RME and RSO. T_c=60°C, P_a=4 and 8MPa, 1000rpm.

The influence of the engine speed on the spray angle was investigated by comparing spray angles at engine speeds of 400, 700 and 1000rpm. When varying the injection speed between 700 and 1000rpm, no significant differences in the steady state spray angle were detected as is shown in Fig. 8.22. The spray angle at 400rpm however, showed a very irregular progress as a function of time for some experiments. Mostly, a steady state spray angle was reached similar to the 700 and 1000 rpm injection, but sometimes the spray angle increased as function of time during the whole injection event (cfr. Fig. 8.22). This was observed frequently and for different fuels, especially at 8MPa.
Figure 8.22 shows that it takes more time for the spray to penetrate and develop at 400 and 700rpm compared to the 1000rpm sprays. This was also found for the other fuels and is due to the lower injection pressure at lower engine speeds. This results in the fact that more time is needed to reach a steady state spray angle.

Similar steady state spray angles for different injection pressures are also reported

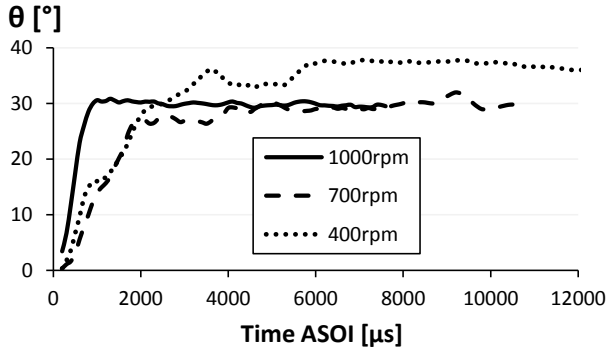

Figure 8.22: Influence of the engine speed on the (moving average of the) spray angle. Injection with AF at T_a=60°C, P_a=8MPa, engine speed of 400, 700 and 1000rpm.

in literature. Takahashi *et al.* [194] showed that once the injection pressure is sufficiently high, the spray angle no longer depends on the injection pressure. Desantes *et al.* [80] stated that at high injection pressures, a further increase in injection pressure can affect the spray angle through cavitation only.
This leads to the justified simplification that the spray angle can be considered constant during the bulk part of the injection duration, as is true for CR systems.
Although the steady state spray angle is similar, slightly higher spray angles were sometimes observed at SOI for higher engine speeds. Takahashi *et al.* [194] mentioned that for relatively low injection pressures, the spray angle increases with increasing injection pressures, due to better atomization. Another explanation is addressed to the 'mushroom shape' at the spray tip that was especially noticable at high engine speeds and high ambient pressures (8*MPa*). During the early moments of the injection this mushroom shape will strongly influence the spray angle, due to the used algorithm (cfr. section 3.3). The same behavior was discussed by Hattori and Narumiya [195]. They state that the mushroom shape is caused by the strong resistance of the ambient gas.

8.5.2 Spray penetration length

Naber & Siebers [79] proposed a correlation for the time-resolved spray penetration *S(t)* for a CR system as a function of the chamber density and the pressure drop across the nozzle (cfr. Eq. 8.5).

$$S(t) = 2\frac{\Delta P}{\rho_a} d_0 t 0.25 \tag{8.5}$$

with d_0 the orifice diameter and ΔP the pressure drop across the nozzle.

As was observed in the previous section, the dependency of the pressure drop

across the nozzle and chamber pressure can be neglected, when only the chamber density is changed. In a first approximation, the injection pressure is considered constant and the diesel penetration is plotted in the right graph of Fig. 8.23 as a function of $P_a{}^{-0.25}$, since a linear relation exists between the chamber pressure P_a and chamber density ρ_a. The left graph represents the direct corresponding measurements of the penetration versus the time after the visual start of injection. Although no common rail injection system was used, the linear relation is reasonably valid for the diesel spray. The analysis for the other fuels gave similar results. The

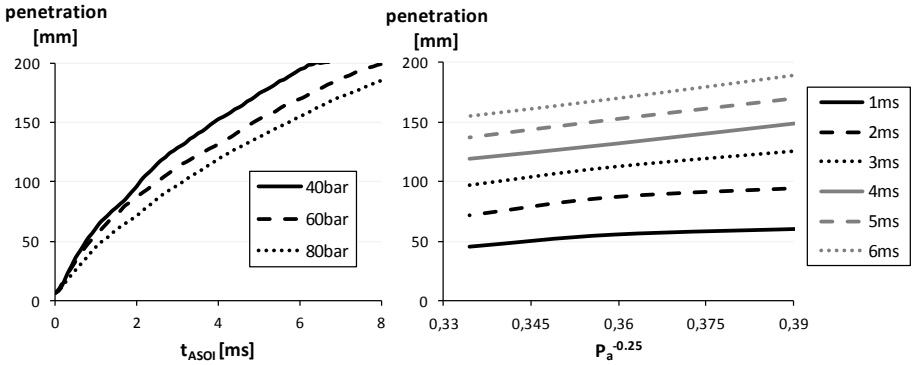

Figure 8.23: left: Influence of the ambient pressure on spray penetration for diesel at T_f=60°C, 1000rpm; right: the correlation validation of penetration as a function of $\frac{1}{P_a}{}^{-0.25}$

influences of the engine speed on the spray penetration can also be derived from Eq. 8.5 due to the nature of the injection system. The higher the engine speed, the higher the pressure difference across the nozzle and thus the higher the velocity of the fuel at the nozzle exit, resulting in faster spray penetrations.

Injections at 400*rpm* for diesel, RME and RSO are shown in Fig. 8.24. The spray penetration is quite different at SOI for 400*rpm* injections compared to the injections at 700 and 1000*rpm*. In the early stages, the spray tip penetration is very slow, while after some time, the spray tip velocity increases. This can be explained by the needle lift, which was found to consist of two phases at 400*rpm*. During the first phase, the needle lifts partially and a small amount of fuel is injected. Afterward, the needle drops again and less liquid is injected. This results in a low spray penetration velocity. When later on the main needle lift starts, a sudden increase in spray penetration velocity is observed. This is clearly reflected in the spray penetration progress: for RME and RSO, a significant decrease in penetration speed is observed, which corresponds to the small drop of the needle after the first phase of the needle lift. Changing the temperature of the fuel (from 20

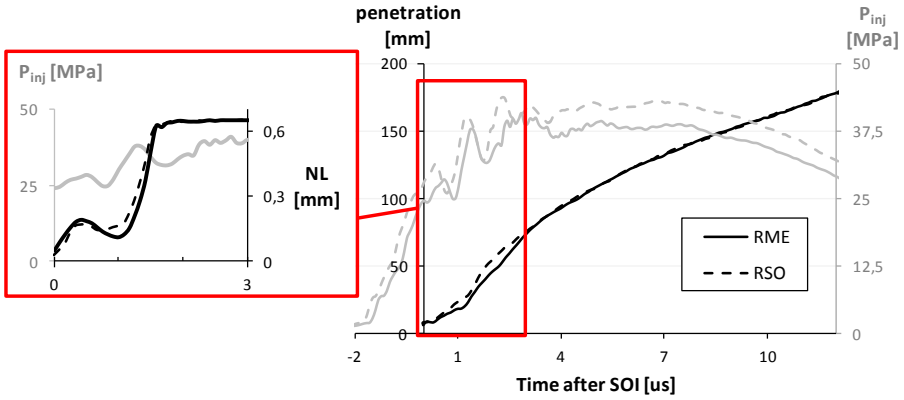

Figure 8.24: Effect of partial lift on the penetration for RME and RSO at T_f = 70°C, 400rpm, T_a = 90°C. The corresponding injection pressure is shown in grey and the needle lift on the zoomed part on the left.

to 90°*C*) did not show significant differences in spray penetration as is shown in Fig. 8.25. However, when zooming in on the plots, some observations can be made (cfr. Fig. 8.26). Although the differences are smaller than the standard deviation, the same trend was found for nearly all PO and AF but not for diesel and RME. A reasonable explanation can be found in the fuel properties. At lower fuel temperatures, the viscosity is significantly higher for the PO and AF, resulting in higher (viscous) nozzle flow losses. The effective injection velocity will be lower and the spray penetrates slower compared to less viscous fuels such as diesel. However, the higher viscosity causes bigger droplets in the spray. These have higher inertia and are less prone to the density resistance and the spray is less slowed down compared to fuel sprays with smaller droplets such as in less viscous sprays. A big reduction in viscosity is found in heating the fuel up 90°*C*.

The influences of the fuel properties are further investigated in Fig. 8.27: the penetration length for injections with diesel, RME, RSO and PO at 8*MPa*, 1000*rpm* and T_f = 65°*C* are compared.

During the early stages of spray formation, the penetration is quite similar for all fuels. This observation differs from most results in literature for CR systems [78, 190, 196], which report a decreased penetration for bio-fuels at the early stages of the injection. However, this can be attributed to the PLN system.

Injection pressures at the needle lift are higher for SVO due to their higher bulk modulus, so that the outlet velocity and thus penetration increases. This counteracts the increased friction due to the higher viscosity and the lower outlet velocity due to the higher fuel density. Together this results in similar spray penetrations at SOI for all fuels tested. In a later stage, the spray tip penetrations of PO, RSO and less clearly AF, are faster than those of Diesel and RME. A first explana-

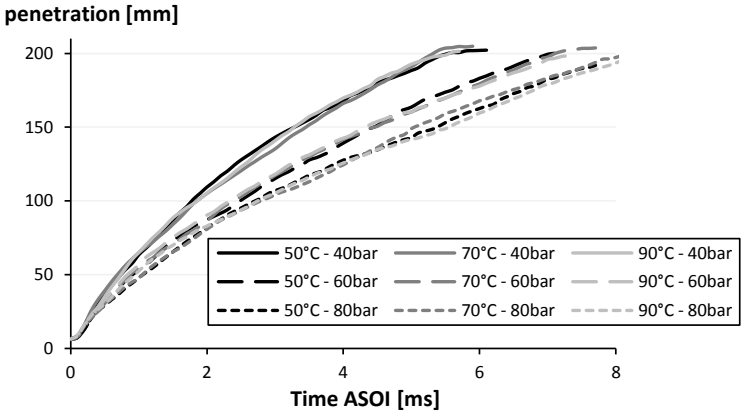

Figure 8.25: Influence of the fuel temperature and ambient pressure on the spray penetration. Injections with PO, at T_c=50°C (black), 70°C (gray) and 90°C (light gray). P_a=4MPa (dashed lines), 6MPa (solid lines) and 8MPa (dotted lines), T_a=140°C).

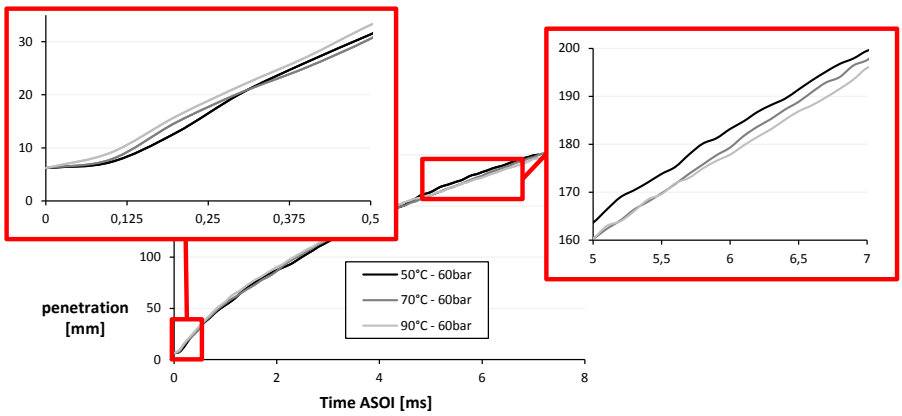

Figure 8.26: Influence of the fuel temperature of PO in more detail (T_c = 50°C (black), 70°C (gray) and 90°C (light gray). P_a=4MPa (dashed lines), P_a=6MPa, T_a=140°C)

tion is the higher injection pressures for SVO and AF when using a PLN system, due to their higher bulk modulus. However, the longer spray penetrations in the fully developed zone for SVO compared to diesel were also observed for CR systems [78, 190, 196]. There should be another explanation as well. This is found in the expression of the aerodynamic drag on a liquid droplet:

$$\alpha = -\frac{8}{3}\frac{\rho_{air}}{\rho_{fuel}} C_w \frac{1}{r} v^2 \tag{8.6}$$

where r is the radius of the droplet, v the droplet velocity relative to the surrounding gas, a the acceleration of the droplet, ρ_f the density of the fuel droplet and C_w the drag coefficient of the droplet.
Equation 8.6 shows that the higher density of SVO causes a decrease in droplet deceleration, causing the longer spray penetrations. Secondly, the droplet sizes of SVO are accepted to be larger than those of diesel and biodiesel [197]. Larger droplets experience less deceleration and result in longer spray penetrations. The larger droplet sizes are mostly attributed to their higher viscosity [78], surface tension [76] or both [197]. These droplet size studies were all conducted for CR systems. For PLN systems, the higher injection pressures of the SVO will decrease droplet sizes [198]. This effect only partly counteracts the influences of viscosity and surface tension on droplet sizes. We can conclude that during the early stages of the injection, the reduction in spray outlet velocity due to the high viscosity and density of the SVO and AF is counteracted by the increase in injection pressure at SOI due to the higher bulk moduli of SVO and AF. In the fully developed zone, the higher injection pressure and the larger SVO and AF droplets result in a longer penetration length.

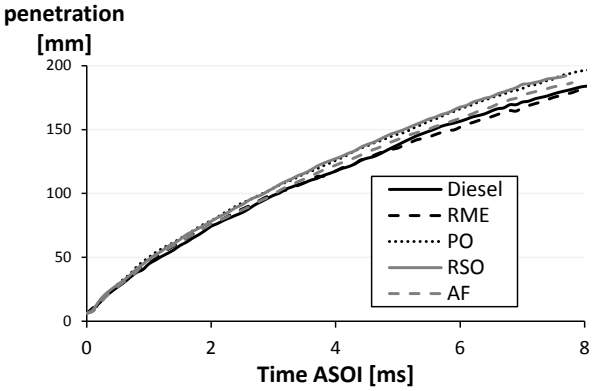

Figure 8.27: Influences of fuel type on the spray penetration. Injections with Diesel, RME, RSO, PO and AF are compared. P_a=6MPa, T_c=60°C.

Since the injection pressure has a big influence on the injection velocity and mass flow rate, the engine speed was varied from 400 to 1000*rpm* for the different fuels. As expected, the penetration increases with engine speed (≈ injection pressure) which is illustrated for AF in Fig. 8.28 for 4 and 8*MPa*.
The results for 400*rpm* consistently show a notch, a point where the penetration, after slowing down suddenly increases. This feature is found more or less at a similar point in time. A closer look at the signals for the injection pressure and needle lift, suggests that this is an artifact of the partial needle lift. It is hard to synchronize the needle lift, injection pressure and spray penetration due to the

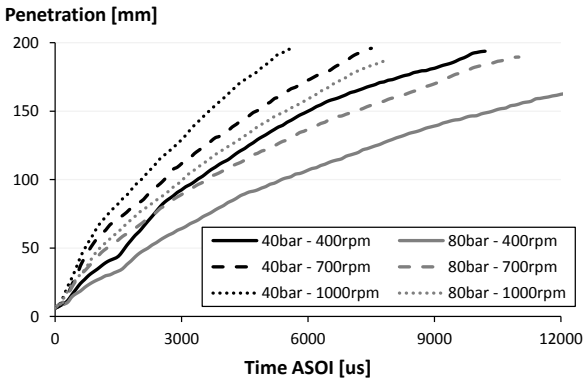

Figure 8.28: Influences of the engine speed and ambient pressure on the spray penetration. Injections with AF at P_a=4 (black) and 8MPa (gray) at engine speed of 400, 700 and 1000rpm.

mechanical complexity of the injection system and fuel properties. Figure 8.29 compares the needle lift and injection pressure at the time instant of the notch after applying delay corrections as described in section 4.3.2. The partial needle lift can be understood as 2 separate injections that follow each other very closely in time. The partial needle lift provides the early injection of a small part of the fuel; the penetration of this part of the spray, slows down as no pushing force exists anymore from the injected fuel. When the needle lifts again, more or new fuel is injected, pushing the already existing spray again forward. This results in a faster penetration, resulting in a notch in the spray penetration development.

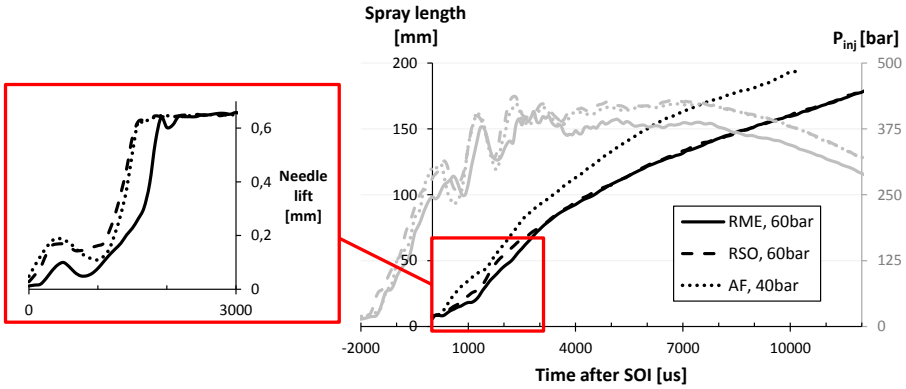

Figure 8.29: Spray penetration for RME, RSO and AF as function of time ASOI together with the corresponding needle lift and injection pressure signals (gray) for an engine speed of 400rpm, P_a=4/6MPa and T_c = 70°C.

8.5.3 Spray penetration velocity

The spray penetration velocity is defined as the slope of the spray penetration profile. The velocity was obtained in 2 ways. First, a sixth order polynomial was fitted to the spray penetration data. Increasing the order did not show any significant improvement. The velocity is defined as:

$$v_{tip,1}(t) = \frac{\delta S(t)}{\delta t} \tag{8.7}$$

The second method calculates the slope between 2 measured points:

$$v_{tip,2}(t) = \frac{S(t+\Delta t) - S(t)}{\Delta t} \tag{8.8}$$

It is important for the interpretation of the results to understand the difference between these 2 definitions. The definition with the polynomial approach will fit a best fit curve through the measured points, which can lead to defects at the end or the beginning of the profile. On the other hand the velocity profile will result in a smooth fifth order profile. This is shown in Fig. 8.30. The solid lines represent the polynomial approach (indicated with suffix "*(corr.)*") while the dashed line represents the filtered signal for slope approach. As can be expected from the

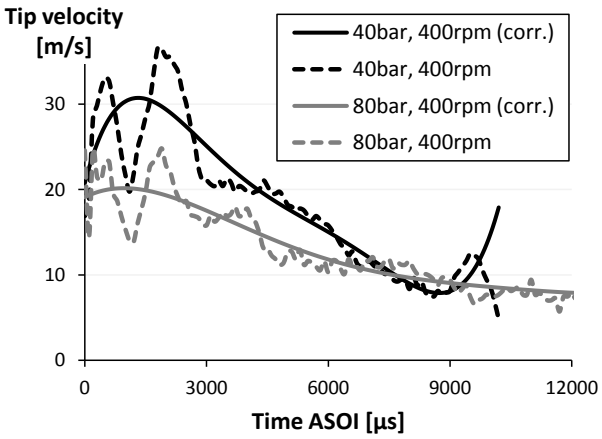

Figure 8.30: The difference between the 2 definitions for the spray tip velocity. T_f = 60°C, 400rpm and T_a=140°C.

discussion in section 8.5.2, the effect of the ambient density and injection pressure can be clearly noticed in Fig. 8.31 (in this case for AF): the spray tip velocity increases with decreasing density and increasing injection pressure (or engine speed). In almost any scenario, except for some cases at 400*rpm*, the velocity profile is S-shaped. This behavior was also observed by Takahashi *et al.* [194]. The

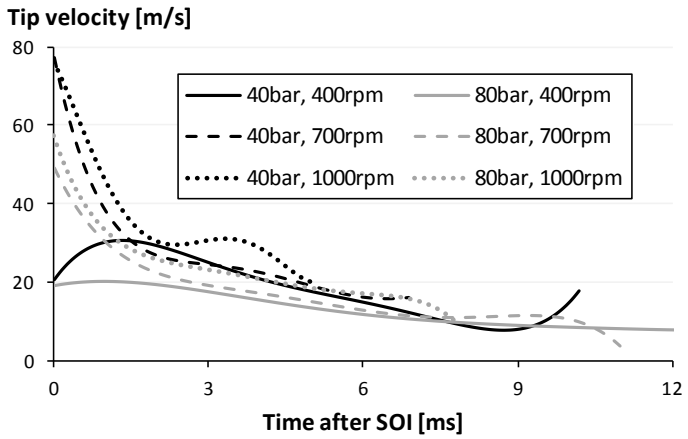

Figure 8.31: Influences of the ambient pressure and the engine speed on the penetration velocity. T_f=60°C and T_a=140°C. The spray tip velocity is calculated as the derivative of the spray penetration

fast decrease of the tip velocity at the later stage of the injection can be related to the existance of the mushroom-shaped spray tip: the attribution of the radial velocity start to become dominant compared to the axial velocity component.

It should be noted that the velocity at time $t = 0ms$ is not the injection velocity: this moment is the moment at which the spray becomes visible and this means the spray has already travelled for $6.2mm$ (cfr. section 3.3). The theoretical injection velocity is expressed by Eq. 8.9:

$$v_{0,th} = \sqrt{2\frac{(P_1 - P_a)}{\rho_l}} \tag{8.9}$$

The real injection velocity will differ from this value with the velocity coefficient C_v due to the turbulence, cavitation and other energy losses as discussed in section 2.3. The effective injection velocity could however not be measured due to the failed attempts to measure the effective mass flow rate. Another difficulty is that the thimble prevents the observation of the spray directly at the nozzle.
Furthermore, the image acquisition of $10kHz$ gives an accuracy of only $100\mu s$ which is found to be rather low for these measurements. For the spray tip velocity, the data starts from $300\mu s$ since the start of the measurements had excessive noise which makes it difficult to predict the effective injection velocity.

Considering Fig. 8.31 for both 700 and $1000rpm$, the distance between these two curves decreases and at $2ms$, the difference in penetration speed is around $5m/s$. This corresponds to the conclusions of Takahashi *et al.* [194]: the further down-

stream from the nozzle, the more difficult for the injection pressure to influence the spray penetration and the more important the influence of ambient density. From this point, the spray penetration seems to stabilize before it slows down at the final stage of injection. The S-shape of the curves, observed at 700 and 1000*rpm*, is similar to those observed by Takahashi *et al.* [194].
At 400*rpm* however, the penetration speed increases during the early stages of injection, which was not observed by these authors. This is mostly due to the partial lift that exist which was not the case for Takahashi *et al.*
For palm oil at high temperatures, the reduced density (related to the Bernoulli equation) and the decreased viscosity (less friction) seem to be dominant over the decreased injection pressure at start of injection. The penetration speed of PO during the early stage of the injection increased with the fuel temperature. However, further downstream of the nozzle, the effect of viscosity on the droplet size and the higher injection pressure seem to be the dominant factors affecting the penetration speed. Again this is seen in Fig. 8.32. Comparing the penetration speed of differ-

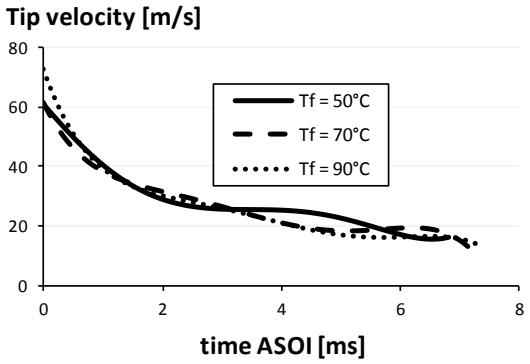

Figure 8.32: Influence of the fuel temperature for PO at an engine speed of 1000rpm, P_a = 6MPa, T_f = 60°C and T_a = 140°C.

ent fuels, one can observe that even in the early stage of injection, the penetration speeds of the highly viscous fuels is higher than those of diesel and RME. So, it is clear that the higher injection pressure is the most important factor.
it can be concluded that the penetration speed is higher for the SVO's during all stages of the injection mainly due to the higher injection pressure compared to diesel and RME. This was also already remarked in Fig. 8.27.

8.5.4 Structural differences

A big limitation of these measured parameters is that no structural difference was detected by the image processing software; 2 sprays with similar penetration development and detected spray angle are not necessary identical. This is especially

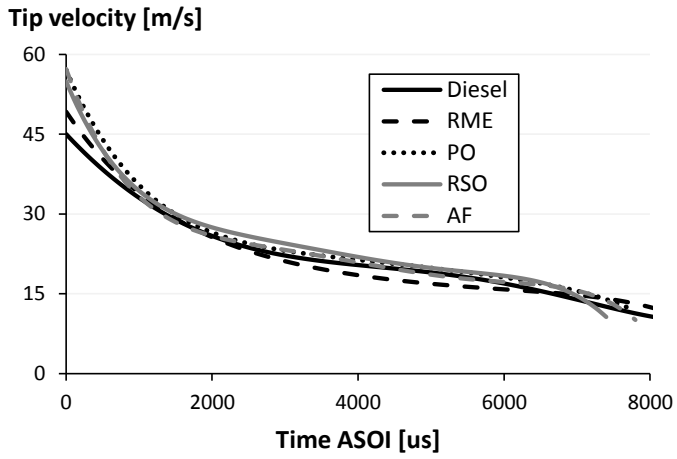

Figure 8.33: Influences of the fuel type on the penetration speed for an engine speed of 1000rpm, P_a = 8MPa, T_f = 60°C and T_a = 140°C.

true for viscous fuels, since the fuel mass or droplet size distribution can differ.
For fuel temperatures above 45°C, no clearly visible structural differences were observed between sprays of different fuels with the applied shadowgraph technique. At lower temperatures RSO droplets are larger than those of diesel and thus for a same volume of fuel, they take less space on the two dimensional spray images than more and smaller droplets. Due to the large droplets, some light can pass through the outer regions of the spray cone and therefore, on the two dimensional spray images, RSO is surrounded by a more clear area (cfr. Fig. 8.34). For diesel and RME sprays, the large amount of small droplets do not allow light to pass through the spray, resulting in very homogeneous two dimensional spray images. This means that increasing the fuel temperature up to 45°C results in a significant improvement of the atomization of the oil. This can be attributed to the decrease in viscosity: e.g. up to 45°C, viscosity of rapeseed oil decreases from 60 to less than 30$mPas$. This results in a significant reduction in droplet sizes and explains why no clear region was observed around the spray anymore.
Finally, the clear region around the spray was more explicit at lower engine speeds. This can be related to the higher *SMD* at lower engine speeds due to the lower injection pressures [198].
Most of the conclusions derived for the structural differences are only hypotheses and more advanced measurement techniques are required. Suggestions are made in chapter 9.

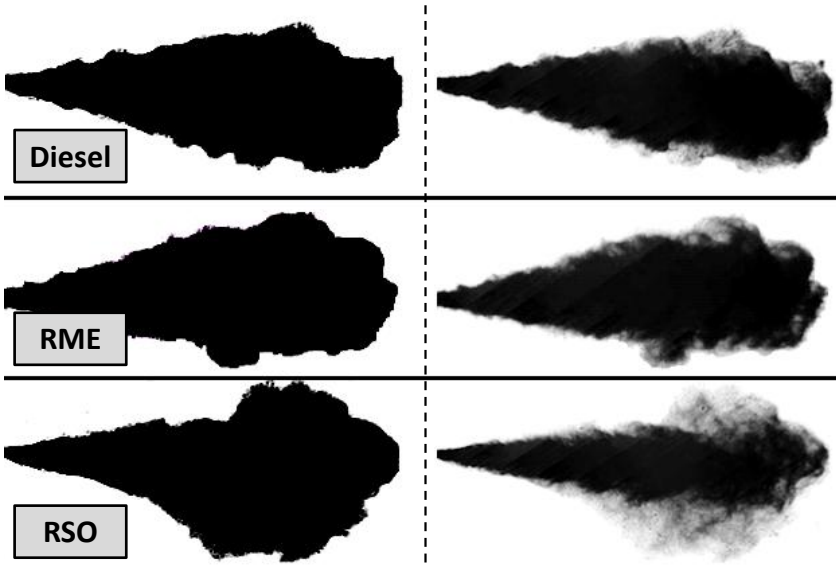

Figure 8.34: The difference in spray structure as detected with shadowgraph imaging: (left) the spray surface area determined by the post-processing software, (right) spray images with equal gamma correction (γ<1)

8.6 Link with engine performance

The earlier injection timing for SVO and AF will impact engine emissions and performance. Experiments of Bari *et al.* [199] revealed that oils (waste cooking oil) and diesel respond identically to injection timing changes. So, based on the knowledge on diesel combustion, one can try to predict the influences of the injection timing on the performances and emissions of engines running on SVO or AF. The earlier start of injection implies that the temperature and pressure inside the cylinder will be lower at the start of injection. As a result, the ignition delay will increase for the SVO and AF. The poorer atomization and lower volatility of the bio-fuels can even reinforce the increase of the ignition delay compared to diesel fuel. The later start of ignition results in an increased amount of heat release in the premixed combustion phase, increasing the level of noise and causing a higher temperature during the subsequent diffusive combustion phase [199]. The period during which the mean temperature inside the cylinder is above 1500K, is a very important factor affecting the formation of thermal NOx. As a result, the increased ignition delay due to the earlier injection, it might lead to higher NOx emissions.

However, the earlier injection timing also has some advantages. First of all, more fuel is burned in the premixed combustion phase. During a premixed combustion

less local over-rich spots are present compared to the diffusive combustion phase. This results in a more complete combustion and lower CO, HC and smoke emissions [199].

Based on the longer injection duration of SVO and AF compared to diesel, a longer combustion duration is expected as well, resulting in a decrease in thermal efficiency. However, the earlier start of injection increases the ignition delay, increasing the amount of fuel that is burned abruptly in the premixed combustion phase. This effect shortens the total combustion period because less fuel has to be combusted during the diffusive combustion phase. It can partially counteract the effect of the longer injection period.

Ivestigation of the reacting sprays should reveal the details of the spray combustion and especially the impact of the chemical composition.

8.7 Conclusions

Spray measurements were conducted in the constant volume combustion chamber GUCCI in inert non-evaporative (ambient temperature T_a up to 150°C and pressures up to 8MPa) and fuel temperatures up to 90°C.
The involved fuels were diesel, rapeseed biodiesel (RME), rapeseed oil (RSO), palm oil (PO) and animal fats (AF). The influences of fuel properties, engine speed and chamber pressure on the injection pressure profile, needle lift, spray length and spray angle were investigated.
The results of the performed spray measurements can be summarized as follow:

- Fuel properties are strongly temperature dependent. Even small changes in fuel temperature result in a significant influence on the injection pressure of a pump-line-nozzle system. Therefore, fuel temperature at the moment of injection was determined and controlled for all experiments (cfr. section 4.6.2).
- The bulk modulus, a measure for the resistance to compression, is the main parameter affecting the injection pressure profile. A higher bulk modulus increases the pressure.
- The higher bulk modulus of crude oils and fats results in an earlier and faster needle lift for experiments at higher fuel temperatures (more than 60°C). In the lower temperature range this effect is counteracted by the higher viscosity of straight vegetable oil and animal fat: viscous forces delay the needle lift.
- The higher density of biofuels results in longer injection durations for pump-line-nozzle injection systems.

- The spray length is strongly influenced by the engine speed (or thus injection pressure) and the chamber gas density. These parameters affect the spray penetration more significantly than the fuel temperature or the fuel type.
- At start of injection, spray penetration is similar for all fuels because of counteracting influences of bulk modulus, viscosity and density. In the later stage of the injection, however, straight vegetable oil and animal fat show slightly faster spray penetrations due to the higher injection pressures and larger droplets of these fuels compared to diesel and rapeseed biodiesel.
- The spray angle is not significantly influenced by engine speed. Chamber gas density is the dominant parameter affecting the spray angle. Similar spray angles were observed for different fuels. However, an influence of fuel temperature was often observed for the more viscous fuels.
- At low temperatures, despite similar spray angles, the spray atomization for straight vegetable oil is worse than diesel and rapeseed biodiesel. This could be qualitatively observed from the spray images. Increasing fuel temperature from 25 to 45°C already enhanced the spray atomization significantly. This is most probably due to the strong decrease in viscosity. Research on droplet sizes and droplet distribution is necessary to quantify these influences of fuel properties on atomization. Probably, the sauter main diameter is the spray parameter that is most significantly affected by the fuel properties.

Since the performed experiments depend on the fuel properties, especially viscosity and bulk modulus, the link to the spray modeling should be considered. According to the spray model of chapter 5, the trend in Fig. 8.26 cannot be explained due to the fact that no droplets are considered. At the other hand, realistic fuel temperatures at start of injection for the oils is usually between 70 and 110°C such that the influence of the viscosity is less pronounced.
Prior to increasing the model complexity, vaporizing spray characteristics should be investigated in a similar way. One might expect that the early spray dynamics are dominated by the injected fuel conditions while the far field spray is dominated by the ambient conditions as is also suggested by Payri *et al.* [89]. This implies a correction in the model for the viscosity near the nozzle and might fade away further downstream.

9
Conclusions & outlook

"No experiment is ever a complete failure. It can always be used as a bad example."

- Paul Dickson -

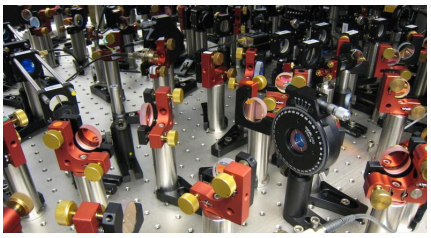

The chapter is organized as follows: a brief summary of all chapters precede the conclusions for the 5 main topics handled in the work: the experimental setup, spray experiments, boundary conditions, spray modeling and surrogates. Finally, suggestions for the future work for the 5 main topics are proposed.

9.1 Summary & conclusions

The situation of the results of this work is summarized in Fig. 9.1. For the experimental part, 3 main subdivisions are separately covered. The first part consists of the construction of an optically accessible combustion chamber (cfr. chapter 4) and the implementation of some basic optical diagnostics (cfr. chapter 3). This subdivision mainly involved the design, dimensioning and acquisition of signals. The second part comprises optical measurements of cold spray injections with different crude oils (cfr. chapter 8) from which some conclusion were drawn, useful for vaporizing sprays in the future. The third part covers the evaluation of the boundary conditions for a diesel engine-like atmosphere (cfr. chapter 4). Here, the gas temperature distribution, gas mixture composition, flow field and fuel temperature, are evaluated in terms of accuracy and deviation.
Next to the experimental part, numerical work was performed. A careful selection of the desired modeling strategy is discussed, together with the implementation of a slightly adapted existing spray model that is able to deal with a variable injection profile (cfr. chapter 5).
Another important numerical issue is the choice of the modeling of the fuel. It is shown for diesel and bio-diesel that this choice is of great importance for a correct performance of the spray model (cfr. chapter 6). Attempts to define a surrogate for crude oils have been formulated and motivated as well.

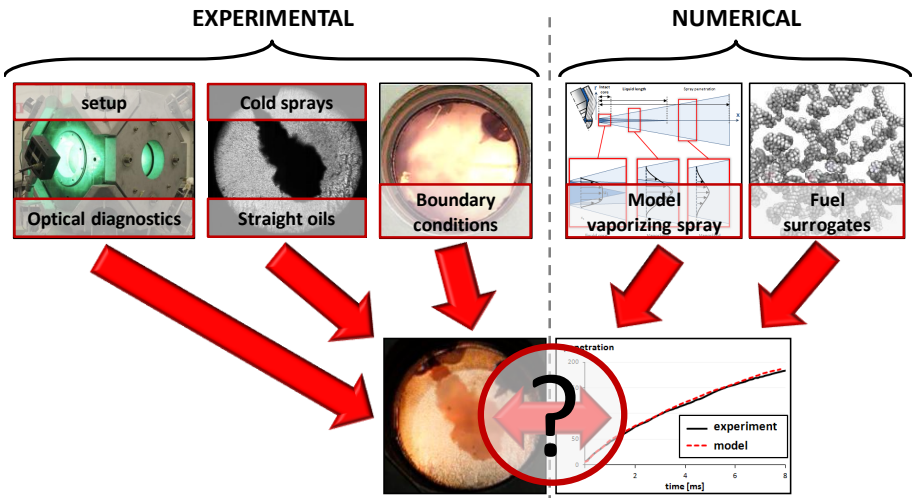

Figure 9.1: The current situation of the results: the upper row are the obtained results, the lower row are the desired results for the future.

All these different parts as shown in the first row of Fig. 9.1 are realized independently from each other, while the main (future) goal is to merge them all together:

validation of a vaporizing (or combusting) spray model of crude oil fuels through experiments. This is indicated by the second row images, where the double arrow represents the interaction between the experiments and modeling work. This could not yet be realized during the time for this PhD. However, it is shown in chapter 7 that this goal is realistic: in cooperation with the combustion group of the Technical University of Eindhoven and their facility, the investigation of a specified spray configuration (baptized as '*Spray A*' by the Engine Combustion Network) was experimentally investigated and sucessfully validated with the proposed spray model.

It is clear that there is still a long way to go, however the building blocks for the research are established in this work.

9.2 Outlook & suggestions for future work

The project goal as described in chapter 1 is not yet completed so suggestions for the near future are mentioned in this section, divided in suggestions for the experimental and numerical part.

9.2.1 Experimental setup & experiments

Fuel mass flow rate

Knowledge and prediction of the injection velocity v_{inj} is of great importance for the spray prediction, since this parameter will initially influence the atomization and penetration. This parameter however requires the level of cavitation in the nozzle hole which can not (yet) properly be measured on the GUCCI-setup. Furthermore, the start of the spray is obstructed by the thimble on the nozzle. The velocity can be obtained from the ratio of the measurement of the spray momentum $\dot{M}$ and mass flow rate $\dot{m}$, considering the spray as an impacting jet on a wall as demonstrated in Fig. 9.2.

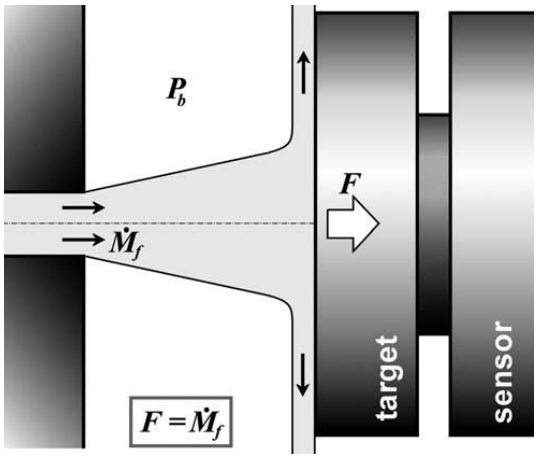

Figure 9.2: Simplified representation how the spray momentum can be measured [44]

The measurement of the momentum or force of the spray, can easily be measured by a force sensor as was mentioned in section 4.3.
The mass flow rate measurements suffer from some problems:

- The injection system is difficult to move.
- Little measurement techniques or sensors are available.
- Most of the techniques require their own setup.

The most commonly used methods are the Bosch fuel [77, 200] rate indicator and Zeugh method [201, 202], which make use of the compressibility of the fuel. But both need their own setup which makes it hard to perform on the current configuration of the GUCCI-setup. Attempts to use the GUCCI as a Zeuch chamber were unsuccessful due to the remaining air bubbles in the fuel which significantly affect the bulk modulus.
Another less common technique makes use of the electrical discharge of the injected fuel [203]. The fuel becomes electrically charged when it rubs against the injection nozzle and the other injection system parts, which act as a single electrode. Fuel droplets hit the sensor electrode and discharge. It is shown by Marcic [203] that the voltage is a measure for the mass flow rate and a schematic representation of this sensor is shown in Fig. 9.3. Attempts were taken to design

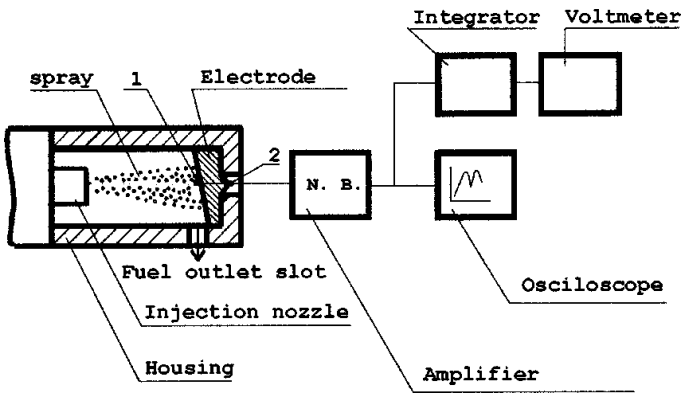

Figure 9.3: Schematic representation of the fuel mass flow rate sensor as designed by Marcic [203]

such sensor applicable to the GUCCI-setup. The current result of the implementation is shown in Fig. 9.4. The sensor is designed to measure simultaneously the spray momentum and mass flow rate. Some of the initial (unsuccessful) results are given in Fig. 9.5. Initially a signal is detected at the time of injection. But the signal loses strength, probably due to a shortcut between the two electrodes by the injected fuel. This can clearly seen from the different succeeding measurements. After each measurement the sensor was cleaned with pressurized air, but clearly still some conducting layer remained. Complete cleaning of the electrodes improved the measurement-to-measurement performance, but the fast decrease of the signal during the measurement was still expected to be caused by a fuel shortcut during injection. This can be prevented by a better isolation of the electrode or to increase the surface area of the measurement electrode. However, these last proposals were not applied anymore and are suggestions for future work.

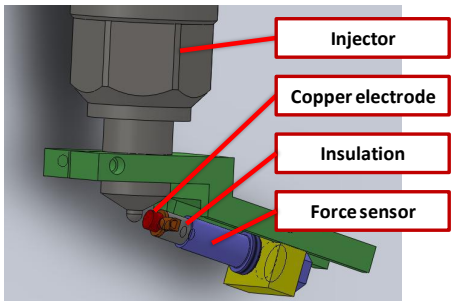

Figure 9.4: Realisation of the mass flow sensor based on electric discharge of the injected fuel with simultaneous spray momentum measurements

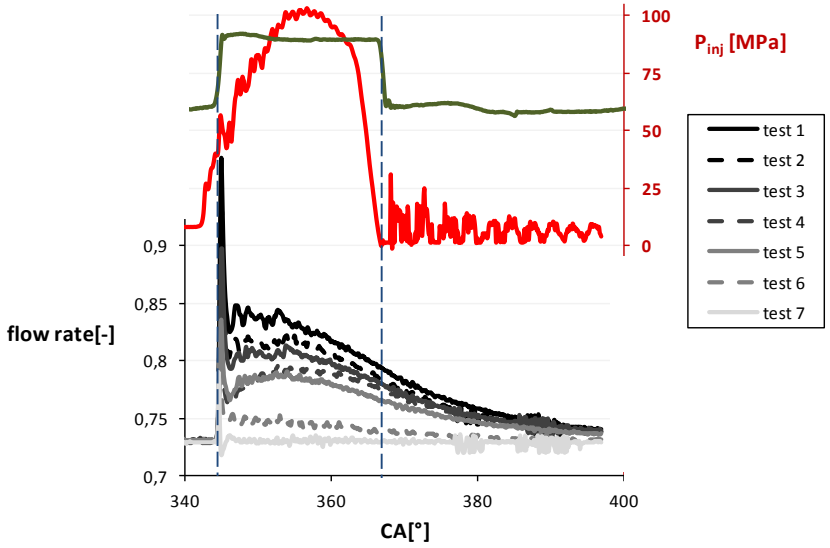

Figure 9.5: Mass flow rate results acquired on the GUCCI-setup (black to grey lines): influence of the previous measurements. The green line represents the needle lift signal and the red graph the injection pressure profile corrected for the speed of sound.

Vapor-liquid mass/volume fraction distribution and spray structure

In chapter 8 it was pointed out that there exists a difference in spray structure when highly viscous fuels are used, but with the current diagnostics this can not be distinguished properly. The knowledge of the vapor and liquid fuel mass distribution is important when considering the ignition and combustion process since it will influence the temperature distribution and emission formation. Optical diagnostics that can deal with this need are necessary. A (simultaneous) combination of Mie-scattering and shadowgraphy/schlieren has already shown [109, 142, 204] to

be a potential way to measure quantitatively the mass fuel fraction and liquid-gas fraction. However, this setup requires a careful calibration and interpretation of the results is not straightforward either [205].
The setup for simultaneous Mie-shadowgraphy and schadowgraphy was already tested as described in section 3.7, but no calibration or quantitative data were generated yet for spray measuments.

Other interesting insight can be gained by performing more detailed optical research as is proven by Shoba *et al.* [66, 73]. They used a long range microscopes to obtain a resolution of $0.6\mu m$ per pixel. Such long range microscope are very expensive, but with the combination of the available zoom lens and 1 or to 2 teleconvertors (2x) it should be possible to obtain details of the spray structures, especially for non-evaporative conditions where the contrast is higher.

9.2.2 Spray & modeling

Evaluation with experiments

No validation of the model with the experiments in the GUCCI-setup was yet performed. The main reason is that the model is developped for vaporizing sprays and the strong hypothesis considers the spray as a homogeneous mixture of ambient gas, fuel vapor and liquid. This is not true when no evaporation is present: far from the nozzle bigger droplets will still exist and the ambient velocity in the spray might differ significantly from the fuel velocity. This would mean that the model will underpredict the spray penetration.
A second issue is the injection velocity. The discharge coefficient is not yet known and the visible part of the spray starts *6.2mm* away from the nozzle exit. This makes it harder to determine the boundary conditions for the model.

The above statements are demonstrated in Fig. 9.6. The experiment of a non-vaporizing diesel spray in the GUCCI-setup is given by the solid grey line. The experimentally obtained injection pressure profile is transformed to the injection velocity profile by the Bernoulli equation and a postulated discharge coefficient C_d. The spray angle θ is taken from the experiments: the average Siebers angle was 29.2° while the average local spray angle was 26°. The spray angle has some effect on the penetration but is less dominant that the injection velocity. Even with a discharge coefficient equal to 1, the penetration is underpredicted.
In the case the injection profile is averaged, the penetration is initially overpredicted but near the end of injection it becomes underpredicted. It is considered to be the consequence of the existence of droplets (with a high inertia).
The evaluation of the model with experiments will only become useful when vaporizing sprays are considered.

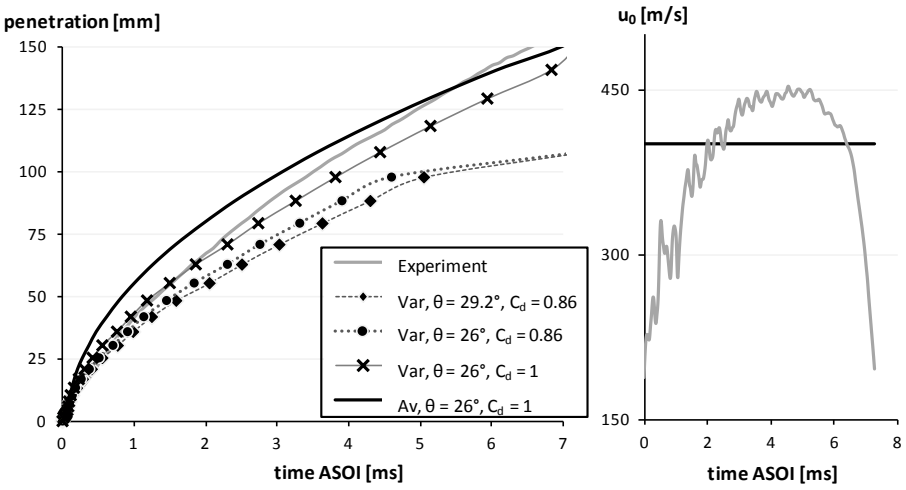

Figure 9.6: Left: attempt to model an experiment of a non-vaporizing diesel spray in the GUCCI-setup for different discharge coefficient C_d, spray angle θ and experimental obtained injection pressure profile (Var) and averaged pressure profile (Av). Right: the injection velocity profile (grey) and averaged injection profile (black).

Spray model: extension to combustion

An extension of the spray model has already been validated by the Valencia group [133]. They considered the spray as 2 different parts: a vaporizing and a combusting spray part. The change from one to the other part is based on flame lift-off measurements: if the penetration exceeds the flame lift-off length, the change is made. As an extension to their contribution, it should be a reasonable task to propose a correlation for the ignition delay τ. The evolution of the ignition delay can then be predicted by the conservation of delay principle (Eq. 9.1 as is widely used for simulations in spark ignition engines [206].

$$\int \frac{dt}{\tau(t)} = 1 \tag{9.1}$$

This information can be obtained from both experiments or chemical reaction kinetic models. For the modeled or experimentally determined ignition limits, the flame lift-off length will be output of the model and it should be possible to distinguish the differences between premixed combustion zone and diffuse combustion zone . A schematic representation of the proposed strategy for a combusting spray is shown in Fig. 9.7.
A frozen chemistry assumption and a single-step irreversible reaction is assumed [133] to determine the heat release and burned properties. This means that the reaction time for the combustion is neglected and the combustion products are formed im-

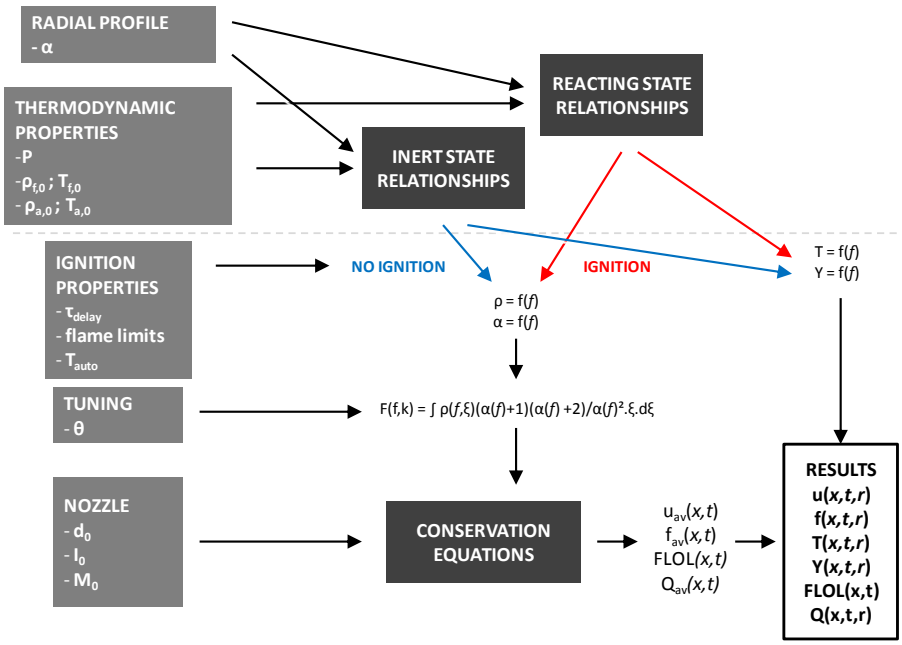

Figure 9.7: Modeling strategy for extension to combustion

mediately according to:

$$C_xH_yO_z + \left(m + \frac{y}{4} - \frac{z}{2}\right) O_2 \rightarrow xCO_2 + \frac{y}{2} H_2O \tag{9.2}$$

Prediction of the emissions can be performed independently and is considered not to influence the spray and combustion process due to the small amounts.

Spray modeling: extension to crude oils

The transient phenomenological model for inert sprays as described by Payri and coworkers [89, 132, 133, 136] was only validated for diesel surrogates (dodecane and cetane). Whether this model is valid for straight oils is still not known since no vaporizing sprays were measured. The droplets for straight oils were bigger in the non-evaporative conditions for low fuel temperature, based on qualitative observation. They however might still be small enough to consider the hypothesis that evaporation of the fuel is dominated by the air entrainment. If so, the radial distribution might be different since more fuel is concentrated near the spray axis compared to regular diesel. The change in radial profile will result in a change

in value of the F-term in the model (cfr. chapter 5). This is basically illustrated in Fig. 9.8 for the spray penetration in which the profile was changed while all other parameters were kept the same. The modified profile consisted of the sum of 2 profiles (*f_core* and *f_edge*) but with different shape factors and amplitude as demonstrated on the left side of the figure. The grey lines on the right figure represent the corresponding profile used for the spray model calculations. The difference is significant, so knowledge of the fuel distribution might be important to get the desired agreement between modeling and experiments.

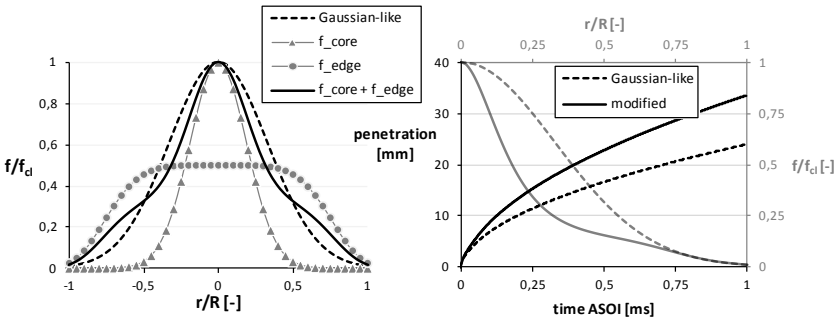

Figure 9.8: Mass flow rate results acquired on the GUCCI-setup: influence of the previous measurements

This is one possible way to deal with bigger droplets while still accepting the mixing-limited hypothesis.
If data is available of the droplet sizes, the shape factors might be written as a function of the SMD (or another parameter related to the droplet sizes)
If the mixing limited hypothesis is not valid, the phenomenological model of Hiroyasu (cfr. section 5.2.1) seems to be a proper (but more complexe) solution since the model is still used in powertrain simulation tools.

A

Determination of the boundary conditions

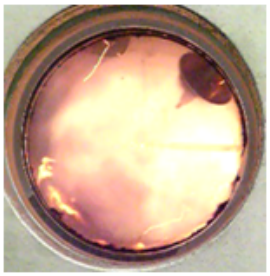

In this appendix, the derivation is given, starting from the desired ambient properties at the start of injection, to the partial pressures required of the gases prior to the precombustion process

A.1 Introduction

The pre-burn or pre-combustion method has been evaluated in the past as a reliable method to create engine-like conditions in a constant volume combustion chamber for optical spray measurements and is widely used. The properties at start of injection are determined by carefully choosing the gas mixture composition prior to ignition. Two spark plugs with high capacity coils allow the mixture to ignite. A piezo-electric pressure sensor monitors the cooling down process by measuring the bulk pressure. Only 4 gases are used for the initial gas mixture, allowing us to define 4 properties at start of injection. The most important ambient gas properties which will influence the spray (and combustion) are:

- amount of oxygen [$vol\%$]: influences the oxidation process
- temperature at SOI: influences the evaporation process
- density at SOI: influences the spray break-up process
- heat capacity at SOI: influences the evaporation process

A.2 Theoretical implementation

Gas properties such as heat capacity, enthalpy, and saturation pressure are considered temperature dependent but independent of pressure. The correlations and coefficients from Perry's chemical engineers' handbook [121] are used. A set of 4 equations and 4 unknowns need to be resolved:

- (eq 1) : expression for the total mass (deals with the desired density)
- (eq 2) : expression for the amount of oxygen
- (eq 3) : conservation of enthalpy (deals with the desired temperature)
- (eq 4) : expression for the desired heat capacity

Assumptions for the pre-combustion process are:

- complete combustion (no soot, CO or H_2)
- no NO_x or dissociation of N_2 and O_2. The amount of dissociation products is smaller than the experimental error or accuracy
- no dissociation
- $\lambda \geq 1$

The pre-combustion process (without dissociation) can be described by

$$a.C_2H_2 + b.O_2 + c.N_2 + d.Ar \rightarrow e.CO_2 + f.H_2O + g.O_2 + c.N2 + d.Ar \tag{A.1}$$

The coefficients *a*-*g* [*mol*], need to be determined. In the following, the index u represents the unburned situation, the index b, the burned situation.
The first equation is derived from the conservation of mass:

$$\begin{aligned} m_{tot} &= m_{u,C_2H_2} + m_{u,O_2} + m_{u,N_2} + m_{u,Ar} && \text{(A.2)} \\ &= m_{b,CO_2} + m_{b,H_2O} + m_{b,O_2} + m_{b,N_2} + m_{u,Ar} && \text{(A.3)} \end{aligned}$$

The relation between the masses of C_2H_2, O_2, H_2O and CO_2 are given by the reaction mechanism:

$$C_2H_2 + \frac{5}{2}O_2 \rightarrow 2.CO_2 + H_2O \tag{A.4}$$

For stoichiometric conditions, the masses become:

$$\begin{aligned} m_{u,C_2H_2} &= M_{C_2H_2}.n_{C_2H_2} && \text{(A.5)} \\ m_{b,CO_2} &= M_{CO_2}.2.n_{C_2H_2} && \text{(A.6)} \\ m_{b,H_2O} &= M_{H_2O}.n_{C_2H_2} && \text{(A.7)} \\ m_{u,O_{2,st}} &= M_{O_2}.\frac{5}{2}.n_{C_2H_2} && \text{(A.8)} \end{aligned}$$

written as a function of the mass of C_2H_2:

$$\begin{aligned} m_{b,CO_2} &= 2.M_{CO_2}\frac{m_{u,C_2H_2}}{M_{C_2H_2}} && \text{(A.9)} \\ m_{b,H_2O} &= M_{H_2O}\frac{m_{u,C_2H_2}}{M_{C_2H_2}} && \text{(A.10)} \\ m_{u,O_{2,st}} &= \frac{5}{2}M_{O_2}\frac{m_{u,C_2H_2}}{M_{C_2H_2}} && \text{(A.11)} \end{aligned}$$

The masses of Ar and N_2 are equal before and after combustion:

$$m_{u,C_2H_2} + m_{u,O_2} = m_{b,CO_2} + m_{b,H_2O} + m_{b,O_2} \tag{A.12}$$

with

$$\begin{aligned} m_{b,O_2} &= m_{u,O_2} - m_{u,O_2,st} && \text{(A.13)} \\ &= M_{O_2}\left[\frac{m_{u,O_2}}{M_{O_2}} - \frac{5}{2}\left(\frac{m_{u,C_2H_2}}{M_{C_2H_2}}\right)\right] \end{aligned}$$

Equation 1: conservation of mass

$$m_{u,C_2H_2} + m_{u,O_2} + m_{u,N_2} + m_{u,Ar} = m_{tot} = \rho_u V_{chamber} \tag{A.14}$$

Equation 2: expression for the amount of oxygen after pre-combustion

The volume percentage of oxygen $vol\%_{b,O_2}$ is equal to the mole fraction of the system:

$$n_{b,O_2} = vol\%_{b,O_2}.n_{b,tot} \tag{A.15}$$

with

$$n_{b,tot} = n_{b,CO_2} + n_{b,O_2} + n_{b,N_2} + n_{b,Ar} \tag{A.16}$$

$$n_{b,tot} = 2\left(\frac{m_{u,C_2H_2}}{M_{C_2H_2}}\right) + \left(\frac{m_{u,C_2H_2}}{M_{C_2H_2}}\right) + \left[\frac{m_{u,O_2}}{M_{O_2}} - \frac{5}{2}\left(\frac{m_{u,C_2H_2}}{M_{C_2H_2}}\right)\right] + \left(\frac{m_{u,N_2}}{M_{N_2}}\right) + \left(\frac{m_{u,Ar}}{M_{Ar}}\right) \tag{A.17}$$

Substitution of Eq. A.15 in Eq. A.16 results in:

$$\left[\frac{m_{u,O_2}}{M_{O_2}} - \frac{5}{2}\left(\frac{m_{u,C_2H_2}}{M_{C_2H_2}}\right)\right] = vol\%_{b,O_2}.[2\left(\frac{m_{u,C_2H_2}}{M_{C_2H_2}}\right) + \left(\frac{m_{u,C_2H_2}}{M_{C_2H_2}}\right) + \left[\frac{m_{u,O_2}}{M_{O_2}} - \frac{5}{2}\left(\frac{m_{u,C_2H_2}}{M_{C_2H_2}}\right)\right] + \left(\frac{m_{u,N_2}}{M_{N_2}}\right) + \left(\frac{m_{u,Ar}}{M_{Ar}}\right)] \tag{A.18}$$

Writing Eq. A.18 as a function of the unburned conditions results in *A*.19.

$$0 = \frac{1}{M_{C_2H_2}}\left[\frac{5}{2} + \frac{1}{2}vol\%_{b,O_2}\right]m_{u,C_2H_2} + \frac{1}{M_{O_2}}\left[vol\%_{b,O_2} - 1\right]m_{u,O_2} + \frac{1}{M_{N_2}}\left[vol\%_{b,O_2}\right]m_{u,N_2} + \frac{1}{M_{Ar}}\left[vol\%_{b,O_2}\right]m_{u,Ar_2} \tag{A.19}$$

Equation 3: conservation of energy

The internal energy of the system before and after combustion is conserved and assuming adiabatic combustion, the conservation of energy can be written as:

$$\begin{aligned}
&m_{u,C_2H_2}.u_{u,C_2H_2}(T_u)+m_{u,O_2}.u_{u,O_2}(T_u)+m_{u,N_2}.u_{u,N_2}(T_u)\\
&\qquad +m_{u,Ar}.u_{u,Ar}(T_u)\\
&\qquad =m_{u,CO_2}.u_{u,CO_2}(T_b)+m_{u,H_2O}.u_{u,H_2O}(T_b)\\
&+M_{O_2}\left[\frac{m_{u,O_2}}{M_{O_2}}-\frac{5}{2}\left(\frac{m_{u,C_2H_2}}{M_{C_2H_2}}\right)\right].u_{u,O_2}(T_b)+m_{b,N_2}.u_{b,N_2}(T_b)\\
&\qquad +m_{b,Ar}.u_{b,Ar}(T_b)\\
&=2.M_{CO_2}\left(\frac{m_{u,C_2H_2}}{M_{C_2H_2}}\right).u_{u,CO_2}(T_b)+M_{H_2O}\left(\frac{m_{u,C_2H_2}}{M_{C_2H_2}}\right).u_{u,H_2O}(T_b)\\
&+M_{O_2}\left[\frac{m_{u,O_2}}{M_{O_2}}-\frac{5}{2}\left(\frac{m_{u,C_2H_2}}{M_{C_2H_2}}\right)\right].u_{u,O_2}(T_b)+m_{b,N_2}.u_{b,N_2}(T_b)\\
&\qquad +m_{b,Ar}.u_{b,Ar}(T_b)
\end{aligned}\tag{A.20}$$

Writing Eq. A.21 as a function of the masses of the gases before combustion results in Eq. A.21:

$$\begin{aligned}
0 \;=\;& [u_{u,C_2H_2}(T_u)+\frac{5}{2}\left(\frac{M_{O_2}}{M_{C_2H_2}}\right)u_{b,O_2}(T_b)-2\left(\frac{M_{CO_2}}{M_{C_2H_2}}\right)u_{b,CO_2}(T_b)\\
&-\left(\frac{M_{H_2O}}{M_{C_2H_2}}\right)u_{b,H_2O}(T_b)]m_{u,C_2H_2}\\
&+\left[u_{u,O_2}(T_u)-u_{u,O_2}(T_b)\right]m_{u,O_2}\\
&+\left[u_{u,N_2}(T_u)-u_{u,N_2}(T_b)\right]m_{u,N_2}\\
&+\left[u_{u,Ar}(T_u)-u_{u,Ar}(T_b)\right]m_{u,Ar}
\end{aligned}\tag{A.21}$$

Temperature T_b is the peak temperature and is unknown in this equation. Limiting this temperature and correlating this with the temperature at the start of injection allows us to define an extra equation by introducing a factor f defined as

$$T_{SOI}=T_u+f(T_b-T_u)\tag{A.22}$$

with $f=1$: injection at the peak temperature; $f=0$: injection after complete cooling down.

In order to avoid the influence from the pre-combustion on the injection, a heterogeneous temperature and a strong flow field, T_{SOI} should be at least 60% of the peak temperature, which corresponds to a factor f of ~ 0.41. The f-factor is taken as small as possible, paying attention that the maximum combustion pressure is not exceeded. For a bursting disk with a bursting pressure of $160bar$ (+/-$10bar$),

an f-factor of 0.37 (maximum theoretical pressure of 145bar) is a good compromise. For high f-factors, the amount of fuel (C_2H_2) decreases and was found to be difficult to ignite.

Equation 4: expression for heat capacity

The heat capacity of the mixture at start of injection should be equal to the desired one. The heat capacity of a mixture is the sum of the mole weighted heat capacities of the single gas components.

$$\begin{aligned} n_{b,tot}.c_{p_{mix}}(T_{SOI}) &= n_{b,CO_2}.c_{p_{b,CO_2}}(T_{SOI}) + n_{b,H_2O}.c_{p_{b,H_2O}}(T_{SOI}) \\ &\quad + n_{b,O_2}.c_{p_{O_2}}(T_{SOI}) + n_{b,N_2}.c_{p_{b,N_2}}(T_{SOI}) \\ &\quad + n_{b,Ar}.c_{p_{b,Ar}}(T_{SOI}) \\ &= 2\left(\frac{m_{u,C_2H_2}}{M_{C_2H_2}}\right)c_{p_{b,CO_2}}(T_{SOI}) \\ &\quad + \left(\frac{m_{u,C_2H_2}}{M_{C_2H_2}}\right)c_{b,p_{H_2O}}(T_{SOI}) \\ &\quad + \left[\frac{m_{u,O_2}}{M_{O_2}} - \frac{5}{2}\left(\frac{m_{u,C_2H_2}}{M_{C_2H_2}}\right)\right] \\ &\quad + \left(\frac{m_{u,N_2}}{M_{N_2}}\right)c_{p_{b,N_2}}(T_{SOI}) \\ &\quad + \left(\frac{m_{u,C_2H_2}}{M_{C_2H_2}}\right)c_{p_{b,Ar}}(T_{SOI}) \end{aligned} \tag{A.23}$$

with

$$\begin{aligned} n_{b,tot} &= n_{b,CO_2} + n_{b,H_2O} + n_{b,O_2} + n_{b,N_2} + n_{b,Ar} \\ &= 2\left(\frac{m_{u,C_2H_2}}{M_{C_2H_2}}\right) + \left(\frac{m_{u,C_2H_2}}{M_{C_2H_2}}\right) \\ &\quad + \left[\frac{m_{u,O_2}}{M_{O_2}} - \frac{5}{2}\left(\frac{m_{u,C_2H_2}}{M_{C_2H_2}}\right)\right] \\ &\quad + \left(\frac{m_{u,N_2}}{M_{N_2}}\right) + \left(\frac{m_{u,Ar}}{M_{Ar}}\right) \end{aligned} \tag{A.24}$$

Writing A.23 as a function of the masses of the gases before combustion results in

A.25.

$$
\begin{aligned}
0 \quad = \quad & \frac{1}{M_{C_2H_2}}[2.c_{p_{b,CO_2}}(T_{SOI}) + c_{p_{b,H_2O}}(T_{SOI}) - \frac{5}{2}c_{p_{b,CO_2}}(T_{SOI}) \\
& -\left(2+1-\frac{5}{2}\right)c_{p_{b,mix}}(T_{SOI})]m_{u,C_2H_2} \\
& +\frac{1}{M_{O_2}}\left[c_{p_{b,O_2}}(T_{SOI}) - c_{p_{mix}}(T_{SOI})\right]m_{u,O_2} \\
& +\frac{1}{M_{N_2}}\left[c_{p_{b,N_2}}(T_{SOI}) - c_{p_{mix}}(T_{SOI})\right]m_{u,N_2} \\
& +\frac{1}{M_{Ar}}\left[c_{p_{b,Ar}}(T_{SOI}) - c_{p_{mix}}(T_{SOI})\right]m_{u,Ar} \qquad \text{(A.25)}
\end{aligned}
$$

A.3 Summary

The matrix for the set of A.14 - A.25 is of the form

$$[A].[x] = [B] \tag{A.26}$$

with

$$\begin{aligned}
A(1,1) &= 1 \\
A(1,2) &= 1 \\
A(1,3) &= 1 \\
A(1,4) &= 1 \\
A(2,1) &= \frac{1}{M_{C_2H_2}}\left[\frac{5}{2} - \frac{11}{2} vol\%_{b,O_2}\right] \\
A(2,2) &= \frac{1}{M_{O_2}}\left[1 - vol\%_{b,O_2}\right] \\
A(2,3) &= \frac{1}{M_{N_2}} vol\%_{b,O_2} \\
A(2,4) &= \frac{1}{M_{Ar}} vol\%_{b,O_2} \\
A(3,1) &= u_{u,C_2H_2(T_u)} + \frac{5}{2}\frac{M_{O_2}}{M_{C_2H_2}} u_{b,O_2(T_b)} - 2\frac{5}{2}\frac{M_{CO_2}}{M_{C_2H_2}} u_{b,CO_2(T_b)} + \frac{M_{H_2O}}{M_{C_2H_2}} u_{b,H_2O(T_b)} \\
A(3,2) &= u_{u,O_2}(T_u) - u_{b,O_2}(T_b) \\
A(3,3) &= u_{u,N_2}(T_u) - u_{b,N_2}(T_b) \\
A(3,4) &= u_{u,Ar}(T_u) - u_{b,Ar}(T_b) \\
A(4,1) &= \frac{1}{M_{C_2H_2}}\left[2c_{p_{b,CO_2}}(T_{SOI}) + c_{p_{b,H_2O}}(T_{SOI}) - \frac{5}{2} c_{p_{b,O_2}}(T_{SOI}) - \frac{11}{2} c_{p_{mix}}(T_{SOI})\right] \\
A(4,2) &= c_{p_{b,O_2}}(T_{SOI}) - c_{p_{mix}}(T_{SOI}) \\
A(4,3) &= c_{p_{b,N_2}}(T_{SOI}) - c_{p_{mix}}(T_{SOI}) \\
A(4,4) &= c_{p_{b,Ar}}(T_{SOI}) - c_{p_{mix}}(T_{SOI})
\end{aligned} \tag{A.27}$$

$$x = \begin{bmatrix} m_{u,C_2H_2} \\ m_{u,O_2} \\ m_{u,N_2} \\ m_{u,Ar} \end{bmatrix} \tag{A.28}$$

$$B = \begin{bmatrix} \rho_{inj} V_{chamber} \\ 0 \\ 0 \\ 0 \end{bmatrix} \tag{A.29}$$

A.3.1 Conversion to partial pressure

The partial pressure p_i for each filling gas i is calculated with the ideal gas law with compressibility $Z = 1$:

$$p_i = \frac{m_i}{M_i} \frac{\overline{R} T_u}{V_{chamber}} \tag{A.30}$$

A.3.2 Additional gas properties

The heat conductivity and dynamic viscosity were calculated at the target conditions for the target mixture (= air, no EGR) and desired mixture in the combustion chamber. Both mixture properties are calculated by the molar weighted single component property corrected with an interaction parameter [**?**].
Calculation of the heat conductivity:

$$k_i = \frac{a_1 T^{a_2}}{1 + \frac{a_3}{T} + \frac{a_4}{T^2}} \tag{A.31}$$

$$k_{mix} = \sum \frac{X_i k_i}{\sum X_j A_{ij}} \tag{A.32}$$

$$A_{ij} = \frac{\left[1 + \left(\frac{k_i}{k_j}\right)^{0.5} \left(\frac{M_j}{M_i}\right)^{0.25}\right]^2}{\left[8\left(1 + \frac{M_i}{M_j}\right)\right]^{0.5}}$$

Calculation of the dynamic viscosity:

$$\mu_i = \frac{b_1 T^{b_2}}{1 + \frac{b_3}{T} + \frac{b_4}{T^2}} \tag{A.33}$$

$$\mu_{mix} = \sum \frac{X_i \mu_i}{\sum X_j A_{ij}} \tag{A.34}$$

$$A_{ij} = \frac{\left[1 + \left(\frac{\mu_i}{\mu_j}\right)^{0.5} \left(\frac{M_j}{M_i}\right)^{0.25}\right]^2}{\left[8\left(1 + \frac{M_i}{M_j}\right)\right]^{0.5}}$$

With A_{ij}, the interaction parameter between component i and j; M_i, the molar mass of component i, a_1-a_4 and b_1-b_4, constants found in the DIPPR database. The

error between the desired and calculated properties is below 5% (cfr. table 4.7) which is reasonably good since the effect is usually neglected in simplified spray and combustion models.

B

Derivation of the model for vaporizing sprays

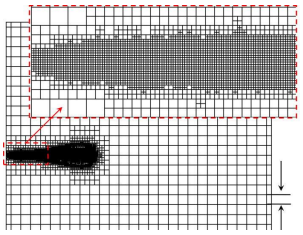

The appendix is organized as follows: in a first section, the properties of mixtures as well as the state relationships are defined. Next the spray model equations are stated and derived. Solver improvements are tackled in a third section.

B.1 Introduction

Spray formation and combustion depend on:

- Physical & chemical properties of the fuel
- Physical & chemical properties of the ambient gas mixture
- Kinetics / interaction fuel and ambient gas mixture

The physical and chemical properties are completely determined by temperature and fuel fraction, since one of the assumptions states that the spray is saturated at each time and spatial position; the air entrainment is the limiting factor for evaporation (= 'mixing limited' hypothesis). As a result the physical and chemical properties can be calculated independently of the spray characteristics (= state relations).

B.2 Properties for gas mixtures

B.2.1 Heat capacity

The heat capacity of a mixture is defined as the sum of the mass weighted heat capacity of the different components:

$$c_{p_{mix}} = \frac{\sum Y_k c_{p_k}}{\sum Y_k} \tag{B.1}$$

B.2.2 Enthalpy

The enthalpy of a mixture is defined as the sum of the mass weighted enthalpy of the different components:

$$h_{mix} = Y_a h_a + Y_{fv} h_{fv} + Y_{fl} h_{fl} \tag{B.2}$$

B.2.3 Density

The density of a mixture is defined by Amagat's law (based on partial volumes):

$$\rho_{mix} = \frac{1}{\frac{Y_a}{\rho_a} + \frac{Y_{fv}}{\rho_{fv}} + \frac{Y_{fl}}{\rho_f l}} \tag{B.3}$$

The densities of the different components are defined at the mixture temperature and pressure.

B.3 State relations

The state parameters involve the fuel density ρ_f, gas density ρ_a, mixture density ρ_{mix}, temperature T, vapor fraction ϕ, fuel enthalpy h_f, gas enthalpy h_a and mixture enthalpy h. In fact, for a defined initial fuel and gas temperature, from a given fuel fraction, the state parameters can be directly determined.

B.3.1 Fuel & gas density

The gas, liquid and vapor fuel density in the combustion chamber are considered as only depending on the temperature; pressure influences can be neglected. The relation is found from the DIPPR database for the specified fuel.

B.3.2 Vapor fraction

The mixing limited hypothesis determines the vapor fraction by the equation:

$$\phi = \frac{P_v}{P_{sat}} = \frac{m_v R_v T_v}{V_v P_{sat}} = \frac{x.m_a R_v T_v}{V_v P_{sat}} = x\frac{P_a V_a}{V_v P_{sat}} = 100\% \text{ (saturation)} \tag{B.4}$$

with $V_v = V_a$, $T_v = T_a$

$$x\left[kg_{fv}/kg_{\text{dry air}}\right] = \frac{Y_{fv}}{Y_a}\left[\frac{kg_{fv}/kg_{mix}}{kg_{\text{dry air}}/kg_{mix}}\right] = \frac{\phi.f}{1-f}\left[\frac{kg_{fv}/kg_{mix}}{kg_{\text{dry air}}/kg_{mix}}\right] \tag{B.5}$$

Equation B.5 results in:

$$\begin{aligned} \frac{\phi.f}{1-f} &= \frac{P_{sat}R_a}{R_{fv}(P-P_{sat})} \\ \phi &= \frac{P_{sat}R_a}{R_{fv}(P-P_{sat})}\frac{1-f}{f} \end{aligned} \tag{B.6}$$

The saturation pressure from equation B.6 represents the mixture saturation pressure as will be explained in section B.3.6.

B.3.3 Mixture density

The density in the above equations is the density of the mixture ρ_{mix} defined as [ref]:

$$\rho_{mix} = \frac{1}{\frac{1-f}{\rho_a} + \frac{\phi f}{\rho_{fv}} + \frac{(1-\phi)f}{\rho_{fl}}} \tag{B.7}$$

The air density ρ_a and the vapor density ρ_{fv} can be obtained from the ideal gas law:

$$\rho_{fv} = \frac{P}{R_{fv}T}$$
$$\rho_a = \frac{P}{R_a T}$$

This results in a relation between the fuel vapor and air density:

$$\rho_{fv} = \frac{R_a}{R_{fv}}\rho_a \tag{B.8}$$

Equation B.7 then leads to

$$\begin{aligned}\rho_{mix} &= \frac{1}{\left((1-f)+\frac{R_{fv}}{R_a}\phi f\right)\frac{1}{\rho_a}+(1-\phi)\frac{1}{\rho_{fl}}} \\ &= \frac{1}{\left(\frac{R_{fv}}{R_a}\frac{\phi}{\rho_{fl}}-\frac{1}{\rho_a}+\frac{(1-\phi)}{\rho_{fl}}\right)f+\frac{1}{\rho_a}} \\ &= \frac{\rho_{fl}}{\left(\frac{R_{fv}}{R_a}\frac{\rho_{fl}}{\rho_a}\phi-\frac{\rho_{fl}}{\rho_a}+(1-\phi)\right)f+\frac{\rho_{fl}}{\rho_a}}\end{aligned} \tag{B.9}$$

B.3.4 Heat capacity & enthalpy

The gas, liquid & vapor fuel specific heat capacity c_p in the combustion chamber is considered only depending on the temperature. The relation is found from the DIPPR database (*http://dippr.byu.edu/students/*) for the specified fuel and gas component. The enthalpy of each component is calculated by integration of the heat capacity c_p over the temperature:

$$h = \int_0^T c_p dT \tag{B.10}$$

The enthalpy of partially vaporized fuel:

$$\begin{aligned}h_f(T) = &\int_0^{T_{evap}} c_{p_{fl}}(T)\,dT \\ &+\phi\left(L_v\left(T_{evap}\right)+\int_0^T c_{p_{fv}}(T)\,dT-\int_0^{T_{evap}} c_{p_{fv}}(T)\,dT\right)\end{aligned} \tag{B.11}$$

B.3.5 Mixture enthalpy

$$h_{mix} = f.h_f + (1-f)\,h_a \tag{B.12}$$

B.3.6 Mixture saturation pressure

When considering a mixture of components the physical behavior changes and one cannot consider the mixture as 2 separate components. An important factor is the saturation pressure or vapor-liquid equilibrium of the mixture.

In an ideal mixture of fluida, according to Raoult's law (cfr. eq. B.13), the mixture saturation pressure is directly dependent on the saturation pressure of each component and the mole fraction of the component present in the mixture.

$$P_{sat_{mix}} = \sum_k \frac{n_k}{n_{tot}} P_{sat_k} \tag{B.13}$$

In the ideal solution, the forces exerted between molecules is the same everywhere. This statement is valid for non-polar molecules with similar size such as a mixture of heptane and hexane. In the case of non-ideal mixtures the mixture saturation pressure might deviate from the linear relation Eq. B.13 as shown in Fig. B.1.

For a mixture in which the molecules interact very little with each other, Raoult's law is approximately valid. Raoult's law states that the vapor pressure of an ideal solution is directly dependent on the vapor pressure of each chemical component and the mole fraction of the component present in the solution. An ideal solution is defined as a mixture in which the intermolar forces between the different molecules are equal to the one between similar ones. As a result, the saturation pressure for an ideal mixture of 2 components is linear while the more the intermolar forces between different molecules changes, the actual mixture saturation pressure deviates from the linear relation (cfr. figure B.1).

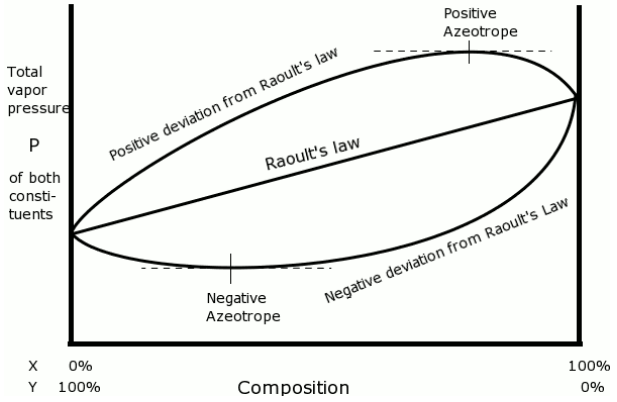

Figure B.1: Relation for the saturation pressure as a function of the component concentration

In the current application, the diesel surrogate mixtures will have big differences in component size and shape. This is due to the main reason of the mixture, which

is to meet similar vaporization and ignition characteristics of diesel. The use of Raoult's law is a strong simplification, but can be justified by the fact that little data is available of the saturation pressure of several mixtures and if more than 2 components are included, the complexity would increase even more. In terms of diesel surrogates, the most commonly proposed components are hydrocarbon molecules, so relatively non-polar. In the case of bio-oils, the size range of molecules is less extreme than for the case of diesel. This might suggest a smaller size range for the surrogates to meet similar vaporization and ignition characteristics as the real oil. However, for these fuels the polarity is much stronger. The mixture saturation pressure implemented in the model is as proposed in Eq. B.13, with the saturation pressure-temperature relation for each component as in Eq. B.14 (A, B, C, D, E are constants, found in the DIPPR database).

$$P_{sat_k} = e^{A_k + \frac{B_k}{T} + C_k log(T) + D_k T^{E_k}} \tag{B.14}$$

B.3.7 Temperature

The temperature is calculated from the relation with the enthalpy.
From the hypothesis of $Le = 1$, one can state:

$$f = \frac{h_{mix}(T) - h_{a\infty}}{h_{f0} - h_{a\infty}} \tag{B.15}$$

The relation between temperature and fuel fraction finally becomes:

$$\begin{aligned} f\left(h_{f0} - h_{a\infty}\right) + h_{a\infty} = (1-f)\int_0^T c_{p_a}(T)\,dT + f\int_0^{T_{evap}} c_{p_{fl}}(T)\,dT \\ + \phi f\left[L_v T_{evap} + \int_0^T c_{p_{fv}}(T)\,dT \right. \\ \left. - \int_0^{T_{evap}} c_{p_{fv}}(T)\,dT\right] \end{aligned} \tag{B.16}$$

This relation is numerically solved by Matlab.
Remark: as a result, all state parameters are calculated as a function of the process variable f. These spray independent look-up tables will be used for the spray model.

B.4 Spray model

B.4.1 Basic spray equations

The model solves the 3 (discretized) laws of conservation: mass (in terms of mass fraction f_{cl}), momentum (in terms of axial spray velocity u_{cl}) and energy (in terms

of enthalpy h_{cl}).
The conservation equations are of the form:

$$\begin{aligned} 0 &= \frac{\delta}{\delta t}\left[\int_0^\infty \rho\,(x,r,t)\,q\,(x,r,t)\,dV\right] \\ &\quad + \frac{\delta}{\delta x}\left[\int_0^\infty \rho\,(x,r,t)\,q\,(x,r,t)\,u\,(x,r,t)\,dV\right] \end{aligned} \tag{B.17}$$

$$-\frac{\delta}{\delta x}\left[\int_0^\infty \rho\,(x,r,t)\,q\,(x,r,t)\,u\,(x,r,t)\,dV\right] \tag{B.18}$$

$$= \frac{\delta}{\delta t}\left[\int_0^\infty \rho\,(x,r,t)\,q\,(x,r,t)\,dV\right] \tag{B.19}$$

With $q = f$ for the conservation of mass, $q = u$ for the conservation of momentum and $q = h$ for the conservation of energy.

A Gaussian-like distribution is proposed for f, u and h with the following self-similarity relation:

$$\frac{u}{u_{cl}} = \frac{f}{f_{cl}} = \frac{h}{h_{cl}} = (1-\zeta^\alpha)^2 \tag{B.20}$$

with $\zeta = r/R(x)$, $R(x)$ the spray radius at axial position x and α the shape factor of the profile.
Substitution with the cross-sectional average $\overline{u}$, $\overline{f}$, $\overline{h}$ defined as

$$\begin{aligned} \overline{q} &= \frac{\int q.dA}{\int dA} \\ &= \frac{\alpha^2}{(\alpha+1)(\alpha+2)} \end{aligned} \tag{B.21}$$

in Eq. B.20 gives:

$$\frac{u}{\overline{u}} = \frac{f}{\overline{f}} = \frac{h}{\overline{h}} = \frac{(\alpha+1)(\alpha+2)}{\alpha^2}(1-\zeta^\alpha)^2 \tag{B.22}$$

B.4.2 Derivation of the spray equations

The basic spray equations from Eq. B.18 are discretized in order to implement the equations in a numerical program such as Matlab.

Discretization of the right hand side of Eq. B.18

$$\frac{\Delta\left[\int_0^\infty \rho\,(x,r,t)\,q\,(x,r,t)\,dV\right]}{\Delta t} = \frac{\left[\int_0^\infty \rho\left(x,r,t^{j+1}\right)q\left(x,r,t^{j+1}\right)dV\right] - \left[\int_0^\infty \rho\left(x,r,t^{j}\right)q\left(x,r,t^{j}\right)dV\right]}{t_{i+1}-t_i} \tag{B.23}$$

The integrals of eq. B.23 can be discretized as well:

$$\int_0^{\infty} \rho\left(x,r,t^{j+1}\right) q\left(x,r,t^{j+1}\right) dV \tag{B.24}$$

$$= \int_i^{i+1} \int_{-R(x)}^{R(x)} \rho\left(x,r,t^{j+1}\right) q\left(x,r,t^{j+1}\right) 2\pi r.dr.dx \tag{B.25}$$

The integration border for the radial direction can be reduced ($-R(x)...R(x) \rightarrow 0...R(x)$) since axisymmetry is assumed. Together with Eq. B.22:

$$\begin{aligned}
&= \int_i^{i+1} \int_0^{R} \rho\left(x,r,t^{j+1}\right) \overline{q}\left(x,t^{j+1}\right) \frac{(\alpha+1)(\alpha+2)}{\alpha^2} \left(1-\zeta^{\alpha}\right)^2 2\pi r\, dr\, dx \\
&= \int_i^{i+1} 2\pi R^2\, \overline{q}\left(x,t^{j+1}\right) \left(\int_0^{1} \rho\left(x,\zeta,t^{j+1}\right) \left(1-\zeta^{\alpha}\right)^2 \zeta.d\zeta \right) dx \\
&= 2\pi \frac{\Delta x}{2} \left({R_i}^2\, \overline{q}\left(x_i,t^{j+1}\right) \int_0^{1} \rho\left(x_i,\zeta_i,t^{j+1}\right) \frac{(\alpha+1)(\alpha+2)}{\alpha^2} \left(1-{\zeta_i}^{\alpha}\right)^2 \zeta_i.d\zeta_i \right) \\
&\quad + 2\pi \frac{\Delta x}{2} \left({R_{i+1}}^2\, \overline{q}\left(x_{i+1},t^{j+1}\right) \int_0^{1} \rho\left(x_{i+1},\zeta_{i+1},t^{j+1}\right) \frac{(\alpha+1)(\alpha+2)}{\alpha^2} \left(1-{\zeta_{i+1}}^{\alpha}\right)^2 \zeta_{i+1}\, d\zeta_{i+1} \right) \\
&= \pi\Delta x \left[{R_i}^2\, \overline{q}\left(x_i,t^{j+1}\right) \int_0^{1} \rho\left(x_i,\zeta_i,t^{j+1}\right) \frac{(\alpha+1)(\alpha+2)}{\alpha^2} \left(1-{\zeta_i}^{\alpha}\right)^2 \zeta_i\, d\zeta_i \right. \\
&\quad \left. + {R_{i+1}}^2\, \overline{q}\left(x_{i+1},t^{j+1}\right) \int_0^{1} \rho\left(x_{i+1},\zeta_{i+1},t^{j+1}\right) \frac{(\alpha+1)(\alpha+2)}{\alpha^2} \left(1-{\zeta_{i+1}}^{\alpha}\right)^2 \zeta_{i+1}\, d\zeta_{i+1} \right]
\end{aligned}$$

with $\Delta x = (x_{i+1} - x_i)$.
The F-term $F_{i+1}^{j+1}(k)$ is defined as:

$$F_{i+1}^{j+1}(k) = \int_0^{1} \rho\left(x_{i+1},\zeta_{i+1},t^{j+1}\right) \left(1-{\zeta_{i+1}}^{\alpha}\right)^{2k} \zeta_{i+1}.d\zeta_{i+1} \tag{B.26}$$

The right hand side of equation B.23 reduces to:

$$\begin{aligned}
\frac{\pi\Delta x}{\Delta t} \Big[&\left({R_{i+1}}^2\, \overline{q}_{i+1}^{j+1}\, F_{i+1}^{j+1}(1) + {R_i}^2\, \overline{q}_i^{j+1} F_i^{j+1}(1) \right) \\
&- \left({R_{i+1}}^2\, \overline{q}_{i+1}^{j}\, F_{i+1}^{j}(1) + {R_i}^2\, \overline{q}_i^{j}\, F_i^{j}(1) \right) \Big]
\end{aligned} \tag{B.27}$$

Discretization of the left hand side of eq. B.18

$$\begin{aligned}
&-\frac{\delta}{\delta x} \left[\int_0^{\infty} \rho\left(x,r,t^{j+1}\right) q\left(x,r,t^{j+1}\right) u\left(x,r,t^{j+1}\right).dV \right] \\
&= -\frac{\Delta}{\Delta x} \left[\int_{x_i}^{x_{i+1}} \int_{-R}^{R} \rho\left(x,r,t^{j+1}\right) q\left(x,t^{j+1}\right) u\left(x,r,t^{j+1}\right) 2\pi r.dr.dx \right]
\end{aligned} \tag{B.28}$$

The integration border for the radial direction can be reduced ($-R...R \rightarrow 0...R$) since axisymmetry is assumed:

$$\begin{aligned}
&= -\frac{1}{\Delta x}\left[\int_0^R \rho\left(x_{i+1},r,t^{j+1}\right) q\left(x_{i+1},r,t^{j+1}\right) u\left(x_{i+1},r,t^{j+1}\right).2\pi r.dr.\Delta x\right] \\
&\quad + \frac{1}{\Delta x}\left[\int_0^R \rho\left(x_i,r,t^{j+1}\right) q\left(x_i,r,t^{j+1}\right) u\left(x_i,r,t^{j+1}\right).2\pi r.dr.\Delta x\right] \\
&= \int_0^R \rho\left(x_i,r,t^{j+1}\right) q\left(x_i,r,t^{j+1}\right) u\left(x_i,r,t^{j+1}\right).2\pi r.dr \\
&\quad - \int_0^R \rho\left(x_{i+1},r,t^{j+1}\right) q\left(x_{i+1},r,t^{j+1}\right) u\left(x_{i+1},r,t^{j+1}\right).2\pi r.dr
\end{aligned} \tag{B.29}$$

Inserting the expression of the radial distributions, the expression leads to:

$$2\pi\left({R_i}^2\,\overline{q}_i^{j+1}\,\overline{u}_i^{j+1}\,F_i^{j+1}(2) - {R_{i+1}}^2\,\overline{q}_{i+1}^{j+1}\,\overline{u}_{i+1}^{j+1}\,F_{i+1}^{j+1}(2)\right) \tag{B.30}$$

The general equation for the set of spray equations (Eq. B.18):

$$\begin{aligned}
&2\pi\left(R_i^2\,\overline{q}_i^{j+1}\,\overline{u}_i^{j+1}\,F_i^{j+1}(2) - R_{i+1}^2\,\overline{q}_{i+1}^{j+1}\,\overline{u}_{i+1}^{j+1}\,F_{i+1}^{j+1}(2)\right) \\
&= \frac{\pi\Delta x}{\Delta t}\left(R_{i+1}^2\,\overline{q}_{i+1}^{j+1}\,F_{i+1}^{j+1}(1) + R_i^2\,\overline{q}_i^{j+1}\,F_i^{j+1}(1)\right. \\
&\left. -R_{i+1}^2\,\overline{q}_{i+1}^{j}\,F_{i+1}^{j}(1) - R_i^2\,\overline{q}_i^{j}\,F_i^{j}(1)\right)
\end{aligned}$$

The conservation of momentum becomes:

$$\begin{aligned}
&2\pi\left(R_i^2\,\overline{u}_i^{j+1\,2}\,F_i^{j+1}(2) - R_{i+1}^2\,\overline{u}_{i+1}^{j+1\,2}\,F_{i+1}^{j+1}(2)\right) \\
&= \frac{\pi\Delta x}{\Delta t}\left[R_{i+1}^2\,\overline{u}_{i+1}^{j+1}\,F_{i+1}^{j+1}(1) + R_i^2\,\overline{u}_i^{j+1}\,F_i^{j+1}(1)\right. \\
&\left. -R_{i+1}^2\,\overline{u}_{i+1}^{j}\,F_{i+1}^{j}(1) - R_i^2\,\overline{u}_i^{j}\,F_i^{j}(1)\right]
\end{aligned} \tag{B.31}$$

Eq. B.31 is written in the form

$$A_u\left(\overline{u}_{i+1}^{j+1}\right)^2 + B_u\,\overline{u}_{i+1}^{j+1} + C_u = 0 \tag{B.32}$$

The parameters A_u, B_u and C_u become as listed in table B.1

A_u	$2\pi {R_{i+1}}^2\,F_{i+1}^{j+1}(2)$
B_u	$\pi\frac{\Delta x}{\Delta t}{R_{i+1}}^2\,F_{i+1}^{j+1}(1)$
C_u	$\pi\frac{\Delta x}{\Delta t}\left({R_i}^2\,\overline{u}_i^{j+1}\,F_i^{j+1}(1) - {R_{i+1}}^2\,\overline{u}_{i+1}^{j}\,F_{i+1}^{j}(1) - R_i^2\,\overline{u}_i^{j}\,F_i^{j}(1)\right)$ $-2\pi R_i^2\,\overline{u}_i^{j+1}\,F_i^{j+1}(2)$

Table B.1: Parameters for the equation of momentum conservation

The conservation of mass becomes:

$$\begin{aligned} &2\pi\left(R_i{}^2\,\overline{u}_i^{j+1}\,\overline{f}_i^{j+1}\,F_i^{j+1}(2)-R_{i+1}{}^2\,\overline{f}_{i+1}^{j+1}\,\overline{u}_{i+1}^{j+1}\,F_{i+1}^{j+1}(2)\right)\\ &=\frac{\pi\Delta x}{\Delta t}\left(R_{i+1}^2\,\overline{f}_{i+1}^{j+1}\,F_{i+1}^{j+1}(1)+R_i^2\,\overline{f}_i^{j+1}\,F_i^{j+1}(1)\right.\\ &\left.-R_{i+1}^2\,\overline{f}_{i+1}^{j}\,F_{i+1}^{j}(1)-R_i^2\,\overline{f}_i^{j}\,F_i^{j}(1)\right) \end{aligned} \tag{B.33}$$

Eq. B.33 is written in the form

$$A_f\,\overline{u}_{i+1}^{j+1}\,\overline{f}_{i+1}^{j+1}+B_f\,\overline{f}_{i+1}^{j+1}+C_f=0 \tag{B.34}$$

the parameters A_f, B_f and C_f become as listed in table B.2

A_f	$2\pi R_{i+1}{}^2\,F_{i+1}^{j+1}(2)$
B_f	$\pi\frac{\Delta x}{\Delta t}R_{i+1}{}^2\,F_{i+1}^{j+1}(1)$
C_f	$\pi\frac{\Delta x}{\Delta t}\left(R_i{}^2\,\overline{u}_i^{j+1}\,F_i^{j+1}(1)-R_{i+1}{}^2\,\overline{u}_{i+1}^{j}\,F_{i+1}^{j}(1)-x_i{}^2\,\overline{u}_i^{j}\,F_i^{j}(1)\right)$ $-2\pi R_i{}^2\,\overline{u}_i^{j+1}\,F_i^{j+1}(2)$

Table B.2: Parameters for the equation of momentum conservation

The energy equation does not provide extra information since the energy is correlated with the mass equation through the assumption that $Le = 1$.

B.4.3 Derivation of the F-terms

The F-term was defined in Eq. B.26.

$$F_{i+1}^{j+1}(k)=\int_0^1\rho\left(x_{i+1},\zeta_{i+1},t^{j+1}\right)\left(1-\zeta_{i+1}{}^{\alpha_{i+1}^{j+1}}\right)^{2k}\,\zeta_{i+1}\,d\zeta_{i+1} \tag{B.35}$$

and can be discretized as

$$F_{i+1}^{j+1}(k)=\sum_{l=0}^{1}\rho\left(x_{i+1},\zeta_{l,i+1},t^{j+1}\right)\left(1-\zeta_{l,i+1}{}^{\alpha_{i+1}^{j+1}}\right)^{2k}\,\zeta_{l,i+1}\,\Delta\zeta_{l,i+1} \tag{B.36}$$

with $\zeta_{l,i+1}=\frac{r_l}{R_{i+1}}$ and $\Delta\zeta_{l,i+1}$ is a constant step size in this work.
Here, the mixture density ρ is a function of the fuel fraction. Since a priori the fuel fraction is not known for a certain relative radial position ζ, the fuel fraction is calculated at the corresponding position according to:

$$f=\frac{(1+\alpha)(2+\alpha)}{\alpha^2}\,\overline{f}\,(1-\zeta^{\alpha})^2 \tag{B.37}$$

The density can now be found in the lookup table of the state relations through interpolation.

B.5 Solver improvements

B.5.1 Variable spatial grid

The algorithm described by the Valencia group uses a constant spatial and time grid size, which might lead to inefficient resolving time when accurate results are required. The grid size is even more important for variable injection profiles if little information wants to be lost.
In order to avoid loss of information the time step should meet the Nyquist criterium:

$$\Delta t < \frac{\Delta x}{U_{max}} \tag{B.38}$$

with U_{max} the maximum velocity in the calculation, which will be the maximum velocity at the nozzle outlet. This time step dt is unlikely able to change during the calculation: for constant injection profiles the time step will necessarily to be constant due to the Nyquist criterium. For time varying injection profiles, the timestep might be altered based on the injection velocity, but can come in conflict when the injection velocity becomes lower than a velocity more downstream (as a result from an earlier high injection velocity).
The other possibility left is the adaptation of the grid along the spray. The grid size can be enlarged since the velocity only reduces along the spray (the initial grid size is based on the maximum velocity). One important issue is that the grid size should be the same for each time step since information is required from the previous time step. The increase of the grid size for a constant injection velocity can be optimized during the spray, especially during the steady state part of the spray since the velocity is not expected to change much. For this reason, the spatial grid is changed after a few time steps (such that a steady state part is already visible). The spatial grid step is then defined as

$$\Delta x_{i+1} = x_{i-k+1} - x_{i-k} \tag{B.39}$$

where k is chosen to avoid influences of the spray tip. For $k > 5$, the calculations should not be influenced anymore. This implies that the first k spatial grid steps are constant as specified in the input file for the model.
So in the case of a variable injection profile, the grid is determined a priori, while the grid for a constant velocity profile can be built up during the calculation.
The implemented grid strategy is schematically shown in Fig. B.2.

B.5.2 Fuel fraction steps

Recalling Fig. 5.7, the value range for the fuel fraction f during the 'liquid core' region (cfr. chapter 5) is large (from $f = 1$ down to 0.257) while only a small fraction of the spray involves the low fuel fraction range. This implies that interpolation of

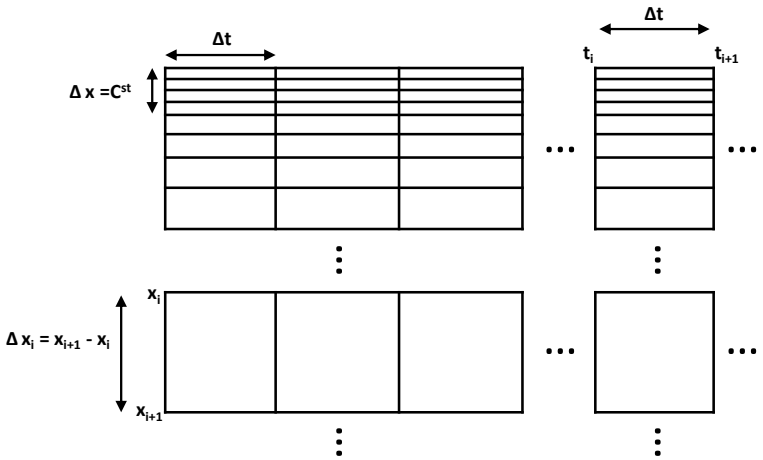

Figure B.2: Applied grid strategy for the spray model

a big part will be less sufficient in the steady spray region (especially for low fuel fraction values). To improve the accuracy for the steady state spray while keeping the resolving at the same level, the grid step for the fuel fraction during the calculation of the state relation look-up table is adjusted. For fuel fractions lower than 0.26 the step is taken smaller while coarser steps are taken for higher fuel fractions.

C

Oil composition & analyzing techniques

The appendix is organized as follows: 2 analyzing methods (GC-MS and HPLC) to characterize the oil composition, are described. This data will be necessary to compose a surrogate fuel for the considered oil. Additionally, measurement techniques for viscosity and saturation pressure are briefly considered. Finally, the composition of common oils is given in terms of the triglycerides.

C.1 Oil composition analyzing techniques

Basically, all oils consist of mixture of tri-glycerides and in order to understand their chemical and physical differences, knowledge of the content of the different glycerides is necessary.

C.1.1 Gas Chromatography - Mass Spectroscopy (GC-MS)

A GC-MS analyser is used to specify the mass content of the different molecules in a liquid. The analyzing technique is based on the difference in volatility of the different molecules. The analyser is divided into 2 main parts: a gas chromatograph and a mass spectrometer.
In the gas chromatograph, the different molecules are detected and specified while the mass spectrometer determines the mass content of the analyzed sample.

The principle of the GC-MS analyzer is schematically presented in the left of Fig. C.1. First, the sample is heated (up to $250°C$) in order to vaporize the liquid before entering the gas chromatograph. Due to the big size of the triglycerides, the molecules are broken in their fatty acids. This is the reason why only the fatty acids can be obtained from the GC-MS technique. After evaporation by the carrier gas (usually *He*), the vapor is transported through a tube, filled with porous particles with a specified size (depending on the application). Due to the molecule size, some molecules are able to pass faster than others. If the interaction with the porous particles is weak, the molecules flow off the column in a short amount of time, and if the interaction is strong, then the residence time is long. Next, the mass spectrometer analyses the incoming molecules by their molecular weight. The obtained data is then compared with a database to finally display the results. The right side of Fig. C.1 shows a typically obtained result for an oil. The height of the peaks is a measure for the mass fraction.

C.1.2 High Performance Liquid Chromatography (HPLC)

High Performance Liquid Chromatography (HPLC) is a chromatographic method also used to separate and quantify the components in a liquid mixture without chemical decomposition of the molecules.
In general, the method involves a liquid sample (the investigated oil in this case) being passed over a solid adsorbent material packed into a column using a flow of liquid solvent. Each component in the sample interacts slightly differently with the adsorbent material, thus differently retarding the flow of each component in the sample.
The crucial difference with GC-MS is the fact that the samples are pressurized between 5 to $35MPa$, which makes it possible to deal with bigger molecules (read:

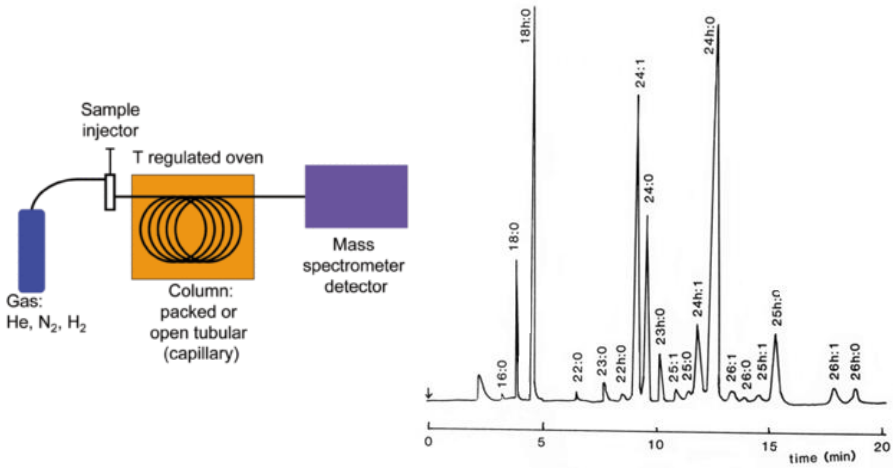

Figure C.1: left: schematical representation of the GC-MS technique, right: typical GC-MS result for an oil

more viscous liquids). This feature however makes the devices more expensive.
The principle of the HPLC analyzer is schematically presented in the left of Fig C.2: the sampler brings the sample mixture into the mobile phase stream which carries it into the column. The pump delivers the desired flow and composition of the mobile phase through the column. The detector generates a signal proportional to the amount of sample component emerging from the column, hence allowing for quantitative analysis of the sample components. The right side shows a typical obtained result for an oil (palm oil in this case). The height of the peaks is a measure for the mass fraction.

C.2 Density

When little accuracy is required, the density can be obtained by weighing a specified volume of the liquid to analyse. This method however becomes time consuming if data for different temperatures is required and the accuracy will decrease due to temperature inhomogeneity of the batch. A more advanced measurement tool/method is necessary.
The density measurement method used in this work is based on the U-vibrating tube. The U-tube, filled with the fuel sample, oscillates at its fundamental frequency, which is a function of the system mass. If the sample volume is constant, it can be proven that the oscillation frequency is a function of the sample density. The measurements were performed with an Anton Paar DMA 5000 density meter (cfr. Fig. C.4). Temperature steps could be applied automatically as such that

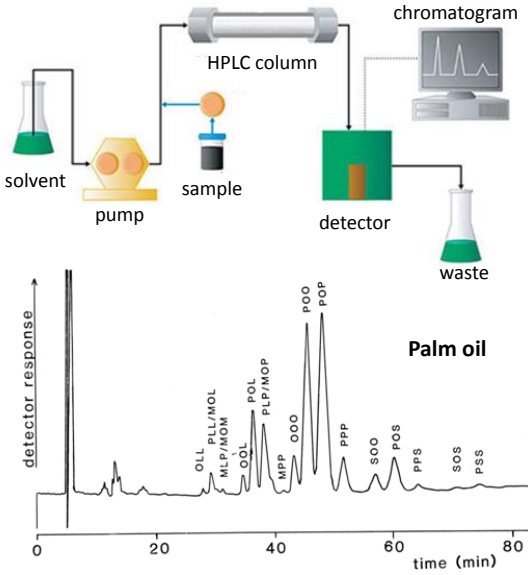

Figure C.2: top: schematical representation of the HPLC technique, bottom: typical HPLC result for palm oil

the temperature dependency of the density could be displayed. The measurements were performed at the department of Applied Analytic and Physical Chemistry (Faculty of Bio-engineering).

C.3 Surface tension

The surface tension at the interface between fuel and air was measured using two different measurement techniques: the Wilhelmy plate and stalagmometric method.
The Wilhelmy plate method consists of a thin plate attached to a balance via a thin metal wire. This plate is lowered to the surface of a liquid. The downward force on the plate, due to wetting, is measured via the measured mass of the droplets on the plate and used to calculate the surface tension using the Wilhelmy equation:

$$\sigma = \frac{F_{downward}}{l.cos(\theta)} \tag{C.1}$$

Figure C.3: The Anton Paar DMA 5000 density meter

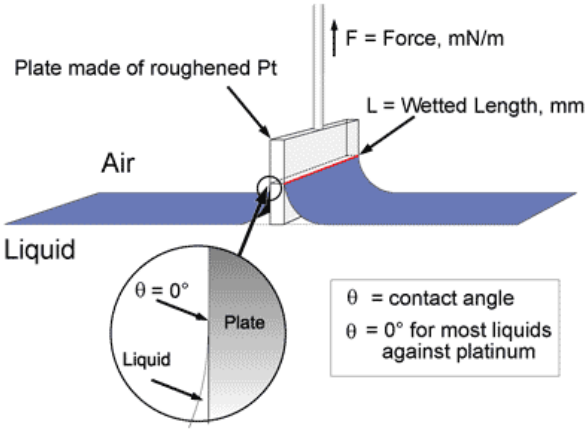

Figure C.4: principle of the Wilhelmy plate method to measure the surface tension

C.4 Viscosity

Several easy and cheap commercial methods exist to determine the viscosity of liquids. Methods like 'falling object'-, 'oscillating object'-, vibrational and rotational methods are commonly used. All these methods will not be described in detail, but all rely on the measuring of the resistance to movement.
Viscosity measurements in this work were performed with a rotative type Brookfield DV II viscometer (cfr. Fig. C.5). This device uses a rotor that is placed in a cup with the liquid to investigate at the desired temperature. The resistance of the liquid will induce extra current in the electromotor to keep the same rotation speed. This extra current is a measure for the viscosity. For the reliability of the test re-

sults, all measurements were repeated several times at different rotation speeds in the range in which the torque varied between 30 up to 70% of the maximum torque of the viscometer. In this torque range, the measurements are the most accurate. The temperature dependency of the viscosity was measured by heating the liquid batch. The same remark as for the temperature dependency of the density should be made: heating the batch induces inaccuracies due to temperature inhomogeneities, and they increase with temperature

Figure C.5: The Rion Viscometer used for the performed viscosity measurements

C.5 Vegetable oil & fat composition

Table C.1 lists again the most important fatty acids that are contained in oils. The triglyceride composition of some common oils is listed in table C.3 (results from a HPLC analysis), while the fatty acid composition is given in table C.4 (results from a GC-MS analysis). It should be pointed out that the composition can differ with the batch and origin, but the tables give an indication and general comparison between the different types of oil. Table C.3 also tend to indicate that the composition is complex and not all HPLC analyzers can detect all combinations, which makes it hard to describe the oils as a function of the triglyceride composition. Furthermore, little data is available for this set of triglycerides.

fatty acid	**abbreviation**	**notation**
lauric acid	La	C12:0
myristic acid	M	C14:0
palmitic acid	P	C16:0
palmitoleic acid	Pl	C16:0
stearic acid	S	C18:0
oleic acid	O	C18:1
linoleic acid	L	C18:2
linolenic acid	Ln	C18:3
arachidic acid	A	C20:0
eicosenoic acid	E	C20:1
benenic acid	B	C22:0
erucic acid	Er	C22:1
lignoceric acid	Lg	C24:0

Table C.1: Most common fatty acid groups contained in biodiesel with the notation Cxx:y, containing xx carbon atoms and y double bonds in each molecule

fat	# C=C	palm	peanut	rapeseed	soybean	sunflower
LnLO	6			5.3	2	
LLO	5		10.4	7.4	8.7	29.1
LnOO	5			10.3	0.3	
LnOP	4			2.1	2.1	
LOO	4	1.2	20.8	21.9	3.1	6.5
LOP	3	10.2	8.6	5.0	12.2	4.0
OOO	3	3.9	12.7	15.6	0.8	0.6
POO	2	21.4	7.9	4.0	1	
SOO	2	2.8	3.0	1.1	0.2	
PPP	0	4.8				
LLP	4		2.3	1.0	21.4	7.0
LOS	3		4.3	2.0	1.3	2.0
LLL	6		1.4	1.0	9.6	36.3
LnLL	7				3.2	
LLnLn	8			2.5		
LnLnO	7			3.4	0.2	
LnLnP	6				0.6	
LnLP	5			0.7	9.4	
LnPP	3			0.1	2.0	
LLS	4		0.8		2.0	
PLP	2	9.4	0.8	0.7	14.8	
LnSS	3				3.0	
POP	1	27.4	1.1	0.7	1.5	
SLS	2				0.3	
SOP	1	5.3		0.5	0.2	
AOO	2		1.2	0.4		
PLB	2		0.5			
OLA	3		0.8	0.3		4.0
OOE	3		1.7	1.2		2.0
LLA	4		0.6			3.0

Table C.2: The triglyceride composition of some commonly used oils [mol%] [173]

fat	# C=C	palm	peanut	rapeseed	soybean	sunflower
OOB	2		2.0	0.1		3.3
OLB	3		2.9	0.5		
LLB	4		1.0			
OOLg	2		1.2			
LOLg	3		1.7			
LLLg	4		0.6	0.3		
SOS	1	1.4		0.1		
MMM	0	0.8				
MPL	2	3.0				
MMP	0	2.4				
ELO	4			10.4		
ELS	3			0.5		
EOP	2			0.7		
EOE	3			0.3		

Table C.3: The triglyceride composition of some commonly used oils [mol%] [173] (continued)

fat	Formula	palm	peanut	rapeseed	soybean	sunflower
La	C12:0	0.2				
M	C14:0	1.1		0.1	0.1	
P	C16:0	44.0	10.0	4.8	10.8	6.2
Pl	C16:1	0.1			0.3	0.2
S	C18:0	4.5	3.8	3.6	4.0	4.7
O	C18:1	39.2	54.4	59.8	23.8	20.4
L	C18:2	10.1	24.7	21.3	53.3	68.8
Ln	C18:3	0.4		10.7	7.6	
A	C20:0	0.4	1.6	0.6		0.2
E	C20:1		1.1	1.3	0.2	
B	C22:0		2.9	0.3		0.1
E	C22:1			0.2		
Lg	C24:0		1.3			0.1

Table C.4: The fatty acid composition of some commonly used oils [mol%] [173]

D

Oil surrogate calculation

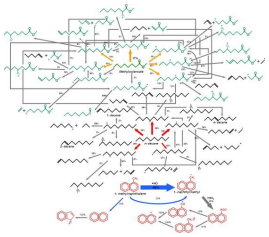

≈ $C_{16}H_{34}$

The appendix is organized as follows: The 4 different equations of the surrogate matching requirement are derived in the different sections: saturation pressure, amount of oxygen contained in the fuel, the amount of double bonds and the conservation of mass.

D.1 Viscosity

The viscosity for a liquid mixture is calculated according to:

$$\mu_i = \frac{b_1 T^{b_2}}{1 + \frac{b_3}{T} + \frac{b_4}{T^2}} \tag{D.1}$$

$$\mu_{mix} = \sum \frac{X_i \mu_i}{\sum X_j A_{ij}} \tag{D.2}$$

$$A_{ij} = \frac{\left[1 + \left(\frac{\mu_i}{\mu_j}\right)^{0.5} \left(\frac{M_j}{M_i}\right)^{0.25}\right]^2}{\left[8\left(1 + \frac{M_i}{M_j}\right)\right]^{0.5}}$$

The viscosity of the real fuel $\mu_f(T_f)$ is measured at the desired injection temperature.
This measured viscosity should be equal to the viscosity of the surrogate fuel at the same temperature. With as a first approximation by putting $A(i,i) = 1$ and $A(i,j) = 0$, the implemented equation becomes:

$$\mu_f(T_f) = X_{TC}\mu_{TC}\left(T_f\right) + X_{PT}\mu_{PT}\left(T_f\right) + X_{ST}\mu_{ST}\left(T_f\right) + X_{LT}\mu_{LT}\left(T_f\right) \tag{D.3}$$

with TC, triacontane; PT, palmitic triglyceride; ST, stearic triglyceride; LT, linoleic triglyceride

D.2 Amount of oxygen

From the Gas Chromatography - Mass Spectroscopy (GC-MS) results, the different fatty acids in the oil can be identified (cfr. section 6.5.3). The results allows us to write the fuel as a combinition of *C12-C24* chains. *Cxx* stands for a fatty acid which contains a total of *xx* carbon atoms. The range is limited to *C12* up to *C24* since this is the main range for bio-oils (only triglycerides are considered).
The amount of oxygen in the real fuel should be equal to the amount of oxygen in the surrogate. This is expressed in terms of oxygen-carbon ratio, knowing that each triglyceride contains 6 oxygen atoms:

$$\begin{aligned} C_{tot} = {} & (C12:0).13 + (C14:0).15 + (C16:0).17 + (C16:1).17 \\ & + (C17:0).18 + (C17:1).18 + (C18:0).19 + (C18:1).19 \\ & + (C18:2).19 + (C18:3).19 + (C20:0).21 + (C20:1).C21 \\ & + (C22:0).C23 \end{aligned} \tag{D.4}$$

$$\frac{2}{C_{tot}} = \frac{6.X_{PT} + 6.X_{ST} + 6.X_{LT}}{X_{TC}.30 + X_{PT}.51 + X_{ST}.57 + X_{LT}.57} \tag{D.5}$$

Writing Eq. D.4 in function of the molar fraction of the surrogate components results in:

$$X_{TC}.30 + X_{PT}.51 + X_{ST}.57 + X_{LT}.57 = \left(3.X_{PT} + 3.X_{ST} + 3.X_{LT}\right).C_{tot}$$

$$0 = [30]X_{TC} + [57 - C_{tot}]X_{PT} + [57 - C_{tot}]X_{ST} + [57 - C_{tot}]X_{LT} \tag{D.6}$$

D.3 Amount of double bonds

From the fatty acid composition the amount of double bonds can be calculated according to Eq. D.7 in terms of mole fraction '$C_{xx:y}$', with y the amount of bonds in the fatty acid and $C_{xx:y}$ the molar fraction of fatty acid with y double bonds.

$$\begin{aligned} C_{xx:1} &= (C16:1) + (C17:1) + (C18:1) + (C20:1) + (C22:1) \\ C_{xx:2} &= (C18:2) \\ C_{xx:3} &= (C18:3) \end{aligned} \tag{D.7}$$

The amount of 'bond reactivity' is attempted to match with the 'bond reactivity' in the surrogate fuel: the double bonds have been found to have an important influence on the ignition delay as discussed in section 1.2. The relative reactivity from section 1.2 is used to construct Eq. D.8, which represents the total amount of equivalent reacting double bonds of the surrogate. The relative reactivity factor 1 is chosen for the acid with 2 double bonds since the only proposed surrogate component, linoleic acid triglyceride, contains 2 double bonds in each of its bonded fatty acid.

$$(0.1).C_{xx:1} + (1).2.C_{xx:2} + (1.5).3.C_{xx:3} = 6.X_{LT} \tag{D.8}$$

D.4 Total mass fraction

Since only 4 surrogate components are used, the total mole fraction needs to be 1:

$$X_{TC} + X_{PT} + X_{ST} + X_{LT} = 1 \tag{D.9}$$

D.5 Summary

The model requires as an input:

- GC-MS data: C12-C24 fatty acids in *mol%*
- the oil viscosity at injection temperature in *mPa.s*

Equations D.3, D.6, D.8 and D.9 lead to a set of equations that needs to be solved to the molar fractions X_i for the different surrogate components i:

$$[A].[x] = [B] \tag{D.10}$$

with

$$\begin{aligned}
A(1,1) &= \mu_{TC}(T_f) - \mu_f(T_f) \\
A(1,2) &= \mu_{PT}(T_f) - \mu_f(T_f) \\
A(1,3) &= \mu_{ST}(T_f) - \mu_f(T_f) \\
A(1,4) &= \mu_{LT}(T_f) - \mu_f(T_f) \\
A(2,1) &= 30 \\
A(2,2) &= 51 - 3.C_{tot} \\
A(2,3) &= 57 - 3.C_{tot} \\
A(2,4) &= 57 - 3.C_{tot} \\
A(3,1) &= 0 \\
A(3,2) &= 0 \\
A(3,3) &= 0 \\
A(3,4) &= 6 \\
A(4,1) &= 1 \\
A(4,2) &= 1 \\
A(4,3) &= 1 \\
A(4,4) &= 1
\end{aligned} \tag{D.11}$$

$$x = \begin{bmatrix} X_{TC} \\ X_{PT} \\ X_{ST} \\ X_{LT} \end{bmatrix} \tag{D.12}$$

$$B = \begin{bmatrix} \mu_f(T_f) \\ 0 \\ (0.1)C_{xx1} + 2.C_{xx2} + (1.5)3.C_{xx3} \\ 1 \end{bmatrix} \tag{D.13}$$

References

[1] A. Bredenberg, The damage done in transportation - which energy source will lead to the greenest highways?, Green and clean journal.

[2] N. Rao, B. Premkumar, M. Yohan, Performance and emission characteristics of straight vegetable oil-ethanol emulsion in a compression ingition engine, ARPN Journal of Engineering and Applied Sciences 7 (4) (2012) 447–452.

[3] O. Nwafor, The effect of elevated fuel inlet temperature on performance of diesel engine running on neat vegetable oil at constant speed conditions, Renewable Energy 28 (2003) 171–181.

[4] M. Kumar, A. Kerihuel, J. Bellettre, M. Tazerout, Experimental investigations on the use of preheated animal fat as fuel in a compression ignition engine, Renewable Energy 30 (2004) 1443–1456.

[5] Y. Liu, Y. Su, C. Tovar, R. Gani, Selection of prediction methods for thermophysical properties for process modeling and product design of biodiesel manufacturing, Industrial and Engineering Chemistry Research 50 (11) (2011) 6809–6836.

[6] A. Babu, G. Devaradjane, Vegetable oils and their derivatives as fuels for CI engines: an overview, 2003, SAE Technical paper in 2003-01-0767.

[7] N. Hemmerlein, V. Korte, H. Richter, G. Schroder, Performance, exhaust emissions and durability of modern diesel engines running on rapeseed oil, 1991, SAE Technical paper in 910848.

[8] J. Dejongh, T. Adriaans, A. Adriaans, Jatropha oil quality related to use in diesel engines and refining methods, Tech. rep. (2007).

[9] R. Altin, S. Cetinkaya, H. Yucesu, The potential of using vegetable oil fuels as fuel for diesel engines, Energy conversion and management 42 (2001) 529–538.

[10] G. Knothe, J. V. Gerpen, J. Krahl, The biodiesel handbook, 2nd Edition, 2010, ISBN 978-1-893997-79-0.

[11] K. Juoperi, R. Ollus, Alternative fuels for medium-speed diesel engines, Wartsila technical journal (2008) 24–28.

[12] K. Simon, K. Wadumesthrige, M. Ara, S. Salley, Investigation of lubricity characteristics of biodiesel in petroleum and synthetic fuel, Energy and Fuels 23 (2009) 2229–2234.

[13] J. Galle, S. Verhelst, R. Sierens, L. Goyos, R. Castaneda, M. V. et al., Failure of fuel injectors in a medium speed diesel engine operating on bio-oil, Biomass and Bioenergy 40 (2012) 27–35.

[14] S. Maelfeyt, The use of pure vegetable oils and animal fats as a fuel in stationary diesel engines (in Dutch), Master thesis, Ghent University (2007).

[15] J. Galle, M. Lagast, Design of the GUCCI-setup and study of the use of bio-fuels (in Dutch), Master thesis, Ghent University (2009).

[16] D. Bacon, F. Braear, I. Moncrieff, K. Walker, The use of vegetable oils in straight and modified form as diesel engine fuels, Beyond the energy crisis opportunity and challenge 3 (1981) 1525–1533.

[17] M. Gupta, Bailey's Industrial Oil and Fat Products, sixth edition Edition, Frying oils, John Wiley & Sons, 2005, ISBN 978-0-471-38460-1.

[18] M. Ziejewski, H. Goettler, Design modifications for durability improvements of diesel engines operating on plant oil fuels, 1992, SAE Technical paper in 921630.

[19] G. Labeckas, S. Slavinskas, Performance of direct-injection off-road diesel engine on rapeseed oil, Renewable Energy 31 (2006) 849–863.

[20] D. Agarwal, L. Kumar, A. A. Kumar, Performance evaluation of a vegetable oil fuelled compression ignition engine, Renewable Energy 33 (2008) 1147–1156.

[21] S. Jones, C. Peterson, Using unmodified vegetable oils as a diesel fuel extender, Tech. rep., University of Idaho (2001).

[22] M. Meijer, J. Galle, L. Somers, J. Griensven, S. Verhelst, High-speed characterization of ECN spray A using various diagnostic techniques, SAE journal Engines 2013-011616.

[23] J. Dec, A conceptual model of DI diesel combustion based on laser-sheet imaging, 1997, SAE Technical paper in 970873.

[24] J. Dec, Ignition and early soot formation in a DI diesel engine using multiple 2-D imaging diagnostics, 1995, SAE Technical paper in 950456.

[25] L. M. Pickett, Understanding diesel spray combustion, Towards Clean Diesel Engines, 2008.

[26] L. M. Pickett, D. Siebers, Fuel effects on soot processes of fuel jets at DI diesel conditions, 2003, SAE Technical paper in 2003-01-3080.

[27] H. Kosaka, T. Aizawa, T. Kamimoto, Two-dimensional imaging of ignition and soot formation processes in a diesel flame, International Journal of Engine Research 6 (2005) 21–42.

[28] G. Bruneaux, Detailed analysis of mixture and combustion of diesel jets by laser lif techniques, Towards Clean Diesel Engines, 2008.

[29] G. Bruneaux, Mixing process in high pressure diesel jets by normalized laser induced exciplex fluorescence part I: Free jet, 2005, SAE Technical paper in 2005-01-2100.

[30] M. Musculus, P. Miles, L. M. Pickett, Conceptual models for partially premixed low-temperature diesel combustion, Progress in Energy and Combustion Science 39 (2013) 246–283.

[31] R. Tatschl, C. K. Sarre, E. Berg, IC-engine spray modeling - status and outlook, International Multidimensional Engine Modeling User's Group Meeting.

[32] M. Blessing, G. Konig, C. Kruger, U. Michels, V. Schwarz, Analysis of flow and cavitation phenomena in diesel injection nozzles and its effects on spray and mixture formation, 2003, SAE Technical paper in 2003-01-1358.

[33] S. Martynov, D. Mason, H. M., Effect of viscous stress on cavitation flow in nozzles, Journal of Fluids Engineering.

[34] S. Martynov, Numerical simulation of the cavitation process in diesel fuel injectors, Phd thesis, University of Brighton (2005).

[35] M. Arai, H. Hiroyasu, Structures of fuel sprays in diesel engines, 1990, SAE Technical paper in 900475.

[36] H. Chaves, M. Knapp, A. Kubitzek, F. Obermeier, T. Schneider, Experimental study of cavitation in the nozzle hole of diesel injectors using transparent nozzles., 1995, SAE Technical paper in 950290.

[37] C. Soteriou, R. Andrews, M. Smith, Direct injection diesel sprays and the effect of cavitation and hydraulic flip on atomization, 1995, SAE Technical paper in 950080.

[38] C. Badock, R. Wirth, A. Fath, A. Leipertz, Investigation of cavitation in real size diesel injection nozzles, Heat and Fluid Flow 20 (5) (1999) 538–544.

[39] N. Dumont, O. Simonin, C. Habchi, Cavitating flow in diesel injectors and atomization : a bibliographical review, Eighth International Conference on Liquid Atomization and a Spray systems, Pasadena, USA, 2000.

[40] J.-S. Han, P.-H. Lu, X.-B. Xie, M.-C. Lai, N. A. Henein, Investigation of diesel spray primary break-up and development for different nozzle geometries., 2002, SAE Technical paper in 2002-01-2775.

[41] D. Schmidt, Cavitation in diesel fuel injector nozzles, Ph.D. thesis, University of Wisconsin-Madison (1997).

[42] R. Payri, V. Bermudez, F. Payri, F. Salvador, The influence of cavitation on the internal flow and the spray characteristics in diesel injection nozzles, Fuel 83 (2004) 419–431.

[43] J. Desantes, R. Payri, F. Salvador, J. Gimeno, Measurements of spray momentum for the study of cavitation in diesel injection nozzles, 2003, SAE Technical paper in 2003-01-0703.

[44] P. Payri, Using spray momentum flux measurements to understand the influence of diesel nozzle geometry on spray characteristics, Fuel 84 (5) (2005) 551–561.

[45] H. Roth, M. Gavaises, C. Arcoumanis, Cavitation initiation, its development and link with flow turbulence in diesel injector nozzles., 2002, Technical paper in 2002-01-2014.

[46] C. Arcoumanis, H. Flora, M. Gavaises, N. Kampanis, Investigation of cavitation in a vertical multi-hole injector, 1999, SAE Technical paper in 1999-01-0524.

[47] L. Somers, R. Baert, R. Klein-Douwel, P. Frijters, W. D. Boer, Macroscopic diesel fuel spray shadowgraphy using high speed digital imaging in a high pressure cell, Fuel 86 (2007) 1994–2007.

[48] R. Klein-Douwel, P. Frijters, X. Seykens, L. Somers, R. Baert, Gas density and rail pressure effects on diesel spray growth from a heavy-duty common rail injector, Energy & Fuel 23 (4) (2008) 1832–1842.

[49] C. Baumgarten, Mixture formation in internal combustion engines, Springer, 2006, ISBN 978-3-540-30835-5.

[50] R. Ochoterena, P. Li, M. Vera-Hernandez, S. Andersson, Influence of cavitation on atomisation at low pressures using up-scaled and transparent nozzles, 23rd Annual ILASS-Europe Conference on Liquid Atomization and Spray Systems, Brno, Czech Republic, 2010.

[51] M. Gavaises, A. Andriotis, Cavitation inside multi-hole injectors for large diesel engines and its effect on the near-nozzle spray structure, 2006, Technical paper in 2006-01-1114.

[52] S. Som, A. I. Ramirez, D. E. Longman, Aggarwal, Effect of nozzle orifice geometry on spray, combustion, and emission characteristics under diesel engine conditions., Fuel 90 (2011) 1267–1276.

[53] M. Gavaises, A. Andriotis, D. Papoulias, N. Mitroglou, A. Theodorakakos, Characterization of string cavitation in large-scale diesel nozzles with tapered holes., Physics of fluids 21 (2009) 1–9.

[54] C. Chryssakis, D. Assanis, C. Bae, Development and validation of a comprehensive CFD model of diesel spray atomization accounting for high Weber numbers, 2006, SAE Technical paper in 2006-01-1546.

[55] F. Karrholm, H. Weller, N. N., Modelling injector flow including cavitation effects for diesel applications, Fluid Engineering Conference, San Diego, USA, 2007, fEDSM2007-37518.

[56] H. Hiroyasu, M. Suzuki, K. Nishida, Simultaneous concentration measurement of vapor and liquid in an evaporating diesel spray, 1993, SAE Technical paper in 930863.

[57] R. Reitz, Y. Zhu, Modeling fuel system performance and its effect on spray characteristics, 2000, SAE Technical paper in 2000-01-1253.

[58] M. Battistoni, C. Grimaldi, Analysis of transient cavitating flows in diesel injectors using diesel and biodiesel fuels., 2010, SAE Technical paper in 2010-01-2245.

[59] A. Kastengren, C. Powell, Z. Tilocco, K. Fezzaa, S. Moon, X. Z. et al., X-ray diagnostics of ECN injector geometry, needle motion, and spray behavior, ECN webmeeting, september, 2011.

[60] C. Powell, D. Schmidt, M. Arienti, ECN2: Nozzle geometry and internal flow, ECN2, Heidelberg, Germany, 2012.

[61] R. Reitz, R. Diwakar, Structure of high-pressure fuel spray, 1987, SAE Technical paper in 870598.

[62] A. Gosman, D. Clerides, Diesel spray modeling: a review, Tech. rep. (1997).

[63] R. Rotondi, G. Bella, C. Grimaldi, L. Postrioti, Atomization of high-pressure diesel spray: experimental validation of a new breakup model, 2001, SAE Technical paper in 2001-01-1070.

[64] G. Stiesch, Modeling engine spray and combustion processes, Springer, 2003, ISBN 978-3-642-05629-1.

[65] J. Manin, M. Bardi, L. M. Pickett, Engine Combustion Network: introduction to micro-visualization, ECN web-meeting, september, 2011.

[66] C. Crua, T. Shoba, M. Heikal, M. Gold, C. Higham, High-speed microscopic imaging of the initial stage of diesel spray formation and primary breakup, 2010, SAE Technical paper in 2010-01-2247.

[67] W. Hua, L. Yong-Chang, W. Ming-Rui, Z. Yu-Sheng, Multidimensional modeling of dimethyl ether (DME) spray combustion in DI diesel engine, Zhejiang University Science 6A (4) (2005) 276–282.

[68] Y. Yi, G. Zhu, R. Reitz, High-pressure spray and combustion modeling using continuous thermodynamics for diesel fuels, 2001, SAE Technical paper in 2001-01-0998.

[69] G. Barosso, B. Schneider, K. Boulouchos, An extensive parametric study on diesel spray simulation and verification with experimental data, 2003, SAE Technical paper in 2003-01-3230.

[70] P. Versaevel, P. Motte, K. Wieser, A new 3D model for vaporizing diesel sprays based on mixing-limited vaporization, 2000, SAE Technical paper in 2000-01-0949.

[71] T. Morel, S. Wahiduzzaman, Modeling of diesel combustion and emissions, Fisita, Praha, Czech Republic, 1996.

[72] C. Bekdemir, Numerical modeling of diesel spray formation and combustion, Ph.D. thesis, technical University of Eindhoven (2008).

[73] T. Shoba, C. Crua, M. R. Heikal, M. Gold, Optical characterisation of diesel, rme and kerosene sprays by microscopic imaging., 24th Annual ILASS-Europe Conference on Liquid Atomization and Spray Systems, Estoril, Portugal, 2011.

[74] J. Lacoste, Characteristics of diesel sprays at high temperatures and pressures, Phd thesis, University of Brighton (2006).

[75] D. Deshmukh, A. M. Mohan, R. V. Ravikrishna, Spray characterization of pongamia pure plant oil in a high pressure chamber, 24th Annual ILASS-Europe Conference on Liquid Atomization and Spray Systems, Estoril, Portugal, 2011.

[76] M. Reddemann, F. Mathieu, D. Martin, R. Kneer, The influence of fuel properties on spray propagation, atomization and evaporation, 23rd Annual conference on liquid atomization and spray systems, ILASS, Brno, Czech Republic, 2010.

[77] W. Bosch, The fuel rate indicator: a new instrument for display of the characteristic of individual injection., SAE World Congress, Detroit, MI, 1966, 660749.

[78] J. Dernotte, C. Hespel, F. Foucher, S. Houille, C. Mounaim-Rousselle, Experimental study of the influence of fuel physical properties on the diesel injection process in nonvaporizing conditions., 24th European Conference on Liquid Atomization and Spray Systems, Estoril, Portugal, 2011.

[79] D. Siebers, J. Naber, Effects of gas density and vaporization on penetration and dispersion of diesel sprays, 1996, SAE Technical paper in 960034.

[80] R. J.M. Payri Desantes, F. Salvador, J. D. L. Morena, Influence of cavitation phenomenon on primary break-up and spray behavior at stationary conditions, Fuel 89 (10) (2010) 3033–3041.

[81] J. Arregle, J. Pastor, S. Ruiz, The influence of injection parameters on diesel spray characteristics, 1999, SAE Technical paper in 1999-01-0200.

[82] C. Crua, Combustion processes in a diesel engine, Phd thesis, Brighton of University (2002).

[83] J.-Y. Koo, J. Martin, Droplet sizes and velocities in a transient diesel fuel spray., 1990, SAE Technical paper in 900397.

[84] X. Wang, Z. Huang, O. Kuti, W. Zhang, K. Nishida, Experimental and analytical study on biodiesel and diesel spray characteristics under ultra-high injection pressure, Journal of Heat and Fluid Flow 31 (4) (2010) 659–666.

[85] K. Varde, D. Popa, L. Varde, Spray angle and atomization in diesel sprays, 1984, SAE Technical paper in 841055.

[86] R. Reitz, F. Bracco, On the dependence of spray angle and other spray parameters on nozzle design and operating conditions, 1979, SAE Technical paper in 790494.

[87] H. Hiroyasu, M. Arai, M. Tabata, Empirical equations for the sauter mean diameter of a diesel spray, I, 1989, SAE Technical paper in 890464.

[88] Y. Ra, R. Reitz, A vaporization model for discrete multi-component fuel sprays, Multiphase Flow 35 (2009) 101–117.

[89] R. Payri, J. Desantes, J. Garcia, F. Salvador, A contribution to the understanding of isothermal diesel spray dynamics, Fuel 86 (2007) 1093–1101.

[90] D. Siebers, Liquid-phase penetration in diesel sprays, 1998, SAE Technical paper in 980809.

[91] J. Barata, Modeling of biofuel droplets dispersion and evaporation, Renewable Energy 33 (2008) 769–779.

[92] L. Pickett, S. Kook, T. Williams, Transient liquid penetration of early-injection diesel sprays, 2009, SAE Technical paper in 2009-01-0839.

[93] C. Espey, J. Dec, The effect of tdc temperature and density on the liquid-phase fuel penetration in a d.i. diesel engine, Transactions of the SAE 104 (4) (1995) 1400–1414.

[94] J. Ghandi, D. Heim, An optimized optical system for backlit imaging, Review of scientific instruments 80 (056105) (2009) 1–4.

[95] M. Musculus, L. M. Pickett, Diagnostic considerations for optical laser-extinction measurements of soot in high-pressure transient combustion environments., Combustion and Flame 141 (2005) 371–391.

[96] H. Bougie, On particulate characterization in a heavy-duty diesel engine by time-resolved laser-induced incandescense, Ph.D. thesis, Radboud University (2007).

[97] D. Siebers, Scaling liquid-phase fuel penetration in diesel sprays based on mixing-limited vaporization, 1999, SAE Technical paper in 1999-01-0528.

[98] D. S.B., H. G.O., S. B.R., Whole-field density by synthetic schlieren, Experiments in fluids 28 (2000) 322–335.

[99] G. Settles, Schlieren and Shadowgraph techniques, Springer, 2006, ISBN 978-3-540-66155-9.

[100] M. Merzkirch, D. Vitkin, W. Xiong, Quantitative flow visualization, Mechanica 33 (1998) 503–516.

[101] J. Manin, C. Genzale, D. Siebers, M. Musculus, Relationship between ignition processes and the lift-off length of diesel fuel jets, 2005, SAE Technical paper in 2005-01-3843.

[102] B. Higgins, D. Siebers, A. Aradi, Diesel-spray ignition and primixed-burn behavior, 2000, SAE Technical paper in 2000-01-0940.

[103] P. Lillo, L. Pickett, H. Persson, O. Andersson, Diesel spray ignition detection and spatial/temporal correction, SAE journal Engines 5 (3) (2012) 1330–1346.

[104] J. Barnard, Cool-flame oxidation of ketones, International symposium on combustion, 1969.

[105] J. Dec, Chemiluminescence imaging of autoignition in a DI diesel engine, 1998, SAE Technical paper in 982685.

[106] G. Zizak, Flame emission spectroscopy fundamentals and applications, Tech. rep., University of Cairo (2000).

[107] L. Arias, S. Torres, D. Sbarbaro, P. Ngendakumana, On the spectral bands measurements for combustion monitoring, Combustion and Flame 158 (3) (2011) 423–433.

[108] Ecn, http://www.sandia.gov/ecn (2010).

[109] L. Pickett, C. Genzale, G. Bruneaux, L.-M. Malbec, H. L., S. J. et al., Comparison of diesel spray combustion in different high-temperature, high-pressure facilities, 2010, SAE Technical paper in 2010-01-2106.

[110] S. Parrish, R. Zink, Development and application of an imaging system to evaluate liquid and vapor envelopes of sprays from a multi-hole gasoline fuel injector operating under engine-like conditions, 23rd Annual ILASS-Americas Conference on Liquid Atomization and Spray Systems, Ventura, CA, 2011.

[111] L. Xu, C. Lu, X. Yi, J. Jia, Image smoothing via l0 gradient minimization, ACM Transactions on Graphics 30 (6) (2011) 12.

[112] M. Bysveen, T. Almas, Ignition and combustion process of a steam injected diesel engine (stid) studied in a constant volume rig, SAE world congress, Detroit, MI, 2003, 2003-01-3249.

[113] M. Larmi, P. Rantanen, J. Tiainen, J. Kiijarvi, Simulation of non-evaporating diesel sprays and verification with experimental data, 2002, Technical paper in 2002-01-0946.

[114] D. Struckmeier, D. Tsuru, S. Kawauchi, H. Tajima, Multi-component modeling of evaporation, ignition and combustion processes of heavy residual fuel oil, 2009, SAE Technical paper in 2009-01-2677.

[115] S. Hermle, S. Renz, Weiterentwicklung eines Referenzexperiments (“Spray Combustion Chamber”) in Bezug auf die Optimierung des Verbrennungssystems von Grossdieselmotoren, Tech. rep., Bundesamt für Energie BFE (2012).

[116] P. Frijters, Fuel composition impact on heavy duty diesel engine combustion and emissions, Phd thesis, Technical University of Eindhoven (2012).

[117] R. Baert, P. Frijters, B. Somers, C. Luijten, Design and operation of a high pressure, high temperature cell for HD diesel spray diagnostics: guidelines and results, SAE World Congress, 2009, Technical paper in 2009-01-0649.

[118] G. Knothe, Kinematic viscosity of biodiesel fuel components and related compounds: influence of compound structure and comparison to petrodiesel fuel components, The Eighth International Conference for Modeling and Diagnostics for Advanced Engine Systems, 2005.

[119] S. Moerman, Study of alternative fuels: designe of a constant volume combustion chamber and study of synthesis gas (in Dutch), Master thesis, Ghent University (2008).

[120] S. Defruyt, C. V. D. Maele, A study of the atomization of biofuels in medium-speed diesel engines, Master thesis, ghent University (2012).

[121] R. Perry, D. Green, Perry’s chemical engineers’ handbook, McGraw - Hill, 1997, ISBN 0-07-115448-5.

[122] M. M., L.-M. Malbec, G. Bruneaux, L. Somers, Engine combustion network: implementation and analysis of combustion vessel spray a conditions, ICLASS, 2011.

[123] Y. Miao, Two dimensional gas temperature measurements of fuel sprays in a high pressure cell, Phd thesis, Technical University of Eindhove (2012).

[124] G. D’errico, L.-M. Malbec, ECN2 Mixing and Velocity session, ECN2, Heidelberg, Germany, 2012.

[125] S. Lorenz, J. Goldlucke, D. Straub, D. Bruggemann, Spray velocity field analysis with optical flow method - an alternative to particle image velocimetry, ICLASS, 2012.

[126] M. Meijer, B. Somers, J. Johnson, J. J. Naber, S.-Y. Lee, L.-M. M. et al., Engine combustion network (ECN): Characterization and comparison of boundary conditions for different combustion vessels, Atomization and Sprays 22 (9) (2012) 777–806.

[127] X. Seykens, L. Somers, R. Baert, Detailed modeling of common rail fuel injection process, MECCA 3 (2005) 30–39.

[128] C. Luijten, Course on combustion, Tech. rep., Technical University of Eindhoven (2010).

[129] N. Bordet, C. Caillol, P. Higelin, A physical 0D diesel combustion model using tabulated chemistry with presumed probability density function approach for engine pre-mapping, Fisita Congress, 2010, fISITA2010-SC-O-16.

[130] E. Giannadakis, M. Gavaises, A. Theodorakakos, The influence of variable fuel properties in high-pressure diesel injector, 2009, SAE Technical paper in 2009-01-0832.

[131] C. Hasse, N. Peters, Eulerian spray modeling of diesel injection in a high-pressure/high temperature chamber, Eleventh International Multidimensional Engine Modeling User's Group Meeting, University of Wisconsin-Madison, Engine Research Center, Detroit, 2002.

[132] J. Garcia, J. Pastor, J. Lopez, J. Pastor, A 1D model for the description of mixing-controlled inert diesel sprays, Fuel 87 (2008) 2871–2885.

[133] J. Garcia, J. Pastor, J. Desantes, J. Pastor, A 1D model for the description of mixing-controlled reacting diesel sprays, Combustion and Flame 156 (2009) 234–249.

[134] J. Oefelein, Thermophysical characteristics of shear-coaxial LOX-H2 flames at supercritical pressure, Proceedings of the Combustion Institute 30 (2005) 2929–2937.

[135] G. Stiesch, M. G.P., A phenomenological heat release model for direct injection diesel engines, CIMAC, Copenhagen, 1998.

[136] J. Desantes, F. Salvador, J. Lopez, J. D. L. Morena, Study of mass and momentum transfer in diesel sprays based on x-ray mass distribution measurements and on a theoretical derivation, Exp. Fluids 50 (2011) 233–246.

[137] H. Hiroyasu, T. Kadota, M. Arai, Development and use of a spray combustion modelling to predict diesel engine efficiency and pollutant emissions, JSME 26 (1983) 214.

[138] G. Bruneaux, Liquid and vapor spray structure in high pressure common rail diesel injection, Atomization and Sprays 11 (5).

[139] J. Pastor, J. Desantes, J. Garcia, J. Lopez, Evaporative diesel spray modeling, Atomization and Sprays 17 (2007) 193–231.

[140] C. Kurvers, C. Luijten, Real gas effects in mixing-limited spray vaporization models, Master thesis, TU Eindhoven (2009).

[141] M. Musculus, K. Kattke, Entrainment waves in diesel jets, 2009, SAE Technical paper in 2009-01-1355.

[142] L. M. Pickett, C. Genzale, J. Manin, M. Musculus, D. Siebers, C. Idicheria, Relationship between diesel fuel spray vapor penetration/dispersion and local fuel mixture fraction, SAE journal Engines 4 (1).

[143] J. Naber, D. Siebers, S. D. Julio, C. Westbrook, Effects of natural gas composition on ignition delay under diesel conditions, Combustion and Flame 99 (2) (1994) 192–200.

[144] J. Farrell, N. Cernansky, F. Dryer, D. Friend, C. Hergart, Development of an experimental database and kinetic models for surrogate diesel fuels, 2007, SAE Technical paper in 2007-01-0201.

[145] C. Flanigan, T. Litzinger, R. Graves, The effect of aromatics and cycloparaffins on DI diesel emissions, 1989, SAE Technical paper in 892130.

[146] C. Mueller, G. Martin, Effects of oxygenated compounds on combustion and soot evolution in a DI diesel engine: broadband natural luminosity imaging, SAE Trans. 111 (4) (2002) 2002–01–1631.

[147] W. Mathews, R. Coverdill, C. Lee, R. White, Liquid and vapor fuel distributions in a small-bore high-speed direct-injection diesel engine, SAE Trans. 111 (4) (2002) 2002–01–2666.

[148] R. Montajir, T. Kawai, H. Naito, H. Suzuki, H. Ishii, Y. G. et al., Visualization experiment in a transparent engine with pure and mixed normal paraffin fuels, 2004, SAE Technical paper in 2004-01- 2018.

[149] P. Stralin, F. Wahlin, H.-E. Angstrom, Effecs of injection timing on the conditions at top dead center for direct injected HCCI, 2003, SAE Technical paper in 2003-01-3219.

[150] H. Wanga, S. Warner, M. Oehlschlaeger, R. Bounaceur, J. Biet, An experimental and kinetic modeling study of the autoignition of a-methylnaphthalene/air and a-methylnaphthalene/n-decane/air mixtures at elevated pressures, Combustion and Flame 157 (2010) 1976–1988.

[151] H. Xu, Z. Yang, M. Chaos, F. Dryer, Surrogate jet fuel mixture formulation and development of experimental databases, JANNAF 42nd Combustion Subcommittee, Boston, 2008.

[152] K. Puduppakkam, L. Liang, C. Naik, E. Meeks, B. Bunting, Combustion and emissions modeling of a gasoline HCCI engine using model fuels, SAE World Congress, 2009, Technical paper in 2009-01-0669.

[153] C. Mueller, W. Pitz, Recent progress in the development of diesel surrogate fuels, Progress in Energy and Combustion Science 37 (2011) 330–350.

[154] M. Huber, B. Smith, L. Ott, T. Bruno, Surrogate mixture model for the thermo-physical properties of synthetic aviation fuel s-8: explicit application of the advanced distillation curve, Energy & Fuels 22 (2008) 1104–1114.

[155] J. Gustavsson, V. Golovitchev, Spray combustion simulation based on detailed chemistry approach for diesel fuel surrogate model, 2003, SAE Technical paper in 2003-01-1848.

[156] R. Natelson, M. Kurman, N. Cernansky, D. Miller, Experimental investigation of surrogates for jet and diesel fuels, Fuel 87 (10-11) (2008) 2339–2342.

[157] N. Peters, H. Barths, H. Pitsch, 3d simulation of di diesel combustion and pollutant formation using a two-component reference fuel, Oil & Gas science and technology 54 (2) (1999) 233–244.

[158] R. Lemaire, A. Faccinetto, E. Therssen, M. Ziskind, C. Focsa, P. Desgroux, Experimental comparison of soot formation in turbulent flames of diesel and surrogate diesel fuels, Proceedings of the Combustion Institute 32 (2009) 737–744.

[159] W. Hentschel, K.-P. Schindler, O. Haahtela, European diesel research IDEA-experimental results from DI diesel engine investigations, 1994, SAE Technical paper in 941954.

[160] S. Som, D. Longman, Z. Lou, M. Plomer, T. Lu, P. S. et al., Simulating flame lift-off characteristics of diesel and bio-diesel fuels using detailed chemical kinetic mechanisms and large eddy simulation turbulence model, Journal of energy resources technology-transactions of the ASME 134 (3).

[161] C. Shaddix, K. Brezinsky, I. Glassman, Analysis of fuel decay routes in the high-temperature oxidation of 1-methylnaphthalene, Combust. Flame. 108 (1-2) (1997) 139–157.

[162] M. Colket, J. Edwards, S. Williams, N. Cernansky, D. Miller, F. E. et al., Development of an experimental database and kinetic models for surrogate jet fuels, 45th AIAA Aerospace Sciences Meeting, Reno, NV, 2007, 2007-0770.

[163] C. Mueller, L. Pickett, D. Siebers, C. Westbrook, Effects of oxygenates on soot processes in DI diesel engines: experiments and numerical simulations, 2003, SAE Technical paper in 2003-01-1791.

[164] B. Buchholz, C. Mueller, Using carbon-14 isotope tracing to investigate molecular structure effects of the oxygenate dibutyl maleate on soot, 2004, SAE Technical paper in 2004-01-1849.

[165] S. Gail, M. Thomson, A wide ranging kinetic modeling study of methyl butanoate combustion, in: Proceedings of the Combustion Institute, Vol. 31, pp. 305–311.

[166] P. Dievart, S. Won, S. Dooley, F. Dryer, Y. Ju, A kinetic model for methyl decanoate combustion, Combustion and Flame 159 (5) (2012) 1793–1805.

[167] O. Herbinet, W. Pitz, Detailed chemical kinetic oxidation mechanism for a biodiesel surrogate, Combustion and Flame 154 (3) (2008) 507â528.

[168] H. Lancheros, M. Fikri, L. Cancino, G. Moreac, C. Schulz, P. Dagaut, Autoignition of surrogate biodiesel fuel b30 at high pressures experimental and moeling kinetic study, Combustion and Flame 159 (2012) 996–1008.

[169] V. Golovitchev, J. Yang, The construction of the combustion models for RME biodiesel fuel for ICE application (2008) 15.

[170] J. Pitz, C. Westbrook, O. Herbinet, E. Silke, Progress in chemical kinetic modeling for surrogate fuels, The 7th COMODIA International Conference on Modeling and Diagnostics for Advanced Engine Systems, Sapporo, Japan, 2008.

[171] J. Eismark, M. Hammas, A. Karlsson, I. Denbratt, D. L., Role of turbulence for mixing and soot oxidation for an equivalent diesel gas jet during wall interaction studied with les, THIESEL 2012 Conference on Thermo- and Fluid Dynamic Processes in Direct Injection Engines, Valencia, 2012.

[172] G. Karau, E. Njagi, A. Machocho, L. Wangai, Phytonutrient, mineral composition and in vitro antioxidant activity of leaf and stem bark powders of pappea capensis, journal of nutrition 11 (2) (2012) 123–132.

[173] Y. Basiron, Bailey's industrial oil and fat products, 6th Edition, 2005, ISBN 978-0-471-38460-1.

[174] V. Gorobei, M. Krutovskikh, O. Vitkovskii, Measurement methods and instruments for the saturated vapor pressure of oil products, Measurement Techniques 49 (3) (2006) 265–269.

[175] K. Sivaramakrishnan, P. Ravikumar, Determination of cetane number of biodiesel and its influence on physical properties, ARPN journal of engineering and applied sciences 7 (2) (2012) 205–211.

[176] F. Harnisch, I. Blei, T. D. Santos, M. Moller, P. Nilges, From the test-tube to the test-engine: assessing the suitability of prospective liquid biofuel compounds, RSC Advances 3 (2013) 9594–9605.

[177] J. Davis, D. Geller, W. Faircloth, T. Sanders, Comparisons of biodiesel produced from unrefined oils of different peanut cultivars, Journal of the American Oil Chemists' Society 86 (2009) 353–361.

[178] D.-C. Cruz-Forero, O. Gonzalez-Ruiz, L. Lopez-Giraldo, Calculation of thermophysical properties of oils and triacylglycerols using an extended constituent fragments approach, Ciencia, TecnologÃa y Futuro, 5 (1) (2012) 67–82.

[179] E. Hammond, L. Johnson, C. Su, T. Wang, P. White, Soybean oil, Bailey's industrial oil and fat products, John Wiley & Sons, 2005, ISBN 978-0-471-38460-1.

[180] R. Payri, F. Salvador, J. Gimeno, Effects of nozzle geometry on direct injection diesel engine combustion process, Applied Thermal Engineering 29 (10) (2009) 2051–2060.

[181] L. Pickett, D. Siebers, C. Idicheria, Relationship between ignition processes and the lift-off length of diesel fuel jets, 2005, SAE Technical paper in 2005-01-0890.

[182] B. Higgins, D. Siebers, A. Aradi, Diesel-spray ignition and premixed-burn behavior, 2000, SAE Technical paper in 2000-01-0940.

[183] S. Choi, Y. Oh, Combustion characteristics of esterified rice bran oil as an altenative fuel in a diesel engine, Automotive Technology 7 (4) (2006) 399–406.

[184] M. Murphy, J. Taylor, R. Mccormick, Compendium of experimental cetane number data, Tech. rep., National Renewable Energy Laboratory (2004).

[185] M. Tat, J. Gerpen, Measurement of biodiesel speed of sound and its impact on injection timing, National Renewable Energy Laboratory (2003) NREL/SR–510–31462.

[186] M. Dzidaa, P. Prusakiewiczb, The effect of temperature and pressure on the physicochemical properties of petroleum diesel oil and biodiesel fuel, Fuel 87 (10-11) (2008) 1941–1948.

[187] R. Payri, F. Salvador, J. Gimeno, G. Bracho, The effect of temperature and pressure on thermodynamic properties of diesel and biodiesel fuels, Fuel 90 (2011) 1172–1180.

[188] J. N. Coupland, D. J. Mcclements, Physical properties of liquid edible oils, JAOCS 74 (1997) 1559–1564.

[189] D. J. Mcclements, M. J. Poveyt, Ultrasonic analysis of edible fats and oils, Ultrasonics 30 (6) (1992) 383–388.

[190] R. Payri, F. Salvador, J. Gimeno, G. Bracho, Effect of fuel properties on diesel spray development in extreme cold conditions, Proc Inst Mech Eng, Part D J Automob Eng 222 (D9) (2008) 1743–1753.

[191] D. Deshmukh, A. Mohan, T. Anand, R. Ravikrishna, High pressure spray characterization of vegetable oils, 23rd Annual conference on liquid atomization and spray ILASS, Brno, Czech Republic, 2010.

[192] A. Hassaneen, Injection characteristics of rapeseed methyl ester versus diesel fuel in pump-line-nozzle injection system, 2008, SAE Technical paper in 2008-01-1590.

[193] S. Steven, Power transformer partial discharge (PD) acoustic signal detection using fiber sensors and wavelet analysis, modeling, and simulation, Ph.D. thesis, virginia Tech. (2002).

[194] H. Takahashi, K. Tomaru, S. Shiga, T. Karasawa, T. Kurabayashi, Characteristics of diesel spray with unsteady and higher injection pressure using a rapid compression machine, 1991, SAE Technical paper in 910226.

[195] H. Hattori, K. Narumiya, Analysis of initial breakup mechanism of diesel spray injected into high-pressure ambience, 2004, SAE Technical paper in 2004-01-0528.

[196] I. Gostic, C. Senghaas, M. Willmann, M. Wensing, How biodiesel/diesel fuel blends affect spray breakup and emissions, 23rd Annual conference on liquid atomization and spray systems, ILASS, Brno, Czech Republic, 2010.

[197] S.-Y. No, Spray characteristics in ci engines fuelled with vegetable oils and its derivatives, 23rd Annual conference on liquid atomization and spray systems, ILASS, Brno, Czech Republic, 2010.

[198] Y. Chi, E. Kim, Measurement of droplet size distribution of transient diesel spray, 1993, SAE Technical paper in 931949.

[199] S. Bari, C. Yu, T. Lim, Effect of fuel injection timing with waste cooking oil as a fuel in a direct injection diesel engine., J Automob Eng 218 (2004) 93–104.

[200] J. Desantes, J. Benajes, S. Molina, C. Gonzalez, The modification of the fuel injection rate in heavy-duty diesel engines., Applied Thermal Engineering 24 (2004) 2701–2714.

[201] . W. Zeuch, Neue Verfahren zur Messung des Einspritzgesetzes und Einspritz-Regelmassigkeit von Diesel-Einspritzpumpen, MTZ 22 (9) (1961) 415– 420.

[202] A. Takamura, T. Ohta, S. Fukushima, T. Kamimoto, A study on precise measurement of diesel fuel injection rate, 1992, SAE Technical paper in 920630 .

[203] M. Marcic, New diesel injection nozzle flow measuring device., Review of Scientific Instruments 71 (4) (2000) 1876–1882.

[204] J. Dec, C. Espey, Soot and fuel distributions in a di diesel engine via 2-d imaging, SAE World Congress, Detroit, MI, 1992, 922307.

[205] L. Pickett, C. Genzale, J. Manin, L.-M. Malbec, L. Hermant, Measurement uncertainty of liquid penetration in evaporating diesel sprays, 23rd Annual ILASS-Americas Conference on Liquid Atomization and Spray Systems, Ventura, CA, 2011.

[206] J. Livengood, P. Wu, Correlation of autoignition phenomena in internal combustion engines and rapid compression machines, International Symposium on Combustion 5 (1) (1955) 347–356.